# MULTISPECTRAL IMAGING FOR PRECLINICAL ASSESSMENT OF RHEUMATOID ARTHRITIS MODELS

by

SOPHIE L. GLINTON

A thesis submitted to the
University of Birmingham
for the degree of
DOCTOR OF PHILOSOPHY

Physical Sciences of Imaging in the Biomedical Sciences
College of Engineering and Physical Sciences
The University of Birmingham
September 2018

## Abstract

Rheumatoid arthritis (RA) is a chronic inflammatory autoimmune condition affecting multiple body systems. Murine models of RA are vital in progressing understanding of the disease. The severity of arthritis symptoms is currently assessed *in vivo* by observations and subjective scoring which are time-consuming and prone to bias and inaccuracy.

The main aim of this thesis is to determine whether multispectral imaging of murine arthritis models has the potential to assess the severity of arthritis symptoms *in vivo* in an objective manner. Given that pathology can influence the optical properties of a tissue, changes may be detectable in the spectral response.

Monte Carlo modelling of reflectance and transmittance for varying levels of blood volume fraction, blood oxygen saturation, and water percentage in the mouse paw tissue demonstrated spectral changes consistent with the reported/published physiological markers of arthritis. Subsequent reflectance and transmittance *in vivo* spectroscopy of the hind paw successfully detected significant spectral differences between normal and arthritic mice. Using a novel non-contact imaging system, multispectral reflectance and transmittance images were simultaneously collected, enabling investigation of arthritis symptoms at different anatomical paw locations. In a blind experiment, Principal Component (PC) analysis of four regions of the paw was successful in identifying all 6 arthritic mice in a total sample of 10. The first PC scores for the TNF dARE arthritis model were found to correlate significantly with bone erosion ratio results from microCT, histology scoring, and the manual scoring method. In a longitudinal study at 5, 7 and 9 weeks the PC scores identified changes in spectral responses at an early stage in arthritis development for the TNF dARE model, before clinical signs were manifest.

Comparison of the multispectral image data with the Monte Carlo simulations suggest that in this study decreased oxygen saturation is likely to be the most significant factor differentiating arthritic mice from their normal littermates.

The results of the experiments are indicative that multispectral imaging performs well as an assessor of arthritis for RA models and may outperform existing techniques. This has implications for better assessment of preclinical arthritis and hence for better experimental outcomes and improvement of animal welfare.

**Acknowledgements**

I would firstly like to thank my project supervisors for all their input to the work, and all their support and consistency in being present to guide, and advise, the progress of the project. Particularly Prof. Ela Claridge, and Dr. Amy Naylor, without whom none of it would have been possible.

I would also like to acknowledge the unique environment of the Physical Sciences of Imaging in the Biological Sciences (PSIBS) Doctoral Training Centre. Through the program I was introduced to new areas of study, and consequently changed my ideas about what I wanted to do in the future. I was also introduced to a brilliant group of people, whose antics I will never forget. Particularly, Nathaniel Wand, for the peculiar journey that we've taken together.

I would also like to thank Dr. Iain Styles, my third supervisor and head of PSIBS for his prompt and helpful answers to my sporadic questions. Also thanks to the Imaging group for their support and conversation in the lab, and to members of the RRG who offered practical help when required. I also have to thank my friends and family for their persistent support, and for pretending to listen to me talk about it all.

Financial support for the project was provided by the EPSRC through a studentship from the PSIBS Doctoral Training Centre (EP/F50053X/1).

# Table of Contents

1 Introduction ........................................................ 1

2 Background ........................................................ 3

2.1 Rheumatoid Arthritis Pathology ........................................................ 3

2.1.1 The Immune System and Autoimmune Disease. ........................................................ 3

2.1.2 Clinical Presentation and Progression of Rheumatoid Arthritis ........................................................ 4

2.1.3 The Structure of the Synovial Joint ........................................................ 5

2.1.4 The Development and Pathophysiology of Rheumatoid Arthritis ........................................................ 5

2.2 Optically Relevant Variation in Rheumatoid Arthritis ........................................................ 8

2.2.1 Hypoxia ........................................................ 9

2.2.2 Blood Volume Fraction ........................................................ 10

2.2.3 Oedema ........................................................ 11

2.3 Imaging of Rheumatoid Arthritis ........................................................ 11

2.3.1 Radiographic Imaging ........................................................ 12

2.3.2 Magnetic Resonance Imaging ........................................................ 12

2.3.3 Ultrasound Imaging ........................................................ 13

2.3.4 Nuclear Imaging ........................................................ 13

2.3.5 Optical Imaging ........................................................ 14

2.4 Mouse Models in Rheumatoid Arthritis Research ........................................................ 17

2.4.1 TNF dARE ........................................................ 18

2.4.2 K/BxN Serum Transfer ........................................................ 20

2.4.3 Collagen Induced Arthritis (CIA) ........................................................ 21

2.5 Assessment of Mouse Model Disease Symptoms ........................................................ 22

2.5.1 In vivo Assessment of Murine Disease ........................................................ 23

2.5.2 Ex Vivo Arthritis Assessment ........................................................ 30

**2.6 Light Interaction with Tissue** ........ 32
2.6.1 Reflection ........ 32
2.6.2 Transmission ........ 32
2.6.3 Physics Concepts ........ 33
2.6.4 The Optical Properties of Biological Tissues ........ 38
2.6.5 Modelling of Photon Transport within a Biological Tissue ........ 40
2.6.6 Methods of Modelling Photon Transport ........ 40
2.6.7 Extracting Optical Properties from Optical Measurements ........ 43
**2.7 Introduction to Multispectral Imaging** ........ 44
**2.8 Hypothesis** ........ 46
**3 Monte Carlo Modelling Optical Reflectance and Transmittance of the Mouse Hind Paw** ........ 47
**3.1 Introduction** ........ 47
**3.2 Equipment and Methodology** ........ 47
3.2.1 The Multi-Layered Monte Carlo Model ........ 47
**3.3 Experimental Method Development** ........ 49
3.3.1 Tissue Optical Parameters ........ 49
3.3.2 Chromophore Concentrations ........ 55
**3.4 Results** ........ 56
3.4.1 Modelling the Spectral Variation with Arthritis ........ 56
3.4.2 Spectral Variation with Localised Parameter Changes ........ 59
**3.5 Discussion** ........ 60
3.5.1 Discussion of Results ........ 60
3.5.2 Limitations ........ 65
3.5.3 Conclusion ........ 65
**4 Spectrophotometry of Rheumatoid Arthritis Mouse Models** ........ 66

**4.1 Introduction** .......... **66**

**4.2 Equipment and Methodology** .......... **66**

4.2.1 Light Source .......... 66

4.2.2 Spectrometer(s) .......... 67

4.2.3 Mouse Models .......... 68

4.2.4 Imaging Protocol .......... 69

**4.3 Experimental Method Development** .......... **70**

4.3.1 Spectrophotometry System set-up .......... 70

4.3.2 System Calibration .......... 71

**4.4 Results** .......... **73**

4.4.1 In Vivo Diffuse Reflectance and Transmission Spectrophotometry .......... 73

**4.5 Discussion** .......... **78**

4.5.1 Discussion of Results .......... 78

4.5.2 Limitations .......... 79

4.5.3 Conclusion .......... 80

**5 Multispectral Imaging System Set-up and Characterisation** .......... **81**

**5.1 Introduction** .......... **81**

**5.2 Equipment and Methodology** .......... **81**

*5.2.1* Light Source .......... 82

*5.2.2* Filters .......... 82

*5.2.3* Illuminating Ring and Optic Fibres .......... 84

*5.2.4* Camera .......... 84

*5.2.5* Polarisers, Diffuser and Mirror .......... 84

*5.2.6* Structural Components .......... 86

*5.2.7* Additional Components .......... 86

**5.3 Experimental Method Development** .......... **86**

5.3.1 Pathways of Light for Reflectance and Transmittance Imaging ........................ 86

5.3.2 Spectral Calibration of the Imaging System..................................................... 89

5.3.3 System Characterisation and Parameter Tuning .............................................. 92

**5.4 Results........................................................................................................................ 99**

5.4.1 Phantom Imaging for Validation of Spectral Calibration Method ........................ 99

5.4.2 Phantom Imaging .............................................................................................. 101

**5.5 Discussion...............................................................................................................103**

5.5.1 Discussion of Results ........................................................................................ 103

5.5.2 Limitations.......................................................................................................... 104

5.5.3 Conclusion ......................................................................................................... 105

**6 Multispectral Imaging of Rheumatoid Arthritis Mouse Models ........................ 107**

**6.1 Introduction.............................................................................................................107**

**6.2 Equipment and Methodology ..............................................................................108**

6.2.1 Mouse Models.................................................................................................... 108

6.2.2 Mouse Imaging .................................................................................................. 109

6.2.3 Histology ............................................................................................................ 109

6.2.4 MicroCT Imaging and Bone Erosion Analysis................................................... 110

6.2.5 Image Registration ............................................................................................ 112

6.2.6 Principal Component Analysis........................................................................... 113

6.2.7 Linear Discriminant Analysis ............................................................................. 114

**6.3 Experimental Method Development....................................................................114**

6.3.1 Multispectral Images of a Mouse Hind Paw....................................................... 114

6.3.2 Multispectral Data Analysis ............................................................................... 115

**6.4 Results......................................................................................................................116**

6.4.1 Multispectral Imaging of the TNF dARE Rheumatoid Arthritis Model ............... 116

6.4.2 K/BxN Serum Transfer Model Imaging ............................................................. 139

6.4.3 Feature Mapping ... 146

**6.5 Discussion ... 152**

6.5.1 Discussion of Results ... 152

6.5.2 Limitations ... 154

6.5.3 Conclusion ... 154

**7 Conclusions and Future Work ... 156**

**7.1 Summary of Findings ... 156**

**7.2 Comparison with Literature ... 159**

**7.3 Wider Implications of Results ... 160**

**7.4 Future Work ... 161**

7.4.1 Further Development of the Imaging System ... 161

7.4.2 Potential Methods for Reducing Image Acquisition Time ... 162

7.4.3 Model Development ... 163

**7.5 Multispectral Imaging for Rheumatoid Arthritis in Humans? ... 164**

**7.6 Final Conclusion ... 165**

**8 Appendices ... 166**

**A1 Implementation of MCML modelling ... 166**

**A2 MCML additional outputs ... 166**

**A3 MCML Model for Alternative Regions of the Paw ... 167**

**A4 Tophat Diffuser vs Lambertian Diffuser ... 169**

**A5 Change in the Spectral Output of the Light Source Over Time ... 170**

**A6 TNF dARE 12 week Imaging RMS Error ... 170**

**A7 K/BxN ST RMS Error ... 171**

**A8 Human Imaging ... 172**

**9 References ... 173**

## List of Figures

Figure 1: Schematic diagram of the typical structure of a synovial joint. ............................ 6
Figure 2: Schematic diagram showing the morphologic changes which typically occur with rheumatoid arthritis. ........................................................................ 8
Figure 3: Examples images for clinical and experimental methods of imaging the effects of rheumatoid arthritis in the hand joints. ............................................................ 16
Figure 4: Photographs showing a single case of a TNF dARE hind paw affected by symptoms of arthritis and a single case of a normal mouse foot. ...................... 20
Figure 5: Increasing severity of CIA symptoms in a mouse front paw. ............................... 22
Figure 6: The complete scoring form used to monitor mouse models of arthritis at the University of Birmingham. ................................................................... 24
Figure 7: Examples of in vivo imaging for symptoms of joint inflammation in rodent models of rheumatoid arthritis. ........................................................................ 29
Figure 8: Haematoxylin and Eosin stained sagittal sections of mouse hind paws. ............. 30
Figure 9: Reconstructed meshes of wildtype and TNF dARE mouse hind paws imaged by microCT. ............................................................................................... 31
Figure 10: Schematic of a block of tissue describing the paths of ballistic and diffusely transmitted photons, specular and diffusely reflected photons, and photon absorption. ....................................................................................... 33
Figure 11: Absorption and scatter coefficients for common biological chromophores and tissues. ........................................................................................... 37
Figure 12: Graph describing the Rayleigh and Mie contribution to the reduced scattering coefficient of typical human dermis. ................................................................ 39
Figure 13: Flow diagram for the basic process of Monte Carlo calculations for propagating photons in a homogenous semi-infinite slab. .................................................. 42
Figure 14: Several examples of simulated photon walks through a tissue slab using the Multi-Layered Monte Carlo (MCML (124)) model of photon propagation through layered media ............................................................................................. 43
Figure 15: The coordinate system used by MCML for modelling photon propagation. ........ 49
Figure 16: Measurements of tissue layer thickness obtained from analysis of H&E stained mouse paw sections. ....................................................................... 51
Figure 17: Absorption coefficient values ($cm^{-1}$) in the wavelength range 450nm to 1000nm for common biological chromophores ............................................................ 52
Figure 18: Scatter coefficients for biological tissues fitted to equation 10. ......................... 54

Figure 19: Reflectance and transmittance spectra from a Monte Carlo model of the ‘midfoot’ mouse hind paw in a ‘normal’ and ‘arthritic’ state. ............................................ 58
Figure 20: The effect of changing individual model parameters on reflectance and transmittance spectra for a Monte Carlo model of the mouse hind paw ............ 61
Figure 21: Root mean squared (RMS) difference resulting from changing individual model parameters for reflectance and transmittance spectra for a Monte Carlo model of the mouse hind paw.......................................................................... 62
Figure 22: Ocean Optics HL-2000-FHSA light source used for collecting spectrophotometry measurements. ....................................................................................... 67
Figure 23: Spectrometers used to collect reflectance and transmittance spectral measurements ........................................................................................ 68
Figure 24: Spectrophotometry system set-up for collecting spectral measurements from mouse models of rheumatoid arthritis. ........................................................ 71
Figure 25: Spectralon reflectance standards used for calibrating spectrophotometry measurements. ....................................................................................... 73
Figure 26: Spectrophotometry reflectance and transmittance data for normal and TNF dARE mice with standard deviation. ........................................................................ 74
Figure 27: Reflectance and transmittance data for CIA mice hind paws. ........................... 77
Figure 28: ThorLabs OSL1-EC light source for the multispectral imaging system............... 82
Figure 29: Spectral transmission of Vis-07 and NIR-10 Varispec filters. ............................ 83
Figure 30: Quantum efficiency of the RetigaExi CCD camera. .......................................... 85
Figure 31: OpenSCAD designs for 3D printed structural components of the system rendered in Meshlab. .......................................................................................... 87
Figure 32: Set-up of the multispectral imaging system. ..................................................... 89
Figure 33: Reflectance and transmittance data required for spectral calibration. ................ 92
Figure 34: Gaussian sigma value describing image blur with changing aperture size......... 95
Figure 35: Signal to noise ratio measured for a series of images of an Edmund Optics focussing tile across wavelengths 450nm to 975nm, taken with the multispectral imaging system. ........................................................................................ 97
Figure 36: Variation of Varispec filter transmission bandwidth and its effect on spectral measurements ........................................................................................ 99
Figure 37: Spectral data from multispectral imaging of phantoms. .................................. 101
Figure 38: Spectral data from multispectral imaging and Monte Carlo modelling of an INO Biomimic optical phantom. ................................................................... 103

Figure 39: Example images demonstrating scoring joints affected by arthritis in increasing severity from left to right. .................... 110
Figure 40: A mouse hind paw mesh generated from a microCT scan and coloured to indicate how the bones of the hind paw were divided into areas for regression analysis with multispectral imaging results. .................... 112
Figure 41: Reflectance and transmittance images taken at a series of wavelengths for a single normal mouse hind paw. .................... 115
Figure 42: Process of multispectral image analysis using a custom Matlab GUI to extract spectral data from regions of interest. .................... 116
Figure 43: Min-max normalised reflectance spectral data from four areas of the TNF dARE mouse hind paws from six 12-week old mice, 3 x TNF dARE and 3 x normal. . 119
Figure 44: Results from principal component analysis of reflectance spectral data from four areas of the TNF dARE mouse hind paws from six 12-week old mice, 3 x TNF dARE and 3 x normal. .................... 120
Figure 45: Min-max normalised transmittance spectral data from four areas of the TNF dARE mouse hind paws hind paws from six 12-week old mice, 3 x TNF dARE and 3 x normal. .................... 123
Figure 46: Results from principal component analysis of transmittance spectral data from four areas of the TNF dARE mouse hind paws from six 12-week old mice, 3 x TNF dARE and 3 x normal. .................... 123
Figure 47: Comparison of the 1st principal component scores from principal component analysis of reflectance and transmittance spectral data from four areas of the TNF dARE mouse hind paws from six 12-week old mice, 3 x TNF dARE and 3 x normal. .................... 125
Figure 48: Comparison of the 1st principal component scores from reflectance spectral data vs the bone erosion scores from microCT from four areas of the TNF dARE mouse hind paws from six 12-week old mice, 3 x TNF dARE and 3 x normal. 127
Figure 49: Comparison of the 1st principal component scores from transmittance spectral data vs the bone erosion scores from microCT from four areas of the TNF dARE mouse hind paws from six 12-week old mice, 3 x TNF dARE and 3 x normal………….. 126.
Figure 50: Two example meshes from the microCT analysis using MArthA described in section 6.4.1.4. .................... 129

Figure 51: Comparison of the mean 1st principal component scores from reflectance and transmittance spectral data vs the histology scores for the TNF dARE mouse hind paws from six 12-week old mice, 3 x TNF dARE and 3 x normal. ............ 130
Figure 52: Comparison of the mean 1st principal component scores from reflectance and transmittance spectral data vs the manual scores for the TNF dARE mice from six 12-week old mice, 3 x TNF dARE and 3 x normal. .................................... 131
Figure 53: Progression of the 1st principal component scores from reflectance spectral data for TNF dARE mice hind paws from six 5-week to 9-week old female mice, 3 x TNF dARE and 3 x normal. ................................................................. 134
Figure 54: Reflectance score, manual score and weight for TNF dARE mice from 5 weeks to 9 weeks. ........................................................................................ 135
Figure 55: Comparison of the 1st principal component scores from reflectance spectral data vs the bone erosion scores from microCT from four areas of the TNF dARE mouse hind paws. Reflectance scores and bone erosion from six 5-week to 9-week old mice, 3 x TNF dARE and 3 x normal. P-values and r-values calculated by Pearson correlation analysis. .................................................................. 136
Figure 56: Min-max normalised reflectance spectral data from four areas of the K/BxN ST mouse hind paw hind paws from four mice, 3 x K/BxN ST and 1 x normal. ...... 140
Figure 57: Results from principal component analysis of reflectance spectral data from four areas of the K/BxN ST mouse hind paws from four mice, 3 x K/BxN ST and 1 x normal. ............................................................................................... 141
Figure 58: Min-max normalised transmittance spectral data from four areas of the K/BxN ST mouse hind paws from four mice, 3 x K/BxN ST and 1 x normal. Mean spectra for the normal group are displayed In blue with standard deviation shown as a pale blue shaded region and in red for the K/BxN ST data. .................................. 143
Figure 59: Results from principal component analysis of transmittance spectral data from four areas of the K/BxN ST mouse hind paws from four mice, 3 x K/BxN ST and 1 x normal. .............................................................................................. 143
Figure 60: Comparison of the 1st principal component scores from reflectance and transmittance spectral data vs the calliper measurements for the K/BxN ST mouse hind paws for reflectance and for transmittance scores from four K/BxN ST mice, 3 x K/BxN ST and 1 x normal.. ....................................................... 144
Figure 61: Reflectance and transmittance spectra for 13122 iterations of the Monte Carlo hind paw model with varying parameters. ..................................................... 147

Figure 62: Feature maps for the TNF dARE mice using linear discriminant analysis of Monte Carlo modelled spectra to define axes relating to muscle oxygen saturation, muscle blood volume fraction and dermis blood volume fraction...................... 148
Figure 63: Feature maps for the K/BxN ST mice using linear discriminant analysis of Monte Carlo modelled spectra to define axes relating to muscle oxygen saturation, muscle blood volume fraction and dermis blood volume fraction...................... 149
Figure 64: Spectral angle maps produced from calculating the angle of intersecting tangents to the spectra at 670nm and 585nm for TNF dARE mice................................ 152
Figure 65: Potential set-up for a multispectral system which would not require anaesthetic.. ........................................................................................................ 161
Figure 66: Results of Monte Carlo MCML simulations of light propagation in the model of normal mouse tissue described in section 3.4.1.............................................. 167
Figure 67: Reflectance and transmittance spectra from a Monte Carlo model of the heel, joints, and toes mouse hind paw in a ‘normal’ and ‘arthritic’ state. ................... 168
Figure 68: Difference in the detected transmittance of a Lambertian scatterer and a tophat diffuser......................................................................................................... 169
Figure 69: Difference over 0 minutes to 100 minutes of the Thorlabs OSL1-EC fibre light source. Difference between x and 100 minutes is plotted for 5 timepoints across the wavelengths 450nm to 975nm. ................................................................ 170
Figure 70: Root mean squared error for the difference between the mean of the raw spectra of the normal mice and the TNF dARE mice in reflectance and transmittance. 171
Figure 71: Root mean squared error for the difference between the mean of the raw spectra of the normal mice and the K/BxN ST mice in reflectance and transmittance... 171
Figure 72: Reflectance spectra and transmittance spectra from human finger joints from 2 different subjects. ......................................................................................... 172

## List of Tables

Table 1: Tabulated values for anisotropy and refractive index used for Monte Carlo modelling of the mouse hind paw. The source reference for each value is given in subscripted brackets. ........ 54

Table 2: Values for blood volume fraction, blood oxygenation (Hb balance), and water concentration (H2O) used in the Monte Carlo model. The values outside the brackets indicate typical values for concentration of the three absorbers within the tissue types. Ranges of values indicated by literature are given within brackets and the subscripted brackets contain references........ 55

Table 3: Parameters sampled by the Monte Carlo model........ 147

## List of Abbreviations

| | |
|---|---|
| **AIA** | Adjuvant Induced Arthritis |
| **ARE** | AU-Rich Element |
| **BOLD** | Blood Oxygen Level Dependent |
| **BVF** | Blood Volume Fraction |
| **CAIA** | Collagen Antibody-Induced Arthritis |
| **CCD** | Charge-Coupled Device |
| **CIA** | Collagen Induced Arthritis |
| **CPC** | Cross Polarisation Colour |
| **CT** | Computed Tomography |
| **DA** | Diffusion Approximation |
| **DMARD** | Disease-Modifying Antirheumatic Drug |
| **DOI** | Diffuse Optical Imaging |
| **DOT** | Diffuse Optical Tomography |
| **EDTA** | Ethylenediaminetetraacetic Acid |
| **FD-DOT** | Frequency-Domain Diffuse Optical Tomography |
| **GPI** | Glucose-6-Phosphate Isomerase |
| **H&E** | Haematoxylin and Eosin |
| **Hb** | Deoxygenated Haemoglobin |
| **$HbO_2$** | Oxygenated Haemoglobin |
| **HHb** | Total Haemoglobin Concentration |
| **HIF-1** | Hypoxia-Inducible Factor |
| **IRF** | Instrument Response Function |
| **LDA** | Linear Discriminant Analysis |
| **MC** | Monte Carlo |
| **MCML** | Multilayered Monte Carlo Model |
| **MHC** | Major Histocompatibility Complex |
| **MI** | Multispectral Imaging |
| **MMP** | Matrix Metalloproteinase |
| **MR** | Magnetic Resonance |
| **MRI** | Magnetic Resonance Imaging |
| **mRNA** | Messenger Ribonucleic Acid |
| **MSOT** | Multispectral Optoacoustic Tomography |
| **ND** | Neutral Density |
| **NIR** | Near-Infrared (700nm to 1000nm) |

| | |
|---|---|
| **NIRF** | Near-Infrared Fluorescence |
| **NSAID** | Nonsteroidal Anti-Inflammatory Drug |
| **OA** | Osteoarthritis |
| **OST** | Optical Spectral Transmission |
| **PAT** | Photoacoustic Tomography |
| **PC** | Principal Component |
| **PCA** | Principal Component Analysis |
| **PET** | Positron Emission Tomography |
| **PIP** | Proximal Interphalangeal |
| **PLY** | Polygon File Format |
| **PSF** | Point Spread Function |
| **RA** | Rheumatoid Arthritis |
| **RAG** | Recombinant Activation Gene |
| **RMS** | Root Mean Square |
| **RTE** | Radiative Transfer Equation |
| **SFDI** | Spatial Frequency Domain Imaging |
| **SLOT** | Sagittal Laser Optical Tomography |
| **SNR** | Signal to Noise Ratio |
| **$SO_2$** | Oxygen Saturation |
| **SPECT** | Single-Photon Emission Computed Tomography |
| **SSM** | Statistical Shape Model |
| **ST** | Serum Transfer |
| **TCR** | T-Cell Receptor |
| **TNF** | Tumour Necrosis Factor |
| **TR-DOS** | Time-Resolved Diffuse Optical Spectroscopy |
| **US** | Ultrasound Sonography |
| **USPIO** | Ultrasmall Superparamagnetic Iron Oxide |

# 1 Introduction

This thesis reports the results of investigating the use of multispectral imaging (MI) for the assessment of mouse models of rheumatoid arthritis. A non-invasive imaging technology which allowed objective assessment of physiological changes could be very useful in extending the efficacy of *in vivo* studies by staging the development of arthritis symptoms more accurately. MI has several inherent advantages over alternative methods of *in vivo* imaging. Visible and near-infrared (NIR) radiation is non-ionising and non-damaging (providing the light intensity is kept within a certain limit). The equipment is generally relatively cheap and no extra clinical procedures are necessary such as the injections required for contrast enhancement. MI has good spatial and good spectral resolution, which is useful in the case of small and heterogeneous tissues like the mouse hind paw. The mouse hind paw is a thin tissue of approximately 2–3 mm depth making it suitable for both reflectance and transmission imaging regimes across the visible and NIR spectrum, as light should traverse the tissues relevant to the symptoms of joint inflammation. Spectral imaging gives information about physiological changes in the tissue which may precede the structural changes imaged by traditional imaging methods. Multispectral imaging could be useful in its own right but could also be potentially used as an adjunct to other optical imaging methods.

## Aims

- Assess whether arthritis causes detectable changes in the visible and NIR infrared region of the spectrum by modelling the observed changes in line with quantitative changes cited in literature.
- Build a multispectral imaging system for the purpose of imaging mouse feet in the visible and NIR wavelengths.
- Correlate spectral changes with other indicators of arthritis damage.
- Establish the credentials of this technique as a possibility for monitoring mouse health.

# 2 Background

This chapter presents the background material covering the following areas of this interdisciplinary work: The medical background, pathophysiology of rheumatoid arthritis (RA), together with the changes induced by disease that impact the optical properties of tissue (section 2.1 and 2.2). Current methods of imaging utilized in clinical and research settings are outlined and used to set developing optical imaging modalities in context (section 2.3). Mouse models of RA are introduced and described in terms of their role in RA research and the methods used to assess mouse arthritis symptoms (sections 2.4 and 2.5). The physics background introduces the basic concepts of light interaction with tissue and the modelling techniques used for simulation of radiative transfer (section 2.6). Finally, an introduction to multispectral imaging is provided (section 2.7).

## 2.1 Rheumatoid Arthritis Pathology

The following section gives background on the development of RA, the timeline of the symptoms of the disease, and the pathophysiology of disease progression.

### 2.1.1 The Immune System and Autoimmune Disease

Rheumatoid arthritis is believed to be an autoimmune disease, arising from deregulation of the hosts immune defence system where it mistakes components of the body’s own tissues for a foreign antigen and attempts to attack and eliminate it as it would for an invading pathogen. The inappropriate recognition of the host tissues causes an inflammatory response that damages the affected area progressively over time, often irreparably, and continues throughout the lifetime of the host.

The mammalian immune system comprises the innate immune system and the adaptive immune system. The innate immune system responds to a set number of highly conserved pathogenic moieties, whereas the adaptive immune system is flexible and has the potential to recognise and respond to any foreign antigen. It is essential for resistance to infection and is responsible for immune memory. In the case of infection, specialised immune cells of the adaptive immune system coordinate a pathogen-specific response by recognising foreign molecules present on the surface of invading pathogens and initiating an inflammatory response to destroy them. In rheumatoid arthritis, this protective process turns against the host, inappropriately recognising and attacking the native tissues.

Developing adaptive immune cells undergo a random genetic mutation process that allows them to recognise a potentially infinite array of molecules, including ‘self’ molecules present in the hosts own body. Normally, these self-recognising cells are deactivated or destroyed in the developmental process, but in the case of autoimmune disease, they escape detection and become activated, driving an inflammatory response against the host’s own tissues (1).

### 2.1.2 Clinical Presentation and Progression of Rheumatoid Arthritis

Rheumatoid arthritis is predominantly a disease of the joints. Early RA is characterised by pain, swelling, redness and stiffness in one or several articular joints, which is generally worse in the mornings or following periods of rest. RA most often arises in middle age and has a noticeable gender bias towards women with 75% of sufferers being female (2). Diagnosis follows a series of clinical tests and physical examinations where the affected joints will be examined individually by clinicians and blood tests will be taken looking for markers of inflammation. The early symptoms do not guarantee full development of RA. In approximately 50% of cases, the symptoms will spontaneously resolve (3). However, for the patients who go on to develop RA, early diagnosis is an important factor in the successful symptom management and treatment, and therefore highly influential in patient prognosis (4). Whilst it cannot currently be cured, targeting early disease with disease modifying anti-rheumatic drugs (DMARDs) and biologics is known to slow the progression of joint damage over time. Other treatments focus on management of pain and inflammation, with steroids or non-steroidal anti-inflammatory drugs (NSAIDs).

### 2.1.3 The Structure of the Synovial Joint

Joints allow flexibility and movement of the skeleton. Some joints such as those in the spine or skull are semi-flexible or fixed, but the majority of joints are formed where two or more bones meet and articulate to allow for mobility and motion. These are known as synovial joints (see Figure 1), eponymously named for the synovial cells which line the joint capsule, forming a tough, fibrous membrane enclosing the joint space that produces synovial fluid. The two ends of the bone are covered in smooth cartilage presenting a low friction interface, lubricated by the fluid that fills the cavity. Figure 1 presents the general structure of the synovial joint.

### 2.1.4 The Development and Pathophysiology of Rheumatoid Arthritis

In early RA, inflammation begins in the synovial membrane. The synovial cells normally form a thin layer one to three cells thick and function as a nutrient source for the avascular cartilage tissue via the production of synovial joint fluid. However, in RA, proliferation of the synovial cells and infiltration of activated immune cells into the joint

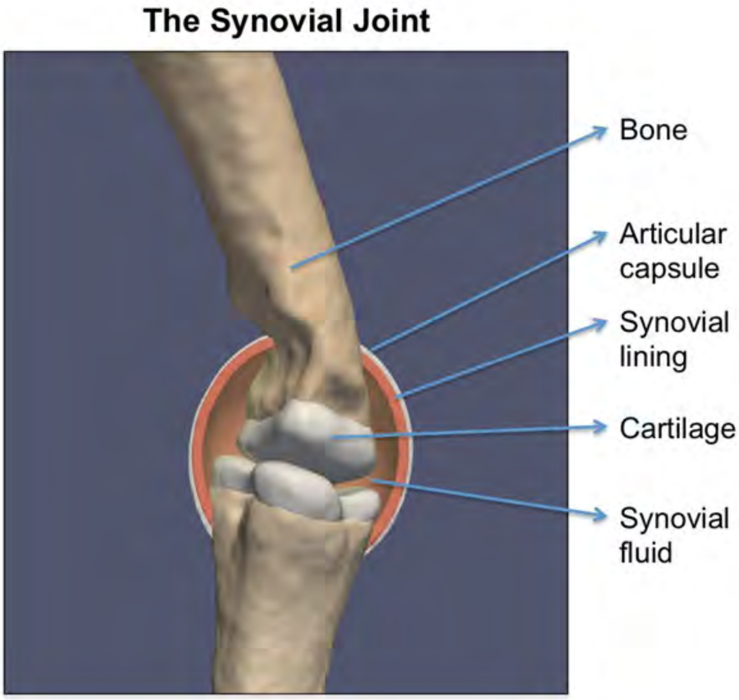

Figure 1: Schematic diagram of the typical structure of a synovial joint. The articular capsule surrounds the joint but in the diagram has been cut in half to show the synovial tissue lining the capsule and the cartilage covered articulating surfaces of the bones. Arrows indicate different tissue types.

tissues causes hyperplasia of the membrane, thickening the synovium by around 10 times (5). Outwardly, symptoms of pain, swelling and redness occur in affected joints. During the inflammatory response the synovial fluid may increase in volume, decrease in viscosity, and vastly increase in immune cell count. However, the cartilage and bone typically remain intact through the early stages of disease rendering radiographic imaging negative of signs of arthritis (6). At this early stage one or several joints can be involved, usually the small joints of the hands and feet.

Persistent synovitis, or synovial inflammation, of over 12 weeks duration is known to be the strongest predictor of full rheumatoid arthritis development (7). As the early stages of disease pathology progress, high metabolic demands of the hyperplastic synovium and immune cell infiltrate lower the oxygen tension in the joint triggering angiogenic processes to form new vasculature. Synovial cells continue to proliferate and assume a more aggressive fibroblastic phenotype (8). The thickened synovium, also known as the pannus, begins to invade the joint space and destroy the underlying cartilage and bone (see Figure 2). Consequently, the joint space narrows and mobility can be reduced. Pain and swelling may persist and patients may experience general malaise, weakness, muscle atrophy, and morning joint stiffness that lasts for several hours. Often joint involvement is symmetric across the body.

The symptoms of joint inflammation continue as the disease progresses, often arising in episodes of acute flare-ups where joints will temporarily become more swollen before symptoms abate in a period of remission. The underlying damage to the hard tissues of the joints progresses both through and between these episodes and the joints can become progressively more deformed, limiting the range of movement. Erosion of periarticular bone is a typical feature observed in advanced rheumatoid arthritis patients by radiographic imaging methods. In a healthy individual, bone remodelling is a tightly regulated process which preserves bone integrity over time. Cells which form bone (osteoblasts) and cells which resorb bone (osteoclasts) are responsible for maintaining bone homeostasis. There is a known regulative association between the immune system and bone remodelling (9), a process which becomes disrupted in RA and tipped in favour of bone erosion. Inflammatory processes have a role in triggering bone erosion through osteoclast activation. Synovitis as well as osteitis correlate with the degree of radiographic bone erosion (10,11). Bone erosions are most observed at the interface between the synovium and the bone, where osteoclasts are known to gather. Bone erosion is an important feature in RA monitoring because increased erosion results in a more severe disease course. In the later stages of the disease, permanent damage to the bone structure and cartilage can lead to loss of joint function. Figure 2 shows a representation of the changes which occur in the joint during RA.

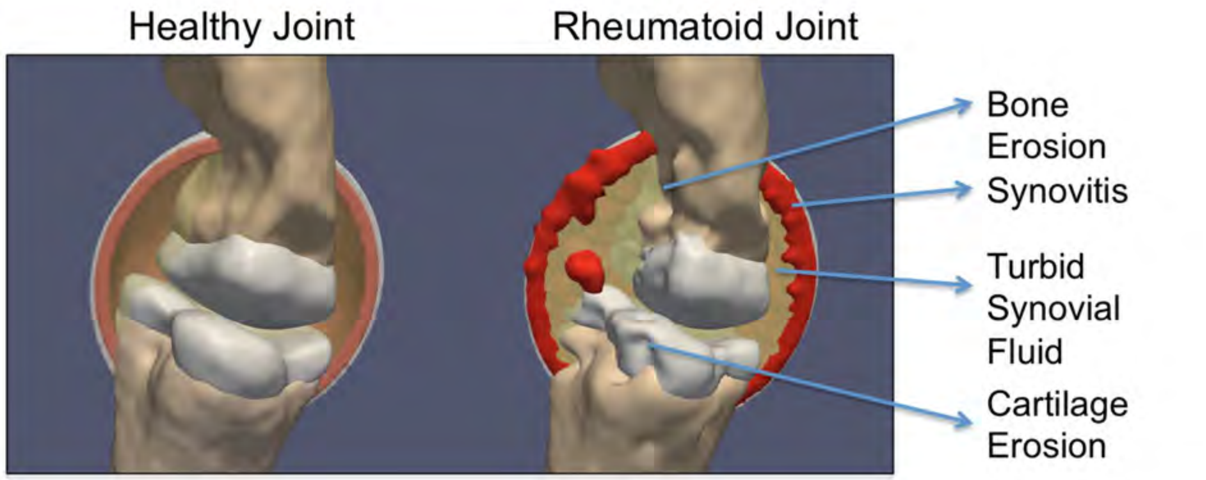

Figure 2: Schematic diagram showing the morphologic changes which typically occur with rheumatoid arthritis. The rheumatoid joint on the right of the image displays hypertrophic expansion of the synovial lining, along with bone and cartilage erosion and increased turbidity of the synovial fluid. These RA symptoms typically occur in mid to late stage RA.

The chronic inflammation associated with RA can also lead to extra-articular manifestations of the disease. Many of the body’s systems can be affected including the pulmonary system, the circulatory system, and the skin and eyes. These extra-articular manifestations are ultimately the cause of increased mortality and a major predictor of decreased life span (12).

## 2.2 Optically Relevant Variation in Rheumatoid Arthritis

Inflammatory conditions in the rheumatoid joint are thought to change the concentrations of biological chromophores present in the articular and periarticular tissues. Evidence for the changes in concentration of biological chromophores is discussed below.

### 2.2.1 Hypoxia

Hypoxia refers to the state of insufficient oxygenation in the tissues and is known to occur in conjunction with inflammation. In the rheumatoid joint, the high metabolic demands of immune cell influx and the phenotypically altered, hypertrophic synovium is known to result in a decrease of dissolved oxygen in the joint tissues (13). Oxygen probes in the form of spectrometers coupled to optically active chemical sensors can directly measure the partial pressure of dissolved oxygen in mmHg. Oxygen partial pressure has been measured as 63mmHg in healthy finger joints compared to 27 mmHg in RA (14) and has more recently been measured as 22.5mmHg in the affected synovium (15). Crucially, the partial pressure of oxygen was shown to correlate with markers of inflammation (15), indicating that hypoxia may correlate with disease severity. This property of RA is relevant to optical imaging because hypoxia in the tissue is thought to reduce the ratio of oxygenated haemoglobin to deoxygenated haemoglobin, two biological chromophores with differing absorption spectra (described in section 2.6.3.2). However, whilst low partial pressure of oxygen will induce lower haemoglobin oxygen saturation in the surrounding tissue, exact values of haemoglobin oxygen saturation are difficult to measure *in vivo.* Blood oxygen level dependent (BOLD) MRI exploits the differing magnetic properties of haemoglobin in its oxygenated and deoxygenated forms and shows decreased signal in rheumatoid joints indicative of decreased oxygenation in the microvasculature of rabbit models of arthritis (16). In modelling the rheumatoid finger joint Milanic *et al.* (17) used values of 95% saturation for the healthy joint and 48% saturation for the rheumatoid synovium, which correspond to the oxygen partial pressure values mentioned above according to the haemoglobin saturation curve. Microscopic multispectral imaging of tendon microvasculature in a model of murine RA has measured haemoglobin oxygen saturation as 94.8 ± 7.0 % for healthy mice and 84.0 ± 13.5 % for inflamed (18). Overall there is reasonable evidence to suggest that hypoxia occurs in the rheumatoid joint and that the haemoglobin oxygen saturation of the local tissues reduces, giving it the potential to change the bulk optical properties of rheumatoid tissue.

### 2.2.2 Blood Volume Fraction

Angiogenesis in the rheumatoid synovium happens in response to inducible factors which are released under hypoxic conditions. There is a marked increase in the expression of cellular factors related to hypoxia (19), such as Hypoxia Inducible Factor (HIF-1), which activates genes associated with the formation of new vasculature (20). In RA, the new vasculature fails to restore normoxia and the joint environment remains hypoxic (13). The formation of new blood vessels brings increased blood flow to the tissue, therefore increasing optical absorption. Biopsy of synovial tissue shows a high proportion of vessels expressing neovascular markers, which is evident even in early disease (21). The degree of synovial vascularity is evidently important in disease pathogenesis as Power Doppler assessment of the synovial vascularity correlates well with radiographic damage (22). Using microCT to measure vascularisation in the knee joints of human TNF transgenic mice perfused with lead containing contrast agent, the vessel volume per tissue volume was seen to increase in 4 concentric, spherical volumes of interest surrounding the synovial cavity, excepting the 1st ROI containing the area immediately around the joint (23). The results of this paper by Gayetskyy *et al*. suggest that blood volume fraction (BVF) increases in the joint tissue and periarticular tissue due to angiogenesis by approximately 60 – 70%, although the immediate synovial area can be seen to decrease. This is hypothesised to be because although vascularisation increases overall, the healthy synovium has better vascularisation which decreases as the synovium hypertrophies, contributing to hypoxia.

### 2.2.3 Oedema

Rheumatoid arthritis symptoms result in local swelling of the joints. In inflammatory conditions, the endothelial barrier of local blood vessels becomes disrupted and vasodilation increases blood flow to the tissue, increasing the outflux of fluid and the extravasation of immune cells into the interstitial space (24). In the majority of mouse models of RA, some form of oedema is evident in the paws as an increase in the volume with symptom development. Given that oedema represents an increase in the tissue volume of water, which has increased absorption coefficients in the longer NIR wavelengths, it is potentially detectable by optical imaging methods. In a paper by Perilli *et al*. measuring soft tissue volume increase with microCT, collagen antibody-induced arthritis (CAIA) mice have an average paw volume increase of 36% (25).

## 2.3 Imaging of Rheumatoid Arthritis

A window of opportunity occurs in RA for the targeting of novel drugs which slow the early progression of disease. With the development of these drugs and the increasing emphasis on early diagnosis, traditional clinical imaging methods are becoming inadequate for detection of early pathology. This has led to increasing interest in the development of novel imaging modalities targeting early disease. Outlined below are some of the clinical techniques for imaging RA pathology, along with more recently developed techniques aimed at detecting changes in the developmental stages.

### 2.3.1 Radiographic Imaging

Imaging has proved a useful addition to clinical examination in rheumatoid arthritis diagnosis and management, improving the accuracy of assessment of inflammation (26). Planar radiographic imaging is commonly used in the assessment of RA in the hands and feet. It is cheap, quick, and can provide longitudinal imaging of the progression of bone erosion and joint space narrowing (figure 3a). Computed Tomography (CT) is thought to be the most sensitive imaging technique for detection of bone erosions but is rarely in clinical use (27). One crucial drawback of radiographic imaging, however, is that early disease is characterised by synovitis before bone erosion occurs which cannot be detected by x-ray imaging. Deformation of the hard tissue is mostly confined to the later stages of disease and therefore radiographic imaging is rarely informative in the diagnostic and early stages of RA. The increasing focus on early diagnosis and treatment has lead to greater use of alternative imaging techniques in clinical assessment. Magnetic resonance imaging (MRI) and ultrasound sonography (US) and are used increasingly in clinical practice to assess soft tissue morphology.

### 2.3.2 Magnetic Resonance Imaging

Magnetic resonance imaging (MRI), where images are taken by exploiting the magnetic properties of hydrogen atoms in the tissue, is also able to detect the soft tissue changes occurring in early RA. Contrast-enhanced MRI (figure 3b) is able to detect all of the physiological changes that can be seen in US, but in addition can detect bone marrow oedema, a symptom of RA known to be the strongest predictor of radiographic disease progression (10). Disadvantages associated with MRI are low availability of facilities and long waiting times, high cost of imaging, and contraindications of imaging due to the magnetic field. The imaging resolution is comparatively low when compared to US and administration of contrast agent is generally required for distinction of the synovial tissue from the joint space (28).

### 2.3.3 Ultrasound Imaging

Ultrasound sonography (US) is able to form images of soft tissues where there is an acoustic window into the tissue (figure 3c). The images are formed by the variation in the reflections of ultrasound waves from the different tissues types, providing more information about soft tissue pathologies than conventional radiographic imaging. Ultrasound imaging of the joints can detect synovial hypertrophy, tenosynovitis, bone erosion, and cartilage thinning. It can also be used for guiding invasive procedures such as biopsy and injections that are often a part of diagnosis and treatment. US is relatively low cost, non-ionising, and informative. However, it is disadvantaged by low availability of ultrasound operators, inter-operator variability, inaccessibility of imaging to tissue beyond the bone, and difficulty with longitudinal imaging assessment. Scoring methods for assessment of symptoms have been introduced to reduce inter-operator variability with some success (29). Power Doppler imaging, where Doppler signals in the ultrasound are amplified for the detection of moving material, is able to detect increased vascularisation in the inflamed synovium even in joints deemed in remission by clinical examination (30).

### 2.3.4 Nuclear Imaging

Alternative imaging techniques have been investigated in the imaging of early and established rheumatoid arthritis but are currently rarely in clinical use. Nuclear imaging techniques like bone scintigraphy, single-photon emission computed tomography (SPECT) and positron emission tomography (PET), produce images by targeting radiotracers to molecular markers associated with inflammation in the joints, but suffer from high cost, low availability, low resolution, and ionising radiation. Research continues to develop new radioisotopes targeting novel cellular markers of inflammatory activity in order to increase its viability as a clinical imaging method (31,32).

### 2.3.5 Optical Imaging

In a research environment, several experimental optical imaging techniques have been applied to the problem of imaging inflammation in rheumatic joints. The most common approach relates to the imaging of non-specific near-infrared fluorescent (NIRF) dye, indocyanine green, for the detection of synovitis through increased NIRF concentration in areas of ‘leaky’ blood vessels in inflamed tissues (figure 3d). Methods of imaging with NIRF dyes have been found to be relatively as successful as MRI and US in the detection of synovitis (33,34), but this finding is contested (35). Currently, indocyanine green is the only NIRF dye approved for clinical use by the Food and Drug Administration in the United States (36).

Thermography, far-infrared imaging for measurement of surface temperature, detects a statistically significant difference between joint temperatures in normal, RA, and osteoarthritis (OA) patients (37), but may struggle in the recognition of mild arthritis symptoms and in small joints (38).

Photoacoustic tomography (PAT) takes advantage of the photoacoustic effect to map the optical absorption properties of a tissue with higher resolution than is achievable in diffuse optical tomography (DOT). In the preliminary assessment of osteoarthritis, PAT was able to detect increased absorption in the joint space of arthritic fingers (39).

Other optically based imaging approaches have included optical spectral transmission (OST), where the transmittance of two or more wavelengths of light are measured and analysed according to how they vary over time or spatially, and diffuse optical imaging (DOI) where multiple light measurements are taken at varying distances and the properties of the tissue are reconstructed either as a static measurement or how they vary over time. Theoretically, the symptoms of arthritis cause changes in the spectral transmission profile of a joint (17). Significant differences were found between healthy and inflamed joints in a system measuring the spectral transmission profile of proximal interphalangeal (PIP) joints in combination with an inflatable pressure cuff in a simple optical spectral transmission approach (40–42).

Other methods attempt to reconstruct the optical properties of the tissue to give an estimation of the distribution of scattering and absorbing distribution of the finger joint. Due to cross-talk between scatter and absorption in biological tissue, this is a non-trivial problem. The first attempt to reconstruct optical properties of the finger joint was a sagittal laser optical tomographic (SLOT) reconstruction where a single wavelength laser was directed at discrete locations along the finger and the transmission profile of light measured on the other side. Applying non-linear error minimisation to an iterative forward model reconstructed an estimation of the optical properties in finger joints of healthy volunteers and patients with RA. They showed a characteristic pattern of scatter and absorption changes. In healthy fingers, a dip in scatter and absorption values occurred in the central region of the joint, whereas, in inflamed fingers the decrease of scatter and absorption values in the joint space was much less pronounced (43–45). More recent continuous-wave imaging methods have included multispectral diffuse optical tomography which aims to use the difference in spectral data to separate the contributions of scattering and absorption (46,47).

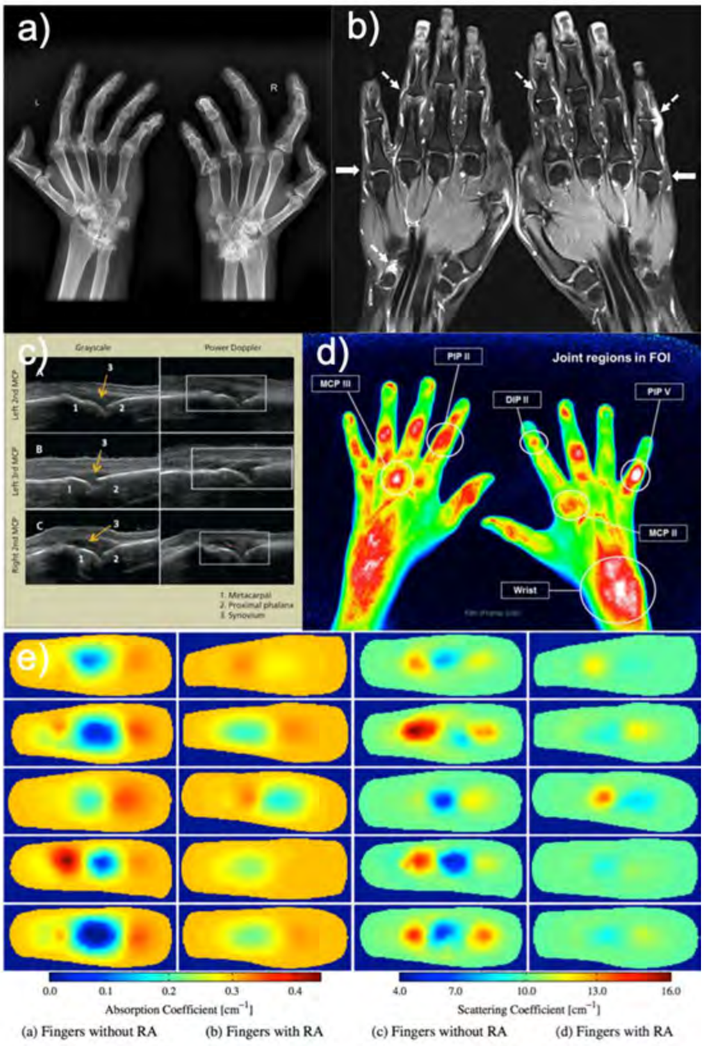

Figure 3: Examples images for clinical and experimental methods of imaging the effects of rheumatoid arthritis in the hand joints. Figures a-e depict x-ray (48), MRI (49), ultrasound (50), near-infrared fluorescence imaging (51) and frequency-domain diffuse optical tomography (52) respectively, reproduced from the cited sources.

Frequency-domain diffuse optical tomographic (FD-DOT) techniques have reconstructed optical properties of human PIP joints, both affected by and unaffected by rheumatoid arthritis. The two groups were found to have statistically significant differences in particular features extracted from the reconstructions. With additional tools for feature extraction and computer aided analysis, the FD-DOT images can provide classification of RA and healthy joints with similar sensitivities and specificities to MRI and ultrasound (53). Figure 3e displays the typical features in a tomographic optical reconstruction where there is an increase of scatter and absorption in the joint space upon development of RA. The low scatter and absorption in the centre of the joint in a healthy finger is thought to be due to the low scatter and absorption coefficients of healthy synovial fluid and cartilage. In rheumatoid arthritis the reconstructed scattering coefficients of the joint space increase, thought to be due to thicker synovium and immune cell infiltrate in the fluid. The reconstructed absorption coefficients increase, thought to be due to hemodynamic changes in the synovial lining (54). Whilst FD-DOT avoids the requirement for contrast agents and ionising radiation, the equipment is expensive and imaging results are difficult to interpret. It is not yet clear whether these methods can distinguish early arthritis symptoms.

## 2.4 Mouse Models in Rheumatoid Arthritis Research

The aetiology of rheumatoid arthritis is difficult to study because patients only present with symptoms once the disease pathways are established. Likewise, studying the progression of the disease requires tissue samples from patients which are painful or impractical to obtain. Cell culture and computational modelling are a vital part of research but cannot completely replicate the multi-tissue effects of disease in a whole organism. Animal models have therefore been developed to aid in research of the condition. Whilst none of the animal models are a perfect replica of RA, they have collectively been used to further the knowledge of the pathological immune processes underlying the disease and in the development of new types of drugs which are now an indispensable part of RA treatment.

Mouse models of RA can simulate aspects of the disease that are of interest to researchers. The breadth of the factors involved in the development of RA has allowed the development of a variety of murine models. These can be broadly categorised as either genetic or induced depending on whether the symptoms were introduced through genetic modifications, or though exposure to inflammation-inducing serum factors. They present with symptoms which include evident inflammation and swelling in the joints of the limbs and paws, as well as erosion of the bone and cartilage in some models. Common murine models which have been included during this research project have been detailed below.

Genetic mouse models have modifications to their DNA which cause disease symptoms to arise spontaneously. Most target the regulation of inflammatory cytokines which are known to be important in RA development and progression. Inducible models involve the introduction of inflammation causing agents into a genetically normal (wildtype) mouse strain, or otherwise non-arthritic genetically-altered mouse. In this case, symptoms tend to peak over the course of several weeks, then they may abate or perpetuate depending on the nature of model (55).

### 2.4.1 TNF dARE

Tumour necrosis factor alpha (TNF-α) is one of the dominant inflammatory cytokines implicated in progression of pathology in rheumatoid joints. It can be expressed by a variety of cells in response to acute inflammatory signals (56). In a resting cell, levels of TNF-α are reduced by the ARE (AU-rich element) regulatory region at the 3’ end of the mRNA transcript. The presence of the ARE region causes degradation of the transcripts and consequent downregulation of TNF-α. Upon activation of the cell with inflammatory signals, the mRNA transcripts are stabilised and consequently translated leading to a rapid upswing in the expression of the protein. In relation to RA, the pathological roles of TNF-α include upregulation of osteoclast activity initiating bone erosion and upregulation of a melange of pro-inflammatory cytokines leading to the recruitment of lymphocytes to the synovial tissue (57).

**Mechanism:** In the TNF dARE mouse, the ARE region of the gene is deleted causing chronic upregulation of TNF-α (58). This mouse model, and other models which upregulate TNF-α, have highlighted the importance of the TNF-α cytokine in disease and led to the successful discovery of several types of TNF-α targeted drug treatments, which are now a mainstay of RA treatment (59).

**Symptoms and appearance**: In the heterozygous TNF dARE mouse, development of chronic polyarthritis and irritable bowel disease begin at approximately 3 weeks of age, overt arthritis around 6 – 8 weeks of age, and by 16 weeks typically nearly all joints are affected (55,58). As symptoms develop discolouration of the paws is evident as they take on a 'brown' appearance (see Figure 4). With advanced symptoms, there is generally visible evidence of deformation of the joints and the heels and wrists can bow assuming a characteristic spoon shape. There is usually little measurable swelling of the footpad, however the toes generally appear thicker than in the normal control. When the mouse is picked up by the scruff so that the feet can be examined, the toes tend to remain bunched rather than spreading out. Peculiar to this mouse model is development of irritable bowel disease analogous to Crohn's disease, resulting in a tendency to be underweight compared to control (wildtype) littermates.

Figure 4: Photographs showing a single case of a TNF dARE hind paw affected by symptoms of arthritis and a single case of a normal mouse foot.

### 2.4.2 K/BxN Serum Transfer

The K/BxN serum transfer (ST) model is an inducible mouse model, where pathology is initiated by the transfer of auto-antibody containing serum obtained from the K/BxN transgenic mouse. Transgenic K/BxN mice are a genetic mouse model which develop a spontaneous form of symmetrical, deforming polyarthritis, highly reminiscent of rheumatoid arthritis, around 4 – 5 weeks of age (60). The intentional target of the KRN T-cell receptor (TCR) is a form of bovine RNase, but crucially for the arthritis model the transgenic KRN receptor also recognises epitopes of glucose-6-phosphate isomerase (GPI) when displayed by the major histocompatibility complex (MHC) class II molecule I-Ag7. GPI is a ubiquitously expressed enzyme involved in the glycolytic pathway. Lymphocyte recognition results in the activation of B cells, releasing autoantibodies specific for GPI. The pathogenesis behind the joint-specific inflammation is not entirely clear but appears to involve recruitment of factors of the innate immune system (61).

A single injection (intravenous or intraperitoneal) of serum from symptomatic transgenic K/BxN mice into a naïve wild-type mouse results in the development of arthritis symptoms within 2 days (62). The main difference between the transgenic K/BxN mouse and the serum transfer K/BxN is the transient nature of the disease symptoms which resolve after approximately 15 days. These mice develop a hyperplastic synovium and show cellular infiltration into the joint as well as damage to the cartilage. They are generally used in studying the innate immune response since the adaptive immune response does not become involved.

**Mechanism**: The anti-GPI autoantibodies introduced during the serum transfer have been found to locate to the joints within minutes. Subsequent formation of immune complexes activate complement pathways and humoral inflammatory processes resulting in a self-limiting joint-specific inflammatory process (63).

**Symptoms and appearance**: Paws can appear swollen and red, often localised to areas such as the heel or single digits. Inflammation is more common in the paws and ankles than the hips and tends to be symmetrical. Symptoms peak around 5 days after serum transfer after which time visible evidence (clinical symptoms) begin to diminish. After 15-21 days, clinical symptoms have usually abated although the effects of cartilage and bone damage may still be evident (61,63).

### 2.4.3 Collagen Induced Arthritis (CIA)

CIA mice are considered the gold standard for research because the method of induction is the most analogous to autoimmune induction in humans. It is an induced form of polyarthritis where mice are inoculated with heterologous type II collagen, a principal component of articular cartilage, mixed with complete Freund's adjuvant, an immunopotentiator used to provoke an immune reaction. The consequent immune response occurs around 20-30 days later displaying many of the same pathological symptoms as observed in rheumatoid arthritis. The development of arthritis in the CIA model is dependent on the MHC haplotype of the mice, therefore the main mouse strain used for the CIA model is DBA/1, due to the expression of H-2q MHC molecules.

Symptoms can also be induced in other mouse strains but different protocols are required and there are lower rates of successful symptom induction. CIA mice tend to have symmetric joint involvement, synovitis, cartilage and bone erosion, and cellular infiltrate in the joint (64).

**Mechanism**: Induction of disease is mainly T-cell dependent (although a weaker form of pathology can be introduced though CIA on a recombinant activation gene (RAG) - 1 deficient background (65)), but the mechanism of pathology is due to the collagen autoantibodies which bind to native collagen in the joints and induce an inflammatory response (66).

**Symptoms and appearance**: In terms of appearance, CIA mice display similar symptoms to K/BxN serum transfer mice where they have red, swollen joints. Joint deformity is also observed (see Figure 5).

Figure 5: Increasing severity of CIA symptoms in a mouse front paw. Reproduced from Hawkins et al (67).

## 2.5 Assessment of Mouse Model Disease Symptoms

Mouse model symptom characterisation is required over the course of an experiment to observe the progress of disease against the experimental hypothesis and also to monitor the mouse's general health. Pain management measures may be introduced if the disease is deemed to exceed a critical threshold, and in severely affected cases, will elicit a humane endpoint. Currently, assessment methods of live mice mainly rely on a clinical assessment where researchers manually examine and score mice for indications of arthritis. Various imaging methods have been applied to the imaging of mouse arthritis models (see section 2.5.1.2), but are not widely used in routine symptom assessment due to the expense, expertise, and added experimental procedure necessary. In most cases, culling the mouse and excising tissues is necessary for a more accurate assessment of the arthritis progression.

### 2.5.1 In vivo Assessment of Murine Disease

#### *2.5.1.1* Scoring System

The scoring system currently used to assess the severity of the symptoms in arthritic mice is based on a number of behavioural and physical observations. Figure 6 shows the scoring sheet that is used for assessment of all arthritis models at the University of Birmingham. The scoring sheet was designed initially in 2012 by Dr Amy Naylor based on discussions with researchers using arthritis models at the Kennedy institute of Rheumatology. Since that time, it has been adapted to better capture welfare parameters and clinical symptoms through consultation with researchers, animal technicians and veterinary surgeons at the University of Birmingham.

The mice are scored for a series of physical traits relating to their health and symptoms of arthritis including their gait, their behaviour around littermates, mouse ‘grimace’ (68), and the appearance of their paws. The mouse is picked up in a ‘scruff’ and held supine so that all four paws can be examined and scored for swelling, deformity, and discolouration.

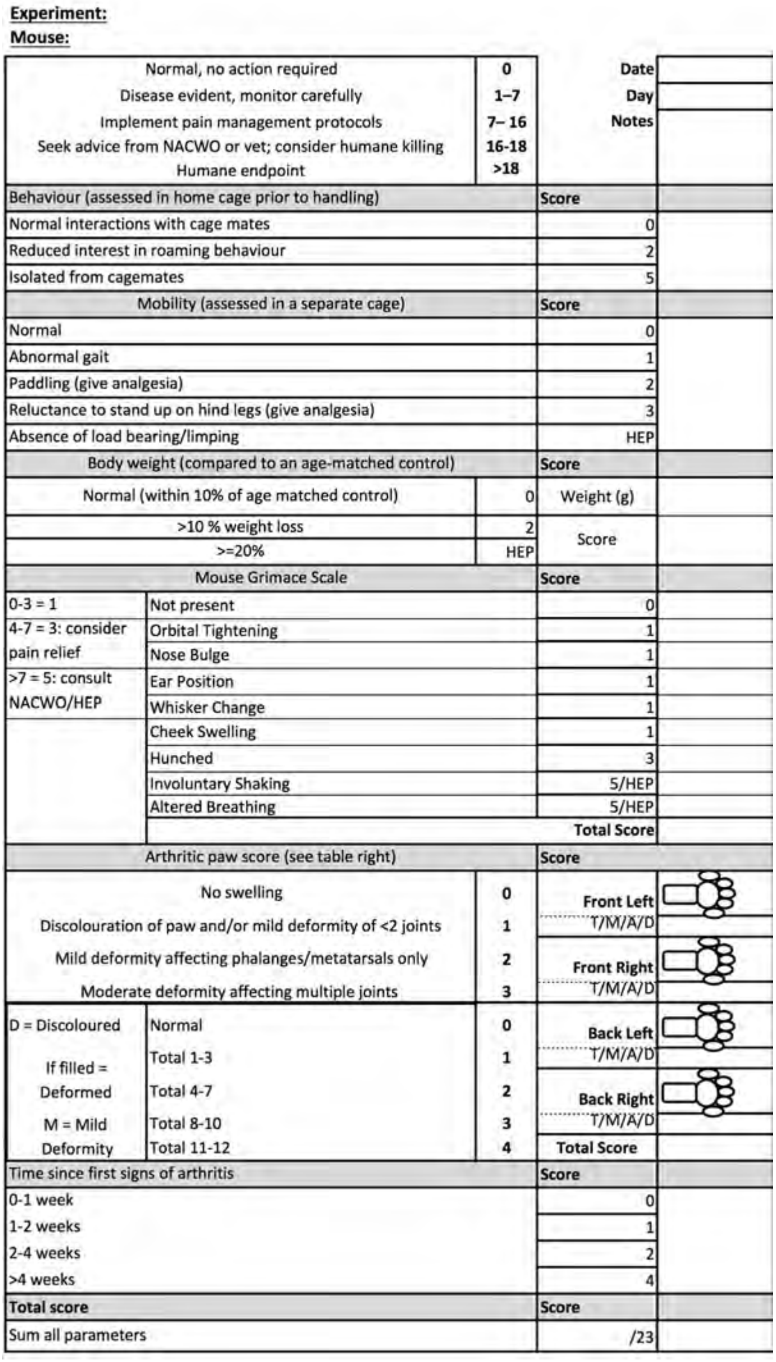

**Experiment:**
**Mouse:**

| | | | | |
|---|---|---|---|---|
| Normal, no action required | | 0 | Date | |
| Disease evident, monitor carefully | | 1–7 | Day | |
| Implement pain management protocols | | 7– 16 | Notes | |
| Seek advice from NACWO or vet; consider humane killing | | 16-18 | | |
| Humane endpoint | | >18 | | |
| Behaviour (assessed in home cage prior to handling) | | | **Score** | |
| Normal interactions with cage mates | | | 0 | |
| Reduced interest in roaming behaviour | | | 2 | |
| Isolated from cagemates | | | 5 | |
| Mobility (assessed in a separate cage) | | | **Score** | |
| Normal | | | 0 | |
| Abnormal gait | | | 1 | |
| Paddling (give analgesia) | | | 2 | |
| Reluctance to stand up on hind legs (give analgesia) | | | 3 | |
| Absence of load bearing/limping | | | HEP | |
| Body weight (compared to an age-matched control) | | | **Score** | |
| Normal (within 10% of age matched control) | | 0 | Weight (g) | |
| >10 % weight loss | | 2 | Score | |
| >=20% | | HEP | | |
| Mouse Grimace Scale | | | **Score** | |
| 0-3 = 1 | Not present | | 0 | |
| 4-7 = 3: consider pain relief | Orbital Tightening | | 1 | |
| | Nose Bulge | | 1 | |
| >7 = 5: consult NACWO/HEP | Ear Position | | 1 | |
| | Whisker Change | | 1 | |
| | Cheek Swelling | | 1 | |
| | Hunched | | 3 | |
| | Involuntary Shaking | | 5/HEP | |
| | Altered Breathing | | 5/HEP | |
| | | | **Total Score** | |
| Arthritic paw score (see table right) | | | **Score** | |
| No swelling | | 0 | **Front Left**<br>T/M/A/D | |
| Discolouration of paw and/or mild deformity of <2 joints | | 1 | | |
| Mild deformity affecting phalanges/metatarsals only | | 2 | **Front Right**<br>T/M/A/D | |
| Moderate deformity affecting multiple joints | | 3 | | |
| D = Discoloured | Normal | 0 | **Back Left**<br>T/M/A/D | |
| If filled = Deformed | Total 1-3 | 1 | | |
| | Total 4-7 | 2 | **Back Right**<br>T/M/A/D | |
| M = Mild Deformity | Total 8-10 | 3 | | |
| | Total 11-12 | 4 | **Total Score** | |
| Time since first signs of arthritis | | | **Score** | |
| 0-1 week | | | 0 | |
| 1-2 weeks | | | 1 | |
| 2-4 weeks | | | 2 | |
| >4 weeks | | | 4 | |
| **Total score** | | | **Score** | |
| Sum all parameters | | | /23 | |

Figure 6: The complete scoring form used to monitor mouse models of arthritis at the University of Birmingham. The form includes a section where the paws of the mouse are scored by visual assessment for traits such as swelling, discolouration and deformity.

This method of scoring is entirely manual, time consuming, and highly reliant upon the experience of the assessor. The data collected are both superficial and subjective in nature and prone to conformation bias where the mouse is known to be arthritic (69).

Depending on the nature of the symptoms, it can be supplemented by quantitative physical measurements such as mouse weight, grip strength, paw thickness, paw volume, and ankle thickness, but such pathological changes are often dependent on model of RA.

#### *2.5.1.2* In vivo Imaging Based Assessment

Specialised small animal imaging systems exist for many of the imaging methods commonly applied to humans. Most of these methods have been applied to small animal models of RA in a research environment, to see how efficiently they detect inflammation.

**MicroSPECT and MicroPET**

Nuclear imaging techniques microSPECT and microPET are used comparatively more often in the imaging of small animal models of rheumatoid arthritis (Figure 7a). Novel radiotracers have been developed and tested for efficacy of arthritis detection in a variety of mouse models using microSPECT imaging, often imaged in combination with microCT for improved anatomic localisation. Targets including proteoglycans (70), macrophage mannose receptors (71), apoptotic cells (72), fibroblast-like synoviocytes (73,74), and integrin αvβ3 (74), have all shown correlation with arthritis symptoms. Tracers aiming to quantify pathological bone destruction correlated with alternate measures of bone destruction (75), tracers targeting cell proliferation saw advanced uptake with mild clinical symptoms in K/BxN serum transfer mice (76), and targeting T-cell activation markers correlated with arthritis symptoms (77). Specialised nuclear imaging techniques achieve a resolution of approximately 1mm$^3$ and have proved able to image several of the molecular events associated with development of symptoms in rheumatoid arthritis models. However, as in clinical imaging, the use of nuclear imaging is restricted by the expense of the imaging equipment, the inconvenience of tracer preparation, and the difficulty in translation to clinical imaging due to regulatory issues (78). Compared to optical molecular imaging techniques, its advantage is the absence of depth-dependent photon attenuation and tissue scattering.

### MicroMRI

Specialised small animal microMRI systems have also been applied to the imaging of RA models, to image morphological changes occurring in both the soft and hard tissues (Figure 7b). The small scale of the joints can be problematic, but symptoms like synovial fibroplasia, oedema, joint effusion, and bone erosion can potentially be defined. Often, contrast agents such as gadolinium or ultrasmall superparamagnetic iron oxide (USPIO) particles are employed to help delineate target tissues. Using contrast agents, metrics of MR imaging have been found to correlate with classic inflammatory parameters and histologic signs of arthritis (79). Longitudinal assessment of inflammation and bone erosion is possible (80) and early signs of disease can be detected (81). USPIO particles have been successfully targeted to macrophages (82,83) and T-cells (84) and using synovial volume to facilitate drug intervention was found to reduce variability of outcome in treatment intervention experiments compared to age (80). As with nuclear imaging techniques, the main disadvantage of microMRI is the expense of the imaging equipment.

### NIRF and Bioluminescence Imaging

Technology for *in vivo* optical molecular imaging techniques involving the injection of fluorescent probes, or the generation of bioluminescence expressing cells, has become more available and more common in the past decade and thus is now used more regularly in experiments. Several methods have been attempted in visualising arthritis symptoms. Like in humans, non-specific near-infrared fluorescence (NIRF) dyes, show significantly more signal in joints affected by arthritis (85,86) due to naturally 'leaky' blood vessels in inflammatory regions (Figure 7c). However, for most fluorescence imaging in RA models, probes are targeted to molecular markers relating to the inflammatory processes to measure specific molecular responses.

In testing a Matrix Metalloproteinase (MMP)-3 targeted probe on CIA mice, significantly higher NIRF signal was found in CIA mouse hind limb joints than in their littermate controls before any clinical signs of disease were visible (87). This molecular imaging probe has proved capable of monitoring drug responses (88). 'Smart' probes activated by target proteases have also been trialled in monitoring therapeutic drug response (89). A folate targeted probe has been used in the K/BxN mouse model to elucidate macrophage activity in the joints (90), and to the F4/80 antigen on the surfaces of macrophages in adjuvant induced arthritis (AIA) mice (91). More recently, commercially available NIRF 'smart' probes cleaved and activated by proteases, neutrophil elastase, MMP's, and cathepsin K were imaged and the intensity shown to significantly correlate with manual scoring and histology scores, and can be delivered in tandem due to separable emission spectra (92).

Molecular imaging is undoubtedly a valuable tool in RA research, offering the ability to monitor the localisation and relative intensity of cellular activity *in vivo*. However, it is disadvantaged by the need for expensive equipment, targeted probes, anaesthetics, and other imaging concerns such as low resolution compared to alternative techniques, around 5mm compared to PET 2mm and MRI 0.1mm (93). It does however have short imaging times compared to scintigraphic methods (91).

### Non-Contrast Enhanced Optical Imaging

Several alternative optical imaging methods not requiring contrast enhancement have been trialled on animal models of rheumatoid arthritis for symptom assessment. Cross polarisation colour (CPC) imaging and laser speckle contrast of the hind paws of AIA mice showed correlation with histological results (94). Multi-wavelength time-resolved diffuse optical spectroscopy (TR-DOS), was used to estimate Hb, $HbO_2$ and, with the aid of dynamic-contrast enhancement, blood flow to the knee joint of an RA model rabbit finding trends towards decreased oxygenation and significantly larger blood flow in the arthritic measurements (95). Thermal imaging has also found significant differences in the surface temperature of arthritic paws compared to normal paws in CIA mice (96) and in AIA rats (97).

### Ultrasound and Photoacoustic Imaging

Alternative methods of imaging applied to small animals are comparatively rare. Despite its increasing clinical usage, literature on the ultrasound (US) imaging of small animal models of RA (Figure 7d) is relatively sparse. The joint space volume and power doppler volume calculated from US images has been found to correlate with synovial volume as calculated from contrast-enhanced MRI in TNF transgenic mice (98), and doppler US score has been found to correlate with histological and clinical scoring in CIA mice (99). Photoacoustic imaging has been experimentally applied to the imaging of small animal joints. Enhancement of signal was found in arthritic rats compared to normal controls, indicating an increase of blood flow and neovascularisation in the joint

(100). In rat tail joints, significant differences in optical absorption were found following carrageen injection to induce arthritis (101). Contrast agents have also been experimentally investigated for photoacoustic imaging of RA models. Gold nanorods improved the imaging of inflammation in CIA mice (102) and more recently, significant differences were found between arthritic models and controls using multispectral optoacoustic tomography (MSOT) with a NIRF dye targeting P-selectin/L-selectin (103).

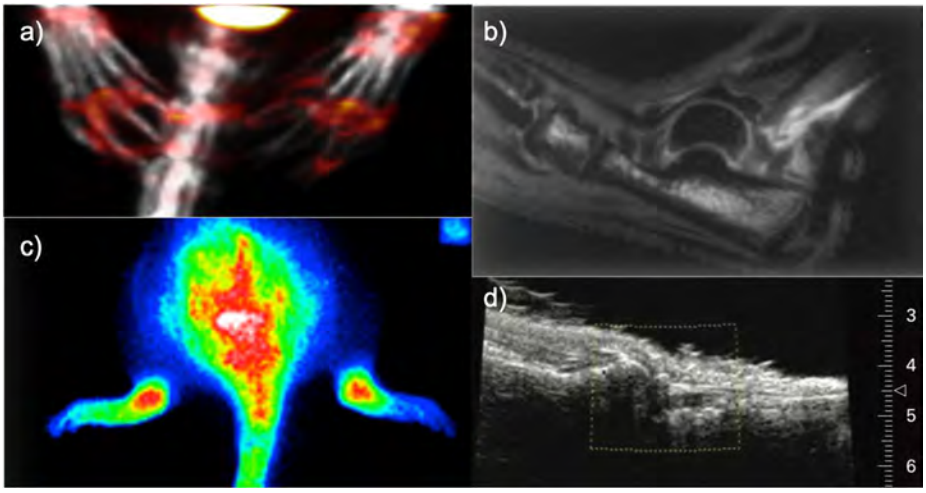

Figure 7: Examples of in vivo imaging for symptoms of joint inflammation in rodent models of rheumatoid arthritis. Consecutively, these images depict a) ultrasound imaging of a mouse ankle joint (99) b) radiolabelled microSPECT/microCT targeting integrin $\alpha_V\beta_3$ expression on osteoclasts in CIA mice (74) c) T1 microMRI of a normal rat ankle (79) and d) non-specific near-infrared fluorescence imaging of a CIA rat (85).

## Multispectral Imaging

Multispectral imaging (MI) is not in common usage for the imaging of murine arthritis. Putten *et al.* (18) applied a multispectral imaging to microscopy of tendon microvasculature of RA mice, but to our knowledge multispectral imaging has not been used for bulk tissue imaging in murine models of RA. In general, multispectral imaging is seldom used for clinical assessment of pathology, but has had several successful applications in research such as imaging of melanoma in human skin (104). Multispectral imaging is covered in more detail in section 2.7.

### 2.5.2 Ex Vivo Arthritis Assessment

#### *2.5.2.1* Histology

Evaluation by histology is considered the gold standard for disease evaluation in RA models, as the pathology can be seen and graded by eye. Disease symptoms such as inflammatory infiltrate, synovial hyperplasia, and bone erosions can be scored from simple Haematoxylin & Eosin (H&E) stained samples (Figure 8). However, the clear disadvantage of such scoring is that obtaining the tissue sample necessitates culling the mouse. In long-term experiments large groups of mice are often required so that mice can be culled at certain time points to investigate the progress of pathology.

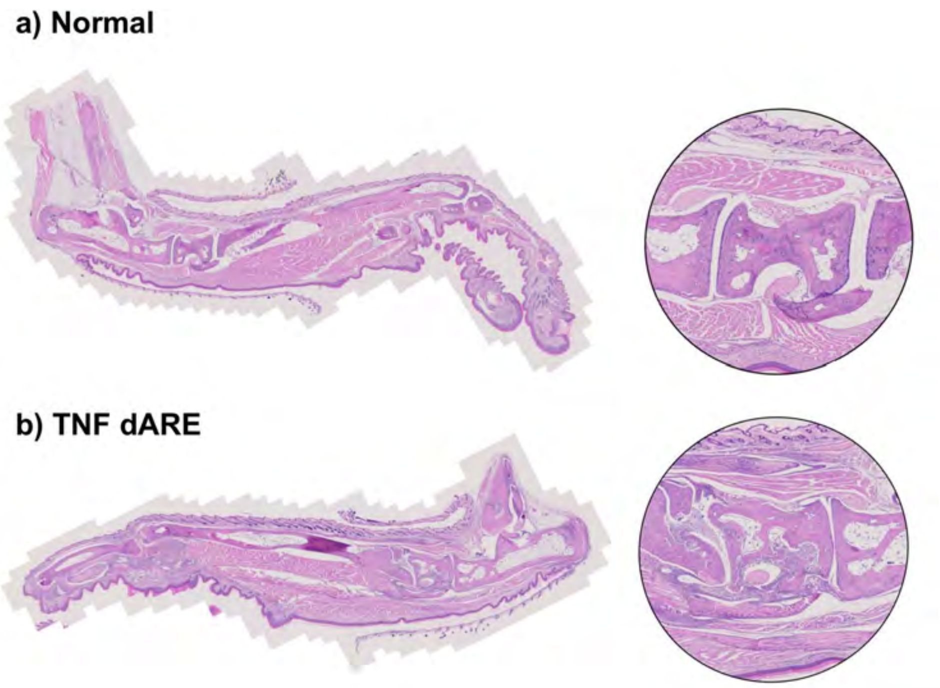

Figure 8: Haematoxylin and Eosin stained sagittal sections of mouse hind paws. Image a) contains a normal paw where no evidence of inflammation can be seen around the joints. Image b) contains a section from a TNF dARE mouse, with evidence of inflammation. In the magnified image on the right, inflammatory infiltrate containing immune cells can be seen around the bone.

#### *2.5.2.2* MicroCT

MicroCT is routinely used in imaging *ex vivo* tissue samples of RA models, containing joints expected to be affected by bone erosion or bone growth. Most mouse models of RA exhibit some degree of bone erosion in the periarticular cortical bone, which can be observed in microCT scans as pitting around the joint area (Figure 9). Reconstructed microCT meshes can be scored by eye according to the perceived progression of bone damage.

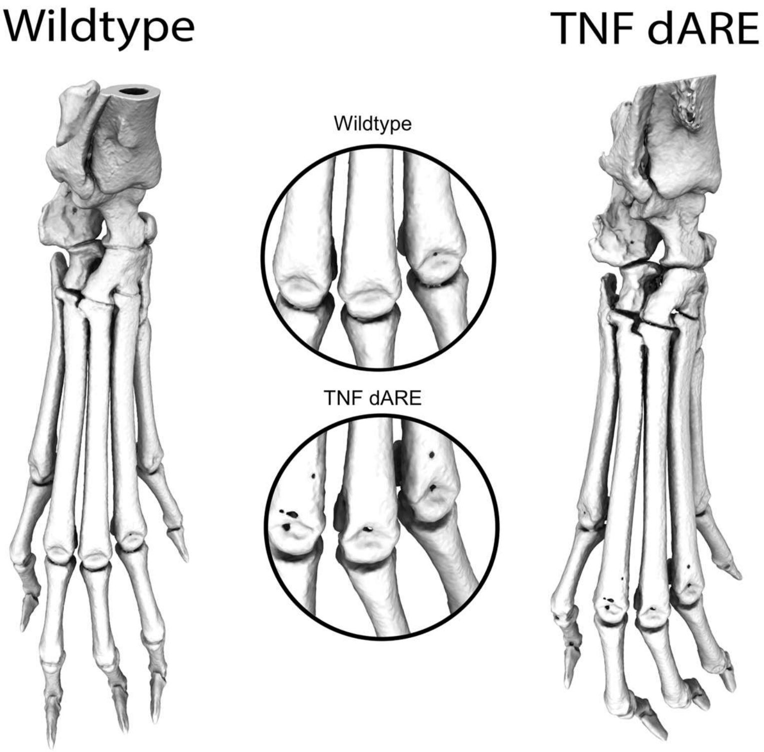

Figure 9: Reconstructed meshes of wildtype and TNF dARE mouse hind paws imaged by microCT. Instances of bone erosion can be seen around the metatarsophalangeal joints in the TNF dARE mouse due to chronic joint inflammation.

For this project an analysis method developed by Brown et al. (105), was used to measure bone deformity in hind paw microCT scans of arthritis models by comparison with a statistical shape model (SSM). A microCT scan gives high-resolution 3-dimensional data about progression of hard tissue damage in arthritis models but contains no information about soft tissue pathology. Figure 9 displays a typical scan of a healthy hind paw with an arthritic TNF dARE hind paw for comparison.

## 2.6 Light Interaction with Tissue

### 2.6.1 Reflection

Most materials will reflect a proportion of the light incident upon them. The incident light can be reflected by either specular or diffuse regimes. Specular reflection occurs when light is reflected from the surface of the material, without propagating into the material itself. In a material with a smooth surface this results in a ‘mirror-like’ reflection, or on a rougher surface, the specular reflection disperses less uniformly. For many materials, however, the majority of reflected light is reflected diffusely. This happens when photons enter beneath the surface of a material, undergo scattering events within and are re-emitted from the surface.

### 2.6.2 Transmission

Light which propagates through the material and exits on the other side is referred to as transmitted. If photons do not scatter along their path the transmission is considered ballistic, otherwise it is diffuse (Figure 10). In most materials a proportion of light will be absorbed. The structure and composition of the material determines which wavelengths will be absorbed preferentially and this pattern of absorption lends a material its colour. Schematic examples of the light - material interactions are displayed in Figure 10.

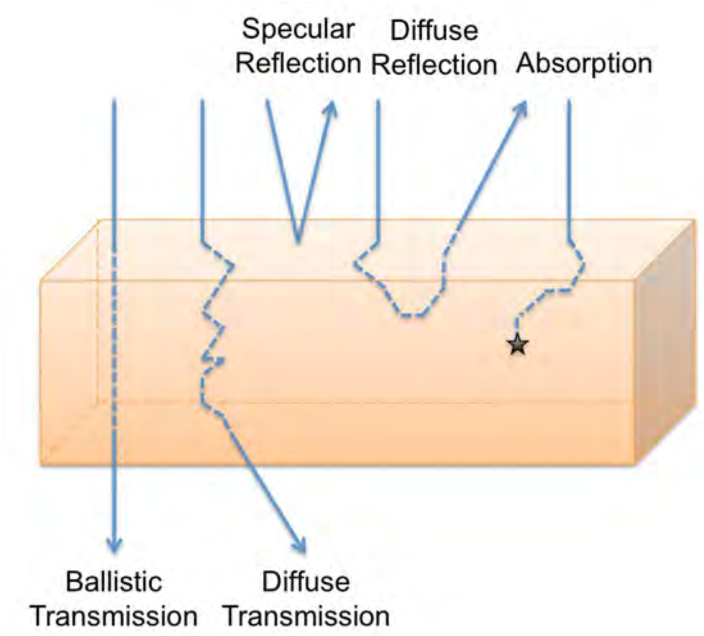

Figure 10: Schematic of a block of tissue describing the paths of ballistic and diffusely transmitted photons, specular and diffusely reflected photons, and photon absorption.

### 2.6.3 Physics Concepts

Optical properties of materials can be characterised by their refractive index, absorption coefficient, scattering coefficient and anisotropy factor. This section provides a brief introduction to these concepts in context of light-tissue interaction.

#### *2.6.3.1* Refractive Index

The refractive index of a material (n) describes the reduction in the velocity of light in a vacuum (c) to the velocity of light in the medium (v) according to

$$n = \frac{c}{v}. \tag{1}$$

The refractive index of a material influences the percentage of light specularly reflected at a material boundary according to Fresnel's equation

$$R = \frac{1}{2}\frac{(a-c)^2}{(a+c)^2}\left\{1 + \frac{[c(a+c)-1]^2}{[c(a-c)+1]^2}\right\} \tag{2}$$

where R is Fresnel reflection, $c = cos(\theta_i)$, $\theta_i$ is the angle of incidence, and $a = n^2 + c^2 + 1$. In Fresnel reflection, the angle of incidence is equal to the angle of reflection about the normal to the surface. Any light that then continues into the material will be refracted at an angle according to Snell's law

$$\theta_t = \arcsin\left(\frac{1}{n}\sin\theta_i\right) \tag{3}$$

where $\theta_t$ is the angle of refraction (106). Biological tissues have an average refractive index higher than that of air. Taking human skin as an example, an incident beam of light first hits stratum corneum of the epidermis. The refractive index mismatch from the air (n=1.0) to the tissue (n≈1.4) leads to Fresnel reflection of approximately 5 – 7% of the incident light. The wavelength dependence of Fresnel reflection is generally relatively small and therefore all wavelengths will be reflected fairly equally.

### *2.6.3.2* Absorption

Photon absorption occurs in a quantised manner where photon energy is converted to a different form through absorption by an atom or molecule called a chromophore. Each chromophore has an associated range of wavelength-dependent absorption coefficients ($\mu_a[cm^{-1}]$), which describe the probability of photon absorption occurring per unit distance. For a given path length through a material containing an absorbing chromophore of a certain concentration, the absorption coefficients of the material can be calculated through the modified Beer-Lambert law

$$A = \log\left(\frac{I_{out}}{I_{in}}\right) = \mu_a \times d \times DPF + G \tag{4}$$

where $I_{in}$ is the incident intensity, $I_{out}$ is the transmitted intensity, and $\mu_a$ is the wavelength-specific absorption coefficient of the material, d is the distance, DPF is a factor which accounts for the increase in the pathlength in a scattering material and G describes the geometry dependent loss of light. In a mixture of chromophores the absorption coefficients of the material can be linearly decomposed to give the concentrations of the individual chromophores. In a mammalian tissue the main absorbing chromophores are melanin, haemoglobin and oxyhaemoglobin as shown in figure11a. To a lesser extent bilirubin and carotene contribute and in the near-infrared (NIR) wavelengths, the absorption of water begins to increase.

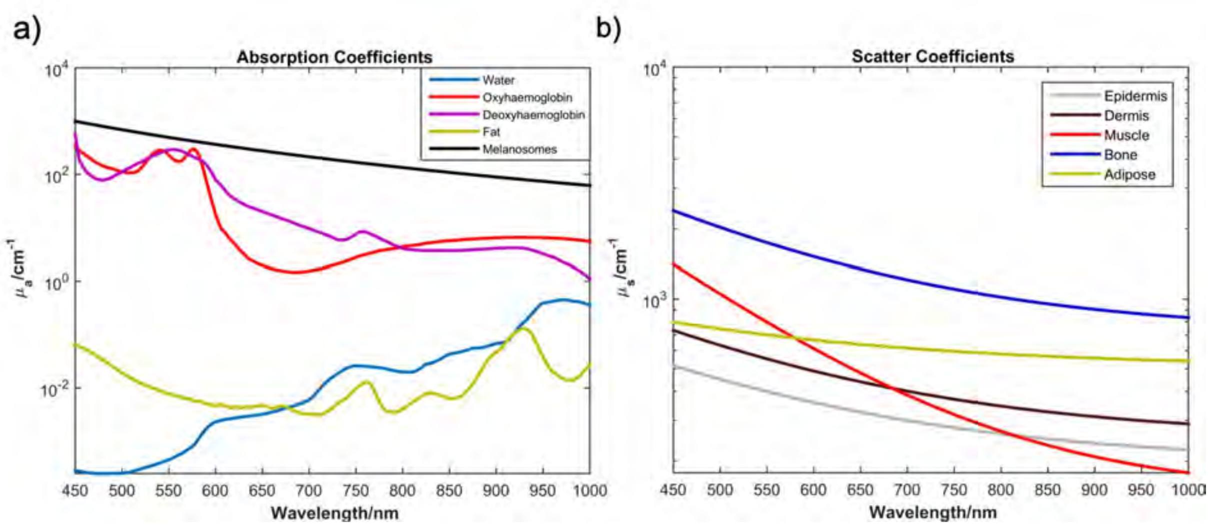

Figure 11: Absorption and scatter coefficients for common biological chromophores and tissues. a) Absorption coefficients ($\mu_a$/cm$^{-1}$) of common biological chromophores in the range 450nm to 1000nm. b) Scatter coefficients ($\mu_s$/cm$^{-1}$) of different tissue types in the range 450nm to 1000nm.

### *2.6.3.3* Scatter

Scattering of a photon refers to the change in the direction of propagation, and the scattering properties of a material can be referred to by its scattering coefficients ($\mu_s$[cm$^{-1}$]), a wavelength dependent value which describes the probability of photon scatter occurring per unit distance, shown in figure11b. Scatter within a turbid material occurs when photons collide with scattering particles which have different refractive indices from that of the medium in which photons propagate. Depending on the size of the scattering particles in relation to the wavelength of light, it is common to refer to two different regimes.

***Rayleigh scattering*** is scattering from particles much smaller than the wavelengths of light, less than a tenth of the size. The magnitude of Rayleigh scattering is highly dependent on the wavelength, with scattering proportional to $1/\lambda^4$ where $\lambda$ is wavelength in nm. This means Rayleigh scattering is most relevant at the shorter wavelengths in the visible region of the spectrum, but much less significant at longer wavelengths. In Rayleigh scattering, the scatter acts as an electrical dipole oscillating in phase with the wavelength of the photon and scatters incident light isotropically (107). Rayleigh scattering can be caused as a result of tissue components such as collagen fibres.

***Mie scattering*** is the scattering of photons from particles of the same order of magnitude as the wavelength of incident light. In tissues it accounts for most of the scattering events in the visible and NIR wavelengths. Mie scatter is anisotropic and predominantly forward oriented. The incident light is therefore mostly scattered at a small angle from its initial direction of propagation. The angular distribution of Mie scattering is proportional to the ratio of the wavelength to the particle size. As particle size increases relative to wavelength, light scattering becomes more forward directed.

Mathematically, Mie theory describes the scattering of light from spherical particles of diameter d and refractive index $n_p$ embedded in the medium of refractive index $n_m$. Given these parameters and the density of scattering centres, the scattering coefficient $\mu_s$ can be computed as a function of wavelength ($\lambda$). The structures in biological tissues responsible for Mie scattering in the visible and NIR wavelengths include cell nuclei, mitochondria, vesicles and collagen fibres, which tend to range from 0.4μm and 2μm in size (108). Because of their relative sizes, the larger angle scattering in a tissue appears to come from mitochondria and the smaller angle scattering from cell nuclei.

Both Mie and Rayleigh scattering are considered elastic scattering processes where the energy of the photon is substantially preserved but the direction is changed. The total scattering coefficients of a tissue is a composite of scatter of Rayleigh and Mie regimes (Figure 12).

An essential parameter for describing the angular scatter distribution is the ***anisotropy value*** (g) which is the average of the cosine of the scattering angle for the tissue

$$\mathrm{g} = \int_{\pi}^{0} \mathrm{p}(\theta)(\cos\theta)(2\pi\sin\theta)\, \mathrm{d}\theta \tag{5}$$

where $\mathrm{p}(\theta)$ is the scattering phase function (defined below). Anisotropy g ranges between -1 and 1, where -1 is complete backscatter, 0 is isotropic scatter, and 1 is complete forward scatter. Mammalian tissues tend to be forward scattering with an average anisotropy value around 0.9 (109).

The probability density of scattering angles for a particular tissue can be described by a ***phase function***, which gives the probability of scatter at different polar angles. In biological tissues, the scattering phase function can be approximated by the Henyey-Greenstein equation (110)

$$\mathrm{p}(\theta) = \frac{1}{4\pi}\frac{1-\mathrm{g}^2}{(1+\mathrm{g}^2-2\mathrm{g}\cos\theta)^{3/2}}\,. \tag{6}$$

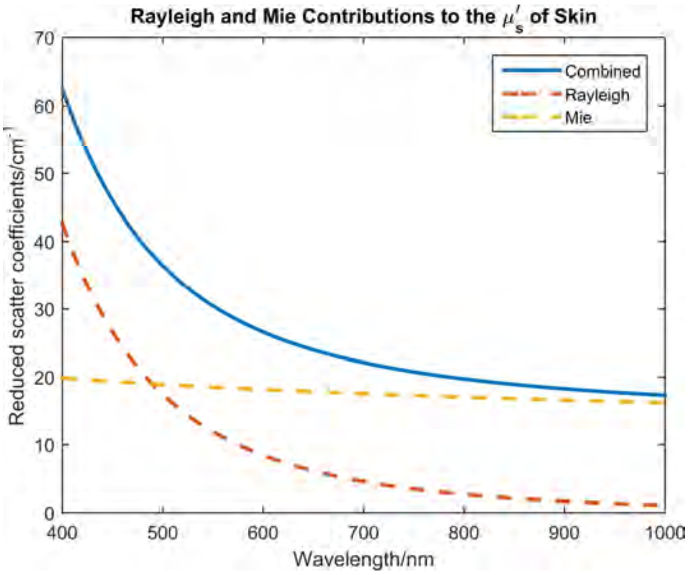

Figure 12: Graph describing the Rayleigh and Mie contribution to the reduced scattering coefficient of typical human dermis. Values predicted by Mie theory applied to values isolated from the measurement of collagen fibres (87).

The ***reduced scattering coefficient*** ($\mu_s$'[cm$^{-1}$]) is a useful parameter for modelling light propagation in a diffusive regime where scatter dominates over absorption (111). It can be calculated from the scattering coefficient and anisotropy via the equation

$$\mu s' = \mu s(1\text{-}g). \tag{7}$$

Additional useful descriptors of scatter within a tissue is the ***Mean Free Path*** (mfp = 1/$\mu_s$), which is equal to the average distance a photon will travel in a tissue before a scattering event.

### 2.6.4 The Optical Properties of Biological Tissues

Biological tissue is a complex, multi-layered, structure composed of a mixture of optical scatterers and absorbers. The absorption coefficients of biological tissues depend on the concentrations and locations of a number of different biological chromophores. The combined effect of their concentrations and position within the tissue gives the tissue its colour (15). Included in figure11a are the absorption coefficient spectra of the main three chromophores that are of interest to this project, haemoglobin, oxyhaemoglobin and water, across a range of wavelengths from 450nm to 1000nm.

Most biological tissues are turbid (optically opaque), due to high density of scattering centres, although exceptions exist such as the lens and cornea of the eye, cerebrospinal fluid, or the synovial fluid (112). Higher scattering coefficients are associated with skin and bone, which contain dense extracellular collagen networks, while lower scattering coefficients are associated with muscle (figure11b).

The light which is scattered and escapes absorption can be re-emitted from the surface of the material or transmitted through it. The angular distribution of diffusely reflected light in biological tissue generally approximates a Lambertian distribution (113), where the apparent brightness of the tissue remains constant regardless of the viewing angle of the observer. In mathematical terms, the luminance is directly proportional to the cosine of the angle between the direction of propagation and the surface normal. Any transmitted light is diffused, with a negligible proportion of ballistic photons. Transmission (I) of light over pathlength (L) without a scattering event can be calculated with

$$\mathrm{I} = \mathrm{I}_0 \mathrm{e}^{-\mu_s \mathrm{L}} \qquad (8)$$

where $I_0$ is intensity of the incident light and $\mu_s$ is the scattering coefficient. Using this equation together with a typical scattering coefficients value for biological tissue (100 - 200cm$^{-1}$), the percentage of true ballistic photons in a tissue slab 2mm thick, the approximate width of a mouse hind paw, is practically zero.

### 2.6.5 Modelling of Photon Transport within a Biological Tissue

Modelling of light interaction with biological tissues is common in many domains. In biomedical imaging the purpose of forward modelling is to simulate the application of a light source to a tissue to gain an estimation of an optical effect such as the reflectance, transmission, or fluence. All modelling methods implement an estimation of photon propagation through a tissue by ascribing tissue properties to a tissue geometry, then simulating the injection of photons from a model light source.

### 2.6.6 Methods of Modelling Photon Transport

Modelling of photon transport within a turbid tissue can be approached through several different methods. Fundamentally, photon propagation within a tissue can be described using the radiative transfer equation (RTE)

$$\frac{1}{c}\frac{\delta L(r,\hat{s},t)}{\delta t} + \nabla \cdot L(r,\hat{s},t)\hat{s} = -\mu_t L(r,\hat{s},t) + \mu_s \int_{4\pi} L(r,\hat{s},t) P(\hat{s} \cdot \hat{s}\,')d\Omega' + Q(r,\hat{s},t)\,. \quad (9)$$

In this equation $L(r,\hat{s},t)$ is the radiance, or the energy flow per unit area per unit solid angle per unit time at position $r$, direction $\hat{s}$, and time $t$. $\mu_t$ is the total interaction coefficient, equal to $\mu_a + \mu_s$ . The scattering phase function $P(\hat{s} \cdot \hat{s}')d\Omega'$ is the probability of light scattering from direction $\hat{s}$ to solid angle $d\Omega'$ about direction $\hat{s}$‘ , and $Q(r,\hat{s},t)$ is the energy emitted from a light source at position $r$, direction $\hat{s}$, and time $t$.

Derived from Maxwell’s equations, the RTE describes the propagation of photons through a medium in terms of absorption and elastic scattering events. However, given that most biological tissues present multi-layer, heterogeneous, complex, scattering media in the Visible and NIR wavelengths, the RTE cannot be solved analytically. The solution can either be resolved with approximations to the RTE or numerical methods.

Methods for solving the problem of photon transport within a tissue include Kubelka-Munk (114), adding-doubling (115), discrete ordinate method (116), four-flux (117) and seven-flux models (118), the diffusion approximation (119), and Monte Carlo (120). Each method has its advantages and disadvantages dependent on the requirements of modelling, but the most ubiquitous for forward modelling of photon propagation in macroscale biological tissues are the diffusion approximation (DA) and the Monte Carlo (MC) method. Given that the DA assumes isotropic scattering and uses the reduced scattering coefficients of the tissue, it is inappropriate for modelling photon propagation over short distances like the mouse hind paw where light may not have been scattered isotopically before exiting the tissue.

The Monte Carlo solution to the RTE is regarded as the most accurate method for modelling photon transport within a complex biological tissue (121), often used as validation for other methods (122–124). The MC method does not make the same approximations as the DA and will therefore model photon propagation accurately even in the case of highly absorbing or low scatter tissues. It is based on repeated random sampling and is a flexible technique, widely applicable to the modelling of under-determined problems. In modelling radiative transfer, MC discretises photons, simulating scattering and absorption events individually according to probabilistic measures determined by properties associated with the tissue. There are several subtly different implementations of the method, but in general the algorithm is thus (shown as a flow diagram in Figure 13 and modelled photon paths in Figure 14). A single photon packet is launched and a proportion of light is reflected at the tissue boundary in accordance with Fresnel's equations. The remainder carries on into the tissue. The weight of the photon is reduced by the probability of absorption with each step, and the new step size and scattering angle calculated based on randomly sampling their respective probability distributions. The photon packet propagates in the tissue until it exits or is completely absorbed. Figure 13 displays a simple Monte Carlo flow chart of the algorithm process.

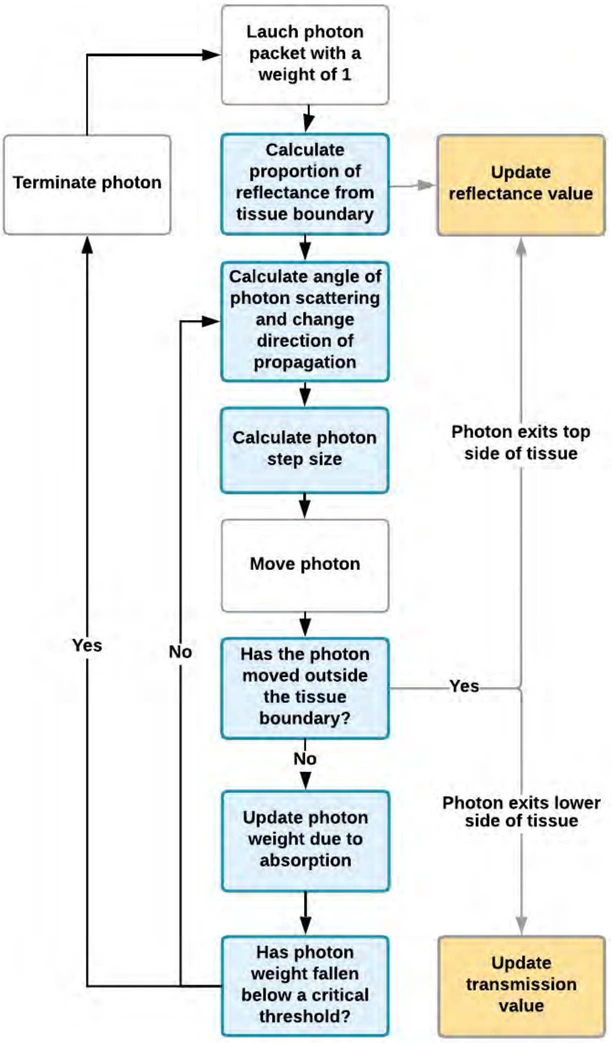

Figure 13: Flow diagram for the basic process of Monte Carlo calculations for propagating photons in a homogenous semi-infinite slab.

Given an appropriate number of photons, the Monte Carlo method is accepted as the most accurate solution to the RTE and serves as a validator for other modelling methods. The main disadvantage of Monte Carlo is the computationally intensive nature of algorithm. Several approaches exist for speeding up Monte Carlo modelling of light, including scaling methods, perturbation MC, hybrid MC methods and variance reduction techniques, but the most effective is computational parallelisation, to which MC is well suited (125).

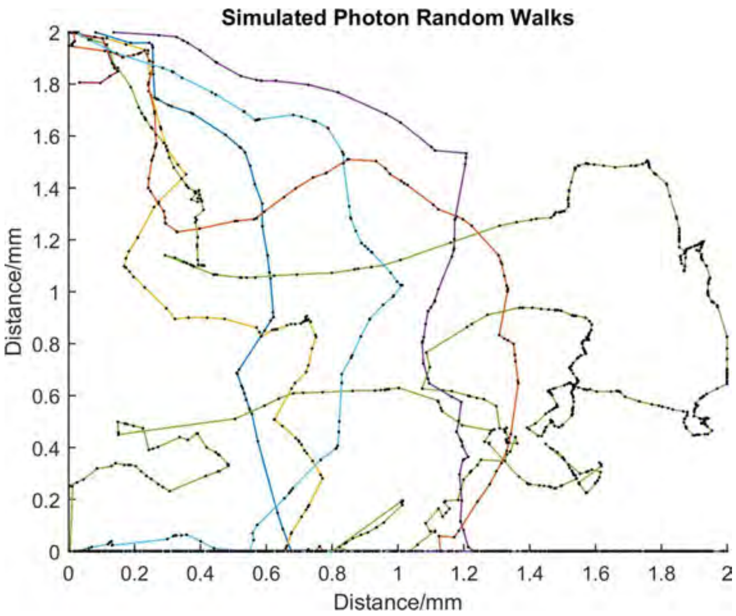

Figure 14: Several examples of simulated photon walks through a tissue slab using the Multi-Layered Monte Carlo (MCML (126)) model of photon propagation through layered media (described in section 3.2.1). Each black dot represents an incidence of scattering.

### 2.6.7 Extracting Optical Properties from Optical Measurements

Given that the optical properties can contain information about the composition of a tissue, many methods exist for the reconstruction of optical properties in tissues. The method of reconstruction depends primarily on imaging method used to obtain the data which can vary vastly. In general, the problem of reconstructing optical properties for a turbid, heterogeneous tissue, is non-linear, ill-conditioned and ill-posed, due to cross talk between scattering and absorption coefficients.

Commonly reconstructed tissue parameters for absolute imaging are the total haemoglobin concentration (HHb), the oxygen saturation ($SO_2$), and the concentration of melanin, or for dynamic imaging the change in the concentration of these parameters from an unknown start value. 3D reconstruction of tissue parameters generally involves inputting estimation values into a 3D model then performing an iterative optimisation procedure to converge the model to a minimum error with real data (43,46). Spatially resolved spectroscopy (SRS) uses the rate of attenuation of light with distance in the tissue to analytically derive values for tissue oxygenation (127). For tissue parameter estimation from multispectral images, different methods have been applied in literature. The modified Beer-Lambert law (equation 4) can be used in conjunction with Monte Carlo models to find a linear relationship using multiple regression to calculate the coefficients of absorbing chromophores (128–130), analytical models have been applied where the behaviour of light in the skin is approximated mathematically (131), and inversion by defining a unique mapping from spectral space to chromophore concentrations using Monte Carlo simulations covering all possible combinations of chromophores (104,132).

## 2.7 Introduction to Multispectral Imaging

Multispectral imaging (MI) refers to imaging modalities which record spectral information at multiple wavelengths, and hyperspectral imaging refers to imaging with hundreds of wavelengths or more. Traditional colour imaging with a standard camera records a colour vector of red, green and blue (RGB) for each individual image pixel. When displayed simultaneously, the colours can be interpreted by the human eye because they correspond to the red, green and blue cone receptors of the retina. However, contracting the full spectral power distribution down to three values represents a significant loss of spectral information. Different spectral distributions can be perceived as identical colours providing their RGB ratio is the same, in an effect known as metamerism. Recording higher resolution spectral information results in a truer representation of the spectral power distribution and better distinguishes spectral features. The range and resolution of recorded wavelengths depends on the instrumentation and on the purpose of imaging. Examples of uses for multispectral imaging are quite diverse and include functions such as remote sensing, examination of paintings, and microscopy (133).

Macroscale multispectral imaging is not currently commonly used in clinical applications, although a number of research-based techniques have been developed with an increasing number of potential applications. The primary application of MI is some form of physiological parameter estimation from reflectance images. Given diffuse scattering in tissue, reflectance MI samples the diffusely reflected light from the surface of a tissue which represents light scattered within approximately 2mm of the surface in the visible wavelengths (134). If applicable, the method of parameter fitting varies from simple mathematical models to model based fitting regimes. The majority of literature focuses on MI of skin and skin lesions (104,135–138), but other applications include fundus imaging (139), endoscopy (140), and laparoscopy (141,142). Many different approaches have been taken to MI with functional modifications including multimodal imaging (143) with additional optical imaging techniques and recently, spatial frequency domain imaging  (SFDI) where structured light of multiple wavelengths is used to estimate tissue scatter (144). Software adaptations have included the use of machine learning algorithms for the purpose of classification (135,142).

## 2.8 Hypothesis

On the basis of the changes in chromophore concentrations believed to occur in tissue affected by arthritis symptoms (section 2.2), and the capability of multispectral imaging to measure the spectral response of materials in addition to spatial data (section 2.7), this thesis examines the hypothesis that symptoms of arthritis in murine models of rheumatoid arthritis can be detected and quantified through analysis of spectral measurements. Stated more formally the hypothesis for the project is:

Symptoms of inflammatory arthritis are detectable in mouse hind paws by multispectral imaging because of disease-induced variation in the relative quantities of biological chromophores.

# 3 Monte Carlo Modelling Optical Reflectance and Transmittance of the Mouse Hind Paw

## 3.1 Introduction

This chapter covers work done on modelling multispectral reflectance and transmittance spectra of the mouse hind paw using a multi-layered Monte Carlo model simulation of photon transport through a layered medium. The aim of this work was to model (*in silico*) tissue changes occurring with arthritis and evaluate the effect on the tissues optical response. To this end, section 3.2.1 describes the choice of computer model, section 3.3.1 describes the optical parameters used in the model. Section 3.3.2 describes the changes induced to simulate arthritis. Section 3.4.1 describes the optical reflectance and transmittance data resulting from the model and section 3.4.2 details the effects of chromophore changes in different tissues.

## 3.2 Equipment and Methodology

### 3.2.1 The Multi-Layered Monte Carlo Model

Modelling the mouse hind paw was approached using the prevalent and highly cited Multi-Layered Monte Carlo (MCML) code published by Wang *et al* in 1995 (126). The MCML program, written in ANSI standard C, was designed for modelling steady-state light transport in a semi-infinite multi-layered tissue. MCML uses dynamic data allocation for tissue and model properties, allowing the user flexibility over the model design and complexity. These attributes make it suitable for modelling the mouse hind paw.

For the modelling experiments outlined below, 30 individual wavelengths were used, shown on the modelled reflectance and transmittance spectra in section 3.4.1. The wavelengths were chosen to capture the spectral features resulting from the presence of biological chromophores in the tissue and they match the wavelengths later used in the multispectral imaging system described in chapter 5. For each wavelength, 500,000 photon packages were simulated, sufficiently sampling reflectance and transmittance spectra to reduce noise artefacts (standard deviation of 10x repeat simulations <= $8.19e^{-4}$ in reflectance and <= $5.31e^{-4}$ in transmittance for all wavelengths). The photon packages simulate individual photons moving through the tissue (Figure 14) and their weight decreases with each scattering movement, simulating the probability of absorption. The weight losses are interpolated from 3D coordinates onto a 2D gridded area representing the tissue (Figure 15), which could be displayed after the Monte Carlo program has terminated. The weights of photons leaving the tissue are recorded, simulating the probability of reflectance/transmittance, angle of exit, and distance from photon entry point. A grid resolution of 5 µm (r, z) was adequate for displaying the layered tissue model (tissue boundaries fell on grid lines), and an angular resolution of 3 degrees, the accuracy to which the angle of photons exiting the tissue is described, was deemed suitable (the Lambertian properties of reflectance and transmittance could be demonstrated – section 8.A2).

In addition to input values for grid size, resolution, and photon variables, MCML required the user to input values for macroscopic properties of the tissue layers, described in section 3.3.1.1. The values of the optical parameters were assumed to be homogenous across the specified tissue layer.

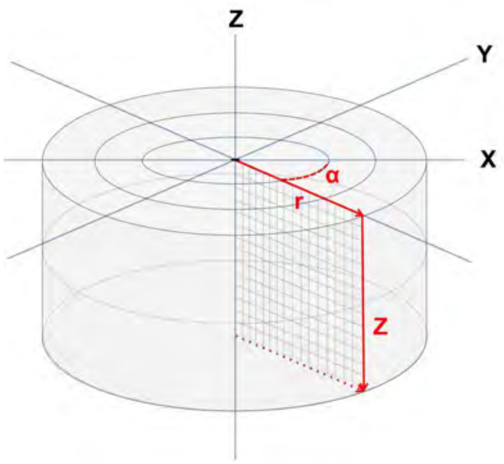

Figure 15: The coordinate system used by MCML for modelling photon propagation. The MCML program (126) uses a 3D coordinate system for modelling photon propagation with results interpolated onto a gridded 2D area described by the r and z axes. The origin of the 2D grid, where photons are injected sits at 0,0 of the (r,z) axes.

## 3.3 Experimental Method Development

### 3.3.1 Tissue Optical Parameters

#### 3.3.1.1 Sourcing the Input Parameters

For the purpose of modelling the mouse hind paw, optical properties were required for several different tissue types across a range of wavelengths covering the visible and NIR spectra. The quantities required for modelling each individual tissue layer were the absorption coefficients ($\mu_a$ [cm$^{-1}$]), scatter coefficients ($\mu_s$ [cm$^{-1}$]), refractive index (n), anisotropy (g) and the tissue layer thickness (d [cm]). The sources of these values are addressed in sections 3.3.1.2 through 3.3.1.3.

#### 3.3.1.2 Tissue Layer Measurements

For estimating the thickness of the tissue layers, images of H&E stained tissue sections from entire mouse hind paws were analysed. Mouse hind limbs were fixed in 4% neutral buffered formalin for 24 hours and then decalcified in 10% EDTA (a calcium-chelating agent) pH7.4 for a period of 3 weeks. Samples were then embedded in paraffin and sectioned along the sagittal axis by microtome, stained with haematoxylin and eosin and mounted with DPX and a coverslip. The slides were imaged by Zeiss Axioscanner and analysed with Zen Blue software, available from (145), taking measurements of typical tissue layer width across the paw.

Ten slides, from a total of 6 mice (the same group of mice as imaged in section 6.4.1.1), were analysed at four anatomical locations to measure the thickness of each of the tissue layers, with the results shown in Figure 16. In this thesis, these areas have been called the heel, midfoot, joints and toes. They were chosen due to broad anatomical differences in the structure of the foot. The 'toes' area included all the digits of hind paw. The 'joints' were isolated to include the area of tissue above the metacarpophalangeal joints connecting the toes to the central region of foot. This area is where the footpads are mostly located, thicker protuberances of skin where the paw is most in contact with the floor. The 'midfoot' encompassed the area above the metacarpal bones of the foot where there is a thicker layer of soft tissue, mostly muscle, between the skin and the bone. The final area was the 'heel', the area of skin over the collection of bones that form the heel of the foot.

Five main tissue types were identified in the paw and the order of the layers used for *in silico* modelling were identified based on these sections. These were epidermis, dermis, muscle, bone and bone marrow. The midfoot was used to model the normal and arthritic spectral responses of the paw shown in section 3.4.1. The thickness of the tissue layers is described from the plantar surface (underside) of the paw to the dorsal (topside) surface, in line with the later reflectance and transmittance results for spectroscopy (chapter 4) and multispectral imaging (chapter 6).

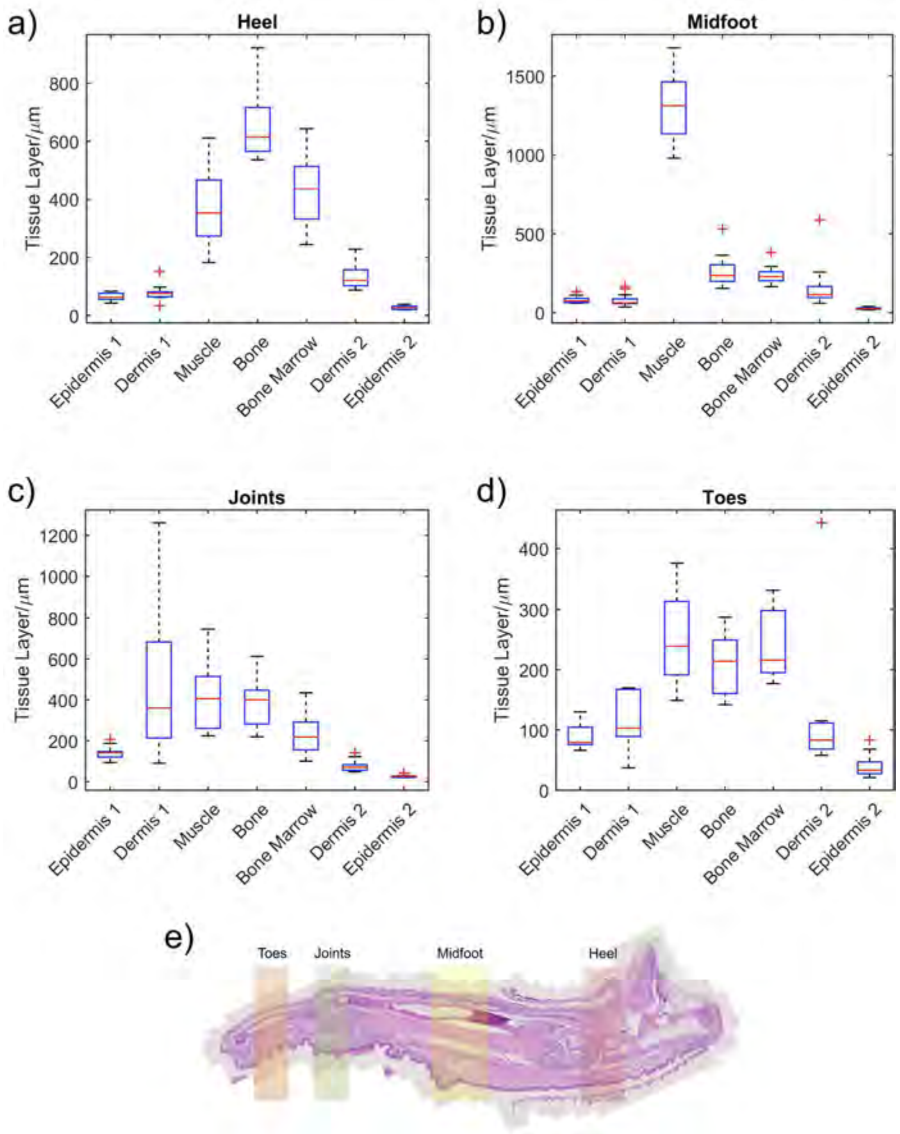

Figure 16: Measurements of tissue layer thickness obtained from analysis of H&E stained mouse paw sections. Ten representative H&E slides were chosen from the group of 6 mice described in section 6.4.1.1 to ensure a good cross section of the four areas of interest. The measurements were divided into four anatomical regions to correspond to heterogeneity in structure a) Heel b) Midfoot c) Joints d) Toes. Epidermis 1 corresponds to the surface layer on the underside of the paw and epidermis 2 corresponds to the surface layer of the top of the paw. In the box plots the central line is the median, the bottom and top edges of the box are the 25th and 75th percentiles, the whiskers extend to the most extreme values not considered outliers and crosses indicate outlier values calculated by Matlab (a value more than 3 scaled median absolute deviations from the median) e) Example H&E section from a mouse hind paw with the anatomical regions described in section 3.3.1.2 highlighted.

#### 3.3.1.3 Absorption and Scatter Coefficients

The optical properties used in the model are described below. For a description of the underpinning physics, covering the interaction of light with biological tissues, see section 2.6.

#### 3.3.1.3.1 Absorption Coefficients:

The major biological absorbers for the Visible and NIR wavelengths are haemoglobin, in its oxygenated ($HbO_2$) and unoxygenated (Hb) forms, and water. The absorption coefficients for these three molecules are shown in Figure 17, along with the absorption coefficients for melanin and adipose which were also considered in the model. Melanin is present in the hair follicles on the upper surface of the mouse hind paw and lipids are present in the adipose tissue of the bone marrow. Haemoglobin is present in all tissues except the epidermis and water is ubiquitous, though concentrations of both may vary depending on tissue type. For Monte Carlo modelling, the absorption coefficients of a tissue were treated as a linear combination of constituent absorbers in each of the five tissue types.

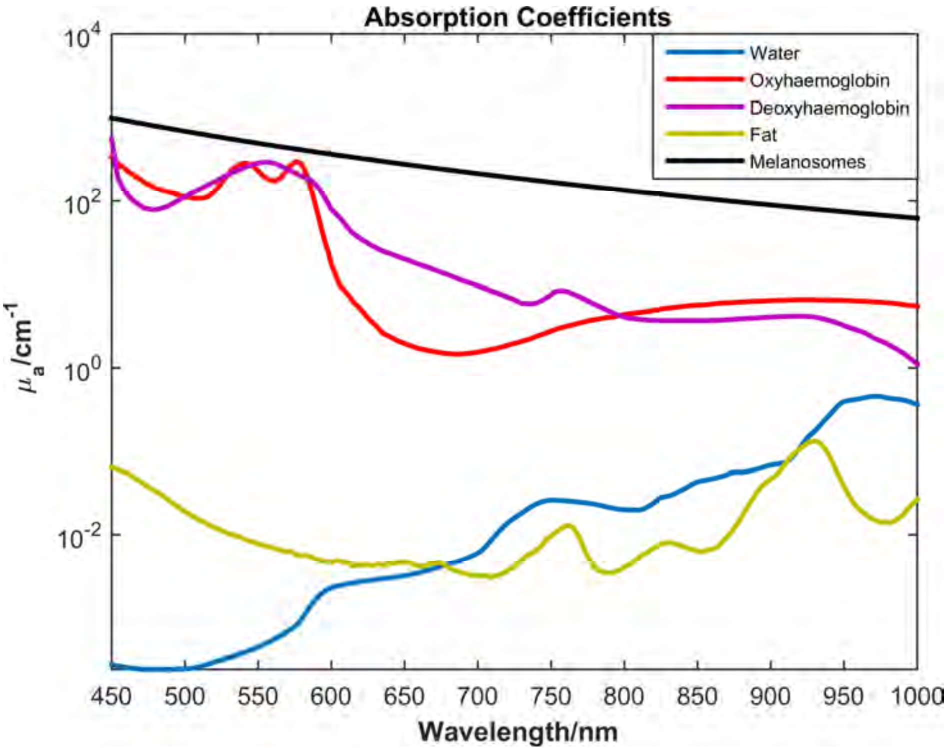

Figure 17: Absorption coefficient values (cm$^{-1}$) in the wavelength range 450nm to 1000nm for common biological chromophores water (146), oxygenated haemoglobin (147), deoxygenated haemoglobin (147), adipose(148), and melanosomes (149).

### 3.3.1.3.2 Scatter Coefficients:

In the case of biological tissues, scattering coefficients generally assume a decreasing exponential relationship with wavelength across the visible and NIR spectrum, due to the combined effects of Rayleigh and Mie scatter. Due to difficulty in measuring scattering coefficients and natural variation in tissue, exact values in literature are rarely consistent between different mechanisms of measurement and often do not cover the full visible and NIR spectra. Jacques *et al* (150) collated values of reduced scatter coefficients from many sources and fitted an empirical equation to the coefficients with a least squares approximation, generalising reduced scatter to cases of skin, bone, fibrous tissue, fatty tissue, and others. This served to average variability between separate sets of scatter measurements and made accurate interpolation between wavelengths possible where measured data were sparse. For MCML modelling of the simulated mouse hind paw, reduced scatter coefficients were converted to scatter coefficients through equation 7 then fitted to the equation

$$\mu s(\lambda) = \mathrm{A} + \mathrm{M}e^{k\lambda} \tag{10}$$

where A, M, and k are independent variables: the parameters M and k describe a decreasing exponential curve and additive offset A was included to improve the fit. The fitting procedure was a least squares fitting of the equation to the coefficient values, implemented using Matlab (151). The scatter coefficients used in modelling the paw are shown as a function of wavelength in Figure 18 and the corresponding values for the parameters A, M, and k in different tissues are shown in the accompanying table.

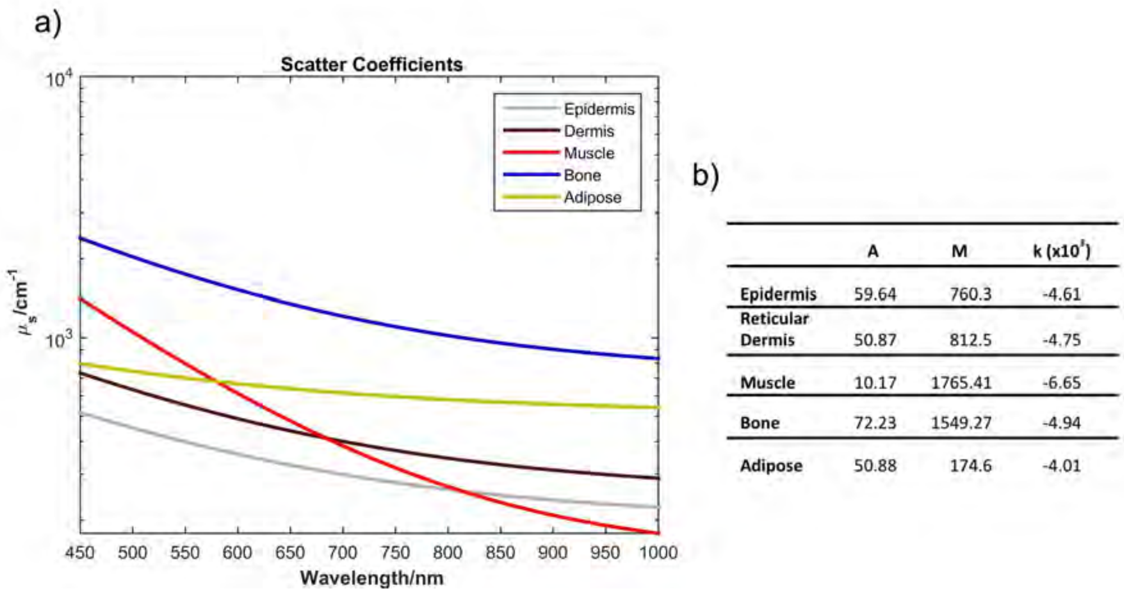

| | A | M | k (x10$^{3}$) |
|---|---|---|---|
| **Epidermis** | 59.64 | 760.3 | -4.61 |
| **Reticular Dermis** | 50.87 | 812.5 | -4.75 |
| **Muscle** | 10.17 | 1765.41 | -6.65 |
| **Bone** | 72.23 | 1549.27 | -4.94 |
| **Adipose** | 50.88 | 174.6 | -4.01 |

Figure 18: Scatter coefficients for biological tissues fitted to equation 10. a) Scatter coefficients (cm$^{-1}$) in the wavelength range 450nm to 1000nm for dermis, muscle, bone, epidermis, and adipose. Values calculated from the fitting of equation 10 to data collated and fitted by reference (150). b) Values for A, M and k in equation 10, for the five tissue types included in the mouse paw model.

### *Anisotropy and Refractive Index:*

For the purposes of modelling the mouse hind paw using MCML, anisotropy (g) and refractive index (n) were assumed to be constant across the visible and NIR wavelengths. The values used in modelling, as well as their sources, are tabulated in Table 1.

| | **Anisotropy (g)** | **Refractive Index (n)** |
|---|---|---|
| **Epidermis** | 0.7 $_{(152)}$ | 1.34 $_{(152)}$ |
| **Dermis** | 0.8 $_{(153)}$ | 1.4 $_{(153)}$ |
| **Muscle** | 0.93 $_{(154)}$ | 1.33 $_{(153)}$ |
| **Bone** | 0.9 $_{(155)}$ | 1.644 $_{(155)}$ |
| **Adipose** | 0.9 $_{(156)}$ | 1.4 $_{(156)}$ |

Table 1: Tabulated values for anisotropy and refractive index used for Monte Carlo modelling of the mouse hind paw. The source reference for each value is given in subscripted brackets.

### 3.3.2 Chromophore Concentrations

For simulating reflectance and transmittance from the mouse hind paw, the optical properties described above (section 3.3.1), remained constant in the tissue model. This section describes the parameters that were varied in order to model the tissue changes in arthritis. The variables of interest for modelling the arthritic paw were the blood volume fraction (BVF), blood oxygenation, and tissue water concentration (see section 2.2 for a description of the biological processes underlying these changes). The objective was to identify how spectral reflectance and transmittance vary as the result of changes in concentrations of the three absorbers, and to indicate the range of expected spectral changes with arthritis symptoms before running experiments with live mice.

| | **Blood Volume Fraction**<br>**Norm (min-max)** | **Hb balance**<br>**Norm (min-max)** | **$H_2O$**<br>**Norm (min-max)** |
|---|---|---|---|
| **Epidermis** | - | - | 20 (157,158) |
| **Dermis** | 2 .5 (0.5 – 8) (150,159,160) | 65 (40 - 80) (150,161) | 65 (50 - 70) (157,158) |
| **Muscle** | 3 (1 – 12) (150,162,163) | 65 (40 – 80) (150,164,165) | 75 (70 – 85) (166,167) |
| **Bone** | 2 (1 – 5) (150) | 65 (40 – 80) (2) | 30 (155,167) |
| **Bone Marrow** | 3 (2 - 8) (168,169) | 65 (40 – 80) (2) | 30 (30 – 40) (168) |

Table 2: Values for blood volume fraction, blood oxygenation (Hb balance), and water concentration ($H_2O$) used in the Monte Carlo model. The values outside the brackets indicate typical values for concentration of the three absorbers within the tissue types. Ranges of values indicated by literature are given within brackets and the subscripted brackets contain references.

Typical values of absorber concentration and ranges of values, shown inside the brackets, are given in Table 2. As with some of the optical values, there is a lot of variation in the literature concerning blood volume fraction, oxygenation and water concentration. The values and ranges established in Table 2 were informed by literature which includes values from various tissue types, from a variety of species, different areas of the body, and using different calculation methods. Given the variation in values, and assuming natural physiological fluctuation in the parameters, Table 2 shows values within ranges commonly identified.

## 3.4 Results

### 3.4.1 Modelling the Spectral Variation with Arthritis

As discussed in section 2.2, inflammation of the joints is thought to induce a change in the concentration of the three absorbers, oxygenated haemoglobin, deoxygenated haemoglobin, and water in the joint and in the local tissues due to the biological processes associated with inflammation. In this section, computer-simulated ‘normal’ and ‘arthritic’ tissues were modelled for their reflectance and transmittance spectra. The changes in absorber concentrations may vary depending on factors like mouse model, time point in disease progression, and possibly other factors such as age/ genetic strain/ gender/ housing conditions, so the model of arthritis used in MCML should be considered a generic *in silico* model of murine paw inflammation and cannot be assumed to accurately model specific *in vivo* murine models of disease. For modelling the normal paw, the norm values in Table 2 were used. For modelling the changes in absorber concentrations in a generic, simulated arthritis the following changes were implemented in the model:

**Blood Volume Fraction:** BVF increased from 3% of tissue volume in the normal tissue model to 5.4% in the arthritis tissue model in the muscle tissue layer, mainly informed by Gayetskyy *et al.* (23), where the increase in vessel volume was measured in successive regions of interest in the tissues surrounding the joint by microCT.

**Oxygen Saturation:** The haemoglobin oxygen saturation values were reduced in the arthritis model from 65% in the normal tissue to 50% oxygenated haemoglobin in the arthritic tissue model in the muscle and bone. This reduction is an estimation mainly informed by Van der Putten *et al* (18) where a 10.8% drop in oxygenation was measured in the microvasculature of the inflamed mouse tendon measured by multispectral microscopy and Rajaram *et al* (95) who measured an 11% drop in oxygen saturation in rabbits inflamed knee joints with time-resolved diffuse optical spectroscopy.

**Oedema:** Oedema was represented in the model by an increase in the water percentage of the muscle by 15%. In reality this would increase the volume and in turn affect the scattering coefficients and other chromophore concentrations, however for the purposes of modelling just the water percentage was altered. Perilli *et al.* (25) showed an increase of 36% in the volume of CAIA mouse paws, supporting the increase of water content in oedema.

Figure 19 displays the reflectance and transmittance spectra calculated for a layered tissue model of a mouse hind paw. ‘Normal’ and ‘arthritic’ reflectance and transmittance spectra are displayed in blue and red respectively, modelled according to the values discussed above. The raw spectra have been interpolated by a cubic spline, estimating the spectral response across all wavelengths from 480nm to 1000nm. The circular marks on the spectra in Figure 19a and b indicate the wavelengths modelled by MCML.

Figure 19 indicates that the incidence of biological chromophore changes present in the arthritic mouse paw should be detectable in the reflectance and transmittance spectral response of the tissue, according to the Monte Carlo modelling results. Figure 19c and Figure 19d displaying the difference between the two spectra indicate that, for reflectance, there is a decrease across all wavelengths between 480 nm to 1000 nm, with the maximum difference located between 600 and 700 nm (7.40% decrease in reflectance at 610 nm). Transmittance, absorption and backscatter in the tissue resulted in very low transmittance in the visible spectrum, and differences between the normal and arthritic spectra were only apparent at wavelengths exceeding ~600nm where light transmission through the tissue is likely to become detectable. The maximum difference in transmittance of 2.46% occurs at 642 nm.

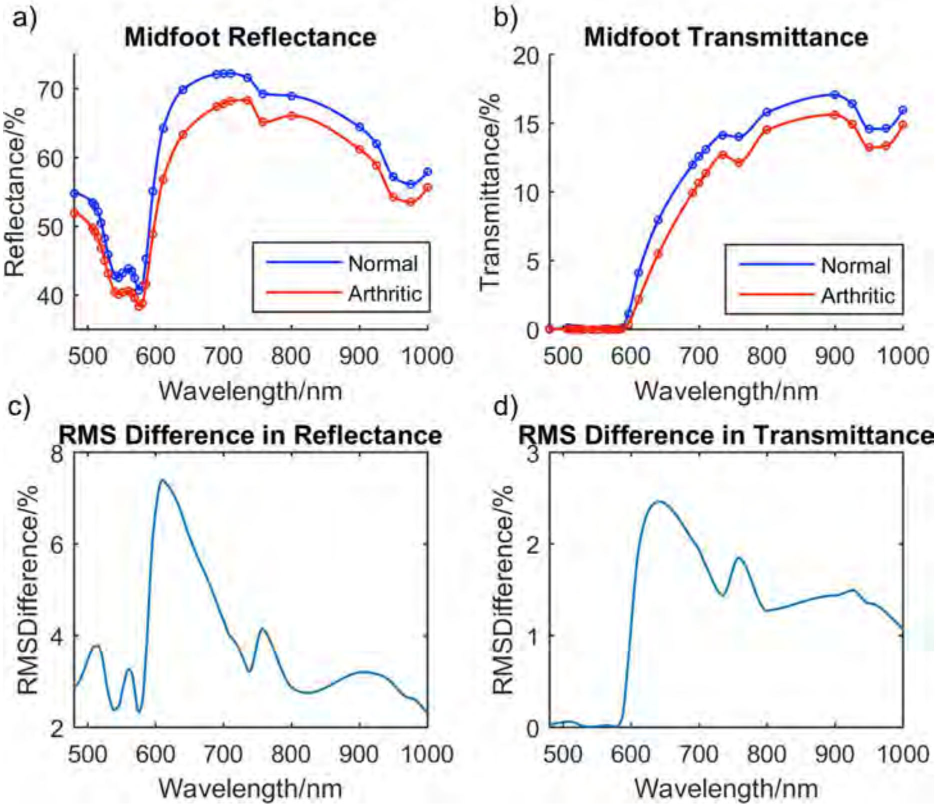

Figure 19: Reflectance and transmittance spectra from a Monte Carlo model of the ‘midfoot’ mouse hind paw in a ‘normal’ and ‘arthritic’ state. a) Reflectance spectra from the Monte Carlo tissue layer model of the mouse hind paw, where a case of a normal (blue) paw and an arthritic (red) paw have been modelled using optical parameters from literature and measurements from H&E tissue sections. b) Transmittance spectra produced from the same model. c) Root Mean Square difference between the normal and arthritic reflectance spectra. d) RMS difference between the normal and arthritic transmittance spectra.

In general, arthritic symptoms lead to a reduction in reflectance and transmittance response across all wavelengths; a logical result considering the predicted increased concentration of biological absorbers in the tissue. Modelling results from the other areas of the feet showed smaller changes (section 8A3), but considering that the thickest muscle layer is found in the midfoot region and the modelled chromophore changes focus on the muscle tissue, this result was expected. Additional outputs of the MCML program for the modelling of the mouse hind paw have been included in the appendices (section 8.A2).

### 3.4.2 Spectral Variation with Localised Parameter Changes

In rheumatoid arthritis, the main site of pathology centres around the joint and the synovial lining of the joint capsule, affecting local tissues as modelled above. Although RA is a systemic disease and can have effects of other tissues, tissue distant from sites of inflammation shows no overt pathological changes.

The MCML model of the central region of the mouse hind paw described above (section 3.4.1) was used to model changing optical parameters in the deeper tissue (e.g. muscle) versus superficial tissue (e.g. reticular dermis). Given that the signal from arthritic inflammation is likely to reside in the deeper tissue layer, it is informative to see whether the spectral response of the tissue is affected by the depth of the chromophore changes.

#### 3.4.2.1 Tissue Layer vs Change in Spectra

This section looks at the effect of tissue layer depth on the spectral effect of chromophore changes. Given the aim of multispectral imaging to look at the spectral changes caused by arthritis symptoms, the imaging system needed to be able to distinguish chromophore concentration changes in superficial tissues from chromophore changes at the site of pathology. Given that the mouse hind paw is a thin structure which contains a variety of different tissue types, the distance between different layers is less than 1mm. Detectable tissue changes resulting from arthritis were expected to be mostly in the muscle layer peripheral to the bone, roughly 0.8mm below the skin surface although this would vary with the anatomy of the paw. In this section we aimed to test whether the chromophore changes in tissue layers adjacent to the bone could be contaminated by cross-talk from chromophore changes in superficial layers of the skin. Figure 20 displays the results for changing the blood volume fractions in the dermis and muscle (Figure 20a and b), the oxygenation in the dermis and muscle (Figure 20c and d), and the water content (Figure 20e and f).

## 3.5 Discussion

### 3.5.1 Discussion of Results

In the Monte Carlo *in silico* model described above, changes in the concentration of all three absorbers produce spectral changes in the reflectance and transmittance response of the tissue. For the concentration changes shown in Figure 20a and b, increasing the BVF causes the largest changes in reflectance and transmittance for the dermis and for the muscle layers.

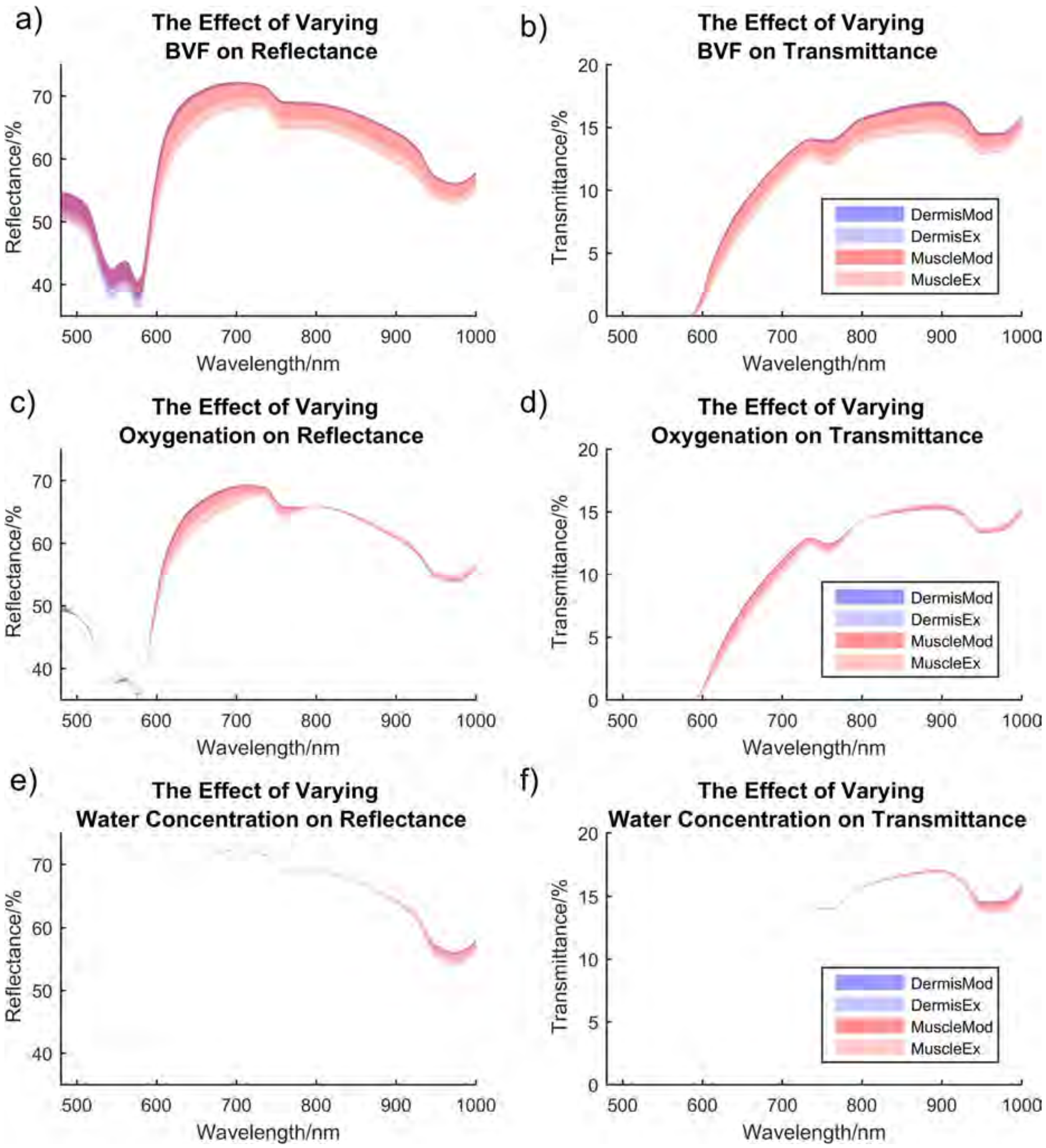

Figure 20:The effect of changing individual model parameters on reflectance and transmittance spectra for a Monte Carlo model of the mouse hind paw a) Spectral changes in the tissue reflectance response resulting from increasing blood volume fraction (BVF) in the dermis (DermisModerate: darker blue 2.5-4.5%, DermisExperimental: pale blue 4.5-5.75%), and the muscle layer (MuscleModerate: darker red 3.0-5.4%, MuscleExperimental: pale red 5.4-6.9%). b) Transmittance spectral response resulting from the tissue changes outlined in a. c) Spectral changes in tissue reflectance resulting from decreasing blood oxygen saturation from in the dermis (darker blue 65-50%, pale blue 50-40%), and the muscle layer (darker red 65-50%, pale red 50-40%). Blood volume fraction was set to 4.5% in the dermis and 5.4% in the muscle. d) Transmittance spectral response resulting from the tissue changes outlined in c. e) Spectral changes in the tissue reflectance response resulting from increasing water concentration in the dermis(darker blue 65-78%, pale blue 78-87%), and in the muscle (darker red 75-90%, pale red 90-100%). f) Transmittance spectral response resulting from the tissue changes outlined in e.

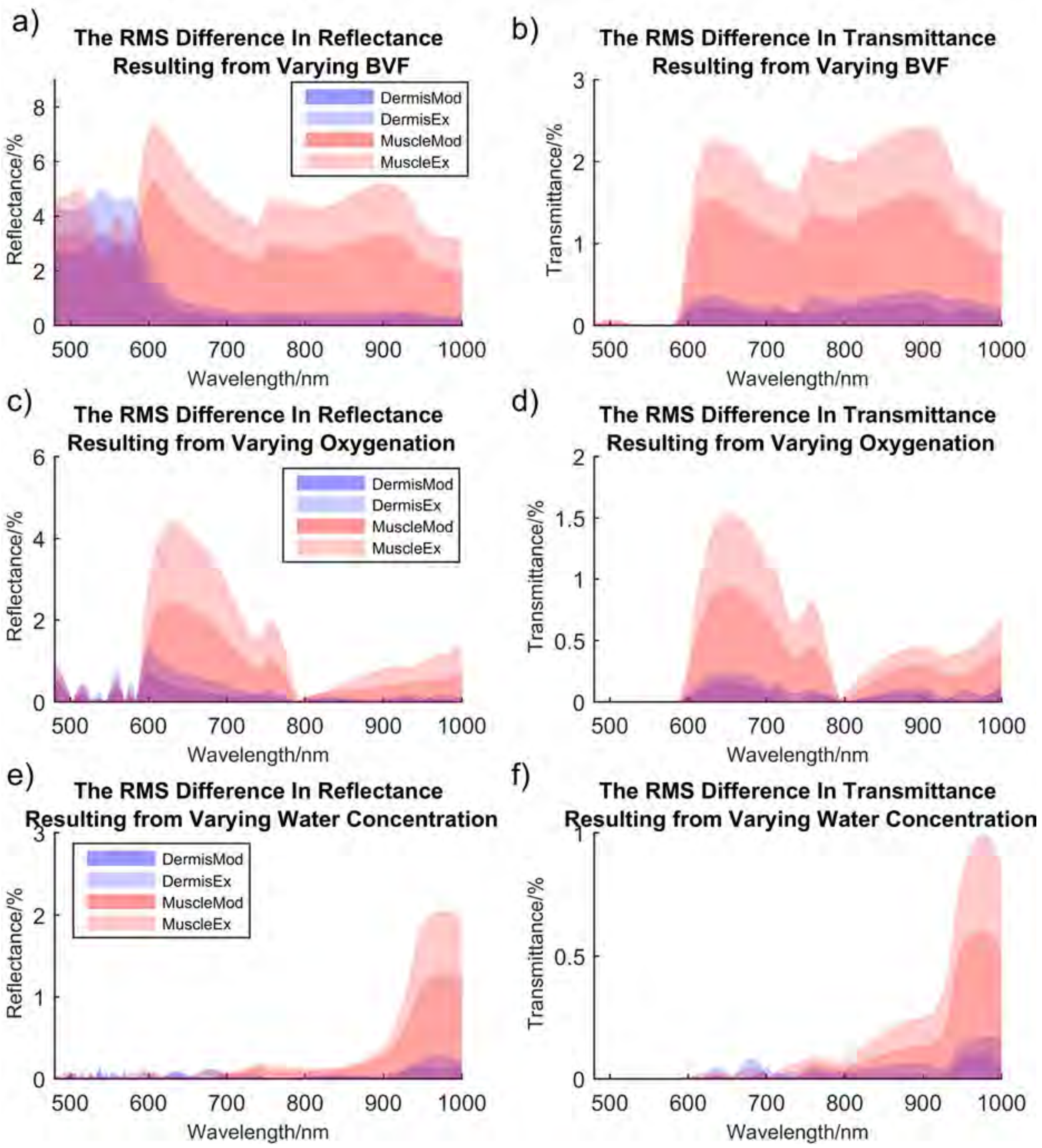

Figure 21: Root mean squared (RMS) difference resulting from changing individual model parameters for reflectance and transmittance spectra for a Monte Carlo model of the mouse hind paw a) The root mean squared difference between the reflectance spectra shown in Figure 20a, where BVF was changed in the dermis (blue and pale blue) and muscle (red and pale red). b) The RMS difference between the transmittance spectra shown in Figure 20b, where BVF was changed in the dermis (blue and pale blue) and muscle (red and pale red). c) The RMS difference between the reflectance spectra shown in Figure 20c where the blood oxygen saturation was altered in the dermis (blue and pale blue) and muscle (red and pale red). d) The RMS difference between the transmittance spectra shown in Figure 20d where the blood oxygen saturation was altered in the dermis (blue and pale blue) and muscle (red and pale red). e) The RMS difference between the reflectance spectra shown in Figure 20e where the water content was altered in the dermis (blue) and muscle (red). f) The RMS difference between the transmittance spectra described in Figure 20f where the water content was altered in the dermis (blue) and muscle (red).

Figure 21a and Figure 21b demonstrate that for reflectance the spectral response of the tissue changes according to the depth of the tissue layer in which the absorber concentration change occurs. Increasing the BVF in the dermis decreases the reflectance response of the tissue primarily in the visible region of the spectrum between 500 and 600nm, whereas increasing the BVF of the muscle causes a decrease in the reflectance across all wavelengths of the visible and NIR spectrum, with a maximum response at around 620nm. In the case of vasodilation/angiogenesis in response to inflammatory activity in the joint, an increase in the BVF would be expected in the local tissues. These simulations suggest that multispectral imaging of the mouse hind paw would detect a decrease in reflectance across all the visible and NIR wavelengths in response to increased BVF in the joint tissue/ muscle.

For the variation of the haemoglobin oxygen saturation, changes detectable in the simulated spectral responses of the tissue were dependent on the BVF. Unsurprisingly, decreasing the oxygen saturation has a larger effect on the spectra if the concentration of blood in the tissues is higher. Consequently, if the blood concentration of the mouse hind paw is lower than predicted by the model, changes in the spectral shape resulting from decreasing oxygen saturation may be difficult to detect.

Changing the blood saturation in the dermis and muscle resulted in approximately equivalent changes in the reflectance response of the tissue for the visible wavelengths from 500 nm to 600nm, but saturation changes in the muscle resulted in larger changes in the reflectance response from 600nm to 1000nm. Another notable feature of saturation change was the isosbestic point at 800nm apparent in Figure 20c and d, showing an increase of reflectance and transmittance at these wavelengths with decreasing saturation. This decrease in absorbance is in opposition to the effect of increasing BVF due to the relative effect of decreasing oxygenated haemoglobin. For imaging live arthritis models, these simulations suggested that changes in oxygen saturation resulting from increased metabolism in the inflamed tissue around the joint should be detectable in the reflectance and transmittance spectrum by an increase in absorption in the 600 – 800nm region.

Measurable changes in the spectral response of the tissue resulting from changing water concentration were primarily contained in the region from 900 to 1000nm. The percentage change of the spectral response was relatively low, which may make it difficult to detect in an imaging system when noise is taken into consideration. Some arthritis models also experience less oedema than others so the presence of spectral changes resulting from water would depend also depend on the model being imaged.

In general, longer wavelength photons sample the tissue to a greater depth, whereas the shorter wavelengths sample the more superficial layers, resulting in concentration changes of the same chromophores having a different effect on the spectral response of the tissue depending on the depth of the tissue layer. The results of these experiments suggest that arthritis-associated chromophore concentrations in the deeper layers of tissue adjacent to the bone should be detectable in the reflectance and transmittance spectra and should be distinguishable from superficial chromophore concentration changes.

The MCML method of modelling photon transport in turbid media is a well-established model used often in modelling photon interactions with layered tissues (125,170–173). Although 3D Monte Carlo methods exist (121), a slab approximation was used for this work to avoid the need for building an accurate 3D mesh. Although the effects of RA have been modelled in human fingers (17), to the authors knowledge this is the first incidence of modelling spectra from arthritic mouse hind paws. This work does however corroborate results detailed from previous imaging experiments in literature (94).

### 3.5.2 Limitations

The limitations of this modelling method were mainly due to difficulty in sourcing optical parameters from the literature and the approximations made by the MCML model. Lack of corroborated values to use as inputs to the model and differences in the geometry of the tissue can introduce uncertainty and error into the resulting spectra, and because of this the results of the model cannot be considered a replacement for real imaging data.

### 3.5.3 Conclusion

Modelling of the mouse hind paw using a multi-layered Monte Carlo based implementation of photon transport indicated detectable changes of the reflectance and transmittance spectra in a simulated model of arthritis. Values from literature were used to model the expected changes in chromophore concentrations. Further investigation with changing chromophore concentrations individually showed that increasing BVF, decreasing oxygen saturation, and increasing water concentration all contributed individually to the changes seen in the tissue spectral responses. They also produced characteristic changes in the tissue reflectance depending of the depth of the tissue layer. The next chapter details the first examples of hyperspectral data from live mouse arthritis models using spectroscopy.

# 4 Spectrophotometry of Rheumatoid Arthritis Mouse Models

## 4.1 Introduction

Modelling the mouse paw using Monte Carlo suggested that spectral changes should be detectable in the 450 to 1000nm spectral region in both reflectance and transmission geometry (section 3.4.1). This chapter discusses the first application of spectral imaging on the mouse paw using spectrophotometry in a reflectance and transmittance format, procuring high-resolution spectral data of the changes occurring due to arthritic symptoms. Section 4.2 introduces the equipment and calibration methods. Section 4.4.1 displays the data taken from live anaesthetised mice and Section 4.5 discusses the findings and issues of spectrophotometry for data collection from live mice.

## 4.2 Equipment and Methodology

The aim of spectrophotometry of live mice was to collect high-resolution spectral data simultaneously in a reflectance and transmittance geometry from the hind paws of live mice. The equipment used in designing the set-up for imaging is described below.

### 4.2.1 Light Source

The light source used for illuminating the subject of imaging was an Ocean Optics HL-2000-FHSA tungsten halogen with a quoted spectral range from 360nm to 2400nm and a 6.7mW output, Figure 22a displays the spectrum of the light source measured in the reflectance geometry of the spectrophotometry system (section 4.3.1) using a 99% reflectance standard.

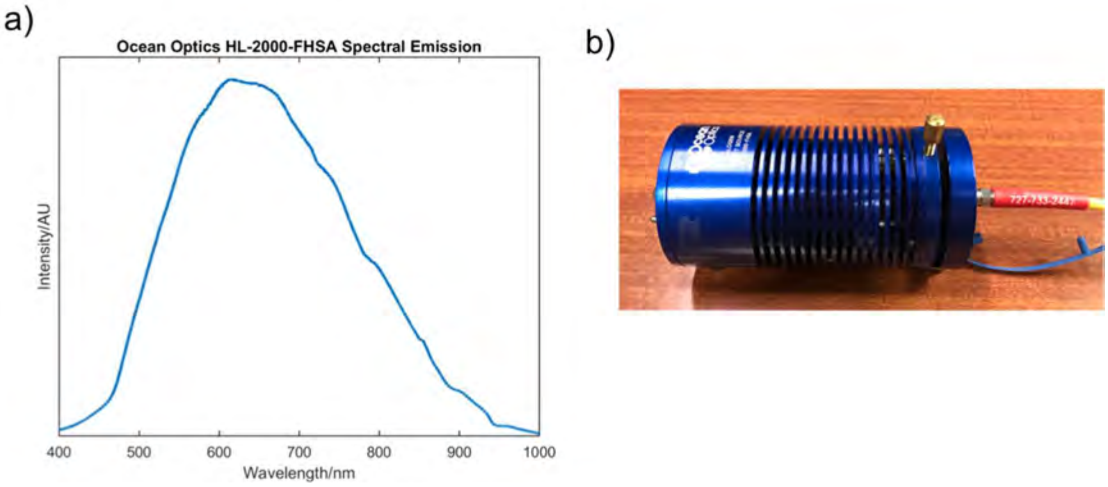

Figure 22: Ocean Optics HL-2000-FHSA light source used for collecting spectrophotometry measurements. a) Spectral output of the Ocean Optics HL-2000-FHSA tungsten halogen light source. b) Photo of the Ocean Optics HL-2000-FHSA light source.

### 4.2.2 Spectrometer(s)

An Ocean Optics Flame-s spectrometer was used to measure diffuse reflectance data. The spectrometer has a wavelength measurement range from 190nm to 1100nm (spectral resolution approximately 0.3nm to 0.4nm increasing linearly over wavelength range), high thermal stability, a variable integration time from 1ms to 65 seconds and a quoted signal to noise ratio of 250:1 at full signal. OceanView software was used to control the spectrometer for taking measurements. The spectrometer was used in conjunction with a bifurcated 2m R200-7-VIS-NIR optic fibre with a 200µm core and a wavelength range from 400nm to 2100nm. For measuring diffuse reflectance, a probe was also designed in openSCAD and printed in black PLA plastic to keep the distance of the fibre from the tissue constant and to locally block background light (Figure 23a). It would not, however, block light which migrated through the tissue.

An Edmund Optics BSR112E-VIS/NIR spectrometer was used to take transmission data from the imaging subject, with a wavelength range from 242nm to 1052nm (spectral resolution varying between 0.3nm and 0.5nm), and a variable integration time. Instead of an optic fibre, a diffuser was placed in front of light input to the spectrometer.

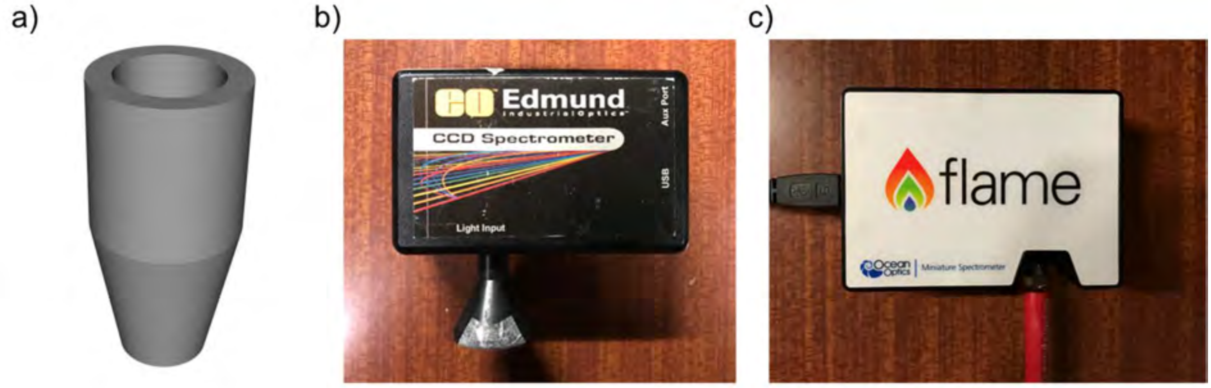

Figure 23: Spectrometers used to collect reflectance and transmittance spectral measurements. a) Reflectance probe designed using openSCAD and Slicer software for holding the reflectance probe optic fibre at a set distance of 3mm from the tissue and blocking background light illumination. b) Photo of the Edmund Optics BSR112E-VIS/NIR spectrometer used for transmittance data. c) Photo of the Ocean Optics Flame-s spectrometer used for reflectance spectroscopy.

### 4.2.3 Mouse Models

All experiments were carried out at the University of Birmingham, UK, following strict guidelines governed by the UK Animal (Scientific Procedures) Act 1986, under PPL licence number 70/8003 and approved by the local ethics committee (BERSC: Birmingham Ethical Review Subcommittee). All mice were fed a standard chow diet and maintained on a 12-hour light-dark cycle.

#### 4.2.3.1 TNF dARE

The TNF dARE colony (58), originally a gift from Prof. George Kollias (BSRC Alexander Fleming Athens University Medical School), was maintained in-house at the University of Birmingham. Mice were genotyped by Transnetyx for the presence of the transgene and were monitored weekly for signs of arthritis. $TNF^{+/dARE}$ mice develop arthritis symptoms whilst littermate controls $TNF^{+/+}$ do not.

Data shown in section 4.4.1.1 were taken from heterozygous C57BL/6 TNF dARE mice and their normal companion littermates on a total of three separate occasions. The data were combined for analysis. Thirteen mice were analysed in total, five of which were $TNF^{+/dARE}$ and eight were $TNF^{+/+}$ controls. The age of the mice when spectrophotometry was performed ranged between the ages of 9 weeks and 13 weeks and both male and female mice were imaged. Two females at 9 weeks of age, one normal and one TNF dARE, six males at 12 weeks, four normal and two TNF dARE, and five males at 13 weeks, three normal and two TNF dARE.

#### 4.2.3.2 CIA

6-8 week old male DBA/1 mice (Harlan) were injected subcutaneously at two sites on the lower back (100μl in total, 50μl at each site) with 1mg/ml complete Freund's adjuvant (Chondrex Inc., cat.no. 7001) containing 1mg/ml bovine type II collagen (Chondrex Inc., cat.no. 2002-2). On day 21 a boost injection of bovine collagen at 1mg/ml in Freund’s adjuvant (as above) was given intraperitoneally. Mice were scored daily for signs of arthritis which has a variable onset but normally begins between 20 and 35 days following the initial injection. Spectrophotometry was performed between 30 and 40 days following the initial injection.

### 4.2.4 Imaging Protocol

Spectrophotometry was performed on the hind paws of the normal and arthritic mice. The mice were anesthetised immediately prior to imaging then reflectance spectrophotometry data were taken from the underside of the paw and transmittance data from the upper side using the method described in section 4.3. Both hind paws were imaged and 3 repeat measurements were taken for each paw, removing and replacing the probes on each occasion. Erroneous measurements where intensity was too low due to bad probe contact with the tissue were discarded and the remaining spectra were mean averaged to give one reflectance and transmission spectrum per paw. As far as possible, the reflectance measurements were taken from the centre of the paw, but due to the surface topology and the small size of the paw, there may be small variation in the location of the measurements. All experiments were carried out at the University of Birmingham, UK following strict guidelines governed by the UK Animal (Scientific Procedures) Act 1986 and approved by the local ethics committee (BERSC: Birmingham Ethical Review Subcommittee).

## 4.3 Experimental Method Development

### 4.3.1 Spectrophotometry System set-up

In order to take measurements in a reflectance and transmittance geometry for live mouse subjects, the hind paw was illuminated by the light source though a bifurcated optic fibre and the reflected and transmitted light detected simultaneously through the use of two separate spectrometers. For measuring diffuse reflectance data, the second half of the bifurcated fibre was directed to the Ocean Optics spectrometer. Using this set-up light illuminates the tissue through the optic fibre then reflected light returns along the same fibre and is detected by the spectrometer. Figure 24a shows a schematic diagram describing the equipment set up. For simultaneous measurements of transmitted light the same set up was retained for illumination, for light collection the Edmund Optics spectrometer was placed directly below the mouse hind paw on the opposite side to the source of illumination. Spectral data were taken in a darkened room.

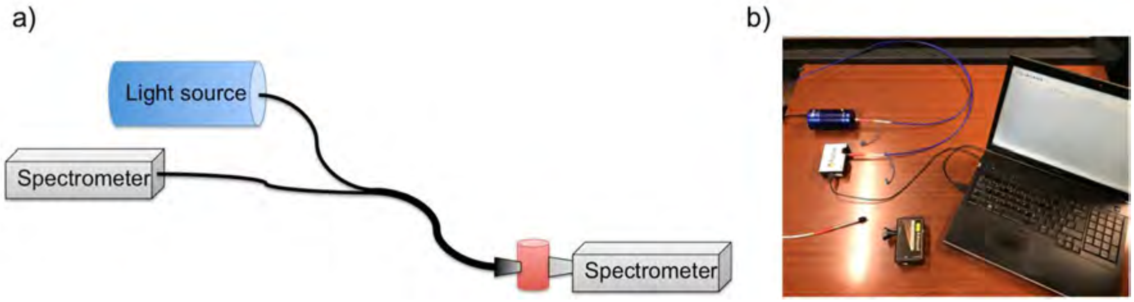

Figure 24: Spectrophotometry system set-up for collecting spectral measurements from mouse models of rheumatoid arthritis. a) Schematic diagram describing the geometry of the system for gathering diffuse reflectance and transmittance data from an imaged object. b) Photo taken of the diffuse reflectance and transmittance spectroscopy system.

### 4.3.2 System Calibration

Given that the calculation of reflectance and transmittance from this spectroscopy system was dependent on the instrument response function (IRF), combining the collective spectral efficiencies of the light source and components of the optical system, the system required calibration so that reflectance and transmittance spectra could be calculated for the imaged object.

For reflectance imaging, Labsphere Spectralon® diffuse reflectance standards, with an optically flat reflectance in the range 250nm to 2500nm ±4%, and ±1% in the photopic range, were imaged in experiments under the same conditions (exposure time, frame averaging, background light) as the object of interest. Figure 25a shows the reflectance percentage of the standards calculated by the spectroscopy system and Figure 25b displays a photo of the 2%, 50%, 75% and 99% reflectance standards. The OceanView software used to control the Ocean Optics Flame-s spectrometer, automated the process of calibration by taking a light reading (reflectance data from the 99% reflectance standard) and a dark reading (reflectance data from the 2% reflectance standard) prior to taking data. The auto-calibrated spectra could then be corrected to 100% manually.

For transmittance spectrometry calibration, a spectrum of relative light source intensity was taken directly by the Edmund Optics Spectrometer with a Neutral Density (ND) filter of Optical Density either 1.0 or 0.6 inserted into the light pathway in order to reduce the light intensity to a level which would not overexpose the CCD. Calibration of the data was done manually using equation 11

$$\mathrm{T}_{\lambda} = \frac{(\mathrm{S}_{\lambda}-\mathrm{D}_{\lambda})}{(\mathrm{I}_{\lambda}-\mathrm{D}_{\lambda})} \times \mathrm{NDTransmission}_{\lambda} \tag{11}$$

where $T_\lambda$ is a vector of object transmission over wavelength, $S_\lambda$ is the raw uncalibrated spectral transmission of the object, $D_\lambda$ is wavelength dependent dark noise, $I_\lambda$ is the ND filtered light source intensity, and $NDTransmission_\lambda$ is the published data for the ND filter transmission at wavelength λ.

Due to noise, the spectral data were mean smoothed across 20 data points giving an effective spectral resolution of 6.7nm in reflection and 7.9nm in transmission. The mean reflectance values for the reflectance standards calibrated by the 99% tile were 75.35%, 50.92% and 1.63%, with coefficients of variation 2.10%, 4.16% and 13.27% respectively. The spectroscopy data from the reflectance imaging of the standards suggests that there is some variation in reflectance across the wavelength range of 400 – 1000nm, but this agrees well with published data (174) and with later multispectral imaging of the reflectance standards (section 5.4.1).

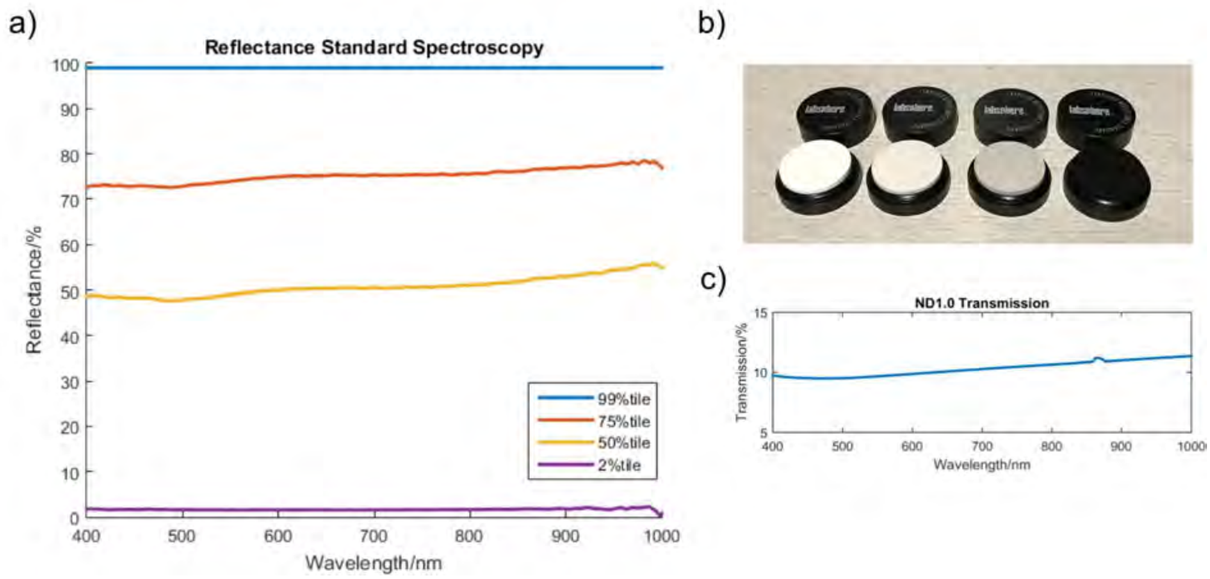

Figure 25: Spectralon reflectance standards used for calibrating spectrophotometry measurements. a) Reflectance spectrophotometry results for the 75%, 50% and 2% reflectance standards calibrated by the 99% reflectance standard. b) Photo of the LabSphere 99%, 75%, 50% and 2% reflectance standards. c) ThorLabs published data for ND1.0 reflective filter transmission.

## 4.4 Results

### 4.4.1 In Vivo Diffuse Reflectance and Transmission Spectrophotometry

This section describes the results from performing diffuse reflectance and transmittance spectrophotometry on the hind paws of a number of live, anaesthetised mice. The aim of these imaging sessions was to examine the spectral differences, previously modelled using Monte Carlo (Section 3.4.1), to see if spectral changes were apparent in real data. Section 4.4.1.1 deals with data taken from the TNF dARE murine model of rheumatoid arthritis alongside normal controls and section 4.4.1.2 discusses data taken from the CIA murine model of RA.

#### 4.4.1.1 TNF dARE Spectrophotometry

The TNF dARE mouse, discussed in section 2.4.1, exhibits a form of erosive polyarthritis arising from the deletion of gene region controlling TNFα expression. Disease arises spontaneously with age and clinical symptoms of redness and deformity are usually apparent around 9 weeks of age, progressing relatively symmetrically. The predictability of arthritis development, and the availability of this mouse model makes it a good candidate for preliminary spectral imaging. Details of the mice used in this experiment are discussed in section 4.2.3.1.

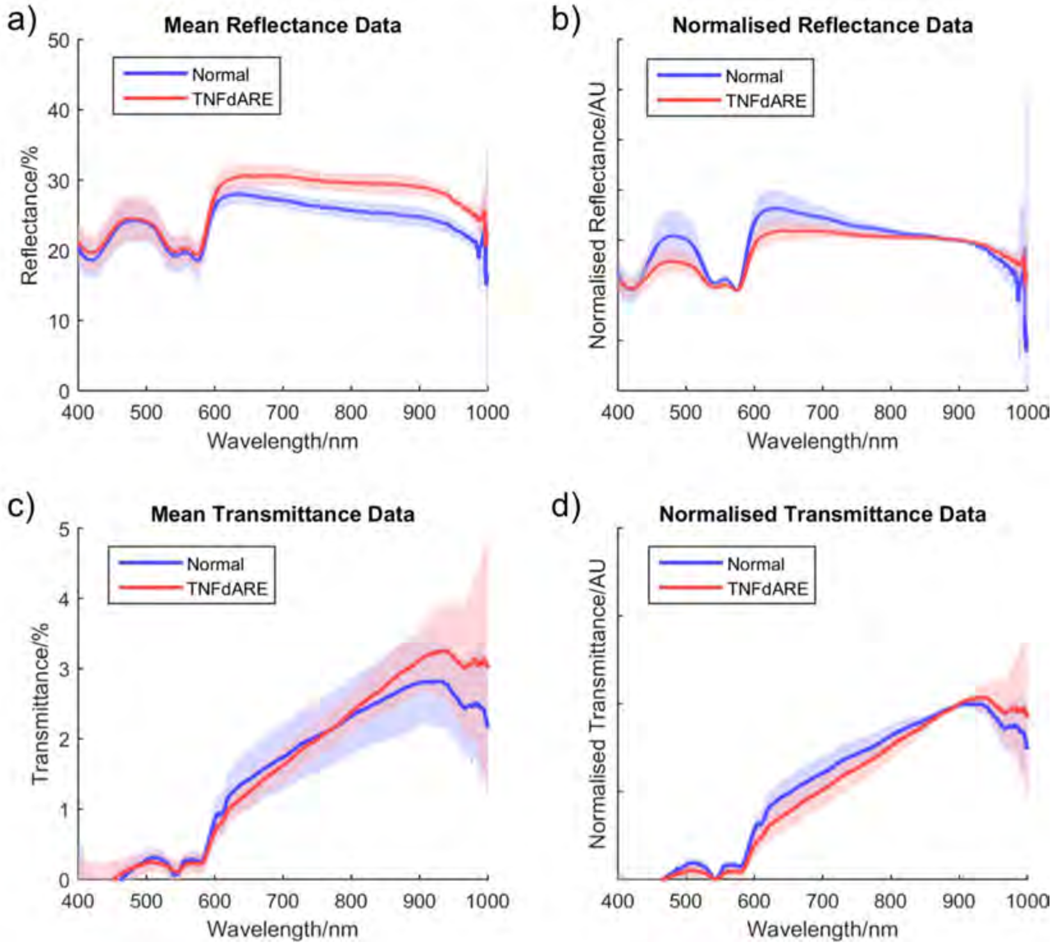

Figure 26: Spectrophotometry average reflectance and transmittance data for normal and TNF dARE mice. N=5 TNF dARE and N=8 normal mice, with spectra taken from two hind paws per mouse giving a total of 16 spectra for reflectance and 21 spectra for transmittance (spectra were removed from the data where repeatability over three repeat measurements was not achieved). Standard deviation for the data is displayed as a shaded region around the mean. a) Mean reflectance spectra from the hind paws of a sample of 10 normal and 6 TNF +/dARE measurements. b) Mean reflectance spectra for the data set shown in Figure 26a min- max normalised by reflectance between 575 and 900nm. c) Mean transmittance spectra from the hind paws of a sample of 12 normal and 9 TNF +/dARE measurements. d) Mean transmittance values for data set transmission of TNF dARE paw measurements min-max normalised by values between 500nm and 900nm.

The results of the TNF dARE spectrophotometry experiments are shown in Figure 26. Figure 26a and Figure 26c show the mean reflectance and transmittance spectra which have been measured and calibrated by the procedure outlined above, and Figure 26b and Figure 26d display normalised data showing the spectrally relevant variation apparent in the measurements. The spectral data were smoothed by a moving mean method, with the size of the window varying depending on the intensity of the light source. The effect of this is to smooth the data more in areas of increased noise but preserve the spectral shape in areas with decreased noise. All spectra were separately min-max normalised between the wavelengths of 575nm to 900nm for reflectance and 500nm to 900nm for transmission, excluding the extreme wavelengths due to increased noise in these spectral regions. The mean and standard deviation were then taken for the normalised data.

In both reflectance and transmittance data, spectroscopy of the hind paws of the TNF dARE model of RA showed spectral differences, indicating that the symptoms of arthritis had changed the optical properties of the tissue to an extent which was detectable by spectrophotometry. In Figure 26b and Figure 26d the mean reflectance and transmittance spectra have been normalised to allow better visualisation of the changes occurring in spectral shape.

Statistical significance for the separation of the spectra was determined by two-sample t-test of the root mean squared (RMS) distance, inter- and intra- diseased and normal mice, for the normalised spectral data. The sum of the RMS distance was calculated for all 16 spectra giving a total of 425 RMS values. The t-test was then performed between two groups, the RMS values for the differences between spectra within the diseased and normal groups, and the RMS values for the spectral variation between groups. For the wavelength range 480 to 950nm, the RMS difference between spectra within the groups was significantly different from the RMS between the groups at a p-value of 0.0251. For normalised transmittance between 480nm and 950nm, the RMS difference between groups was statistically significant at a p-value of 0.0351.

#### 4.4.1.2 CIA Spectrophotometry

The results from spectrophotometry of the TNF dARE model of arthritis showed differences apparent in the reflectance and transmittance spectra of the hind paws. A small experiment was also conducted on the CIA mouse model of RA. The CIA mouse, described in section 2.4.3, has a different phenotype to the TNF dARE. Polyarthritis appears as classic inflammatory symptoms of swelling (oedema) and redness, and joints may be affected in a more localised and non-symmetrical pattern. The mice used in this experiment are introduced in section 4.2.3.2.

Figure 27 shows the raw spectra and normalised spectra from a small experiment imaging 2 mice, one symptomatic CIA mouse and one experimental control. Reflectance spectra were taken from the top of the hind paw and transmission spectra were taken from the underside of the foot. The data shown in Figure 27 has been processed using the same smoothing and normalisation methods as described for the TNF dARE data.

Evident spectral differences were apparent for both reflectance and transmittance data in one paw of the CIA mouse (paw 1). Notably, the same paw was scored to be more highly affected in the manual examination.

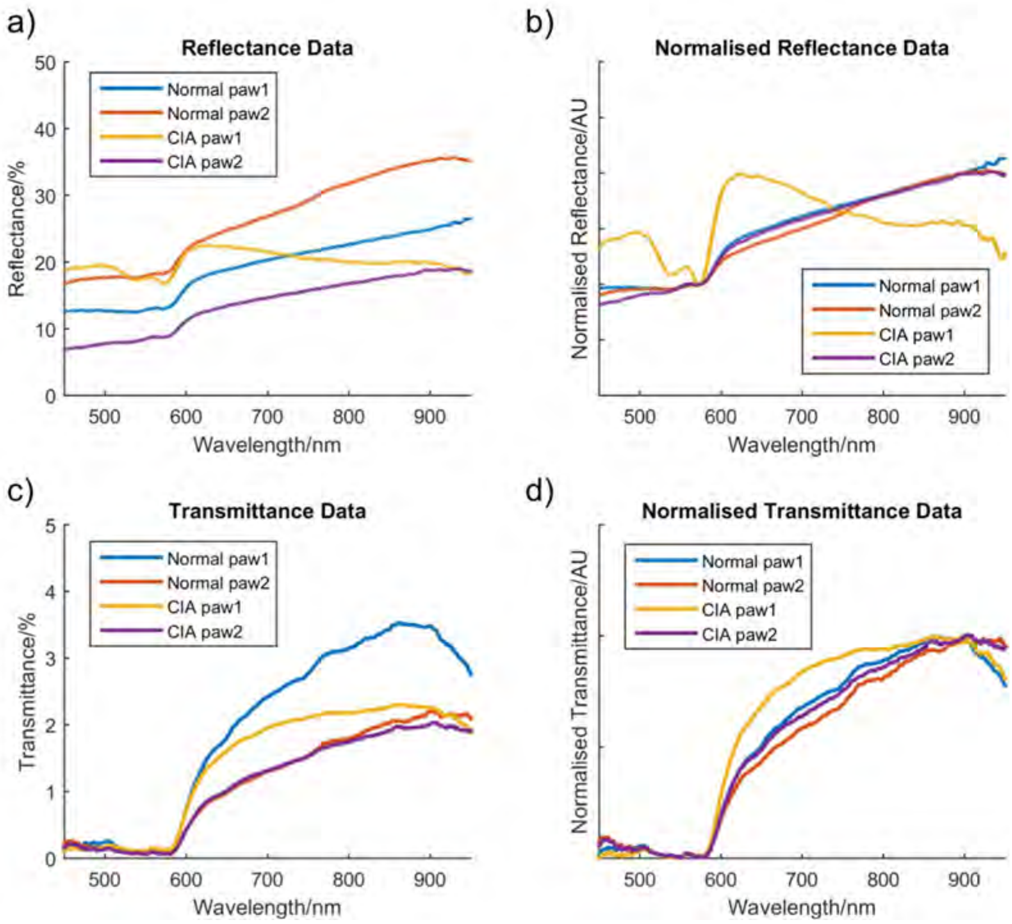

Figure 27: Reflectance and transmittance data for CIA mice hind paws, N=1 CIA and N=1 normal with spectra taken from two hind paws per mouse giving a total of four spectra. a) Raw reflectance data taken from the tops of the hind paws of 2 mice, 1 CIA symptomatic and one normal control. Data from separate feet are indexed by colour. b) Mean reflectance measurements from the data shown in Figure 27a, min-max normalised. c) Raw data for transmittance taken from the same 2 mice d) Min-max normalised transmittance values taken for the data shown in Figure 27c.

Whilst no firm conclusions can be drawn from such a small group number, the results indicate that the CIA mouse does show spectrally detectable changes in tissue optical properties concurrent with arthritis symptoms, and that the spectral changes induced are different to those of the TNF dARE model of RA. The spectral effects in the CIA mouse were not symmetrical, the reflectance spectra show a decrease of reflectance across the NIR wavelengths in one paw and a more defined ‘w’ shape in the 500nm to 600nm region indicative of a higher concentration of oxygenated haemoglobin. The transmittance data shows a relative increase of transmission in the 600 to 800nm region suggesting that the overall oxygenation of the tissue is increased.

## 4.5 Discussion

### 4.5.1 Discussion of Results

The spectrophotometry data has provided an indication that the optical changes in the hind paws of mouse models of RA may be detected by hyperspectral/multispectral imaging techniques. Whilst there was considerable intragroup variation in the raw data, normalising the spectra by the procedure described in Section 4.4.1.1 allowed the relative changes in spectral intensity between the arthritic and normal group to become clearly apparent. These changes were statistically significant according to the RMS distances. In the normalised data, both transmittance and reflectance appear to have relatively reduced intensity in the 600nm to 800nm region. Assuming that the pathlength of the light is equivalent between the arthritic and normal mice, this change is indicative of a decrease in the ratio of oxygenated haemoglobin to non-oxygenated haemoglobin, which has a higher absorption in this region. A similar effect is seen in section 3.4.2 when decreased oxygenation is modelled with Monte Carlo. In contrast, the CIA data appeared to show increased transmission in between 600 and 800nm region perhaps suggestive of an increase in oxygenation. This supports the idea of different pathological processes occurring in the two different arthritis models where the CIA mouse has a more ‘inflammatory’ phenotype.

There is also some evidence that the absorption of water can be seen in the TNF dARE data where the decrease in absorption at 967nm coincides with the peak in water absorption coefficients at 975nm (Figure 26), although the data are more susceptible to noise in this spectral region. This peak is also apparent in the Monte Carlo model of the paw. There is no clear difference between the normal mice and TNF dARE mice

There also appears to be a variation in the spectral changes detected between different types of arthritis models. As discussed in section 2.4.1, the TNF dARE mouse exhibits an ‘erosive’ phenotype where bone erosion and inflammatory cell infiltration can occur independently of typical ‘inflammatory’ symptoms of swelling and redness. This parallels the human disease where bone erosion can progress between episodes of inflammation with subclinical synovitis (175). These data suggest that the processes involved in these two different mouse models may involve chromophores which produce distinct spectral changes.

### 4.5.2 Limitations

There were limitations associated with the spectrophotometric method of measuring spectral differences. With no spatial information and difficulty in verifying consistency in probe to tissue contact, covariant factors may influence the resulting spectra.

Cross-population analysis of spectrophotometric data relies on the spatial data remaining relatively constant. Whilst spectrophotometry of the TNF dARE mouse group did reveal some spectral changes, exact and reproducible placement of the probe was difficult to achieve due to the small size of the mouse hind paw and the complex surface topography of the paw, which has many small protrusions of the dermis, called footpads, for cushioning the foot. The tissue structure of the hind paw is heterogeneous and spatial data cannot be ruled out as a factor in influencing spectral variation. Likewise, in transmission, variation in light intensity may result from measuring different tissue thicknesses resulting from measurements taken different areas of the hind paw.

Other confounders with data collection include the reduced signal to noise ratio (SNR) at the extreme wavelengths, mainly due to low intensity output of the tungsten halogen light source. Whilst exposure time for the spectrometer could be increased to compensate low signal, the dynamic range of the spectrometer CCD limited exposure time in order to not overexpose the highest intensity wavelengths. In future experiments, the spectral output of the tungsten halogen bulb could be tuned with filters to attenuate the highest intensity wavelengths and adjusting exposure time accordingly, to increase SNR at the extreme wavelengths.

### 4.5.3 Conclusion

Overall, spectrophotometry confirmed that spectral changes in reflectance and transmission data occur in line with modelling predictions. The positive results from these data set foundations for the design of a multispectral imaging system, described in the following chapter, which could image in the both a reflectance and transmission geometry, providing spatial data as well as spectral data for the mouse hind paw.

# 5 Multispectral Imaging System Set-up and Characterisation

## 5.1 Introduction

The aim of this chapter is to describe the set-up, calibration, and imaging proficiency of the multispectral imaging system designed for the *in vivo* imaging of mouse models of rheumatoid arthritis. The chapter begins by describing the equipment and instrumentation (section 5.2), then discusses the spectral calibration of the system and the calibration of system components (section 5.3), and finally displays the results of a phantom imaging experiment with known optical properties (section 5.4).

## 5.2 Equipment and Methodology

The aim of this multispectral imaging system was to gather multispectral reflectance and transmittance data from the hind paws of anaesthetised mice. The wavelengths used ranged from 480nm to 1000nm for both reflectance and transmittance imaging of the whole hind paw. This range of wavelengths was chosen to ensure that the multispectral imaging system could capture the electromagnetic regions with variability in absorption of haemoglobin and water. Imaging for reflectance and transmittance ensured that spectral data from deep and superficial tissue layers were detected.

For the imaging of live, anaesthetised mice, the structural and functional design of the imaging system had to take several things into consideration. It is recommended for mouse welfare that the duration of anaesthesia is kept as short as possible. If anaesthesia exceeds 15 minutes, external heat should be applied via a warming mat to help maintain the body temperature. The anaesthetic equipment included a tube for the administration of isoflourane, a scavenger tube, and a nose cone to fit around the face of the mouse. The system had to be easily dismantled for transportation, to allow the location of experiments to vary. And finally, the imaging procedure has to take place in a surgery theatre where background light levels may be difficult to control.

The performance of the imaging system as a whole depended on the performance of its components. Before outlining the imaging pathway for reflectance transmission imaging (section 5.3.1), the relevant characteristics of the individual components are described below.

### *5.2.1* Light Source

The light source used for this imaging system was the Thorlabs OSL1-EC high intensity fibre light source, with a tungsten-halogen 150W bulb, coupled to an optic fibre. The lamp takes approximately 20 to 40 minutes for thermal stabilisation of the spectral emission (section 8.A5). The spectral emission profile ranges from approximately 390nm to 1020nm and is displayed in Figure 28b.

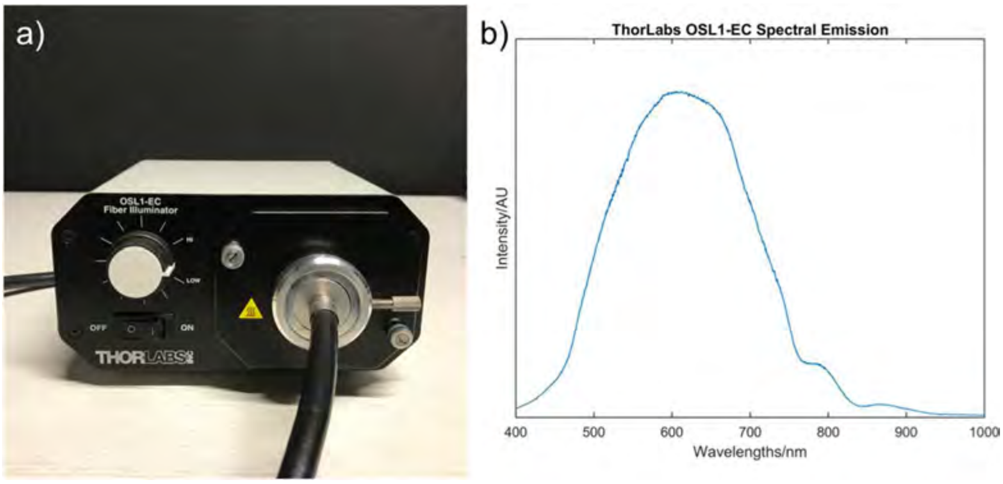

Figure 28: ThorLabs OSL1-EC light source for the multispectral imaging system. a) ThorLabs OSL1-EC Tungsten Halogen 150W fibre light source. b) Spectral emission profile of the ThorLabs OSL1-EC fibre light source measured with an Ocean Optics Flame-s spectrometer.

### *5.2.2* Filters

To image at selected wavelengths, two PerkinElmer VariSpec liquid crystal tuneable filters were used, a Vis-07 VariSpec covering a wavelength range of 400nm to 720nm and a SNIR-10 VariSpec covering a range of 650nm to 1100nm. The Vis-07 filter has a response time of 50ms and an average bandwidth of 7nm, the NIR-10 filter a response time of 150ms and an average bandwidth of 10nm. Both VariSpec filters possess a 20mm filter aperture, a maximum optical throughput of 500mW/cm$^2$, and a wavelength accuracy calculable by Bandwidth/8±0.5nm. The typical transmission outside of the bandpass is quoted to be 0.01% or less. The use of liquid crystal tuneable filters allows fast, automated, vibrationless switching of bandpass filters between imaging wavelengths under computer control.

Light was focussed upon entry and exit of the VariSpec filters. A series of lenses focused the light exiting the Thorlabs fibre aiming to collimate light before entry into the VariSpec. Likewise, lenses focused the light exiting the VariSpec filter onto the optic fibres guiding light to the stage, preventing too much light being lost by absorption into the body of the VariSpec.  The fibres were held in place by 3D printed components and the lenses used for focusing light were Thorlabs LA and LB lenses with focal distances ranging from 35mm to 150mm. The normalised spectral transmission of the filters' transmittance with the Thorlabs OSL1-EC is shown in Figure 29b.

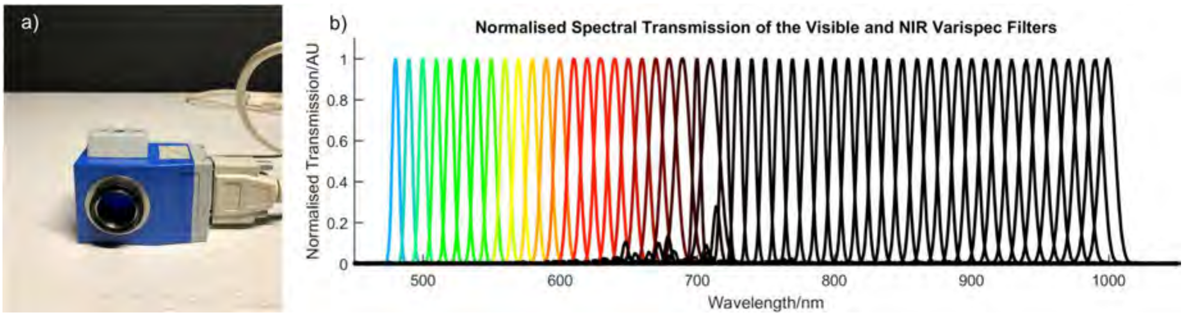

Figure 29: Spectral transmission of Vis-07 and NIR-10 Varispec filters. a) Photo of the Vis-07 Varispec used to bandpass filter selected wavelengths for multispectral imaging. b) Graph showing the normalised transmission of the Vis-07 and NIR-10 Varispec filters with spectral input from the Thorlabs OSL1-EC high intensity fibre light source in 10nm steps.

### *5.2.3* Illuminating Ring and Optic Fibres

For the reflectance multispectral imaging application of the system, an illumination ring placed around the lens was used for shadow-free illumination of the sample. An Edmund Optics 2” fibre optic ring light guide with a working distance from 1.5 to 9 inches, a wavelength range of 400nm to 2000nm and an output beam angle of 18 degrees was placed around camera lens for imaging.

In addition, two Thorlabs 91cm, SM1, 5mm core light guides were used to carry the illuminating light to the VariSpec filters and from the VarSpec filters to underneath the stage platform for the transmittance imaging function.

### *5.2.4* Camera

The camera used in this imaging system was a RetigaExi monochrome firewire CCD camera from Qimaging, with 1.4 megapixel (1392x1040), 12 bit digital output, flexible exposure time control (10µs to 17.9 minutes), gain control (0.7 to 30x gain), offset (-2048 to 2047), and optional binning. The quantum efficiency of the camera adapted from published graphical data is shown in Figure 30b (176). The Retiga EXi was coupled with a 3.3x macro zoom, c-mount (MLM3X-MP 0.3X-1X 1:4.5) lens from Computar, with a 90mm focusing distance, and variable magnification from 0.3x to 1.0x and variable f-stop from F4.5 to F22 due to an inbuilt manual iris ring. The lens settings used in the system, addressed in section 5.3.3, allowed focusing over an area of 40mm x 30mm from a distance of 100mm.

### *5.2.5* Polarisers, Diffuser and Mirror

Several additional optical components were used to alter the path or properties of the filtered light, moving through the system. A Thorlabs reflective neutral density filter

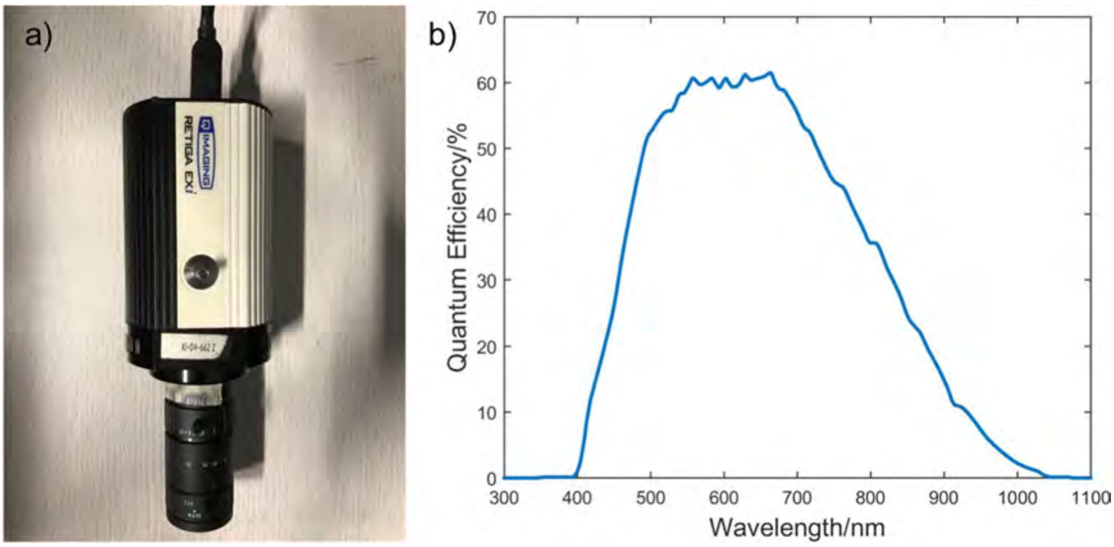

Figure 30: Quantum efficiency of the RetigaExi CCD camera. a) The RetigaExi monochrome firewire CCD camera used in the multispectral imaging system. b) Values of quantum efficiency as a function of wavelength for the RetigaExi (176).

ND = 4.0 was used as a mirror to reflect light exiting the light guide at 90 degrees for illumination from under the stage. This reflected input light was homogenised with a Thorlabs circle tophat diffuser (177), with flat intensity through a 50 degree scattering angle around the surface normal and a wavelength range from 380nm to 1100nm. Two linear polarisers were positioned in the system immediately after the diffuser and directly in front of the camera lens (section 5.3.1.2). The first polariser, set into the stage, was a 25mm x 25mm Wire Grid reflective polarising film from Edmund Optics (178), Extinction ratio 4250:1, with a wavelength range extending from 400nm to 1200nm. In front of the lens was a Thorlabs linear polariser with extinction ratio 1000:1 and a quoted optimal wavelength range from 600nm to 1100nm (polarisation was found to be sufficient for the purposes of this system below 600nm).

### *5.2.6* Structural Components

Additionally, the unique requirements for the set-up of this system meant that several custom structural components were necessary. The stage, a holder for the ring optic fibre, a holder for the polarising filter, and a shade for blocking background light from the stage platform (Figure 31a - d) were designed using openSCAD and Slic3r software, then printed in black PLA plastic using a 3D printer. The stage was designed to allow the addition of a warming mat for the anaesthetised mouse (Figure 31c) and the additional components were designed so that the ring optic light was held at a consistent working distance of 9cm and the camera lens at 10 cm from the stage platform (Figure 31a, b and d) and directly above the polarising filter set into the stage.

### *5.2.7* Additional Components

A black non-reflective coating was used to cover stage imaging platform and the background light block, to try and reduce stray light effects. Acktar Spectral Black$^{TM}$ coated foil was used, which has a hemispherical reflectance ranging between 2% in the visible wavelengths to approximately 2.5% in the NIR. Other components of the system included a laptop for controlling the equipment and storing the data and a clamp stand to hold components of the system in place.

## 5.3 Experimental Method Development

### 5.3.1 Pathways of Light for Reflectance and Transmittance Imaging

#### *5.3.1.1* Reflectance Imaging

Reflectance imaging is designed to take spatial and spectral data for the diffusely reflected light of an object of interest. For reflectance multispectral imaging, the broadband light emitted from the tungsten halogen lamp was filtered through the two

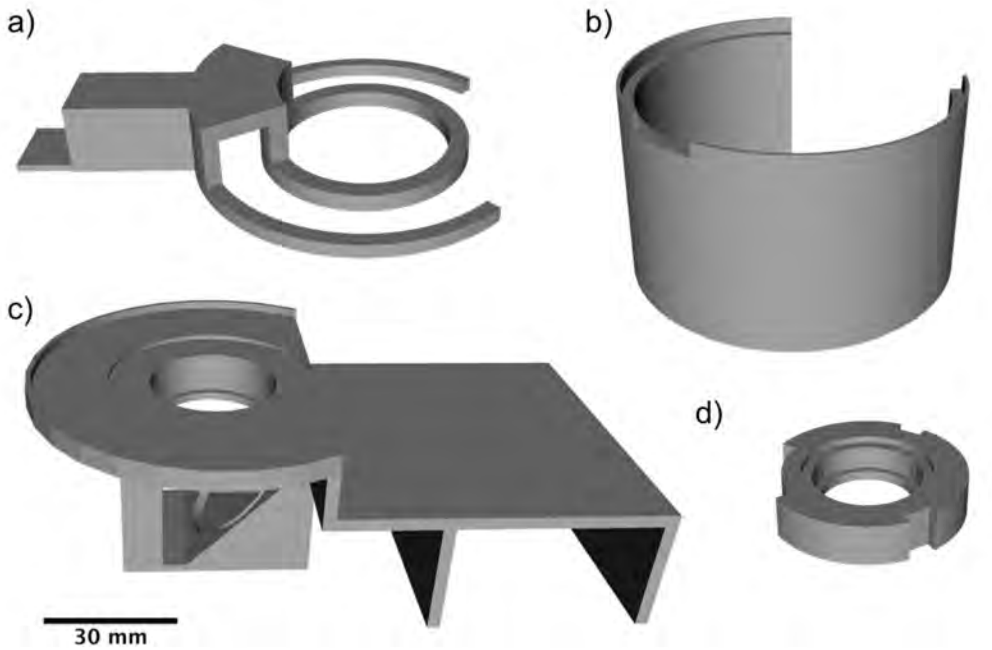

Figure 31: OpenSCAD designs for 3D printed structural components of the system rendered in Meshlab. The images show a) a holder for the ring optic component. b) A structure to go around the stage for the dual purpose of blocking background light and fixing the height and relative position of the camera lens and ring optic arrangement. c) The imaging stage with a hole in the imaging platform for a diffuser, and a differential height to allow the addition of a warming mat. d) A holder for the polarising filter and camera lens.

Varispec filters (section 5.2.2) in sequence, resulting in a range of illuminating wavelengths from 480nm through to 1000nm. Software allowed each of the individual Varispec filters to be operated automatically, matching the filter wavelength switching to the exposure times of the camera. The changeover between the different filters was manual.

The sample was illuminated sequentially with the chosen wavelengths through the ring optic arrangement around the camera lens. This arrangement produced relatively uniform, shadow-free illumination of the subject. The coefficient of variation of light intensity (averaged across all wavelengths) was 12.5%, 9.2%, 9.9% and 9.7% for the 2%, 50%, 75% and 99% reflectance standards respectively, giving an indication of the intensity variation of the projected light across an 8.04cm$^2$ area. Reflected light was then detected and imaged by a CCD camera. Figure 32c shows a schematic describing the light path through the imaging system for reflectance.

#### *5.3.1.2* Transmittance Imaging

For the transmittance imaging protocol, the same set-up was maintained for the Varispec filters and the light source, allowing continuity in the experiment between reflectance and transmittance imaging. By replacing the ring optic fibre with a separate optic fibre at the output of the Varispec filter, the filtered light could be directed underneath the platform holding the subject of imaging. The 3d-printed stage was designed to hold a mirror that reflected the light output from the fibre at 90 degrees.

In order to get flat illumination of the subject, the light from the optic fibre was first passed through a diffuser, before passing through a linear polariser in the base of the stage. The imaging object was therefore illuminated from below by widefield, linearly polarised light. This arrangement made it possible to calibrate and calculate the transmittance spectra.

A second polariser was placed in front of the lens of the camera at a polarisation angle 90 degrees to the first. Photons multiply scattered through the imaging object would be depolarised before emission from the tissue and would therefore be transmitted through polariser in front of the camera lens. Photons exiting the stage and travelling directly to the second polariser would remain polarised and therefore be blocked. The beneficial effect of such a system is blocking the background light of the stage from detection with the camera, preventing overexposure and bloom artifacts in the images. Figure 32d shows a schematic of the transmittance imaging pathway through the imaging system.

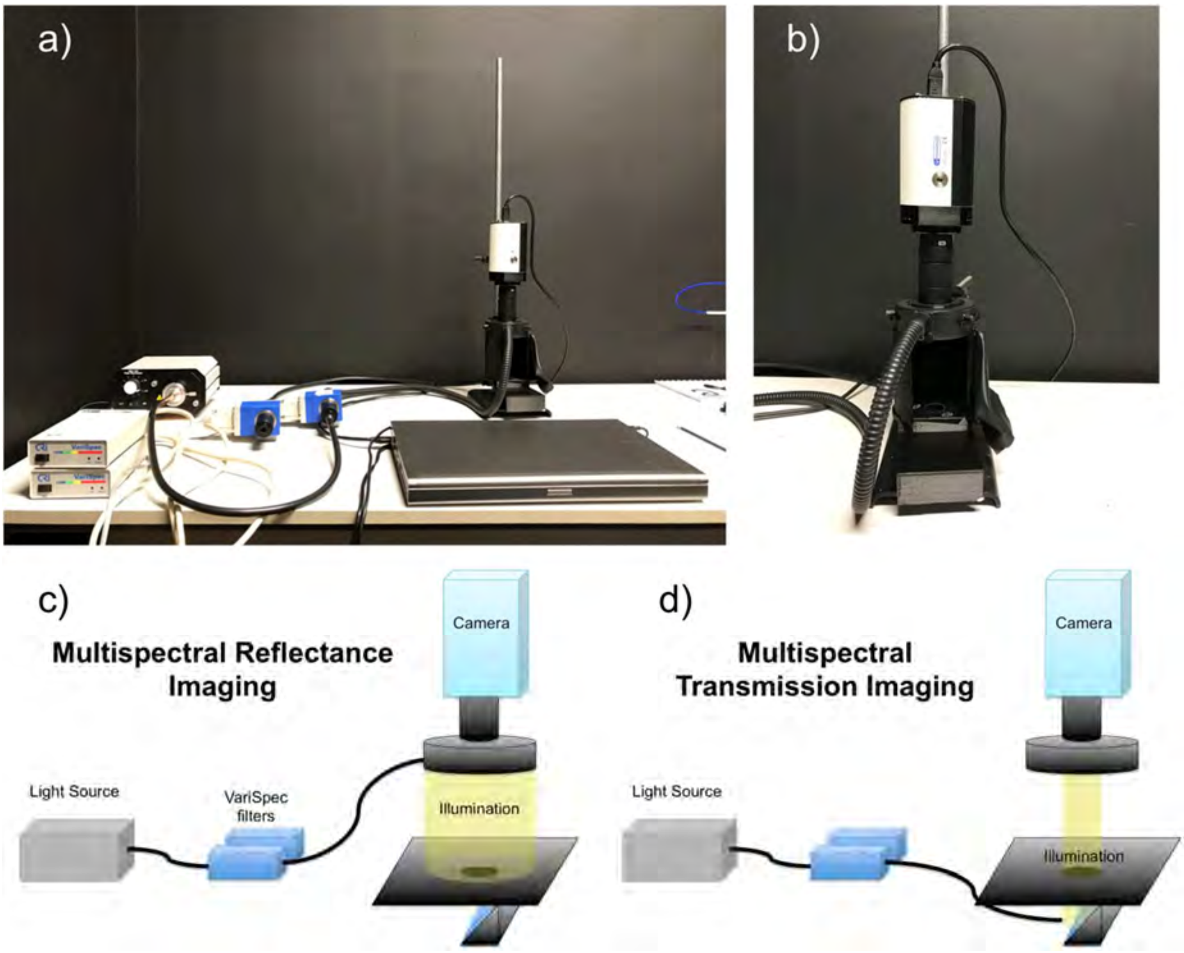

Figure 32: Set-up of the multispectral imaging system. a) A photo showing all components of the full multispectral imaging system. b) A photo of the imaging stage, with the ring light illumination and RetigaExi camera mounted on a clamp stand. c) A schematic of the reflectance mode of imaging where filtered light illuminates the stage platform. d) A schematic presenting the transmittance mode of imaging where the filtered light illuminates the sample through a polariser set into the stage.

### 5.3.2 Spectral Calibration of the Imaging System

The aim of the multispectral imaging system was to extract the percentage reflectance or transmittance of the incident light for a series of wavelengths, spatially resolved across an imaged object. Hence calculating the percentage of reflected/transmitted light was dependent on knowing the value of the incident intensity.

Calculating the incident intensity of the illuminating light for the system across all imaging wavelengths is a function the light source output spectra, convolved by the wavelength dependent efficiencies of the Varispec filters, the optic fibres, the camera quantum efficiency, any additional effects from optical components, and geometry-dependent effects. Given that not all of these quantities were known and some would be difficult to measure, a calibration method using optical standards was used as a proxy to direct calculation of incident intensity.

The images produced by the system were calibrated using diffuse reflectance standards for reflectance and neutral density filters for transmission, allowing calculation of percentage reflectance/ transmittance by dividing the object image by an image of a known optical standard. A description of the reflectance standards used for calibration is given in section 4.3.2. Data extracted from published graphical results for hemispherical reflectance of the standards used in this project are displayed in Figure 33a (174). This method of calibration required that the imaging settings were kept constant, the tile was larger than the object, and assumed Lambertian reflectance for the tile and tissue (113). Equation 12 describes the process of reflectance calibration.

$$[\mathrm{R}] = \frac{[\mathrm{I_{Object}}]-[\mathrm{I_{Dark}}]}{[\mathrm{I_{RefStandard}}]-[\mathrm{I_{Dark}}]} \tag{12}$$

where [R] is an image where the pixels represent the percentage of reflected light, and $[\mathrm{I_{Object}}]$, $[\mathrm{I_{Dark}}]$, and $[\mathrm{I_{RefStandard}}]$ are images of the object of interest at sequential wavelengths, the dark noise, and the reflectance standard respectively.

For transmission calibration, the polariser directly in front of the lens was removed and an image was taken of the light coming through the diffuser and polariser inset into the stage. To reduce the light intensity to a level that would not overexpose the CCD, a Thorlabs reflective ND filter of optical density 2.0 (transmission varies from 0.72%

transmission at 480nm to 1.20% transmission at 1000nm) was positioned in front of the stage polariser, whilst keeping the imaging conditions constant. Thus the relative intensity of the input light for transmission could be measured, and the transmittance of the object calculated by division with images of the illuminating light. Figure 33c shows published data of wavelength-dependent transmission for the ND filter (179) and Figure 33d displays the transmission for the polariser. Equation 13 describes the calibration of the transmission images.

$$[T] = \frac{[I_{Object}]-[I_{Dark}]}{[I_{ND2}]-[I_{Dark}]} \times \frac{\overrightarrow{S_{ND2trans}}}{\overrightarrow{S_{Polariser}}} \tag{13}$$

where [T] is an image where the pixels represent the percentage of transmitted light and $[I_{Object}]$, $[I_{Dark}]$, and $[I_{ND2}]$ are images of the object of interest at sequential wavelengths, the dark noise, and the ND2 filtered light respectively. Multiplying by the ND2 filter transmission efficiency per wavelength $\mathrm{S_{ND2trans}}$ and dividing by the transmission of the lens polariser $\mathrm{S_{Polariser}}$ corrected for the imaging conditions of the object and allowed spectrally calibrated calculation of transmittance.

Although it is not accounted for in equation 13, the object transmittance is likely to be underestimated due to the effect of calibration by light diffused by the tophat diffuser, compared to the Lambertian transmittance of the object (modelled for the mouse paw in section 8.A4). Calculation shown in section 8A4 estimates that transmittance is underestimated by a factor of approximately 5.

In order to analyse the data, a GUI was built using Matlab so that the user could select areas of interest in the image and extract spectral data by location. An average of the spectra was taken over selected circular regions of 69 pixels with 2x2 binning, at a distance of 10cm, corresponding to an area of approximately 0.23mm$^2$. This area was chosen so as to reduce noise which was evident in the spectral measurements taken from single pixels, but still be small enough to sample distinct regions of a mouse paw. Section 6.3.2 shows an example image of area selection in the mouse hind paw using the GUI.

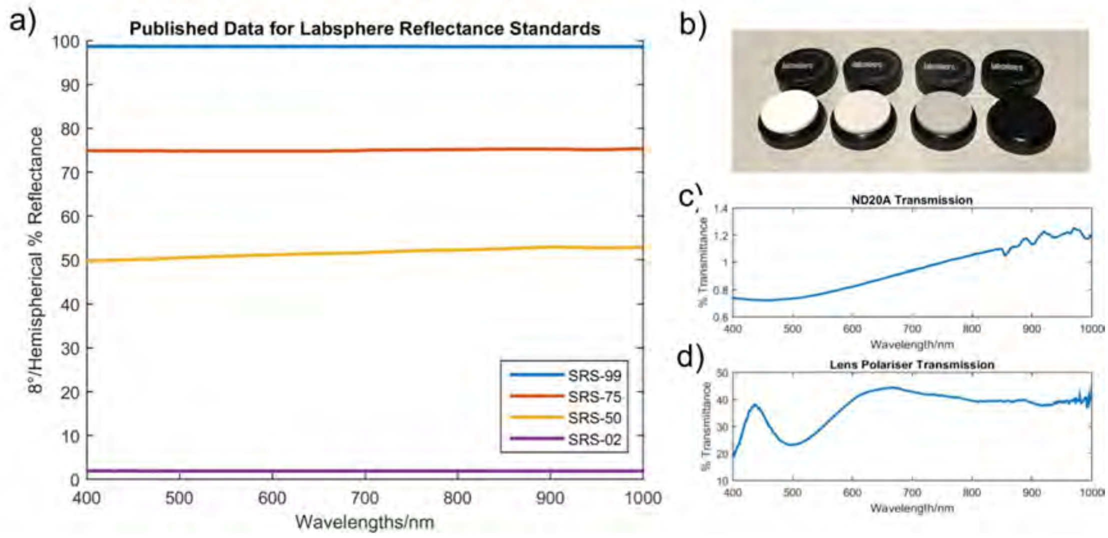

Figure 33: Reflectance and transmittance data required for spectral calibration. a) Data for hemispherical reflectance for Labsphere reflectance standards extracted from published graphs for the standards 99%, 75%, 50% and 2% tiles used in imaging experiments (174) b) Photo of the aforementioned reflectance standards. c) Spectral transmission profile of the Thorlabs ND20A used in multispectral transmission calibration, provided by Thorlabs d) spectral transmission of the Throlabs polariser positioned in front of the lens.

### 5.3.3 System Characterisation and Parameter Tuning

Understanding of the properties and limitations of the imaging system was critical to ensure the data were of the highest possible quality and important to the post-processing of the data which it may affect. Sections 5.3.3.1 through 5.3.3.2 address the effect of changing focal depth and signal to noise ratio (SNR) arising from the physical effects of the broad wavelength range used and section 5.3.3.3 addresses the effect of varying bandwidth with wavelength in the Varispec bandpass filters.

#### 5.3.3.1 Point Spread Function Calculation

Point spread function (PSF) is a measure of the ability of the imaging system to focus on a point source of light. This is a well-known problem for microscopes which are diffraction-limited due to the physical properties of light, but in the case of the multispectral imaging system described above the challenge lay in the extent of the change in wavelength. The increasing wavelength causes the light to refract at a smaller angle in the lens, leading to blurring of sharp contrast areas in the image in the NIR spectral region. This effect had the potential to limit the usefulness of the data by causing spectral smearing and therefore was necessary to characterise.

The macro zoom lens used to focus light onto the CCD is manually operated making refocusing time-consuming, and could lead to lack of continuity in the apparent size of the object. Given that we aim to compare the spectra for an area on a mouse paw through a small group of pixel vectors in the z-stack, change of magnification though different wavelength images would risk losing accurate preservation of the local spectra.

Changing the aperture size was one possible method of controlling for PSF. Decreasing the size of the aperture increased the depth of the focal plane by effectively blocking more unfocussed background light. This was beneficial for the reducing the loss of focus at the longer wavelengths, but reduced the number of photons reaching the CCD and therefore the signal to noise ratio (SNR) of the image. The challenge was to choose the aperture to obtain the best compromise between small PSF and high SNR.

For calculating the PSF and the SNR, a set of images were taken at a series of wavelengths and several different aperture settings. The images were of an Edmund Optics focusing tile, with an example image included in Figure 34b. All of the images for the different aperture settings were taken under the same lighting conditions and the same exposure times.

The σ-value of the PSF is a measure of the Gaussian spread where the larger the σ-value the greater the width of the Gaussian bell-curve, and if convolved with an image, the more blurred the appearance of the image. Equation 14 shows the mathematical context of the σ-value and  Figure 34a shows the σ-value of the PSF of the focusing tile images as calculated by a genetic optimisation algorithm. A single line of pixels was isolated from each wavelength image across one of the focusing squares shown in Figure 34b. The algorithm then generated random Gaussian distributions according the equation

$$G = \left(\frac{1}{\sqrt{2\pi\sigma^2}}\right) e^{-\frac{v^2}{2\sigma^2}} \tag{14}$$

where G is a Gaussian vector, v is a vector the length of the pixel intensities. These Gaussians were then convolved with a randomly generated step function representing a tile perfectly in focus and the error calculated between the computationally generated pixels and the real ones by squared sum of the difference. The random generation of numbers occurred inside bounds set by the user to constrain the algorithm and reduce the number of iterations required to reach a minimal error value. The algorithm iterated until the Gaussian with the lowest error was found.

The lens used by the system was a macro lens where the F-stop number was variable between 4.5 and 22 according to both the aperture size and the lens position. To isolate the effect of changing aperture size on the image, 5 evenly-spaced markers were drawn onto the lens varying the aperture from fully open (mark 1) through to half open (mark 5).

Figure 34a shows the plot of the σ-value against wavelength for the different markers of the aperture settings.

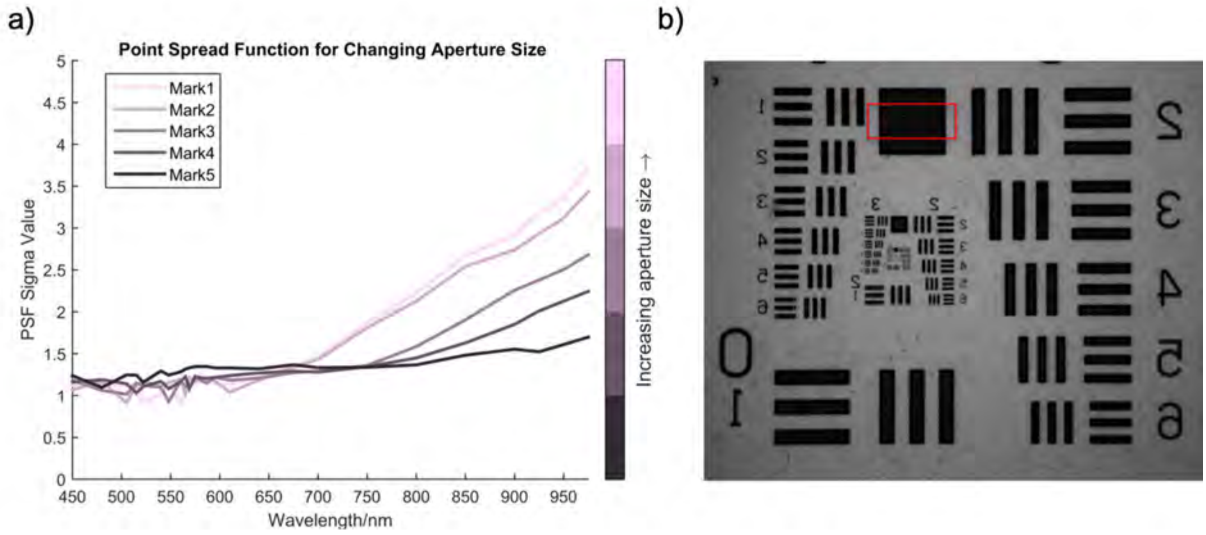

Figure 34: Gaussian sigma value describing image blur with changing aperture size. a) Optimal fitting of the σ-value for a Gaussian equation to images taken by the multispectral imaging system across the wavelengths range 450nm to 975nm. A series of images was taken for an increasing aperture size in the lens, demonstrating the imaging effects of narrowing the focal plane. b) Image taken at 750nm and 'Mark 2' aperture of an Edmund Optics focussing tile used to assess Point Spread Function and Signal to Noise Ratio in the multispectral imaging system.

### 5.3.3.2 Signal to Noise Ratio Calculation

Image noise is a combination of Poisson noise and dark current noise. Dark current noise is a result of thermal agitation of electrons within the CCD. It follows an approximately Gaussian distribution but can result in fixed pattern noise noticeable at longer exposure times, due to variability in the sensitivity of individual CCD sensors.

This could be corrected for by dark frame subtraction, where an image of equal exposure time was taken in complete darkness and subtracted from the data image. Poisson noise is a result of statistical variation in the distribution of photons. It has a root mean square value proportional to the square root of the image intensity. This is generally the primary source of image noise except in low light conditions.

Figure 35 shows the signal to noise ratio calculated from the images of the focusing tile. An averaged value was taken from the lighter area of the image (signal) and compared to the dark area (noise) in the focusing tile for each individual wavelength (180).

$$\mathrm{SNR[dB]} = 20 \times \log_{10}\left(\frac{\mathrm{RMSsignal}}{\mathrm{RMSnoise}}\right) \tag{15}$$

where SNR is the signal to noise ratio in decibels, RMS signal is the root mean squared value of a lighter area of the image and RMS noise is the root mean squared value from a dark region of the image.

There is an almost linear drop in SNR between the aperture settings for each wavelength indicating the effect of Poisson noise (Figure 35). Whilst this effect could be countered by brighter illumination or longer exposure times, the intensity of illumination was limited by the brightness of the light source and exposure times should be kept minimal for live mouse imaging.

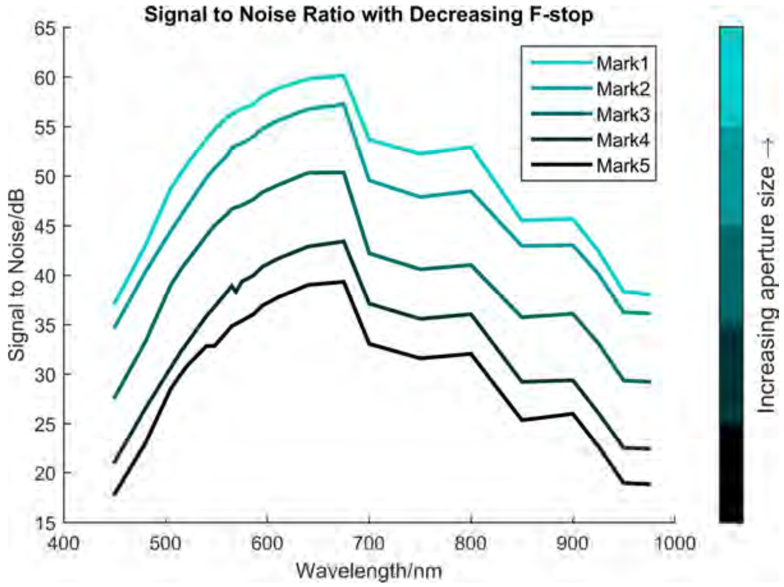

Figure 35: Signal to noise ratio measured for a series of images of an Edmund Optics focussing tile across wavelengths 450nm to 975nm, taken with the multispectral imaging system. Each series of images was taken with a change in the aperture size and the data demonstrate the increasing signal to noise ratio with increasing aperture size.

The ideal aperture size for the system would therefore be the widest aperture which still fell within an acceptable PSF. When imaging, small amounts of blur in the NIR were not found to affect the spectral results, increasing the aperture size offered a significant improvement in the imaging time. Mark 3 ( F11< Fstop >F22 ) was chosen for imaging of live mice because the image blurring was not found to affect accuracy.

### 5.3.3.3 Bandwidth vs Spectra

In the multispectral imaging system, two Varispec filters were used to filter light from a broadband illumination source to a series of selected wavelengths. The Varispec filters filter light across a series of wavelengths in a Gaussian centering around the desired wavelength (see Figure 29). The spectral response calculated by the imaging system did not therefore belong to a single wavelength as was presumed by Monte Carlo modelling of the tissue, but was the sum of the spectral response across a series of wavelengths. If the true reflectance/transmission spectra of the tissue were non-linear across the wavelengths covered by the Varispec filters spectral bandwidth, then the assumption that the image formed from the Varispec-filtered light was representative of the single pre-set wavelength would become invalid. However, the effect could be insignificant if changes in the spectral response were not detectable. This section details the effect that the filter bandwidth had on the calculated spectral response using a simulated reflectance spectrum computed by Monte Carlo modelling of the mouse hind paw model described in section 3.4.1. To calculate the effect of the filter bandwidth, the spectral response functions of the light source output filtered by the Varispec filters was measured using a spectrophotometer (Figure 36a). The spectral functions were then normalised by dividing the intensity values by the area under the curves  (Figure 36b) and convolved by the Monte Carlo spectrum to simulate the process of multispectral imaging (Figure 36c).

Two individual Varispec filters were used to cover the width of wavelengths utilised by the multispectral imaging system. The effect of increasing wavelength could be seen to increase the bandwidth (full width at half maximum varies from 3.6nm to 9.3 nm) lineally for both Varispec filters with increasing wavelength, due to the method in which the Varispec filters light. For the Monte Carlo simulated reflectance and transmission spectra of the mouse hind paw, this lead to a maximum error of 1.26% at 975nm in reflectance and 0.41% at 1000nm for transmission. This error may vary slightly in accordance with the spectral response of the tissue. Overall, although there is likely to be small difference between the real reflectance values and the ones calculated by the multispectral imaging system at longest wavelengths, the characteristic shape of the spectra is retained.

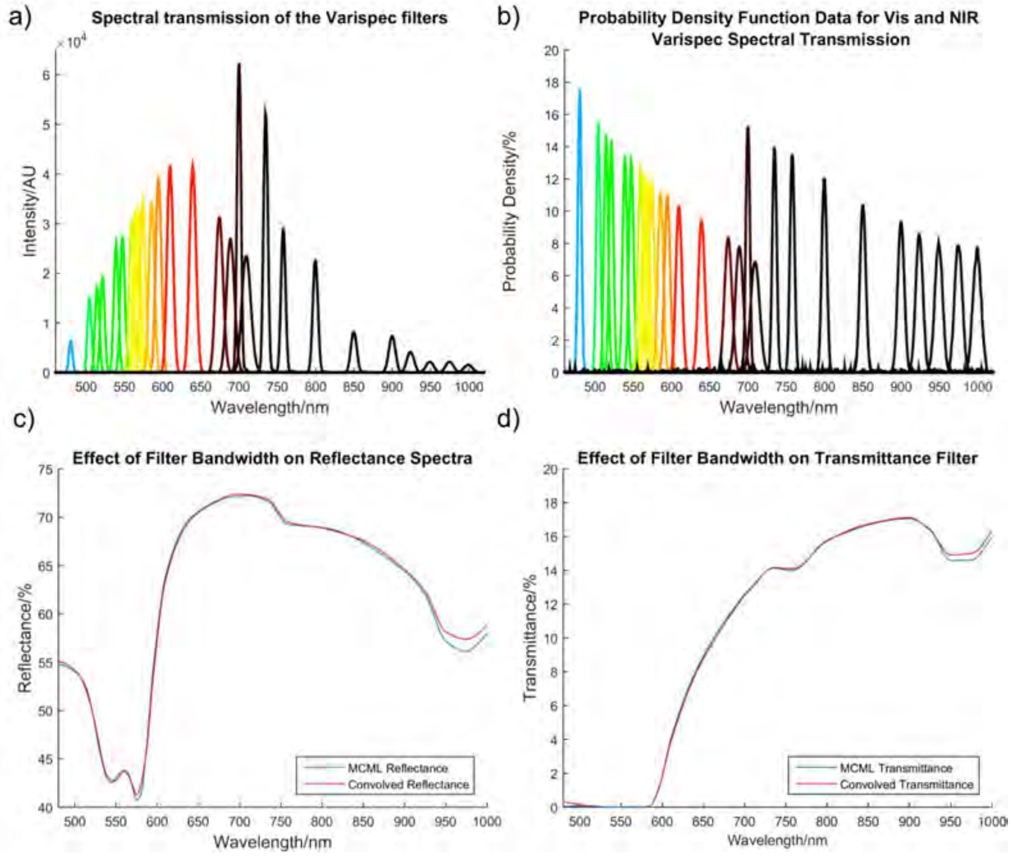

Figure 36: Variation of Varispec filter transmission bandwidth and its effect on spectral measurements. a) Relative intensity of all the sequential wavelengths used in in vivo imaging detected at the stage platform in the reflectance configuration of the system. b) Probability density functions calculated from the Varispec Vis and NIR filter transmissions at the wavelengths used for biological imaging. c) Modelled reflectance spectra before (blue) and after (red) convolution the Varispec spectral functions. d) Modelled transmittance spectra at the wavelengths before (blue) and after (red) convolution with the Varispec spectral functions.

## 5.4 Results

### 5.4.1 Phantom Imaging for Validation of Spectral Calibration Method

To determine the accuracy of the calibration method for reflectance imaging, several reflectance standards were imaged and the value for percentage reflectance calculated by calibration with the 99% reflectance standard. The tiles were imaged separately using wavelengths from 480nm to 1000nm in 10nm steps. Figure 37a shows the results of this experiment. Exposure times, displayed graphically in Figure 37c were chosen to get an 'optically flat' response from the reflectance standards. In total the imaging time for the standards was approximately 73 seconds, excluding the time taken to switch the light input from the Varispec filters.

The transmission mode of the multispectral imaging system was verified against hyperspectral data from spectrometer on an optical phantom model of skin (photo shown in Figure 37d). For the spectrophotometry data, the phantom was illuminated through the stage with broadband light, then calibrated by imaging the stage illumination though ND2, and dividing the spectral data by the known transmission of the filter to recover the spectral transmittance of the phantom. Figure 37b displays the transmittance spectra recovered from the multispectral imaging and spectrophotometry.

For reflectance imaging, the average reflectance intensity for the calibrated images of the 75%, 50% and 2% tiles across the wavelengths of 480 to 1000nm were 74.49% (coefficient of variation 0.84%), 51.30% (coefficient of variation 1.32%), and 1.55% respectively (coefficient of variation 5.45%). Any inaccuracies in the reflectance data may arise from differences in height of the tile surfaces, noise in the images, or deviations from the exact reflectance percentage quoted for the tile. For transmittance imaging, the absolute difference in percentage varied between 0 and 0.2% between the wavelengths of 480nm to 930nm.

For reflectance imaging, the average reflectance intensity for the calibrated images of the 75%, 50% and 2% tiles across the wavelengths of 480 to 1000nm were 74.49% (coefficient of variation 0.84%), 51.30% (coefficient of variation 1.32%), and 1.55% respectively (coefficient of variation 5.45%). Any inaccuracies in the reflectance data may arise from differences in height of the tile surfaces, noise in the images, or

deviations from the exact reflectance percentage quoted for the tile. For transmittance imaging, the absolute difference in percentage varied between 0 and 0.2% between the wavelengths of 480nm to 930nm.

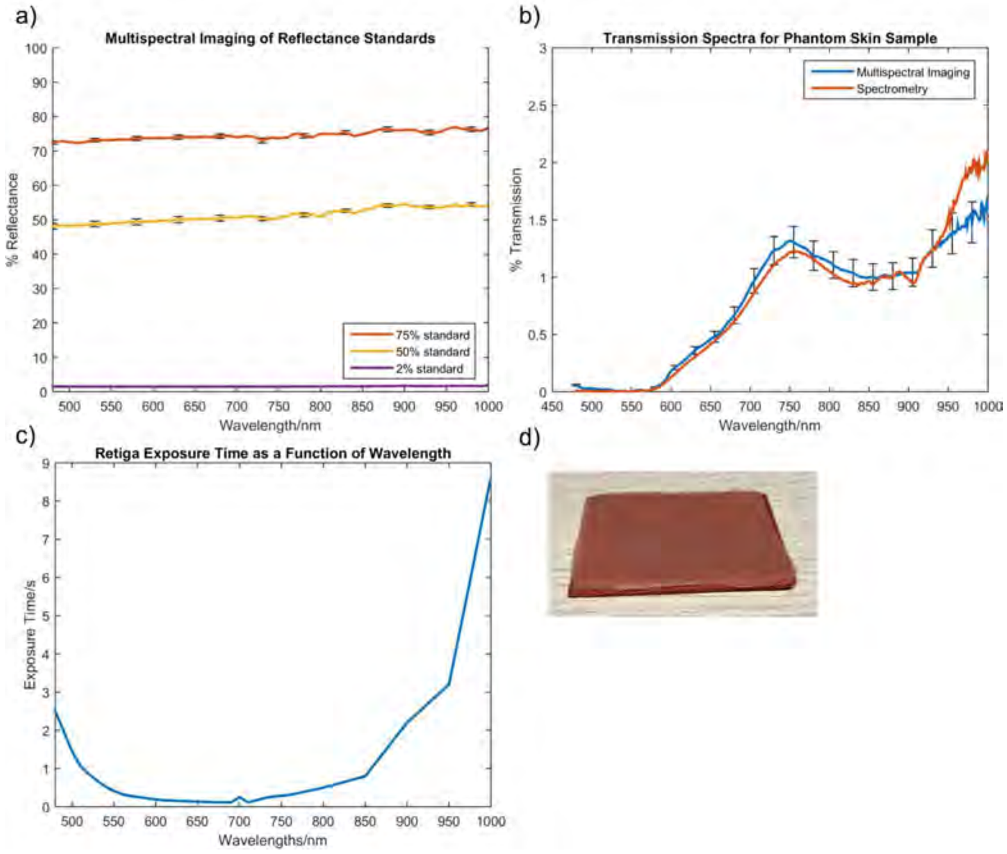

Figure 37: Spectral data from multispectral imaging of phantoms. a) Multispectral reflectance imaging of a series of reflectance stands. The average reflectance spectra were calculated from 30 spatially separate measurements in the image. b) Normalised multispectral transmission average spectra from 30 spatially separate measurements of an optical skin phantom, compared to a transmission spectrum measured by spectrometry. c) Exposure times used per wavelength. d) Photo of the skin phantom used in transmittance imaging.

### 5.4.2 Phantom Imaging

Imaging an object with known optical properties allows a comparison between the reflectance spectra predicted by MCML modelling and the reflectance spectra evaluated by the multispectral imaging system.

This section details the Monte Carlo modelling of an optical phantom (INO biomimic optical phantoms), in comparison with the reflectance spectra recovered from the multispectral imaging process. The homogenous, cuboidal, phantom (Figure 38c) had known reduced scatter ($\mu_s$') and absorption coefficients ($\mu_a$) for the wavelength range 590nm to 1000nm, recovered from a geometry-specific fitting using time-resolved diffuse optical imaging data (181). Figure 38a displays the optical properties of the phantom. For the MCML program input, the $\mu_s$' values were used for $\mu_s$ with an anisotropy (g) value of 0, and the $\mu_a$ values were used directly, together with a depth value of 25mm. The reflectance data from the multispectral imaging system were calibrated as above with imaging wavelengths from 480nm to 999nm in steps of 10nm, and an average reflectance spectrum was computed from 30 randomly selected areas of the image. Figure 38b displays the MCML modelled reflectance spectra with the average of the measured spectra. The experimental set-up was designed so that the surface of the block was at the same imaging distance as the corresponding image of the reflectance standard.

Figure 38b displays the recovered spectral reflectance of the optical phantom as compared to the reflectance spectra modelled using the MCML Monte Carlo method. There is a clear resemblance in the shape of the spectra, showing that the effects of the phantom's optical properties are broadly recognisable in the reflectance spectra detected by the multispectral imaging system. However, the error between the modelled spectra and the imaged spectra is maximum at 4.7% for 750nm.

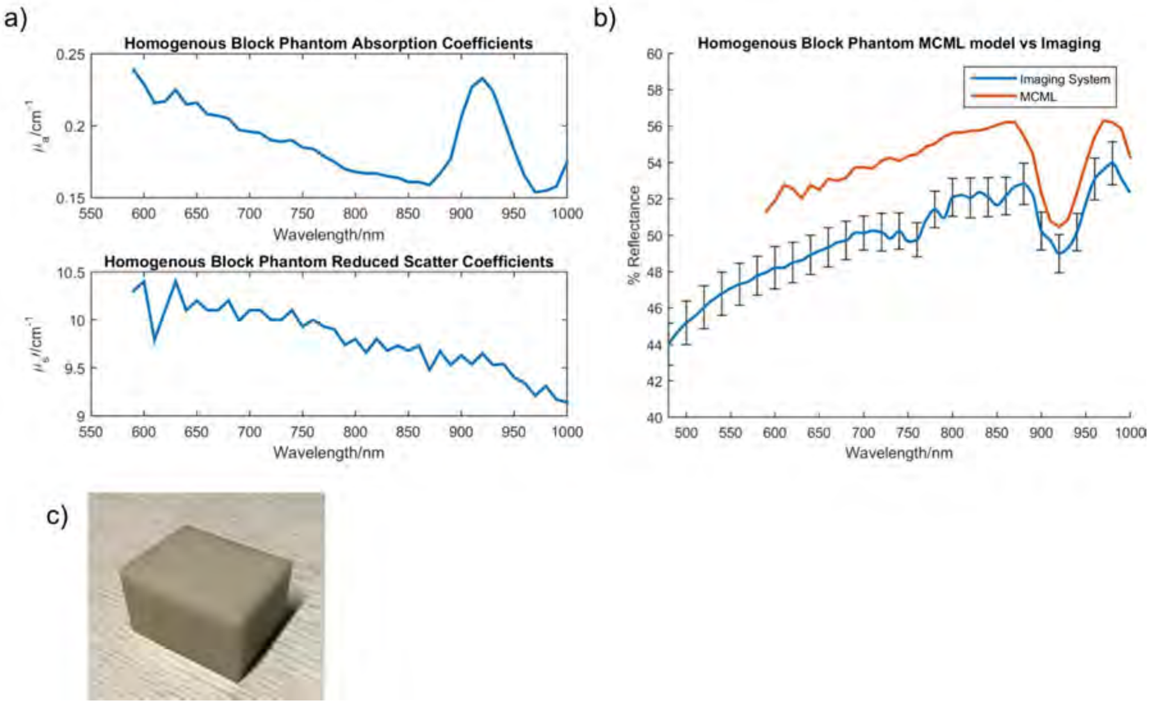

Figure 38: Spectral data from multispectral imaging and Monte Carlo modelling of an INO Biomimic optical phantom. a) Absorption and reduced scatter coefficients for INO Biomimic optical phantom sourced from reference (181). b) Comparison of the MCML modelled reflectance spectrum for the optical phantom vs the reflectance spectrum recovered from multispectral imaging. c) Photo of the INO Biomimic optical phantom.

Reasons for the difference between the modelled and imaged spectra is likely due to the difference between the geometry of the image in reality vs the point-source, semi-infinite set-up assumed in the MCML model. In addition, the MCML model assumes single wavelength data whereas the imaging system images across the bandwidth imposed by the use of the Varispec filters. Also, approximately 2% of the reflectance calculated in MCML is due to specular reflectance, which theoretically is not detected by the imaging system.

## 5.5 Discussion

### 5.5.1 Discussion of Results

The multispectral imaging system detailed above offers the ability to take multispectral data in both a reflectance and transmittance geometry at a flexible series of wavelengths, across the visible and near infrared spectrum, for relatively small objects. In this case, the design and layout of the stage is especially suited to the imaging of the hind limbs of small animals, and the implementation of imaging meets the demands of the application. Comparing this system to commercially available imaging systems is apposite, although indirect, due to considerable variation in the method of data gathering in commercial multispectral and hyperspectral imaging systems. Relatively cheap, fast, solutions for multispectral imaging exist in the form of multispectral cameras with a small number of bandwidths fixed by filters or LED illumination. The advantage of these kinds of systems is the potential for fast data acquisition, ease of use, and low cost. The disadvantage is the inflexibility and low spectral resolution. However, this may represent a potential future avenue for this work if a small number of optimal imaging wavelengths could be found to work effectively in diagnosing symptom severity in mouse models of murine arthritis. The system has comparatively lower spectral resolution than other commercially available hyperspectral imaging systems such as push broom cameras, but such cameras are generally expensive, they rely on moving the object relative to the camera and require time to capture a full image.

### 5.5.2 Limitations

There are several caveats of the imaging system that influence the recovered reflectance and transmittance data. In reflectance imaging, due to the method of calibration used, it is assumed that the object of interest is flat and is imaged at the same distance as the reflectance standard. Given that intensity has an inverse proportional relationship with distance, if the surface height of the object varies, then the calculated reflectance of the object may vary linearly in wavelength according to equation 16

$$\mathrm{I} \propto \frac{1}{\mathrm{d}^2} \text{ or } \frac{\mathrm{I}_1}{\mathrm{I}_2} = \frac{\mathrm{d}_2^2}{\mathrm{d}_1^2} \tag{16}$$

where I is intensity and d distance. Similarly, the angle of the imaged surface compared to the reflectance standard will also affect the calculated percentage of reflectance. For a lambertian surface, Lamberts Cosine Law states that the radiant intensity of a surface is directly proportional to the cosine of the angle between the surface normal and the measurement angle (equation 17). The same principle applies in reverse for illuminating a surface at a non-perpendicular angle. In the case of topologically heterogeneous objects such as the mouse hind paw, the incident illumination will not always be normal to the surface and hence detected reflectance will be reduced for uneven areas according to the cosine law

$$\mathrm{I}_\mathrm{o} = \mathrm{I}\cos(\theta) \tag{17}$$

where $\mathrm{I}_\mathrm{o}$ is the detected intensity, I is the input intensity, and $\theta$ is the angle between the direction of measurement and the surface normal.

### 5.5.3 Conclusion

This chapter describes the development of a multispectral imaging system made specifically for the purpose of imaging mouse paws in a reflectance and transmittance geometry. Combining multispectral reflectance and transmittance (or multispectral imaging with fluorescence imaging) is recognized as a method of increasing data output (182–186), but is still relatively rare in medical multispectral/hyperspectral imaging (187). Tuneable filters were used which are common in imaging stationary objects and generally faster than point scanning methods (188). Overall, the elements of the design of the system are relatively standard methods used in multispectral imaging, but geared towards the novel function of imaging mouse feet. The following chapter introduces the results of multispectral imaging for mouse models of arthritis.

# 6 Multispectral Imaging of Rheumatoid Arthritis Mouse Models

## 6.1 Introduction

This chapter presents the results of multispectral imaging and analysis for two different mouse models of rheumatoid arthritis: TNF dARE and the K/BxN serum transfer, which have been described previously (section 2.4). The results of the imaging have been analysed and compared to other indicators of disease, with the aim of assessing the mice for the severity of their pathology and gaining an insight into the underpinning physiology. An experiment was also carried out to see if arthritis could be detected earlier using the multispectral method compared to standard clinical measurements of deformity or swelling which only capture late stage disease in TNF dARE mice and degree of swelling but not composition in K/BxN serum transfer mice.

The symptoms exhibited by the TNF dARE and K/BxN serum transfer mouse models of RA manifest as erosive (characterised by progressive joint erosion and deformity) or inflammatory (characterised by measurable swelling of the paw) respectively. The initial results from spectrophotometry suggested that these different pathological processes result in differing spectral characteristics. This chapter extends the research with multispectral imaging of live mice and validates the results by correlating them with different measures of disease progression including clinical scoring, calliper measurements of paw swelling, scoring of H&E stained histology slides to measure the inflammatory infiltrate and degree of bone erosion, and microCT bone erosion analysis.

## 6.2 Equipment and Methodology

### 6.2.1 Mouse Models

The experiments were carried out on two different mouse models of rheumatoid arthritis. The first mouse model, the TNF dARE, is a classically erosive, genetic model of RA which shows symmetrical progressive symptoms beginning at approximately 5 weeks of age (detectable by histology), manifesting in clinically detectable joint deformation and discolouration at approximately 12 weeks; an age at which the animals are commonly used in experiments for investigating fully developed arthritis. The second mouse model, the K/BxN serum transfer, is distinctly different from the TNF dARE model, exhibiting non-symmetrical swelling and a ‘redness’ of colouring, often affecting individual digits or areas of the foot. The pattern and number of joints affected in each individual mouse is variable and unpredictable. The arthritis peaks between 7 and 12 days after the initial injection of K/BxN serum and is clinically resolved after 21 days. All experiments were carried out at the University of Birmingham, UK, following strict guidelines governed by the UK Animal (Scientific Procedures) Act 1986, under PPL licence number 70/8003 and approved by the local ethics committee (BERSC: Birmingham Ethical Review Subcommittee). All mice were fed a standard chow diet and maintained on a 12 hour light-dark cycle.

#### 6.2.1.1 TNF dARE

Details of the TNF dARE colony used in experiments have been introduced in section 4.2.3.1. Two groups of heterozygous C57BL/6 TNF$^{+/dARE}$ mice and their normal companion TNF$^{+/+}$ littermates were imaged using the multispectral system described in section 5. Both imaged groups contained six female mice, three of which were TNF$^{+/dARE}$. For data described in section 6.4.1.1 the mice were aged 12 weeks at the time of imaging, and for data in section 6.4.1.2 the mice were imaged at three timepoints from the ages of 5 weeks, 7 weeks, and 9 weeks old.

#### 6.2.1.2 KBxN ST

Imaging data from K/BxN serum transfer mice are discussed in section 6.4.2. 6-8 week old male C57Bl/6 mice, supplied by Harlan, were injected intravenously with 100μl K/BxN serum (a gift from Harris Perlman, Northwestern University, USA). Arthritis was monitored daily and was evident clinically at between 1-2 days following injection. Mice were imaged on day 12 following injection.

### 6.2.2 Mouse Imaging

For all imaging experiments, mice were anaesthetised for the duration of the imaging session using 3% isoflourane and a standard anaesthetic set up. A nose cone was used to maintain anesthetisation of the mouse during imaging session. The mouse was positioned lying prone on top of a warming pad with one hind paw extending backwards and resting on top of the stage polariser. The right paw was imaged first, then the left paw was moved into position above the polariser and imaged second. Full acquisition of reflectance and transmittance imaging data took approximately 7 minutes per mouse and mice were culled by a schedule 1 procedure, once all imaging data had been obtained. Hind limbs were then dissected for microCT and histology.

### 6.2.3 Histology

Staining sections of the dissected paws with haematoxylin and eosin allows the soft tissue pathology and bone erosion to be seen and scored at a cellular level. Full brightfield images of the stained sections were taken with a Zeiss Axioscanner. The histology scoring procedure was then carried out (by Sophie Glinton) whilst blinded to the genotypes of the mice. The protocol was as follows: for slides where the cartilage interface of individual joints could be clearly seen on the imaged section, the joints were given a score of 0 – 3 for severity. 0 = normal with no evidence of inflammation, 1 = presence of inflammatory infiltrate without joint erosion, 2 = inflammation plus erosion of cartilage and/or bone but normal joint architecture intact; 3 = inflammation with severe joint erosions to the extent that joint architecture appears deformed. Examples of joint images are given in Figure 39. A mean score was taken for all the joints evident on each slide and for all the slides belonging to each mouse to give an average score for arthritis severity for each foot.

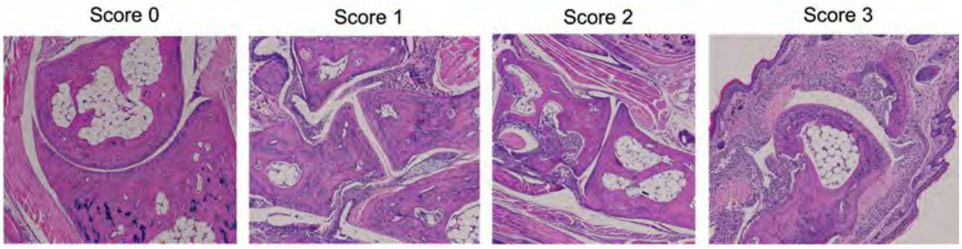

Figure 39: Example images demonstrating scoring joints affected by arthritis in increasing severity from left to right. Score 0: no evident inflammation around the joint; score 1: visible inflammatory infiltrate but no damage to the joint structure; score 2: evidence of inflammatory infiltrate and erosion of the hard tissues; score 3: infiltrate with clear deformation of the joint.

### 6.2.4 MicroCT Imaging and Bone Erosion Analysis

After the mice were culled, hind legs were dissected at the hip joint and stored in a 10% formalin solution for a period of 24 hours before transferal to 70% ethanol. Samples were imaged using a SkyScan 1172 micro-CT scanner from Bruker micro-CT, which was operated using the accompanying software. The microCT settings were adjusted for good contrast for bone imaging: A voltage of 60kV and a current of 167uA was used in conjunction with an aluminium filter. Exposure time was set to 580ms with a rotation step size of 0.45 degrees and a frame average of 4. Raw data was then reconstructed using nRecon software (Bruker). Flat field correction was performed and if necessary, misalignment compensation applied. Images were then reconstructed to an approximate image volume of 2000 x 2000 x 1187 voxels. CTAnalyser v1.12 (176) software was used to extract an isosurface mesh of the bony structures in the mouse hind paw. A global threshold was used to isolate bones from background and kept consistent between samples. The mesh was then extracted through a marching cubes algorithm and stored in polygon file format (PLY) (190). In order to meet the requirements for the microCT analysis software (see section 2.5.2.2 for description) (105), further mesh processing was carried out in Meshlab (1.3.2), open source software for mesh manipulation. Poisson surface reconstruction was used to smooth the appearance of the mesh. The inner surfaces of the bones were selected by setting a threshold with an ambient occlusion filter, then deleted, leaving only the outer surfaces of the bone. The complexity of the mesh was reduced through quadric edge collapse decimation to the approximate point density of the atlas used for registration in the software. Processing the samples gives a bone erosion ratio per bone, or the proportion of the bones surface area affected by erosions.

In the experimental results shown in this chapter either an average bone erosion ratio was taken as a mean of all the individual bone erosion values for each of the bones in the hind paw, or a mean was taken for a particular region of the foot by dividing the bones into separate areas as shown in Figure 40 corresponding to the areas analysed in the multispectral imaging analysis.

Figure 40: A mouse hind paw mesh generated from a microCT scan and coloured to indicate how the bones of the hind paw were divided into areas for regression analysis with multispectral imaging results.

### 6.2.5 Image Registration

Comparatively long exposure times at the longest and shortest wavelengths, the time-consuming switching between the two Varispec filters, and the breathing motion of the anaesthetised mouse meant that small movements of the paw occurred between the images taken at different wavelengths. The GUI method for extracting spectra from areas of the image relies on the same pixel region of each wavelength frame corresponding to the same region of the paw and therefore images were registered to align the paw within the multispectral image cube, for both the reflectance and transmittance data. The images were registered using a rigid, pixel-intensity based registration method within the Image Processing Toolbox in Matlab. Prior to registration, the images were calibrated and dark corrected, then registered to the image frame taken at 690nm.

### 6.2.6 Principal Component Analysis

A statistical method was required to extract meaningful information from the multispectral data. The data produced from the GUI data extraction is multidimensional, effectively incorporating 520 wavelengths, from 4 different foot locations, for each separate hind paw of each separate mouse in an imaging session. In the experiments described in sections 6.4.1 through 6.4.2, principal component analysis (PCA) was used to analyse all of the data produced from the GUI data extraction (section 6.3.2) to assess the spectral changes occurring with arthritis symptoms.

PCA calculates an orthogonal linear transformation of the data covariance matrix through Eigen decomposition, which maps the data to a new set of axes, known as principal components (191). The first principal component, or eigenvector, has the largest associated loading (eigenvalue), meaning that it corresponds to the direction of the largest variation in the data. Subsequent principal components describe directions of variation in order of descending size. Since most variation in the data is generally captured by the first few eigenvectors, the dimensionality of the data can be reduced.

When performed on the multispectral data, PCA also produces a series of scores for each individual spectra, describing the coordinates of the spectra when transformed into the new axes of the principal components, effectively ranking the mice for how pronounced their spectral variation is. PCA for all mouse imaging sessions was computed using functions available in the Statistics and Machine Learning toolbox of Matlab.

### 6.2.7 Linear Discriminant Analysis

In common with PCA, linear discriminant analysis (LDA) defines a transformation of the data into a more useful form. In the case of LDA, the input data are classified manually into 2 or more groups and the algorithm defines an axis (comparable to the eigenvectors in PCA) which best separates the two groups (192). Scores of individual data points can then be defined according to the axis. In section 6.4.3, LDA is used to define axes which best separate the spectra resulting from changes in chromophore concentrations in the Monte Carlo model (section 6.6.1).

## 6.3 Experimental Method Development

### 6.3.1 Multispectral Images of a Mouse Hind Paw

Figure 41a and c show raw images for one complete set of reflectance and transmittance data from an anesthetized mouse's hind paw, taken with the system described in section 5.3.1. In Figure 41b and d the images have been false-coloured according the imaging wavelength to represent their physical appearance when imaging.

Figure 41 shows that imaging the paw at different wavelengths changes the appearance of the paw in both reflectance and transmittance. More blurring of the image is evident at the longest wavelengths, due to the different refraction of successive wavelengths within the lens altering the focal plane of image. There is also some specular reflectance apparent on the paw, but this was not found to be a major obstacle in processing the data. In the transmission images, it is clear that transmission of the visible wavelengths is very low for most of the foot, although most wavelengths traverse the toes. However, for the longer wavelengths the effect of reduced absorption and scatter can be seen as the whole foot is transilluminated.

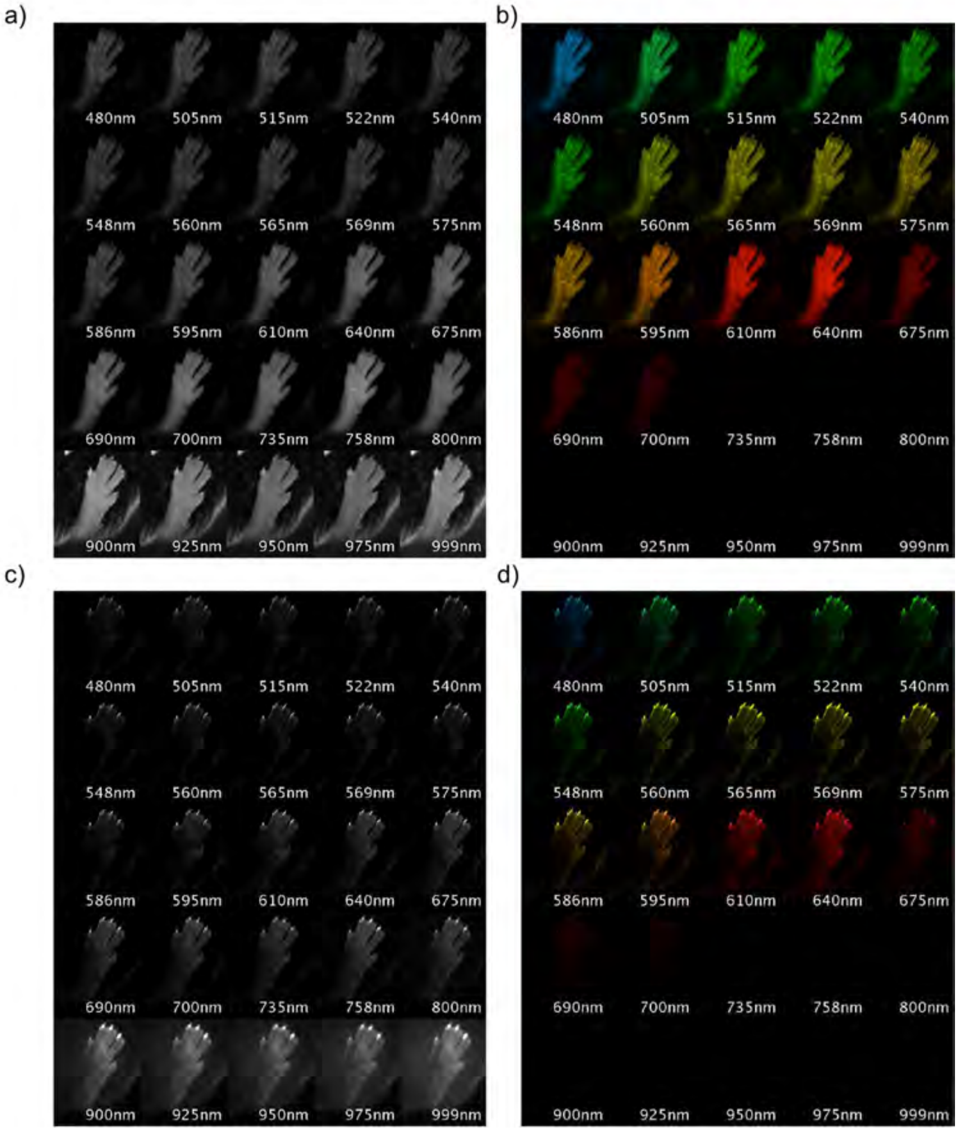

Figure 41: Reflectance and transmittance images taken at a series of wavelengths for a single normal mouse hind paw. a) Raw reflectance images of a mouse hind paw taken at the annotated wavelengths. b) The images from a, false-coloured according to the wavelength of illumination. c) Raw transmittance images of the same mouse paw taken at the same wavelengths using the twin polarizer transillumination system. d) False-coloured transmittance images of the same mouse hind paw.

### 6.3.2 Multispectral Data Analysis

The raw images taken by the multispectral imaging system were processed in order to extract the spectral characteristics of the mouse feet (Figure 42). A GUI system was designed in order to manually select regions of the feet for spectral analysis. As described in section 3.3.1.2, the images of the paw were analysed according to the four areas of the heel, the joints, the midfoot, and the toes due to broad anatomical differences in the structure of the foot that were found to influence the spectral properties of the tissue. For further spectral analysis, 10 spectra were taken from each area and averaged so that 4 mean spectra corresponding to the 4 paw regions could be taken from each multispectral dataset. Figure 42 details the workflow of the spectral analysis method with an example from one mouse paw image. A full set of images taken at each wavelength for reflectance and transmittance for one example mouse paw is included in the appendices (section 6.3.1).

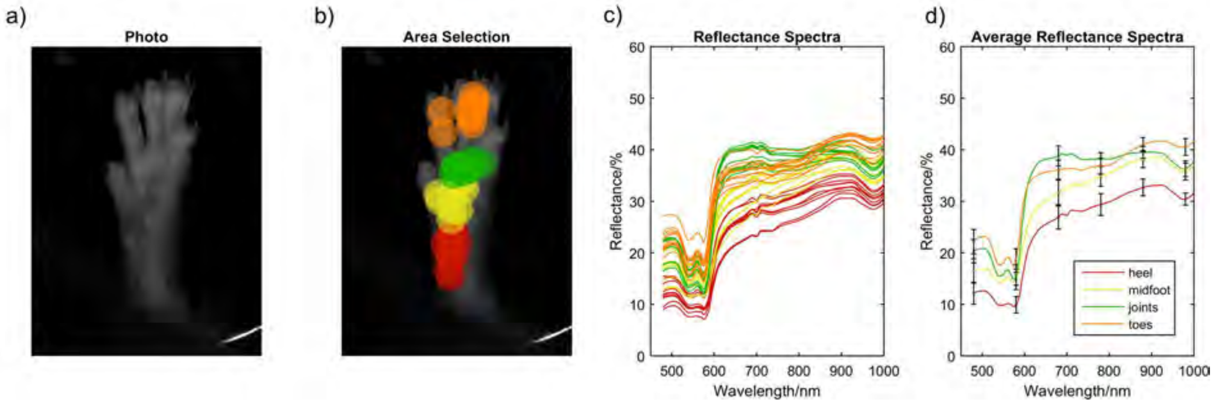

Figure 42: Process of multispectral image analysis using a custom Matlab GUI to extract spectral data from regions of interest. a) Image of a mouse hind paw taken from the multispectral system, made by averaging all spectral frames. b) Image showing the areas manually selected for spectral analysis according to the four anatomical areas toes, joints, midfoot and heel. c) Graph showing all the reflectance spectra extracted from the image by the circular regions indicated and colour-coded in b. d) The reflectance spectra calculated from the mean of the 10 areas selected for each region of the hind paw.

## 6.4 Results

### 6.4.1 Multispectral Imaging of the TNF dARE Rheumatoid Arthritis Model

Multispectral imaging was performed on TNF dARE mice in a blinded, randomised experiment. Section 6.4.1.1 details the imaging of a group of six TNF dARE mice at 12 weeks of age, taking multispectral data at a time period when the mice are expected to exhibit symptoms detectable by manual scoring. Three of the mice were TNF dARE heterozygous and the remaining three mice were normal control littermates. The results of imaging were compared with the results from histology, manual scoring and microCT data.

Section 6.4.1.2 details a series of multispectral imaging sessions on TNF dARE mice taken from the ages of 5 weeks to 9 weeks when the mice have histological signs of inflammation, but may not yet outwardly display clinical symptoms. In general, heterozygous TNF dARE mice first exhibit detectable signs of arthritis in histology around 3 weeks old (193) and the clinical symptoms (swelling, discolouration, deformation, behavioural changes) become detectable around 6 – 8 weeks (55). This phase where arthritis symptoms are established is important in research, as the early phase of rheumatoid arthritis represents a window of therapeutic opportunity which is thought to influence long-term prognosis (194,195). The results of these two experiments are discussed together in section 6.4.1.3.

#### 6.4.1.1 TNF dARE 12 Week Multispectral Imaging

The multispectral imaging method described above (section 6.3.2) was used to image the TNF dARE mouse model of rheumatoid arthritis. The data has been compared to a number of other metrics for assessing the severity of inflammatory symptoms (section 6.4.1.1.4). The mice were scored according to the clinical scoring method immediately prior to imaging (see section 2.5.1.1 for scoring sheet), then the spectral information from the imaging analysed as described above (section 6.3.2 and 6.2.6). The same process has been used in all subsequent experiments for the analysis of multispectral reflectance data. In all experiments, manual scoring was carried out blindly by a researcher experienced in *in vivo* models of RA and with these models in particular. The details of the mice used in this experiment are discussed in section 6.2.1.1.

#### ***6.4.1.1.1*** **Reflectance**

Figure 43 displays the mean spectral reflectance from the healthy group and the arthritic group, where the spectra have been min-max normalised to emphasise the wavelength-dependent spectral variation between the two groups. Figure 44a displays the score along the 1st principal component for each area of the foot individually grouping the spectra for that region from all mice. PCA was performed on the raw (non-normalised) reflectance data. The raw spectral reflectance data can be seen in Figure 44b where mean spectra for each foot region have been superimposed on to a statistical shape model (SSM) (196). The SSM's demonstrate the effect of the variation captured in the 1st principal component, for individual anatomical regions where the variation in the 1st principal component has been projected around the mean spectral response by 3 standard deviations either side.

The 1st principal component (PC) was found to be the most effective in being able to split the group of healthy mice from their arthritic littermates. For this experiment, the 1st PC of the reflectance data explains a mean of 95.3% of the data variance for the 4 areas, computed by calculating the percentage of the eigenvalue for the 1st PC divided by the sum of all eigenvalues.

Reflectance multispectral imaging of the TNF dARE mouse revealed a general decrease in intensity with arthritis symptoms which can be seen in Figure 44b, as well as a spectral shape change where reflectance in the 480nm to 550nm and 600nm to 800nm spectral regions are relatively decreased, apparent in Figure 43.

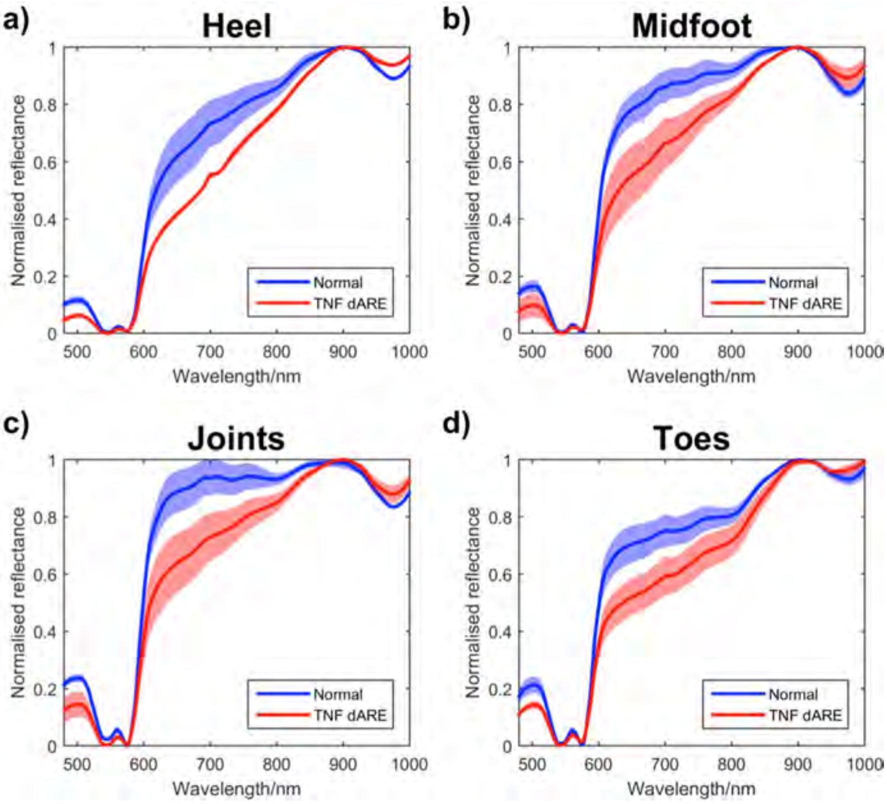

Figure 43: Min-max normalised reflectance spectral data from four areas of the TNF dARE mouse hind paw, from six 12-week old mice, N=3 TNF dARE and N=3 normal with two paws imaged per mouse giving a total of twelve multispectral datasets. Mean spectra for the normal group are displayed In blue with standard deviation shown as a pale blue shaded region and in red for the TNF dARE data. a) Average normal vs average TNF dARE reflectance spectra for the heel region of the hind paw b) Average reflectance min-max normalised spectra for normal vs TNF dARE for the middle region of the foot. c) Average reflectance min-max normalised spectra for the joints region of the foot. d) Average min-max normalised spectra for the toes region of the foot.

Monte Carlo modelling of the arthritic mouse hind paw in chapter 3 showed a decrease in reflectance across all wavelengths, which is maximal between 600nm and 700nm. This suggests that as modelled, there may be an increase in absorbing chromophores present in the tissue, particularly an increase in blood volume fraction and a decrease in oxygen saturation.

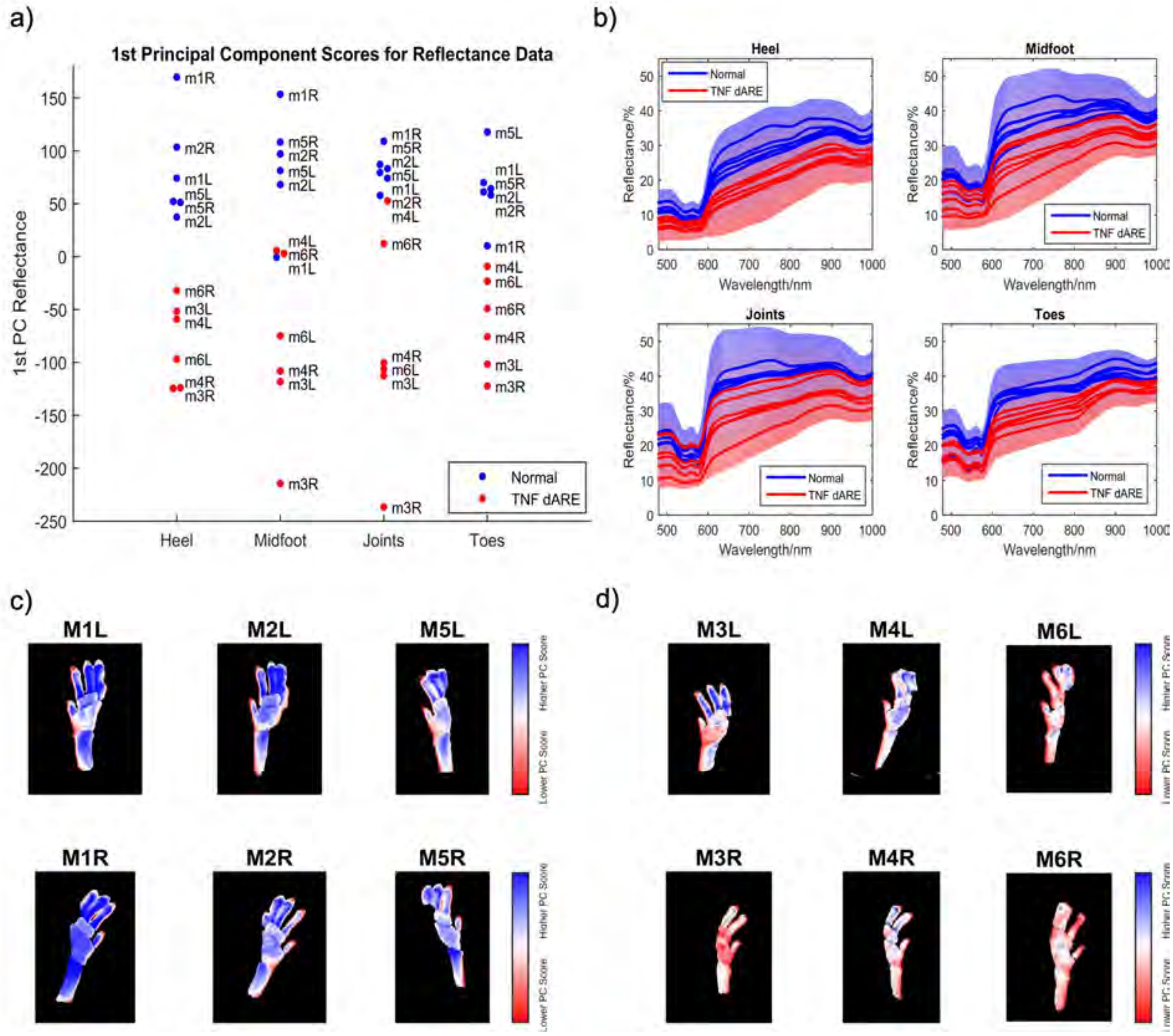

Figure 44: Results from principal component analysis of reflectance spectral data from four areas of the TNF dARE mouse hind paws from six 12-week old mice, N=3 TNF dARE and N=3 normal with two paws imaged per mouse giving a total of twelve multispectral datasets. a) Scores for the 1st principal component extracted from PCA of all the reflectance data for each individual area of the foot. Spectra from each mouse paw are labeled m1 to m6 with right and left hind paws indicated by R and L. Each have been colourised according to their genotyping. b) Reflectance spectra for each hind paw from the group of 6 mice, separated into 4 anatomical regions. The spectra have been superimposed onto a statistical shape model describing 3 standard deviations of variation within the 1st principal component. c) Normal mice mapping of 1$^{st}$ PC score value for individual pixels of the four selected regions of the paw. d) TNF dARE mice mapping of 1$^{st}$ PC score value for individual pixels of the four selected regions of the paw.

Using PCA to isolate directions of variation in the dataset exploited the fact that the primary cause of variation between the mice appeared to be a result of physiological changes induced by arthritis symptoms. Evidentially, the 1st principal component of the data represented an average of 95.3% of variance for the 4 anatomical areas and separated the normal mice from the TNF dARE mice, while (for this experiment) there was no separation in subsequent PC's, which seemingly did not contain variation relating to arthritis symptoms. In the reflectance data shown in Figure 44b, the variation explained by the 1st principal component refers to a decrease in reflectance across all wavelengths, particularly affecting the 600nm to 800nm spectral region. It is likely that this corresponds with 'greying' of the paw described in the TNF dARE mouse model and is likely due to several physiological processes occurring in tandem. The 1st PC scores have been represented visually in Figure 44c and d where the PC score is given for individual pixels and colormapped where blue is a higher score and red is a lower score. The lower average score can be clearly seen for the TNF dARE mice (Figure 44d) compared to the normal mice (Figure 44c) and some TNF dARE displayed a more heterogenous score across the paw, for example M3L, compared to others which appear more consistent, for example M6R.

The PCA analysis displayed in Figure 44a also highlighted details not revealed by standard clinical scoring methods: There appeared to be variation between paw regions and between hind paws of the same mouse despite being a symmetric model of arthritis. There was also apparent variation within the group of normal mice, demonstrating why scoring by eye, which relies on normal mice being scored 0, may be problematic.

The significance of the difference between the two groups of spectra was tested using the method described in section 4.5, where a matrix describing the sum of the RMS difference per wavelength of every spectra was tested by a 2 factor student t-test to assess whether the intergroup difference was significantly more than the internal group difference. For the reflectance data of the TNF dARE and normal mice, the difference was significant across all areas (p-values: heel = 0.0112, midfoot = 0.000859, joints = 0.000111, toes = 3.10e-07).

### *6.4.1.1.2* Transmittance

The transmittance data from the multispectral imaging experiment has been analysed similarly (figure 45 and figure 46). In the case of transmittance, PCA was performed on min-max normalised data rather than the raw data due to the influence of the thickness of the tissue on spectral variation. When performed on the raw spectral data, the variation capturing the changes in arthritis were split across two principal components, whereas PCA on normalised data split the groups of mice in the 1st principal component explaining 91.5% of the variation. This method of analysis was used for all subsequent transmittance mouse imaging experiments discussed below.

In the normalised transmittance data (figure 45), a trend for a change in the spectral shape can be seen where transmittance is relatively decreased in the 600nm to 800nm region of the spectrum.

The peak in increased absorbance at 600 – 700nm in both the reflectance and transmittance spectra is strongly indicative of decreased oxygen saturation in the tissue. This peak correlates with the spectral changes seen with decreased oxygen saturation in the Monte Carlo model (section 3.4.1). The RMS differences between the average spectra of the normal and the TNF dARE groups have been included in the appendices (section 8.A6).

Similar to the PCA scoring results of reflectance, the 1st PC score could be seen to vary between the paws on the same mouse, between different regions of the paw, and within the group of normal mice.

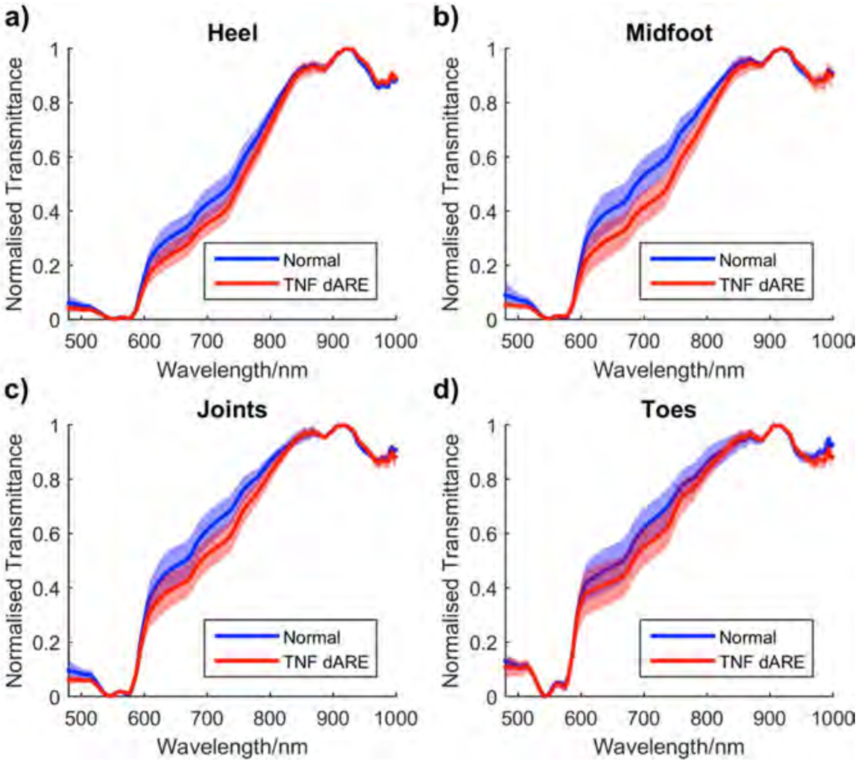

Figure 45: Min-max normalised transmittance spectral data from four areas of the TNF dARE mouse hind paws from six 12-week old mice, N=3 TNF dARE and N=3 normal, with two paws imaged per mouse giving a total of eleven datapoints (M1L removed because spectral imaging failed due to paw movement during exposures). Mean spectra for the normal group are displayed In blue with standard deviation shown as a pale blue shaded region and in red for the TNF dARE data. a) Min-max normalised data for the heel region of the paw. b) Min-max normalised spectral data for the midfoot region of the paw. c) Min-max normalised data for the joints region of the paw. d) Min-max normalised data for the toes region of the paw.

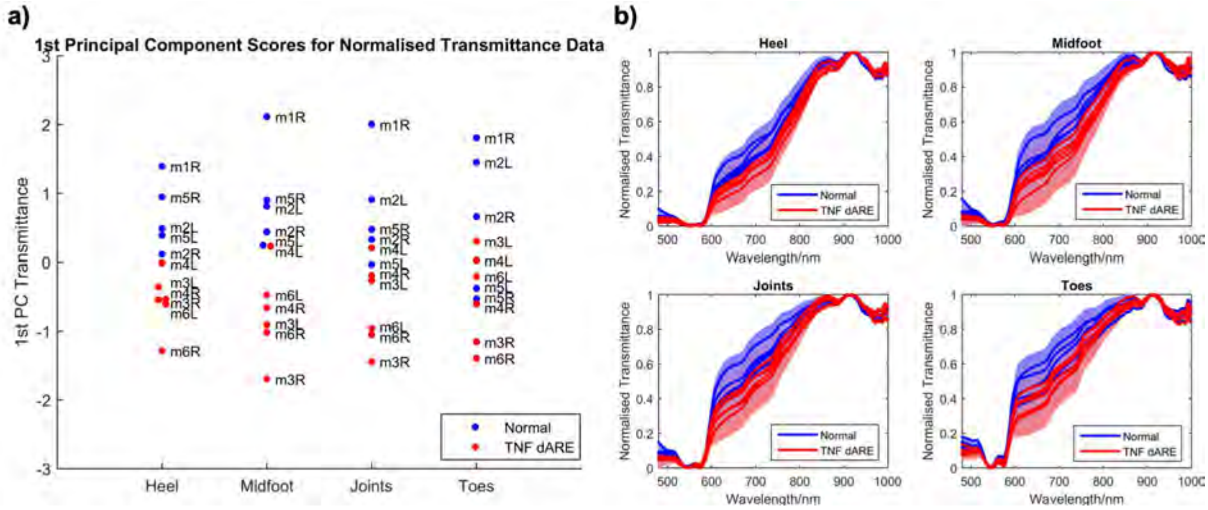

Figure 46: Results from principal component analysis of transmittance spectral data from four areas of the TNF dARE mouse hind paws from six 12-week old mice, N=3 TNF dARE and N=3 normal, with two paws imaged per mouse giving a total of eleven datapoints (M1L removed - spectral imaging failed due to paw movement). a) Score along the 1st principal component for the normalised transmittance data for each area of the foot. Spectra from each mouse paw are labeled m1 to m6 with right and left hind paws indicated by R and L. b) Normalised transmittance spectra for each hind paw from the group of six mice for four anatomical regions. The spectra have been superimposed on a statistical shape model of the variation contained by the 1st principal component.

When performed on the raw (non-normalised) transmittance spectral data, the 1st PC spectral variation corresponded to a relatively linear decrease in spectral intensity and the 2nd to a decrease of transmittance in the visible wavelengths. Variation due to arthritis appeared to be contained within the first two PC's making the scoring system inconsistent. Applying PCA to normalised data effectively removed the linear spectral decrease from the data and focussed on changes in spectral shape. Whilst a linear drop in spectral intensity also occurred in the reflectance data and could be attributed to the arthritic group, intensity in the transmittance data is more sensitive to the thickness of the tissue which is unlikely to be a symptom of arthritis in the TNF dARE model where swelling does not occur, but more likely due to the angle of the foot whilst imaged or the size of the mouse. Notably however, it does appear to be predicative of arthritis in the toes in line with the observation that TNF dARE mice tend to have thickening of the toes.

In calculating the significance of the difference between the groups using 2-factor student t-test, only the heel had a significant separation between the group of spectra from the normal mice and the group of TNF dARE spectra (p-values: heel = 0.0194, midfoot = 0.286, joints = 0.852, toes = 0.387).

#### ***6.4.1.1.3*** **Correlation of Reflectance and Transmittance PCA Scores**

The reflectance and transmittance PCA scores were compared in Figure 47 by Pearson correlation for individual paws (Figure 47a), as well as individual paw regions (Figure 47b). The reflectance and transmittance spectra may not be expected to correlate exactly due to the different paths the photons take through the heterogenous tissue. However, given that the imaged tissue was thin and both reflectance and transmittance tissues would be affected by chromophore concentration changes in similar local tissue regions, a correlation could be apparent. The graphs in Figure 47 have been annotated with the p-values calculated by Pearson correlation.

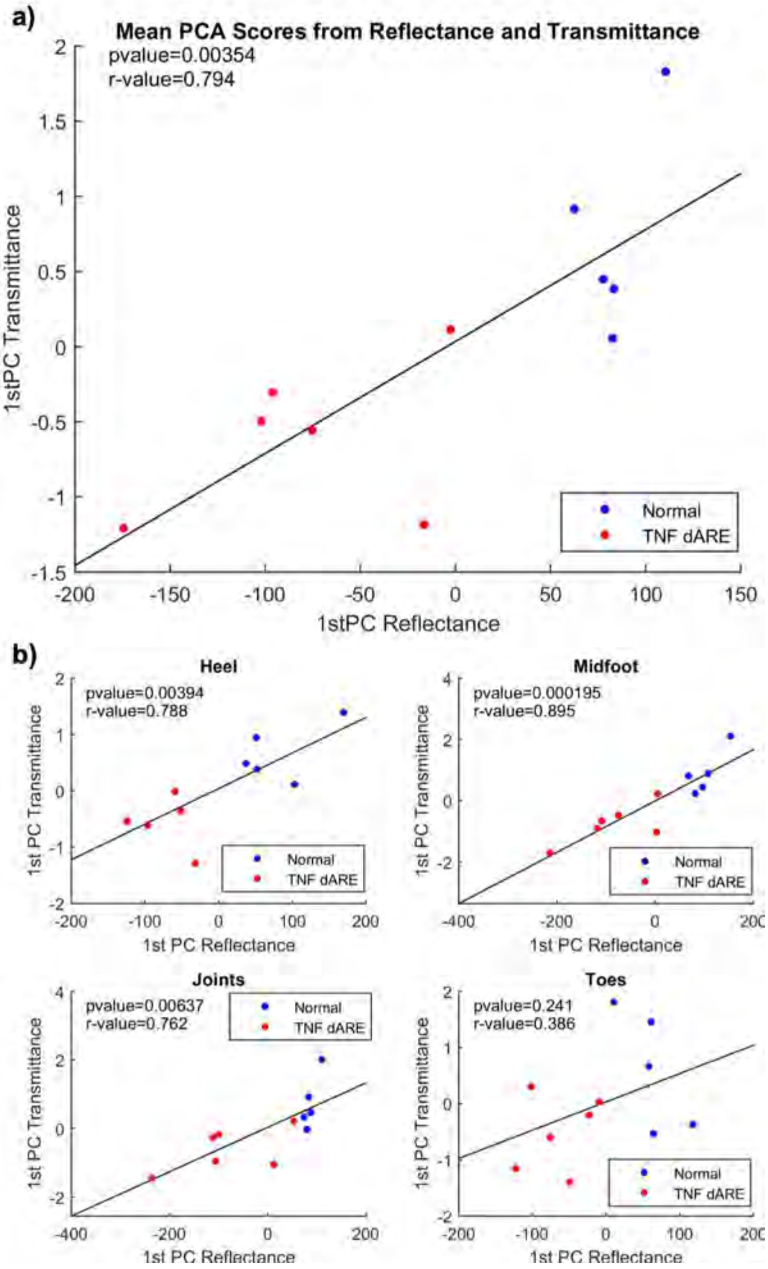

Figure 47: Comparison of the 1st principal component scores from principal component analysis of reflectance and transmittance spectral data from four areas of the TNF dARE mouse hind paws from six 12-week old mice, N=3 TNF dARE and N=3 normal, with two paws imaged per mouse giving a total of eleven datapoints (M1L removed because transmittance imaging failed due to paw movement during exposures). P-values and r-values calculated by Pearson correlation analysis. a) Comparison of the 1st prinicipal component scores for reflectance, averaged for each hind paw, to the 1st principal component scores for min-max normalised transmittance. b) Comparison of the 1st prinicpal component scores for reflectance against the 1st principal component scores for transmittance for each individual area of the hind paw.

Significant correlations could be seen ($p < 0.05$) for the individual paw scores and for all the individual areas of the paws (except the toes), suggesting that the scores of the reflectance and transmittance spectra were influenced by the same local tissue physiological changes discussed above.

#### *6.4.1.1.4* Correlation of Spectral Variation with Other Indicators of Disease

Multispectral imaging of the TNF dARE mouse model identified and characterised changes in the spectral response of the tissue between a group of normal and TNF dARE mice. This section aims to establish whether the spectral changes detected by the multispectral imaging system correlate with other signs of disease severity, to determine whether spectral imaging has potential as a method of disease assessment.

To investigate whether the spectral variation correlated with several established methods of measuring disease progress, three measurements were taken of the TNF dARE mice. MicroCT data for all mouse hind paws were scored for bone erosion ratio using MArthA software, histology sections of the feet were prepared and scored for signs of arthritis as described in section 6.2.3, and the mice were scored manually for signs of arthritis using an accepted clinical scoring method prior to imaging (see score sheet in section 2.5.1.1). Pearson correlation p-values have been calculated between the PCA scores from the spectral data,and the metrics of arthritis symptoms produced by these methods.

#### MicroCT Bone Erosion

The bone erosion ratio scores produced by MArthA were compared to the multispectral reflectance (Figure 48)  and transmittance (Figure 49) PCA scoring at both the level of each area of the paw and for the average scores of each individual paw, using the method discussed in section 6.2.4.

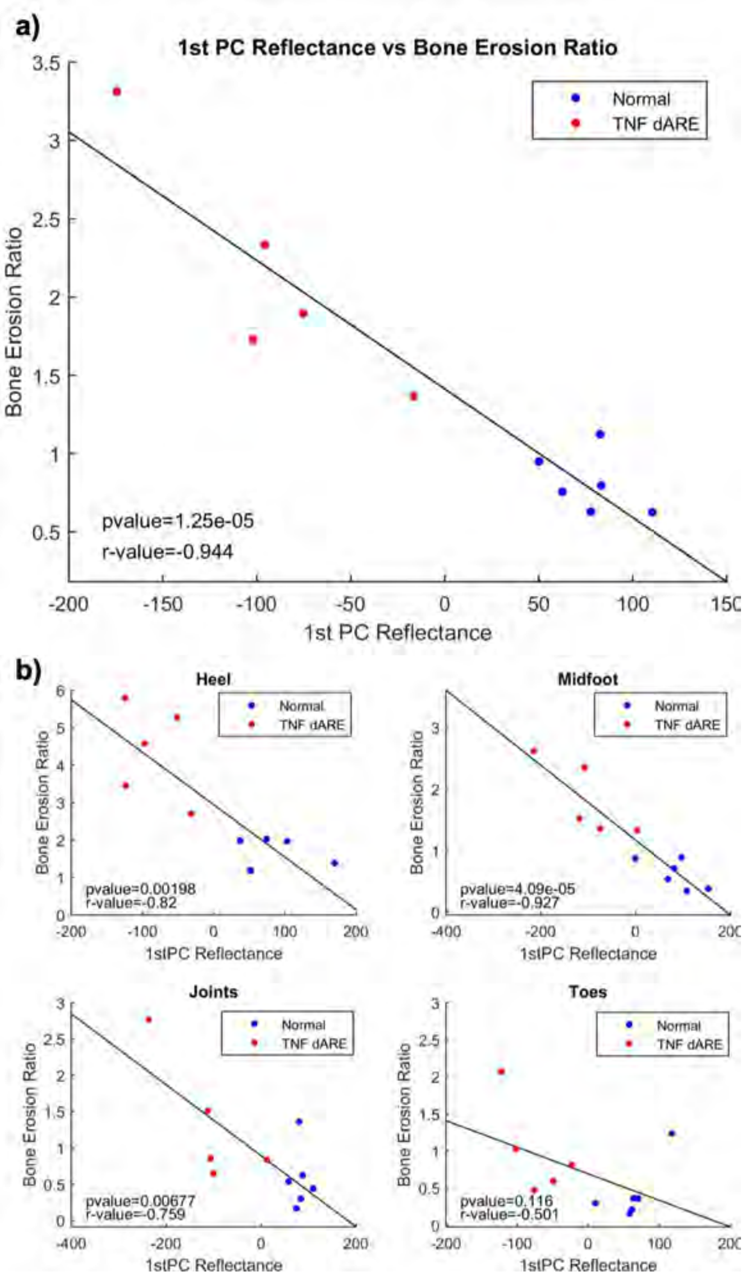

Figure 48: Comparison of the 1st principal component scores from reflectance spectral data vs the bone erosion scores from microCT from four areas of the TNF dARE mouse hind paws from six 12-week old mice, N=3 x TNF dARE and N=3 x normal, with two paws imaged per mouse giving a total of eleven datapoints (M4L removed because failed registration in MArthA software). P-values and r-values calculated by Pearson correlation analysis. a) Comparison between the 1st PC reflectance scores per foot and the average bone erosion output from MArthA. b) Comparison between the 1st PC reflectance scores per area of each hind paw and the average bone erosion output of MArthA for the relevant bones of the paw.

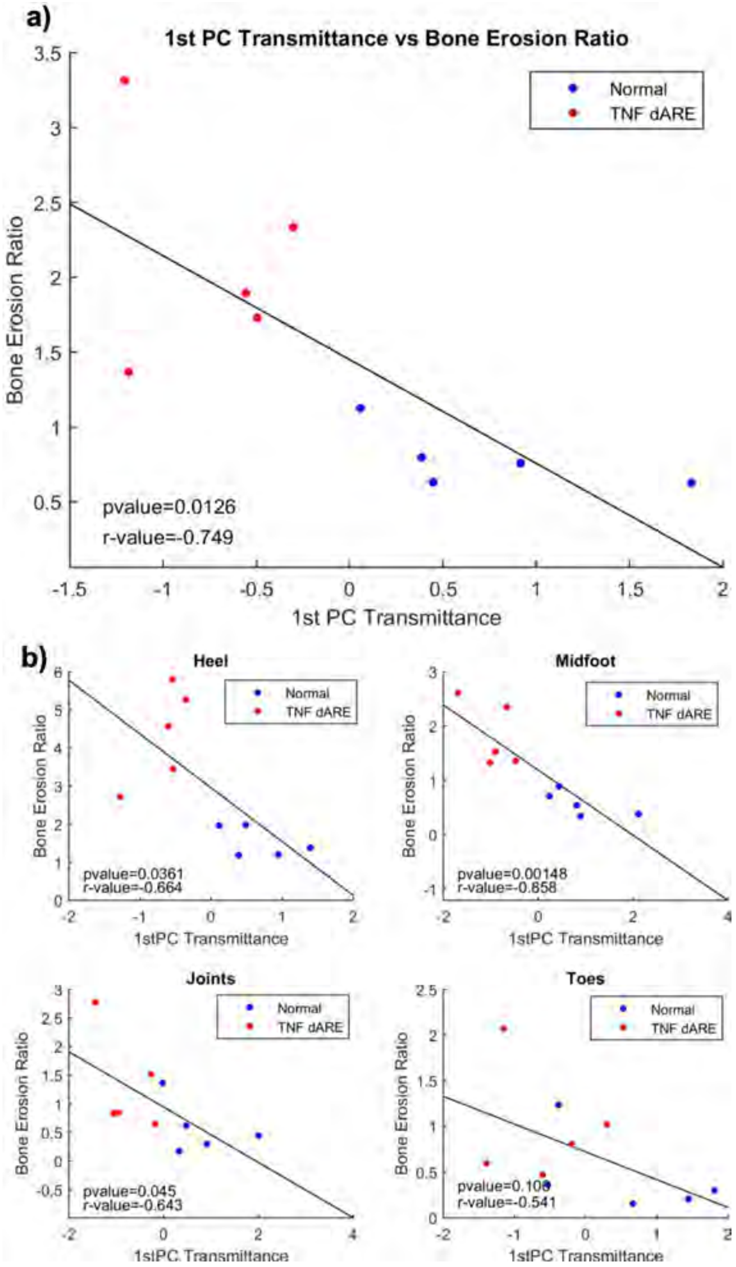

Figure 49: Comparison of the 1st principal component scores from transmittance spectral data vs the bone erosion scores from microCT from four areas of the TNF dARE mouse hind paws from six 12-week old mice, N=3 TNF dARE and N=3 normal, with two paws imaged per mouse giving a total of ten datapoints (M4L removed because failed registration in MArthA software, M1L removed because transmittance imaging failed due to paw movement during exposures). P-values and r-values calculated by Pearson correlation analysis. a) Comparison between the 1st PC normalised transmittance scores per foot and the average bone erosion output from MArthA. b) Comparison between the 1st PC normalised transmittance scores per area of each hind paw and the average bone erosion output of MArthA for the relevant bones of the paw.

For both reflectance and transmittance a significant relationship ($p\text{-value} < 0.05$) existed in this dataset between the PCA score and the Bone Erosion score determined by MArthA for each individual paw. However, the individual areas of the paws showed correlations that are significant in some areas but not others.

For the individual feet, the p-value remained significant for reflectance (0.0283), but not for transmittance (0.765) when the TNF dARE group was analysed alone without the normal mouse data (although the group number was low (5 hind paw values)). This correlation suggests that the severity of arthritis is associated with the degree of change in the tissue spectral response. This would be a necessary relationship to fully establish if the spectral score were to be used as a tool for grading arthritis severity.

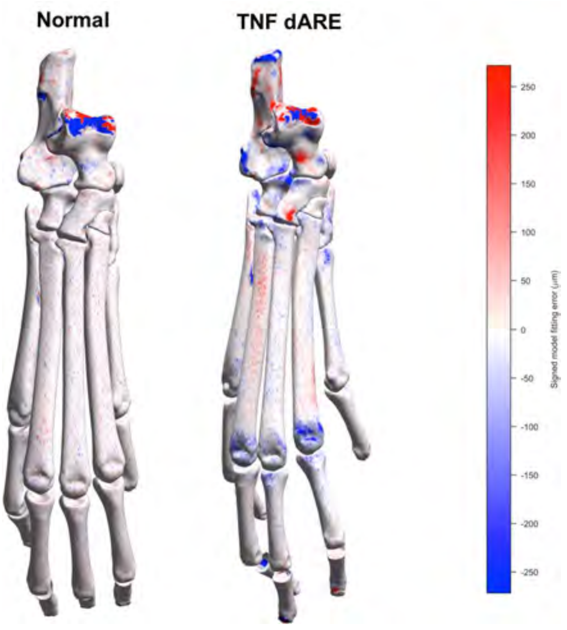

Figure 50: Two example meshes from the microCT analysis using MArthA described in section 6.4.1.1.4. The mesh is coloured according to the Euclidean signed error where blue indicates areas of bone erosion and red indicates areas of bone deposition. The mesh produced from microCT of the normal mouse displays no distinct regions of erosion, whereas areas of erosion can be seen affecting many of the bones of the heel and around the metacarpophalangeal joints of the TNF dARE.

Changes in tissue spectral response are unlikely to be a direct result of erosion, but the results from this experiment indicate that the more the spectral tissue response is perturbed from normal, the more erosion activity is occurring in the hard tissue. Figure 50 displays a heatmap of bone erosion output from MArthA analysis of two of the mice from this experiment, indicating typical regions of erosion found in the TNF dARE model. Blue regions correspond to bone erosion and red to bone growth.

### Histology

Histology scores were taken for one hind paw from each of the 6 mice and have been compared to the corresponding PCA scores in Figure 51.

Significant relationships were seen for both the reflectance and transmittance data with the histology scoring results, although unfortunately the sample number for this experiment was very small. The histology scores were based on the presence of inflammatory infiltrate as well as the extent of joint erosions. The strong correlation therefore corroborates the result of microCT analysis indicating increased erosion with 1st principal component score and suggests a relationship between inflammatory infiltrate and spectral tissue response.

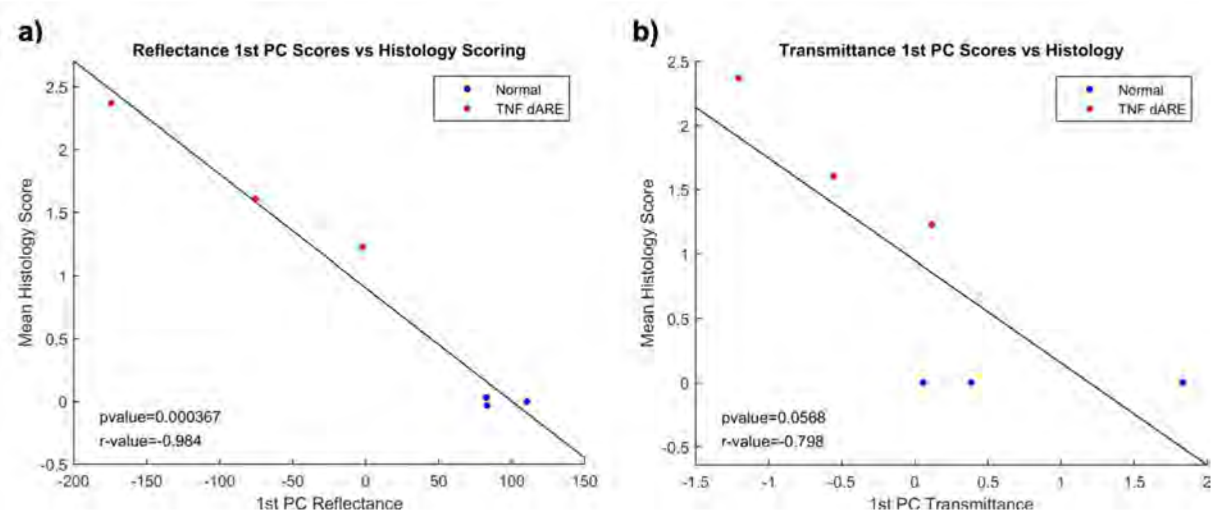

Figure 51: Comparison of the mean 1st principal component scores from reflectance and transmittance spectral data vs the histology scores for the TNF dARE mouse hind paws from six 12-week old mice, N=3 TNF dARE and N=3 normal, with histology results taken from one paw per mouse giving a total of 6 values. P-values and r-values calculated by Pearson correlation analysis. a) Comparison between the results of Haemotoxylin and Eosin histology scoring for six mouse paws and the 1st principal component reflectance scores. b) Comparison between the results of Haemotoxylin and Eosin histology scoring for six mouse paws and the 1st principal component transmittance scores.

## Manual Scoring

The manual clinical scoring procedure produces one arthritis score per mouse and has been compared to the mean principal component score per mouse for reflectance and transmittance in Figure 52a and b.

Both the reflectance and transmittance Pearson correlations with the blinded manual scoring results gave significant p-values. In this experiment, all TNF dARE mice were correctly identified by blinded manual scoring and the mouse with the most extreme spectral response in both reflectance and transmittance was given the highest clinical score.

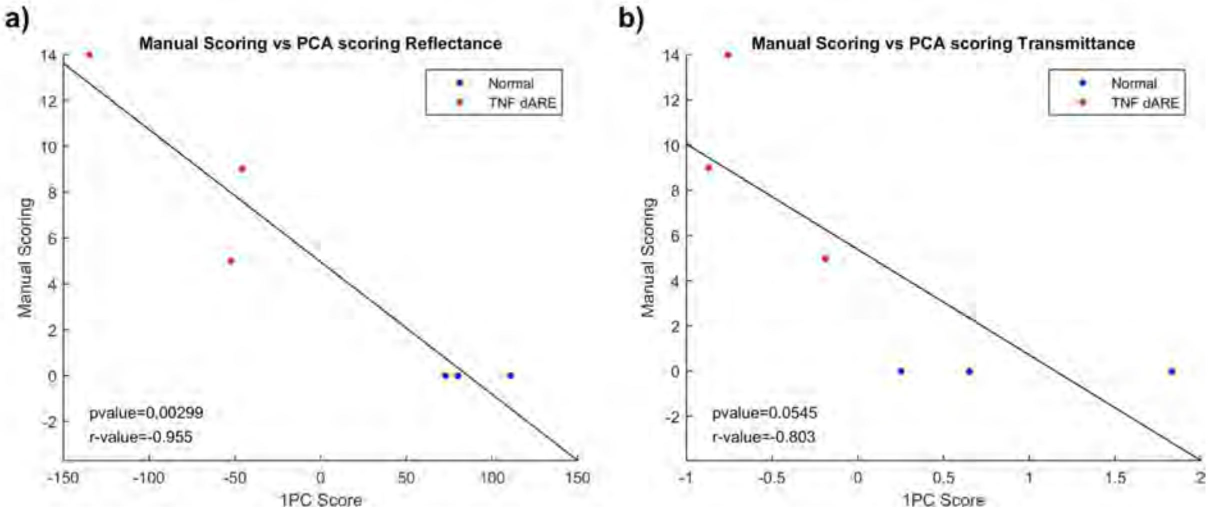

Figure 52: Comparison of the mean 1st principal component scores from reflectance and transmittance spectral data vs the manual scores for the TNF dARE mice from six 12-week old mice, N=3 TNF dARE and N=3 normal, with two paws imaged per mouse and averaged giving a total of six values. P-values and r-values calculated by Pearson correlation analysis. a) The correlation between the manual scoring method for assessment of arthritic mouse models vs the mean 1st PC reflectance results per mouse. b) The correlation between the manual scoring method for assessment of arthritic mouse models vs the mean 1st PC normalised transmittance results per mouse.

Discolouration of the hind paws constitutes only a small component of the clinical scoring method, which includes scores for deformity of the joints in both the front and back limbs, scores for altered appearance, gait, and behaviour. Significant correlation with clinical scores would therefore suggest that the degree of discoloration of the paws is relevant to the health of the overall mouse.

#### 6.4.1.2 Longitudinal TNF dARE Imaging

Data shown in the previous experiment found a change in the optical characteristics of TNF dARE mice to be associated with the exhibition of arthritis symptoms and pathology. The aim of this experiment was to image TNF dARE mice at an earlier timepoint in arthritis progression, to observe whether multispectral imaging could pick up differences at an early developmental stage of disease, before it is clinically detectable. Also, to follow how the developing arthritis symptoms influence the multispectral imaging results within the same subject mice. A group of 6 mice, 3 TNF dARE and 3 controls, were scored blindly by the manual scoring procedure once per week from the ages of 5 weeks to 9 weeks and imaged for reflectance and transmittance at 5 weeks, 7 weeks and 9 weeks. The mice were culled at the end of the week 9 imaging session and the hind limbs taken for microCT analysis before the genotypes of the mice were revealed. Details of the mice used in this experiment are discussed in section 6.2.1.1.

PCA was employed for the analysis of the multispectral data to score the mice for spectral variation. The analysis was applied to the full group of temporal spectra so that the PCA score related the spectra from the three imaging timepoints to the same eigenvector. Figure 53 displays the 1st principal component reflectance scores for each individual paw (Figure 53a) and for each area (Figure 53b) over the 5 week timeframe. The PCA scores have been compared to the progression of manual scoring results (Figure 54) and the resulting bone erosion data from MArthA (Figure 55).

For this experiment, transmittance results have not been included. As with the results of the 12 week TNF dARE imaging, there were slight trends towards decreased transmittance in the 600nm to 800nm region of the spectrum, but the PCA scores showed a lot of overlap of the two groups and hence were unable to effectively grade arthritis symptoms.

#### 6.4.1.2.1 Reflectance

The PCA scores from the longitudinal reflectance imaging of the TNF dARE mice indicate spectral changes apparent in the model as early as 5 weeks of age, across every region of the foot. The scores remain relatively consistent for each individual mouse paw across the five week imaging period (Figure 53a). If the 1st PC score is correlated with arthritis severity as suggested in section 6.4.1.1.4, this would indicate that the most symptomatic mice may be detectable from an early age. It also indicates that transient fluctuations in physiology are not overriding spectral changes happening due to arthritis. This result is encouraging that spectral imaging could be used to indicate the presence of arthritis at an earlier age than would be possible with manual scoring.

When applying a 2-factor student t-test to the RMS distances between individual spectra for all timepoints separately, nearly all tissue regions for each timepoint showed significant separation between the spectral groups (p-values given in order heel, midfoot, joints, toes: Week5; 0.000369, 6.10e-05, 0.00383, 0.0108 Week7; 1.21e-06, 5.36e-06, 0.000778, 0.398 Week9; 0.191, 0.0140, 0.0735, 0.000733).

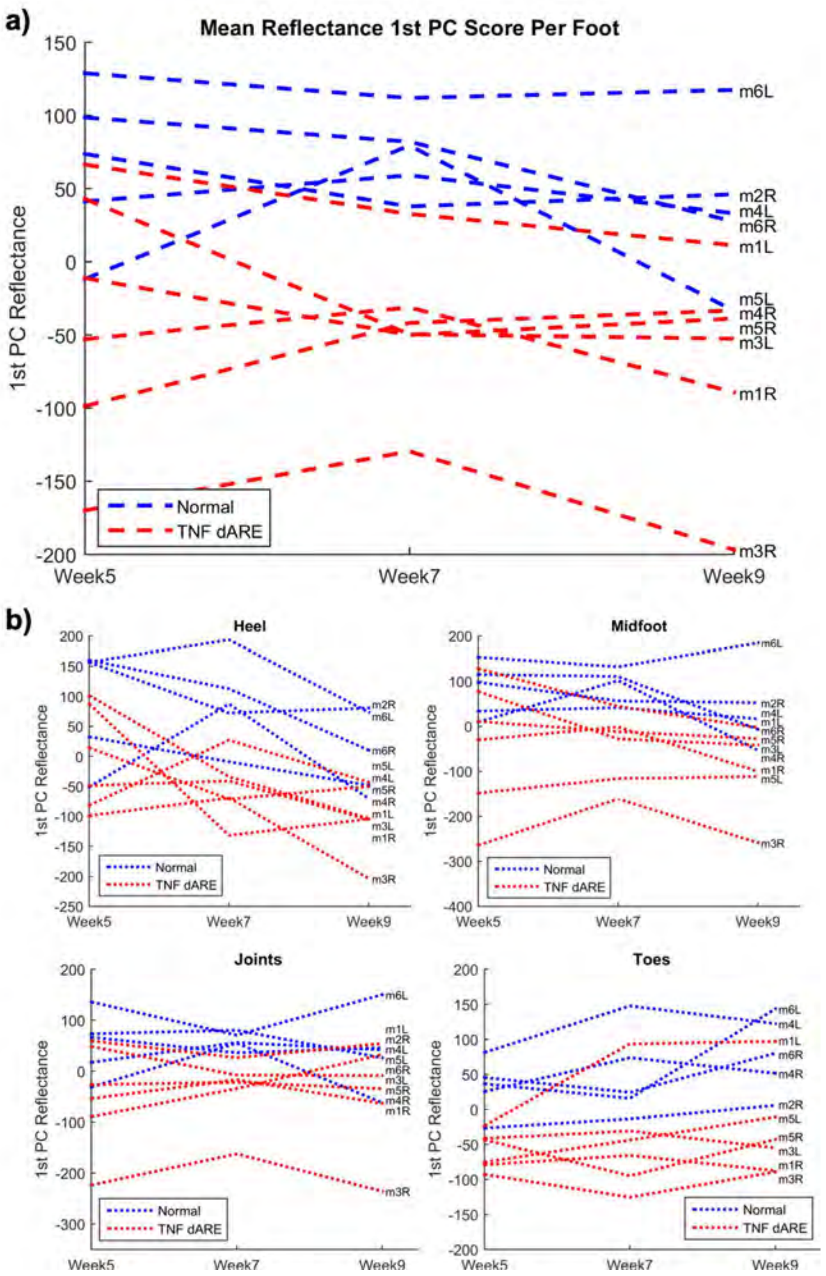

Figure 53: Progression of the 1st principal component scores from reflectance spectral data for TNF dARE mice hind paws from six 5-week to 9-week old female mice, N=3 TNF dARE and N=3 normal, with two paws imaged per mouse giving a total of eleven values (M2L removed due to failiure of spectral imaging). a) Mean reflectance 1st PC scores from 5 weeks to 9 weeks of age for each individual paw from a sample of three TNF dARE mice (red) and three Normal controls (blue). Mice are indexed accoring to number and left/ right paw on the right of the graph b) Mean reflectance 1st PC scores from 5 weeks to 9 weeks of age for each area of each individual paw from a sample of 3 TNF dARE mice and 3 normal controls.

### *6.4.1.2.2* Correlation with Other Indicators of Arthritis

#### Manual Scoring

Clinical scoring was performed once weekly over the five weeks in a blinded randomised manner. Figure 54a shows the mean 1st principal component reflectance score per mouse from the 3 imaging sessions and Figure 54b shows the manual scores for the weekly timepoints.

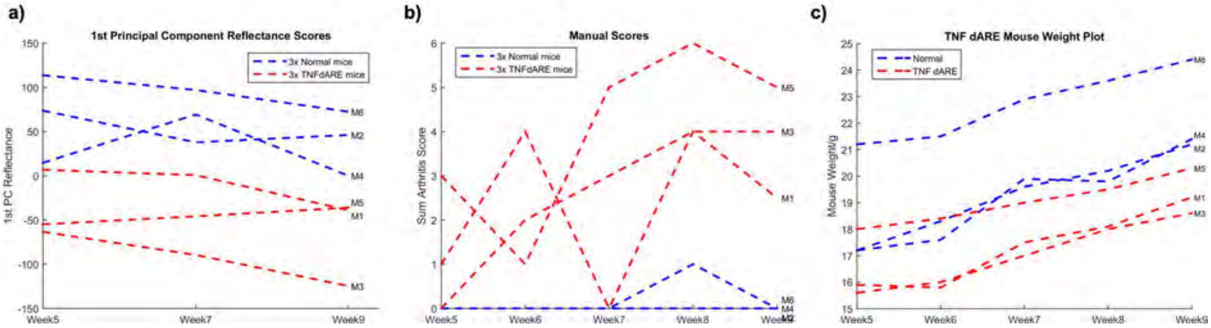

Figure 54: Reflectance score, manual score and weight for TNF dARE mice from 5 weeks to 9 weeks. Scores from six 5-week to 9-week old female mice, N=3 TNF dARE and N=3 normal, imaging taken for two paws per mouse and averaged giving a total of six values. a) Mean reflectance 1st PC scores (across both hind paws) for each mouse (M1 – 6) in the longitudinal TNF dARE imaging experiment, imaging timepoints at week 5, week 7 and week 9. Disease status is indicated by the colour of the label (blue = normal, red = TNF +/dARE). Individual mice are indexed by number on the righthand side of the graph. b) Manual score for the same group of mice, scored weekly from 5 weeks to 9 weeks of age. Any score above 0 indicates arthritis symptoms detected by scoring method. c) Mouse weights taken at weekly timepoints from 5 weeks of age to 9 weeks.

There is noticeably less consistency in the manual scoring than in the scores from the 1st principal component of reflectance. Given that the TNF dARE is a genetic, chronic, and progressive model of arthritis, large fluctuations in the arthritis score are probably not representative of the severity of the symptoms. Pearson correlation analysis between the 1st PC scores, manual scores, and mouse weights show that only the correlation between 1st PC scores and weights is significant (p-values: weight vs PCA scores 0.0230, weight vs manual scores 0.4429, PCA scores vs manual scores 0.7234). Even with the benefit of additional parameters for assessment, clinical scoring assessed two arthritic mice to be normal, one at 5 weeks of age and one at 7 weeks in the longitudinal imaging experiment.

## Bone Erosion

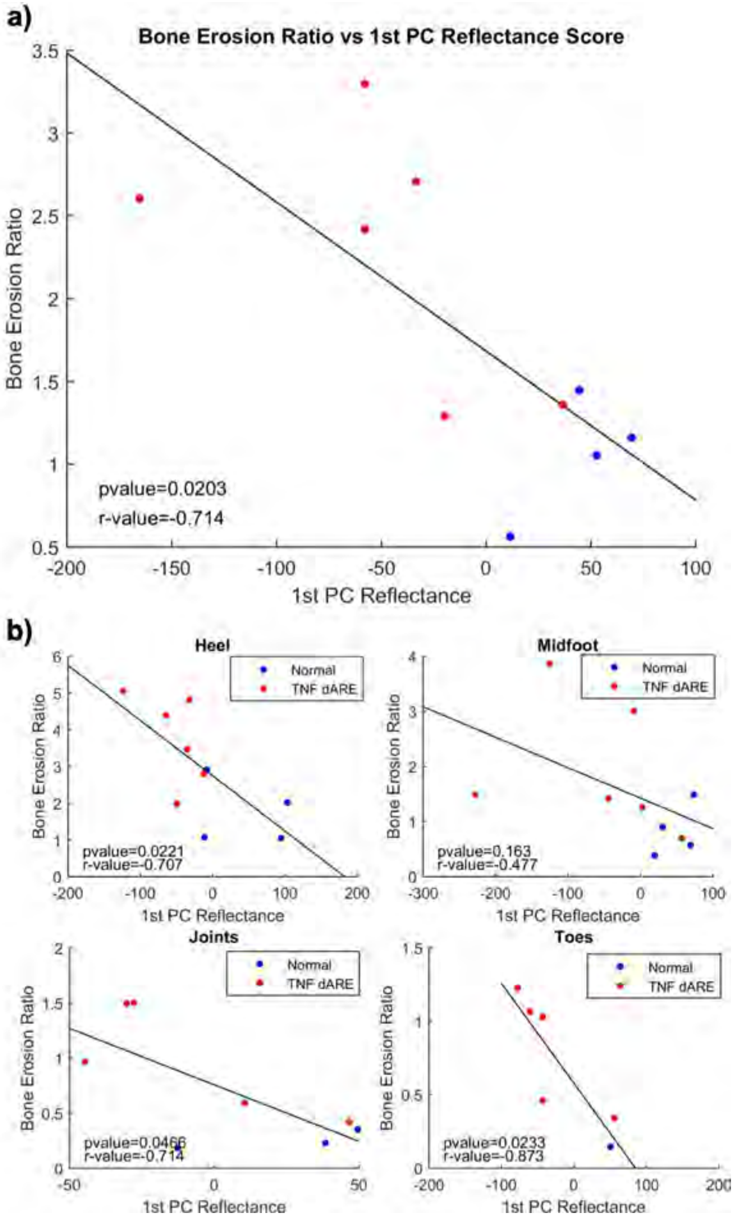

Figure 55: Comparison of the 1$^{st}$ principal component scores from reflectance spectral data vs the bone erosion scores from microCT for the TNF dARE mouse hind paws. Reflectance scores and bone erosion from six 5-week to 9-week old mice, N=3 TNF dARE and N=3 normal, with imaging and bone erosion scores performed for two paws per mouse giving a total of ten values (M2L imaging failed, M6L bone erosion registration failed, <10 values for individual areas where individual bones failed to register). P-values and r-values calculated by Pearson correlation analysis. a) Comparison of 1st principal component reflectance score (meaned across the measurement timepoints) against the mean bone erosion ratio produced by MArthA, for each individual foot. b) The 1st principal component reflectance score for each individual area compared against the mean bone erosion ratio for each area.

For comparison with the results of bone erosion calculated by MArthA, the 1st principal component reflectance scores were averaged over the three imaging sessions to take into account disease progression. Figure 55a displays the results for the average score per paw versus the bone erosion ratio. Figure 55b shows how the principal component and erosion scores compare per region of the foot.

As with the 12 week imaging experiment for the TNF dARE model, a significant correlation was found between the bone erosion ratio and the 1st PC reflectance score, indicating a relationship between the spectral deviation away from the spectral response of the normal mice and the degree of bone erosion in the joints.

#### 6.4.1.3 TNF dARE Imaging Discussion

The imaging experiments of the TNF dARE model have shown a consistent pattern of spectral change with the onset of arthritis symptoms in the hind paws. Principal component analysis of spectral data from the TNF dARE mouse model of arthritis was able to isolate the variation in groups of spectral data and provide a useful metric for the spectral variation relative to the group of spectra. The spectral score for the 1st principal component has been found to correlate significantly with several alternative indications of arthritis symptom progression, suggesting that the physiological changes that influence the spectral response of the tissue are relevant to the pathological progression of arthritis. Multispectral imaging also provides a more detailed dataset than manual scoring and correlates better with alternative pathological measures such as degree of bone erosion and histological evidence of inflammation.

Progression of the spectral scores over time were not obvious from the experiments in section 6.4.1.2. However, it was a small sample set so the data were sensitive to outliers and it may be that progression in spectral score would have been detectable over a longer timescale.

Both experiments detailed above found that spectral variation was apparent among the group of normal mice as well. Although the mice are the same age, sex and from the same genetic background, small differences in their physical size and tissue composition are expected, potentially resulting in the spectral variation seen. The amount of variation between the healthy mice could be interpreted as an indication that the variation in the TNF dAREs may not be a direct result of arthritis symptoms, however, the scores from the experiments show good correlation with other arthritis markers. It is possible that differences present in the tissue of the healthy mice may predispose certain mice to worse arthritis symptoms.

Given the spectral changes predicted by the Monte Carlo arthritis model, it is likely that decreased oxygen saturation of haemoglobin is resulting in the consistent decrease of reflectance and transmittance seen affecting the 600 to 800nm spectral region. The relatively consistent decrease in reflectance affecting all wavelengths may be due to increased blood concentration, however, other factors which could produce a similar effect would be changes in the scattering properties of the tissue or the surface of the paw being imaged at an angle.

Of all the arthritis assessment methods used in the experiments, histology scoring is the most directly related to soft tissue pathology. Whilst the number of samples was low, the experiments were indicative that inflammatory infiltrate and bone erosion visible on the slides correlated with the spectral score. An interesting experiment to conduct in future would be to investigate whether spectral changes were apparent in the tissue before the onset of joint erosion, when inflammatory infiltrate became detectable in the histology, since physiological changes affecting spectral response such as hypoxia and increased blood flow are likely to begin with inflammatory cellular infiltrate. Other possibilities would be comparing the spectral score to the amount of inflammatory infiltrate to see if there was a correlation there.

Bone erosion is an important topic in the study of RA as the gradual destruction of the joints contributes to limiting the abilities and quality of life of people with RA. The presence of focal bone erosions near the joint can be used as a marker for response in therapeutic intervention and the success of biologic drugs is in part due to slowing the progression of erosions (197,198). The correlations found between the spectral scores and the bone erosion may therefore be a useful measurement in these kinds of studies.

### 6.4.2 K/BxN Serum Transfer Model Imaging

As described in section 2.4, different murine models of rheumatoid arthritis can have different physical manifestation of symptoms. The experiments described in this section detail the results of multispectral imaging for the K/BxN serum transfer model of arthritis. Details of arthritis induction in the mice used in the experiment are discussed in section 6.2.1.2.

A group of four mice were imaged with one normal control and three symptomatic K/BxN serum transfer mice. The mice were scored according to the clinical scoring protocol, including calliper measurements of the feet for assessing the degree of swelling.

### 6.4.2.1 Reflectance

Figure 56 displays the normalised mean reflectance spectra together with the standard deviation for the normal and the K/BxN serum transfer mice. As with the TNF dARE experiments, Figure 57a displays the 1st principal component scores from the raw reflectance data, along with a statistical shape model describing the variation in the dataset and the superimposed raw spectral data (Figure 57b).

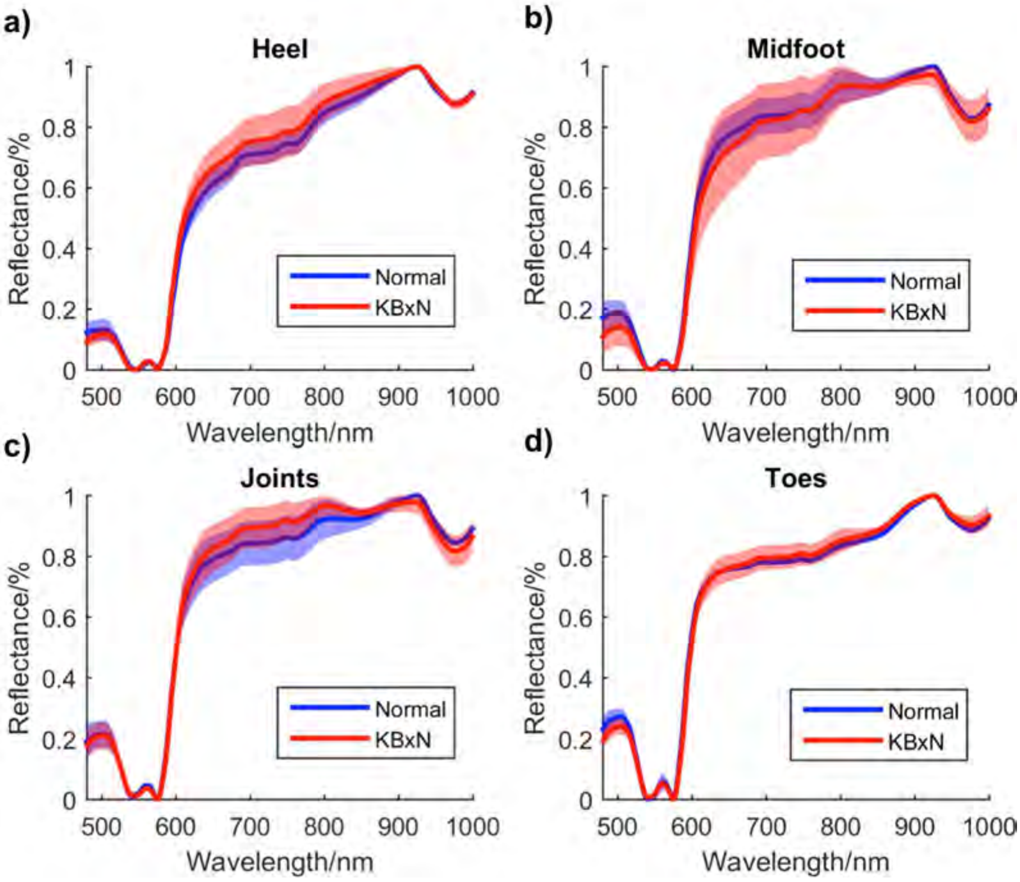

Figure 56: Min-max normalised reflectance spectral data from four areas of the K/BxN ST mouse hind paw from four mice, N=3 K/BxN ST and N=1 normal, with two paws imaged per mouse giving a total of eight spectra. Mean spectra for the normal group are displayed In blue with standard deviation shown as a pale blue shaded region and in red for the K/BxN ST data. a) Average normal vs average K/BxN ST reflectance spectra for the heel region of the hind paw from a group of 4 mice. b) Average reflectance min-max normalised spectra for normal vs K/BxN ST for the middle region of the foot. c) Average reflectance min-max normalised spectra for the joints region of the foot. d) Average min-max normalised spectra for the toes region of the foot.

Testing the significance of the RMS distance with 2-factor student t-test between all the spectra of the normal and K/BxN serum transfer groups showed that only the toes

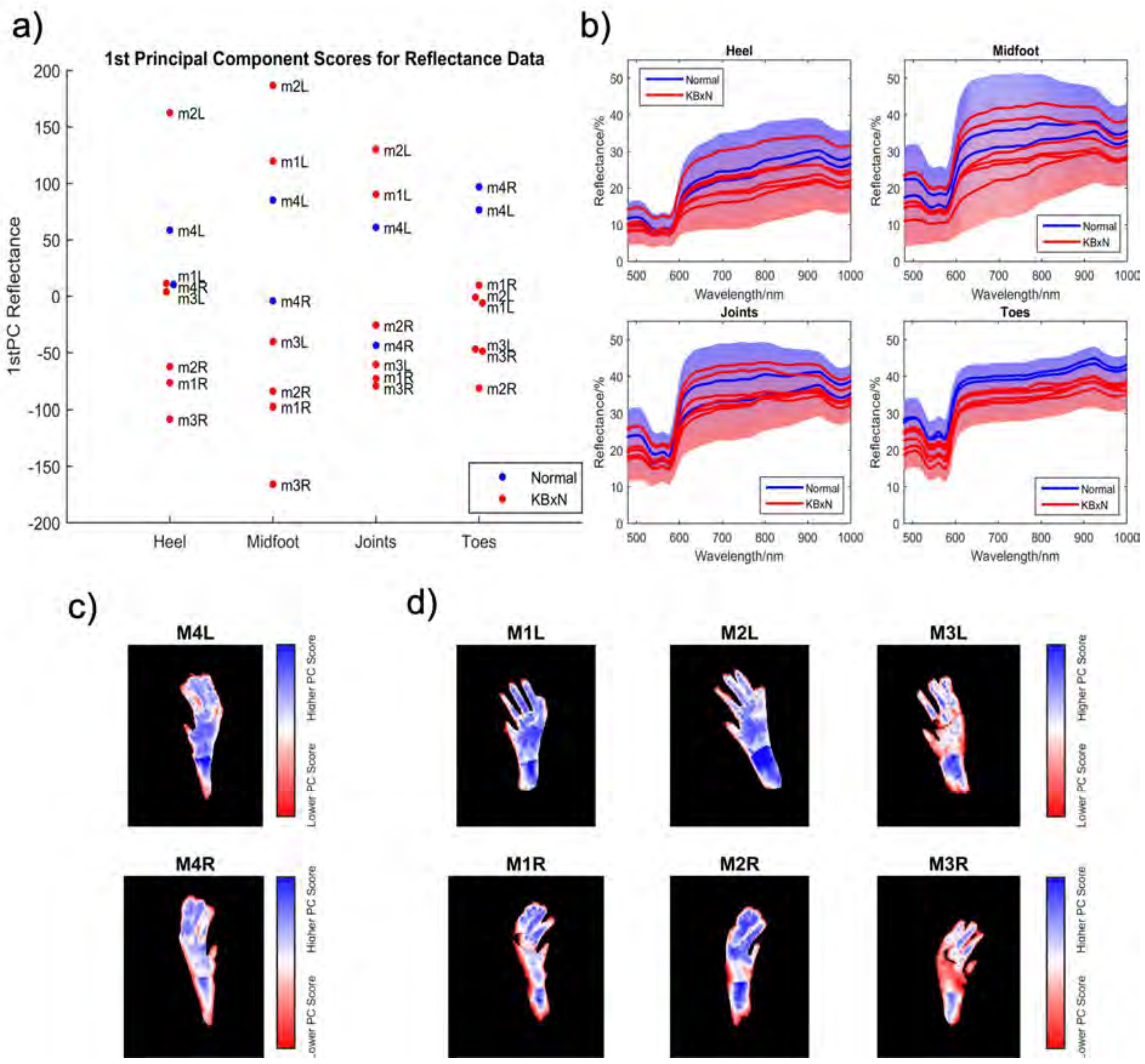

Figure 57: Results from principal component analysis of reflectance spectral data from four areas of the K/BxN ST mouse hind paws from four mice, N=3 K/BxN ST and N=1 normal, with two paws imaged per mouse giving a total of eight values. a) Score along the 1st principal component for the reflectance data for each area of the foot. Labels indicate mouse number and left/right hind paw. b) Reflectance spectra for each hind paw from the group of four mice, separated into 4 anatomical regions. The raw spectra have been superimposed on a Statistical Shape Model of the variation contained by the 1st principal component shown as a shaded region c) Normal mouse mapping of 1st PC score value for individual pixels of the four selected regions of the paw. d) K/BxN ST mice mapping of 1st PC score value for individual pixels of the four selected regions of the paw.

area was significant for this experiment (p-value heel: 0.0969, midfoot: 0.228, joints: 0.629, toes: 0.0014).

In common with the TNF dARE model, there was variation in the spectral shape around the 600 to 800nm region which relates to oxygen saturation. However, the effect appeared less predictable, with some of the mice showing greater reflectance in this region and some showing less.

Initial review of the PCA scores for the K/BxN serum transfer reflectance data shows that the scores for the normal mice vs the K/BxN serum transfer mice do not form distinct groups, like those seen in the TNF dARE experiments. However, as noted previously, this arthritis model exhibits symptoms less symmetrically than the TNF dARE and it is possible that certain paws may remain unaffected by arthritis symptoms. Correlation analysis with the calliper scores in section 6.4.2.3 support this theory. As with the TNF dARE model, the 1st principal component of reflectance described most of the variation in the dataset with an average percentage of 96.8% for the four areas of the feet.

#### 6.4.2.2 Transmittance

Figure 58 shows the mean normalised transmittance data for the normal vs K/BxN serum transfer mice with the standard deviation indicated by the coloured region around the mean spectra. Figure 59 shows the scores for each spectra resulting from performing PCA on the normalised transmittance data.

As with the reflectance data the K/BxN serum transfer paws and the normal controls did not form distinct groups, but there was correlation in the scores for reflectance and transmittance in all areas except the joints. In general, transmittance was lower in the 600nm to 800nm region of the spectrum for the K/BxN ST mice, in common with the TNF dARE mouse.

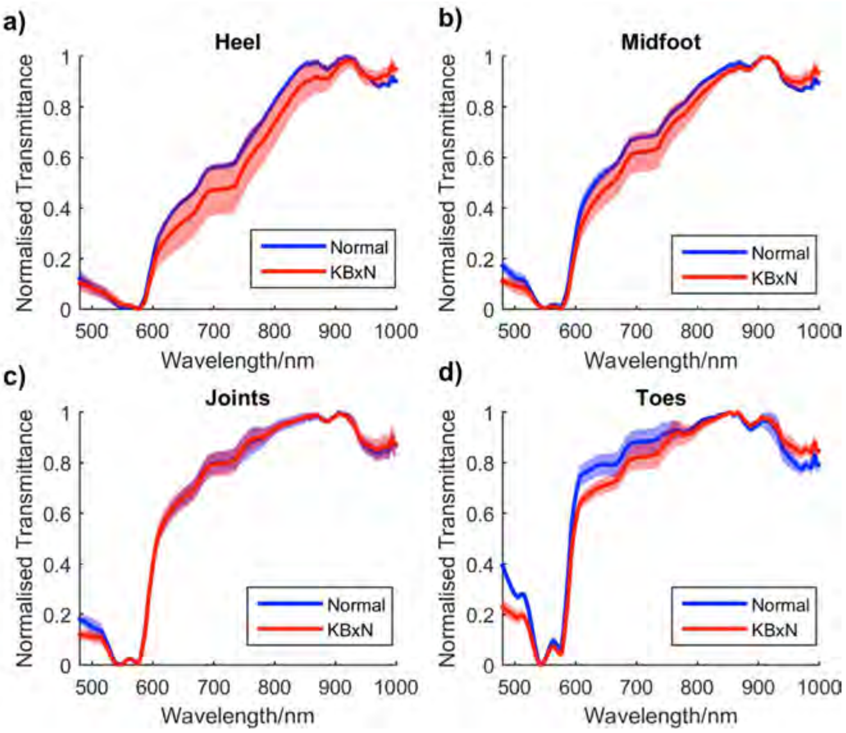

Figure 58: Min-max normalised transmittance spectral data from four areas of the K/BxN ST mouse hind paws from four mice, N=3 K/BxN ST and N=1 normal, with two paws imaged per mouse giving a total of seven values (M1L imaging failed due to movement of the mouse during imaging exposure). Mean spectra for the normal group are displayed In blue with standard deviation shown as a pale blue shaded region and in red for the K/BxN ST data. a) Average normal vs average K/BxN ST transmittance spectra for the heel region of the hind paw from a group of four mice. b) Average transmittance min-max normalised spectra for normal vs K/BxN ST for the middle region of the foot. c) Average transmittance min-max normalised spectra for the joints region of the foot. d) Average min-max normalised spectra for the toes region of the foot.

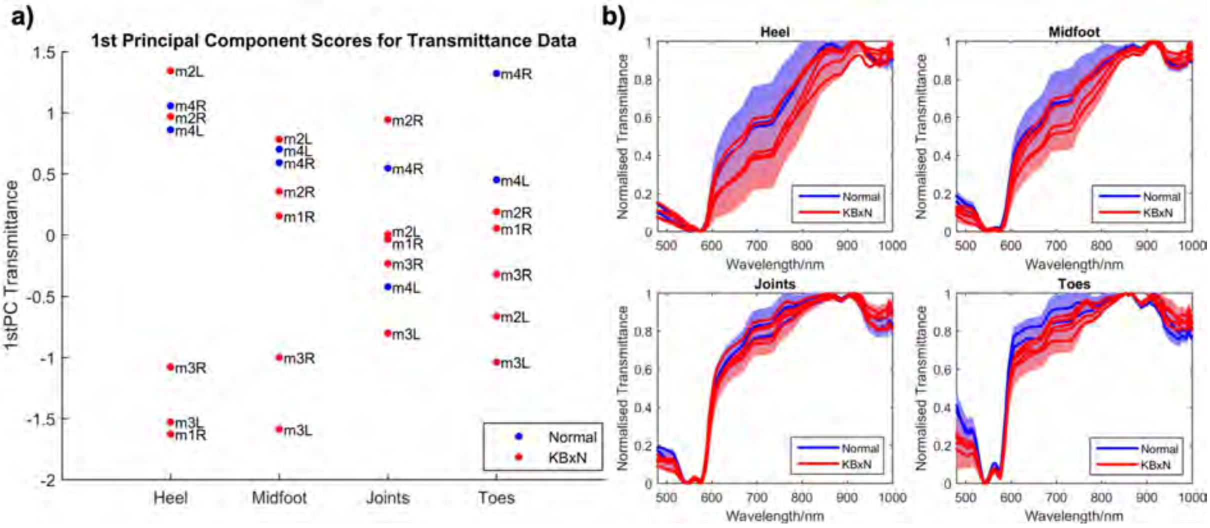

Figure 59: Results from principal component analysis of transmittance spectral data from four areas of the K/BxN ST mouse hind paws from four mice, N=3 K/BxN ST and N=1 normal, with two paws imaged per mouse giving a total of seven values (M1L removed due to movement of the mouse during imaging). a) Score along the 1st principal component for the normalised transmittance data for each area of the foot. b) Normalised transmittance spectra for each hind paw from the group of four mice, separated into four anatomical regions. The raw spectra have been superimposed on a statistical shape model of the variation contained by the 1$^{st}$ principal component.

Testing the significance of the RMS distance for the normalised transmittance spectra of the diseased mice versus the normal mice showed that the midfoot and toes were significant (p-value heel = 0.416, midfoot = 0.0470, joints = 0.942, toes = 0.0132).

### 6.4.2.3 Correlation of Spectral Variation with Other Indicators of Disease

#### Calliper Measurements and Manual Scoring

K/BxN serum transfer mice are an inflammatory model of arthritis and exhibit swelling of the paws which can be measured by callipers. In Figure 60, the scores for each paw resulting from PCA of the reflectance and transmittance spectra have been compared to the dorsal to ventral width of the mouse hind paws for the reflectance (Figure 60a) and transmittance (Figure 60b) principal component score average per paw.

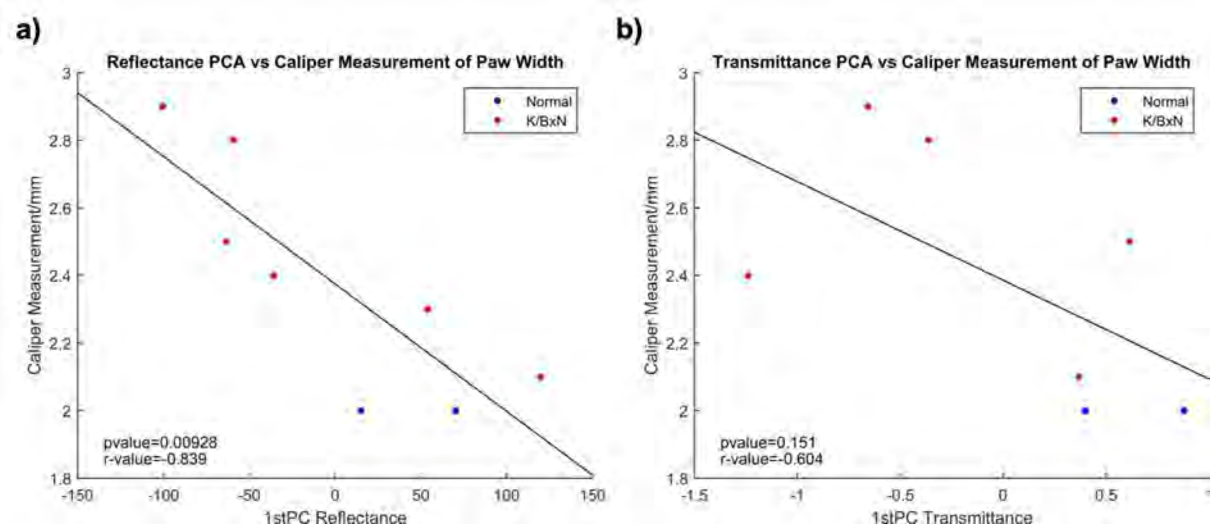

Figure 60: Comparison of the 1$^{st}$ principal component scores from reflectance and transmittance spectral data vs the calliper measurements for the K/BxN ST mouse hind paws from four K/BxN ST mice, N=3 K/BxN ST and N=1 normal, with two paws imaged per mouse giving a total of eight values for reflectance and seven values for transmittance (M1L imaging failed due to movement of the mouse during imaging exposure). P-values and r-values calculated by Pearson correlation analysis. a) 1st principal component scores for reflectance have been compared to the width of the hind paws in mm. b) 1st principal component scores for transmittance have been compared to the width of the hind paws in mm.

A significant correlation was found between the reflectance principal component score and the paw width suggesting that spectral change in the reflectance response of the model is concurrent with swelling.

No correlations were found comparing the PCA scores with the manual scores per mouse (manual scores M1: 13, M2: 9, M3: 12, M4: 0), but PC scoring and manual scoring both rated mouse 2 as least affected, and mouse 3, which was given the highest manual score for swelling and discolouration in the hind paws (M1: 4, M2: 3, M3: 5, M4: 0), was the most affected according to the 1st principal component reflectance scores.

When the significance of the relationship between calliper measurements and 1st principal component score is tested after removing the normal controls, it remained significant for reflectance at p-value = 0.0169, but not for transmittance (p-value = 0.558).

#### 6.4.2.4 K/BxN Serum Transfer Discussion

Although the K/BxN serum transfer model has a different appearance to that of the TNF dARE, the PCA method of analysis was flexible enough to distinguish the spectral effects of arthritis when a normal control is included. The spectral results were less consistent for the K/BxN ST mice reflecting the less predictable, less symmetric nature of the model compared to the TNF dARE. Some similar trends were seen in the spectral reflectance and transmittance data, such as a relative decrease in reflectance and transmittance in the 600nm to 800nm spectral region, but the RMS difference between the mean of the arthritic group and the mean of the normal group was different for the TNF dAREs and the K/BxN STs (shown in section 8.A7), where the K/BxN ST model had a relatively larger spectral change in the 800nm to 1000nm wavelengths. This could be due to the difference in the phenotype of the arthritis models. For the K/BxN ST model, the 4th principal component also appeared to separate the arthritic mice from the normal mice suggesting that the spectral change due to arthritis was not completely captured within the 1st PC for this model.

### 6.4.3 Feature Mapping

#### 6.4.3.1 LDA Mapping

Multispectral data inherently provide information about relative concentration of chromophores in biological tissue. For the multispectral images taken in section 6.4.1.1 and section 6.4.2, spatial maps of the chromophore features were constructed. They display oxygen saturation, BVF in the deeper tissues, and BVF in the more superficial tissue for the TNF dARE mice in section 6.4.1.1, and for the K/BxN ST mice in section 6.4.2.

Axes describing the chromophore concentration were isolated from simulated data using linear discriminant analysis (LDA) described in section 6.2.7. A library of Monte Carlo tissue spectra (Figure 61) from the mouse paw model (section 3) were classified according to particular chromophore changes. The parameter values input into the model were used to label each spectra as group one or two depending on the concentration of the chosen chromophore (group 1 high, group 2 low and mean). LDA was then performed to find axes discriminating the spectral changes. For example, spectra where oxygen saturation in the muscle layer of the model was altered were classified into two classes of oxygen saturation, regardless of other changes in the tissue. LDA of the data then identified the spectral variation corresponding to the increasing oxygen saturation in the muscle.

To generate the spectra, GPUMCML (199) was run iteratively for every possible combination of the parameters shown in Table 3, in total the number of spectral simulations was 13122 and the reflectance and transmittance spectra from each run were saved. Figure 61 displays the mean spectra and the standard deviation for reflectance and transmittance. Given the additional computational demand of the full simulation, a GPU parallelised version of the MCML code was used in combination with a Tesla C2070, or GeForce GTS 450 GPU card.

Table 3: Parameters sampled by the Monte Carlo model

| **Dermis BVF** | **Muscle BVF** | **Dermis Depth/ µm** | **Muscle Depth/ µm** | **Melanin Conc** | **Dermis SO2** | **Muscle SO2** | **Muscle Water Conc** | **Bone Depth/ µm** |
|---|---|---|---|---|---|---|---|---|
| 0.04, 0.08, 0.12 | 0.04, 0.08, 0.12 | 90, 100, 110 | 100, 250, 500 | 0.0087, 0.087 | 0.3, 0.48, 0.7 | 0.35, 0.49, 0.84 | 0.63, 0.79, 0.95 | 100, 300, 600 |

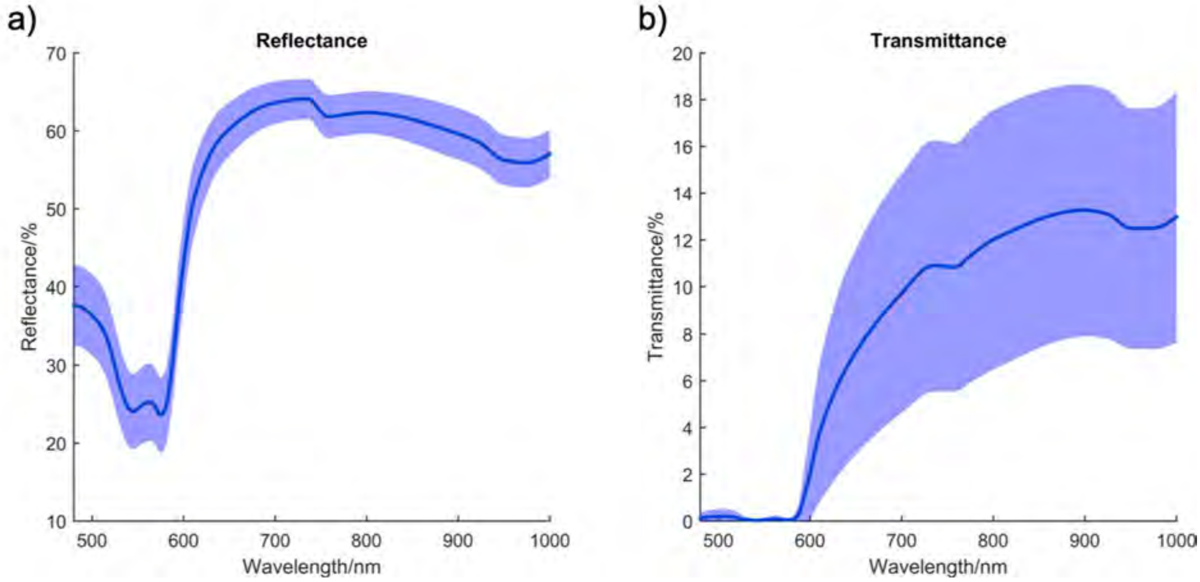

Figure 61: Reflectance and transmittance spectra for 13122 iterations of the Monte Carlo hind paw model with varying parameters. The blue line shows the mean spectrum and the paler blue shows the standard deviation. a) The mean and standard deviation for the reflectance spectra. b) The mean and standard deviation for the transmittance spectra.

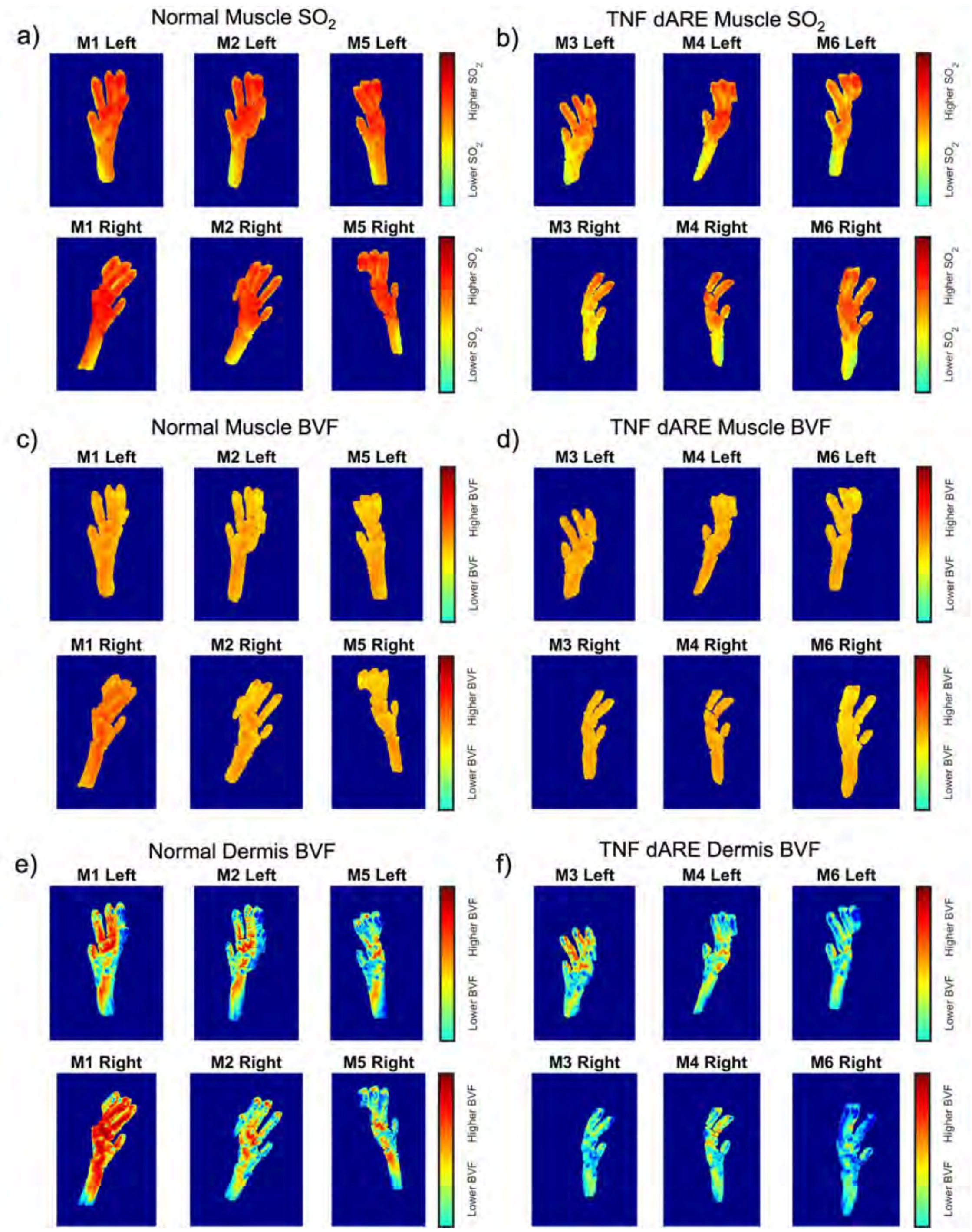

Figure 62: Feature maps for the TNF dARE mice using linear discriminant analysis of Monte Carlo modelled spectra to define axes relating to muscle oxygen saturation, muscle blood volume fraction and dermis blood volume fraction. a) and b) Normal control littermates (a) and TNF dARE$^{+/-}$ (b) mouse hind paws from the experiment described in section 6.4.1.1. Individual pixels in the image are scored according to an axis defined by LDA, isolating the spectral effects of oxygen saturation in the muscle layer of the Monte Carlo model. c) and d) As above, normal control littermates (c) and TNF dARE$^{+/-}$ (d) mouse hind paws. Individual pixels in the image are scored according to an axis defined by LDA, isolating the spectral effects of changing BVF in the muscle layer of the Monte Carlo model. e) and f) As above, normal control littermates (e) and TNF dARE$^{+/-}$ (f) mouse hind paws. Individual pixels in the image are scored according to an axis defined by LDA, isolating the spectral effects of changing BVF in the dermis layer of the Monte Carlo model.

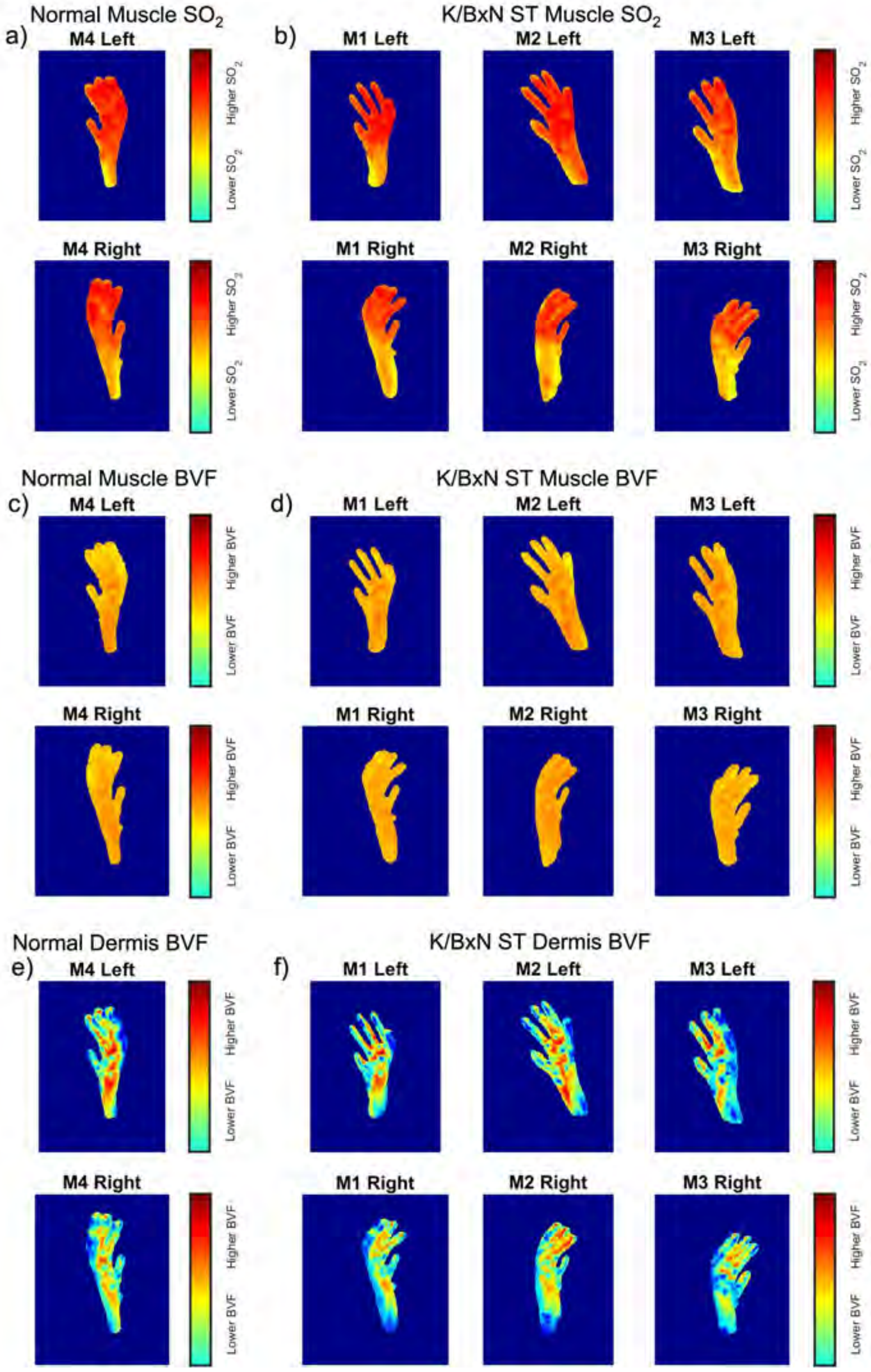

Figure 63: Feature maps for the K/BxN ST mice using linear discriminant analysis of Monte Carlo modelled spectra to define axes relating to muscle oxygen saturation, muscle blood volume fraction and dermis blood volume fraction. a) and b) Normal (a) and K/BxN serum transfer (b) hind paw images from the experiment described in section 6.4.2. Individual pixels in the image are scored according to an axis defined by LDA, isolating the spectral effects of oxygen saturation in the muscle layer of the Monte Carlo model. c and d) As above, normal (c) and K/BxN serum transfer mice (d). Individual pixels in the image are scored according to an axis defined by LDA, isolating the spectral effects of BVF in the muscle layer of the Monte Carlo model. e and f) Normal (e) and K/BxN serum transfer mice (f). Individual pixels in the image are scored according to an axis defined by LDA, isolating the spectral effects of BVF in the dermis layer of the Monte Carlo model.

In Figure 62 and Figure 63, the spectra from individual pixels are scored according to the LDA axes and colour mapped. Several features of the mouse hind paws could be seen in a general observation of the maps. Areas of higher blood concentration appearing in the muscle and dermis BVF maps appeared to show the pattern of larger blood vessels in the tissue. The footpads could be seen as areas of lower blood concentration but high oxygenation and the heel, where large veins are close to the tissue surface, appears to be generally less oxygenated than the central region of the foot and the toes. There was also notable variation among the healthy mice, particularly for mouse 1 in Figure 62 where blood concentration appeared to be higher, most strikingly in the dermis BVF map. It is unclear what the origin of the difference was. It may be a result of a temporal change caused by a higher temperature of the warming pad or a longer anaesthetic time, or it could be an anomaly in the spectral data.

For the TNF dARE mice (Figure 62), lower oxygenation could be seen particularly in the heel region of the foot, but extending in to the midfoot, joints and toes regions for several of the mice. No clear differences could be seen when isolating the blood concentration in the muscle layer, however, the dermis map appears to show lower blood concentration in the TNF dARE's. For the most part, the footpads appear to remain well oxygenated and there is still a gradient of oxygenation visible from the heel to the toes.

For the K/BxN ST mice (Figure 63), the worst affected paws according to the calliper measurements were the right side paws for all of the mice. The hypoxia map data appear to reflect these scores with larger regions of lower oxygen saturation visible in the heels and midfoot. The effect of arthritis on blood concentration is not completely clear. Even though the K/BxN ST mouse is of a more ‘inflammatory’ phenotype, the presence of blood vessels makes it difficult to judge whether there is an increase in blood concentration locally in the arthritic tissue. There may be a suggestion of increased BVF in the muscle BVF map of a mouse visually affected by swelling of the heel area such as the right paw Mouse 2, but more research would be needed to establish a relationship.

Overall, according to this method, the effects of arthritis on chromophore concentrations of haemoglobins do not appear to be highly localised to joint regions and the most notable effect for both arthritis models is decreasing haemoglobin oxygenation. These maps are based on a spectral changes calculated from Monte Carlo models and unfortunately cannot be evaluated against a ground truth. They should however provide some indication of relative chromophore change where unique spectral effects due to chromophore changes can be determined.

#### 6.4.3.2 Spectral Angle Mapping

An alternative method for mapping the spectral data from the mouse paw figures is presented below in Figure 64. Images of the TNF dARE paws from section 6.4.1.1 have been colour mapped according to the angle between tangential lines of the spectra at 670nm and 585nm. Monte Carlo modelling of the mouse hind paw shows this angle increases with decreasing oxygen saturation (Figure 17, Figure 19, Figure 20c). This method of mapping the spectra is independent of the Monte Carlo model, obtaining the angle measurements directly for the spectra associated with individual pixels.

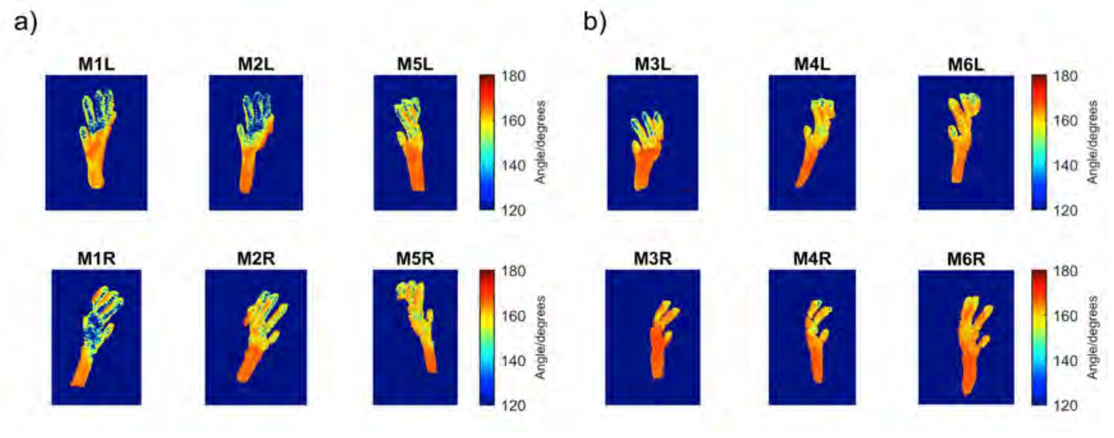

Figure 64: Spectral angle maps produced from calculating the angle of intersecting tangents to the spectra at 670nm and 585nm for TNF dARE mice. a) Maps of the normal mouse hind paws produced from calculating the angle of intersecting tangents to the spectra at 670nm and 585nm. Increases in this angle were found to be related to decreasing oxygenation in the Monte Caro model. b) Maps of TNF dARE mouse hind paws produced from calculating the angle of intersecting tangents to the spectra at 670nm and 585nm.

It is interesting to note that angle maps shown in Figure 64 show changes consistent with the changes predicted by LDA mapping where the TNF dARE mouse present a larger spectral angle indicative of lower oxygenation than in the normal mice. They are also consistent with the 1st PC score mapping in Figure 44 showing that some paws are more spectrally heterogeneous and some show more constant spectral values. Suggestions of anatomical features such as the veins in the heel can be seen for some of the mice.

## 6.5 Discussion

### 6.5.1 Discussion of Results

The results of this chapter indicate that adopting multispectral imaging into the assessment of RA models could have potential benefits. A method of accurately gauging the severity of mouse symptoms *in vivo* could be a useful addition to experiments such as therapeutic intervention studies, for which progression of arthritis symptoms could be traced more accurately over the timeframe of the experiment. The results also indicate that arthritis symptoms could potentially be picked up earlier than by manual scoring which would be useful for research following the early development of arthritis symptoms. There is also the matter of mouse welfare in RA experiments. Mice are generally given analgesia when they exhibit signs of pain, for example limping or reduction in voluntary movement, however, it is known that mice disguise pain (200,201), for which an accurate measure of arthritis progression could guide the introduction of analgesics. Also, many studies assume that a group of arthritic mice are equally affected by disease, or use large numbers to get significant results, so better grading of the severity of arthritis could lead to more rigorous experimental analysis and potentially reduce mouse numbers needed for a significant outcome.

This work would benefit from future experiments to further investigate the capacity of spectral imaging for assessment of mouse arthritis. It would be interesting to image more mouse models of RA, particularly for the recovery models where it would be useful to see if the spectral effects resulting from arthritis abate with the reduction in inflammation. If the technique proved valuable in the hind paws, it could be extended to include the front paws as well.

Principal component analysis was a good method of capturing the spectral change resulting from arthritis and reducing the dimensions of the data to a single dimension giving a useful indication of spectral variation. However, applying PCA to small experiments such as those in this chapter will only give a score relative to the other spectra along the axis of the first eigenvector for the dataset. In future, if a large dataset were to be collected from different mouse models, it may be possible to define a global coordinate system to grade severity of arthritis symptoms from spectra in a way that would allow comparison between experiments, and possibly between different arthritis models. This work has focused on scoring the mice rather than classifying them because genotyping already exists for identifying arthritic mice in the genetic models and induced models can be marked by ear tagging to be made identifiable.

### 6.5.2 Limitations

The correlation analysis with other indicators of arthritis assumes a linear relationship with spectral perturbation which may not be the case. If more data were gathered, the nature of these relationships could be fully investigated.

One of the main difficulties with imaging the mouse hind paw with the multispectral imaging system described in chapter 4.3 is the difficulty in getting the mouse hind paw to lie reliably flat. The knee joint obstructed the limb from being extended backwards sole-upwards on a flat surface, particularly for the arthritic mice whose joints may already be less flexible. In some cases this resulted in the foot being tilted whilst imaged. This particularly affected the transmittance data, where the light path through the tissue could become much longer if the paw was tilted, resulting in more variation in the measurement. Normalising the transmittance data appeared able to correct for this to some extent, but reflectance data consistently produced better correlation with other indicators of arthritis and transmittance data were unable to separate the normal mice from the TNF dARE mice in section 6.4.1.2.

### 6.5.3 Conclusion

As discussed in section 2.5.1.2, multispectral imaging is a novel method of analyzing arthritis symptoms in mice. PCA is often used in multispectral imaging for unmixing spectral signatures in the imaging of heterogenous materials (202–205). Likewise LDA dimensionality reduction has been used in classifying multispectral image data (206–208). However, the particular application of these methods to the data can vary. In general, they are applied directly to image data. In this research, PCA was applied to selected groups of spectral data where the variation due to heterogenous tissue changes was removed as a factor and therefore the spectral features introduced by arthritis symptoms were isolated in the 1st principal component as the primary cause of variation. The LDA model was applied directly to image data but only after training on MCML model spectra making it a supervised method of isolating chromophore concentration-induced spectral changes. The advantage of multispectral imaging data is the ability to apply multivariate analysis methods and explore more of the tissue parameters as in section 6.4.3. In comparison to other papers, as discussed in section 7.2, this work also showed success across multiple mouse models.

The following chapter concludes the outcomes of this research project and discusses future possibilities for research in the field of multispectral imaging for mouse models of rheumatoid arthritis.

# 7 Conclusions and Future Work

## 7.1 Summary of Findings

*In vivo* assessment of mouse models of rheumatoid arthritis is an area for which the capability of several existing imaging tools has been evaluated in literature, but the practicality and accuracy of such techniques is debatable. It is also clear that there are issues associated with relying on manual scoring methods such as the one described in section 2.5.1.1 due to bias and inaccuracy. However, given the notion of discoloration included as a part of the scoring criteria, spectral measurements were proposed as a method of capturing the natural change in the tissue with the development and progression of arthritis symptoms. The aim of this thesis was therefore to investigate the ability of multispectral imaging methods to detect native changes in the tissue driven by joint inflammation. To this end, several novel experiments were carried out to evaluate the potential for multispectral imaging as an arthritis assessment method.

Prior to imaging experiments with live mouse models, Monte Carlo simulations of the mouse hind paw were used to investigate the effect of changing concentrations of biological chromophores in the tissue in line with predictions informed by current literature. Changing blood volume fraction, blood oxygen saturation, and water percentage were found to contribute individually to reflectance and transmittance spectral changes in an 'arthritic' model. The spectral response of the simulated tissue also varied depending on the depth of the tissue layer where the changing chromophore concentration was modelled. These *in silico* experiments suggested spectral changes could be detectable in live mouse models.

Following on from these simulated experiments, reflectance and transmittance spectroscopy of the hind paw successfully detected significant differences between normal mice and TNF dARE arthritic mice. Promising results were also obtained for CIA mice. Whilst spectroscopy was not found to be the most reproducible or easily implemented method for obtaining spectral data from mouse hind paws, these experiments confirmed that differences in the tissue reflectance and transmittance were detectable *in vivo*.

To gain information about tissue location and investigate whether arthritis symptoms could be further localised to areas of tissue using spectral imaging, this project developed a non-contact multispectral imaging system specifically designed to investigate the reflectance and transmittance spectra of mouse hind paws (Chapter 5). A system of sequential illumination with successive wavelengths of light was designed where the illumination could be manually directed to the surface of the underside of the paw in reflectance mode or redirected to illuminate the paw from below without having to move the mouse. A novel method using polarisers was employed to ensure the quality of the transmittance image data.

Multispectral imaging of mouse hind paws detected reflectance and transmittance changes concurring with arthritis symptoms, with some degree of anatomical localisation. Analysing the spectra separately for four regions of the paws using Principal Component Analysis, the first principal component was found to isolate the spectral effects of arthritis symptoms. The scores pertaining to individual spectra could then be used to evaluate the individual mice relative to others in the experiment. The first principal component scores for the TNF dARE arthritis model were found to correlate significantly with bone erosion ratio results from microCT, blinded histology scoring, and the blinded manual scoring method. These results suggest that the degree of spectral change detected in multispectral data is related to the progression of arthritis.

The reflectance and transmittance spectra were found to vary across the paw due to the underlying anatomical structure. They differ between healthy mice and were perturbed by symptoms of arthritis. The nature of these changes is likely to involve multiple optical parameters, but trends in the spectral data suggest that decreased oxygen saturation is likely to be responsible for spectral changes in arthritic mice. It is also possible that increased blood volume fraction contributed to the more or less uniform decrease in reflectance, but separating this effect from scattering changes, or the difference resulting from imaging the uneven surface morphology, is complex and was beyond the scope of this thesis. Changes explicitly resulting from increased water percentage were also difficult to detect due to the low absorption in the wavelengths imaged and the decreased signal to noise ratio of measurements in the relevant spectral regions.

Multispectral imaging detected changes in spectral responses of the mouse hind paw at an early stage in arthritis development for the TNF dARE model, before clinical signs were manifest. Imaging results for the K/BxN serum transfer model of arthritis were analysed by the same PCA-based method and found to correlate with calliper measurements of the paw. This demonstrates that spectral changes occur in tandem with inflammatory events in the tissue. Overall, this research supports the use of multispectral imaging for the assessment of arthritis progression and severity in murine RA models.

## 7.2 Comparison with Literature

The requirement for a reliable method of tracking mouse arthritis symptoms is recognized (67,209), as it has potential to refine and reduce the number of mice used in experiments by overcoming issues introduced by inter-animal variation. As reviewed in section 2.5.1.2, different imaging techniques have been applied specifically to the *in vivo* assessment of murine models of RA including fluorescence imaging (92,210), infrared thermography (96), PET imaging (76,77), microMRI (80), and optical techniques (94). In some cases the authors propose these methods specifically for longitudinal assessment of arthritis symptoms in experiments (92,94,211). Other methods for assessment have included software for monitoring gait (212) and behaviour (213).

Whilst multispectral imaging of mouse arthritis models cannot be used to probe molecular mechanisms like fluorescence molecular tomography or PET, it has potential advantages in the context of monitoring murine arthritis. Primarily, multispectral imaging does not require the expensive equipment and imaging times necessitated in fluorescence imaging and PET. Although the system described in this thesis requires anesthetics and a seven-minute imaging time, Section 7.4.1 outlines potential methods for streamlining the system design so that the imaging time could be reduced and aesthesis might not be required.

Due to the ill-posed nature of the fluorescence inversion problem, fluorescence molecular tomography (FMT) is known to have errors associated with estimation of fluorophore concentration, requiring *a priori* structural data from integrated multimodal imaging systems to improve the estimation (214–216). Error in quantitation may ultimately result in inaccurate grading of arthritis symptoms. For multispectral imaging, no injections of molecular markers are required, minimizing pain and distress for the animals in the imaging protocol. And, in contrast to PET/SPECT/CT imaging methods, no harmful radiation is used. Another potential value of the multispectral imaging method is that it could benefit research focusing on the role of hypoxia or angiogenesis in rheumatoid arthritis and hence assist understanding of these mechanisms in the pathology of arthritis.

## 7.3 Wider Implications of Results

Several of the outcomes of this research are relevant to the field of arthritis research, particularly for *in vivo* imaging. For the multiplexed imaging of fluorophores *in vivo*, multiple filters are being incorporated into some imaging devices to extend into multispectral imaging detection (217–219). The multiple wavelengths assist in spectral unmixing of fluorophore signals and removal of tissue autofluoresence. If multispectral reflectance/transmittance data could be taken with the same device, then the natural perturbation of chromophores in the tissue may be found to correlate with molecular changes in arthritis.

This project found that changing tissue properties in the hind paws of the mouse significantly altered the reflectance and transmittance response of the tissue, indicating greater absorbance in the tissue in a wavelength-dependent manner. Given that quantitative FMT assumes similar tissue properties between subject mice, the outcome of this research is relevant to the results of fluorescence imaging studies, since the percentage of light reaching the fluorophore, and the percentage of Stokes-shifted light detected, is dependent on absorption by the tissue.

## 7.4 Future Work

### 7.4.1 Further Development of the Imaging System

In order to facilitate widespread adoption of the system, the multispectral imaging system could be redesigned to reduce the imaging acquisition time and cost.

Acquisition time could be decreased through several techniques (section 7.4.2) and a system could theoretically be set up which did not require anaesthetizing the animals. This would reduce distress and handling time and make more imaging timepoints possible over the timeframe of an experiment. Figure 65a shows a restraining device commonly used for administering tail injections. If a device like this were placed above an adapted multispectral imaging system, reflectance data could be taken for all 4 of the mouse paws simultaneously, as demonstrated in the schematic diagram in Figure 65b.

If a system could be designed which did not stress the animal, then the number of times the mouse could be assessed would essentially be limitless, which is not the case with most alternative imaging methods due to ethical reasons.

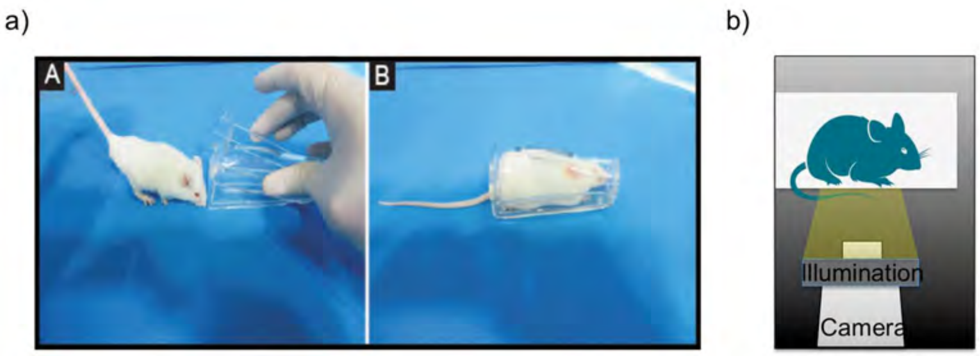

Figure 65: Potential set-up for a multispectral system which would not require anaesthetic. a) A picture of the type of device commonly used to restrain mice for administering tail injections. The source of the image is given in reference (220) b) A theoretical set up for a multispectral imaging system which could allow imaging of the arthritis models paws without the need for anaesthetics.

### 7.4.2 Potential Methods for Reducing Image Acquisition Time

#### *7.4.2.1* Reflectance vs Transmittance Imaging

The outcome of modelling the mouse hind paw and the results of imaging both indicated that reflectance multispectral imaging produces more distinctive results than transmittance. Both showed larger RMS differences between the normal and arthritic groups, and reflectance PCA scores generally correlated better with alternative measures of arthritis. Although transmitted light is likely to have traversed more tissue layers, information from the visible region of the spectrum is mostly lost due to very low transmission, reducing the usable spectral data. The model also predicts lower absolute change in the transmittance percentage between the normal and arthritic mice, suggesting that the average percentage of the photon pathlength spent in the tissues affected by arthritis is less in transmittance. Therefore, for imaging mice, reflectance multispectral imaging alone is sufficient for arthritis assessment. However, if the imaging system were extended to larger animals or imaging of humans, it may be the case that in thicker tissue the transmittance spectra would be more sensitive to arthritis symptoms. The penetration of the reflectance may be insufficient to sample the affected tissue region and the increased transmission pathlength may increase sensitivity to optical contrast.

#### *7.4.2.2* Wavelength Optimization

Although the number of wavelengths used in this project were informative, it is likely that there is some redundancy in the data. If the number of imaging wavelengths were reduced, the imaging time would naturally decrease making the technique a more feasible method for arthritis assessment. For continuous-wave DOT, optimal sets of a chosen number of wavelengths are selected through minimizing the residual norm of the least squares reconstruction and the condition number of the extinction coefficient matrix (221–223). For calculating the best wavelengths in multispectral imaging, criteria such as the 1st principal component score and condition number of the absorption coefficients could be used in an optimization to preserve the accuracy of arthritis assessment but with a reduced number of imaging wavelengths.

#### *7.4.2.3* Spectral Estimation

Another potential option for the future of this work is to simplify the data gathering process to the use of cheap, easily available equipment, such as RGB cameras, and use more sophisticated post-processing algorithms to estimate the spectral data. Using *a priori* spectral data such as RGB photos of colorchecker charts with known reflectance spectra, the underdetermined problem of RGB to multispectral estimation becomes a regression problem solvable through methods such as neural networks and kernel regression (224,225).

#### *7.4.2.4* Illumination

Another option for reducing the acquisition time would be to change the method of illumination to a fixed alternative such as narrow bandwidth LED’s, or lasers. Using dedicated fixed wavelength illumination, imaging time could be reduced through comparatively stronger illumination at the low emission regions of a tungsten halogen light source. A cheaper filter-based alternative to the tuneable filters used in this project would be interference filters with a computerized filter wheel.

### 7.4.3 Model Development

Using the semi-infinite tissue layer model, the initial aim for a direct inversion (104) mapping the remitted spectra to tissue parameters was not achieved. The mouse paw is a problematic surface for spectral imaging owing to being nonuniform and the semi-infinite layer model potentially oversimplified the problem. 3D implementations of Monte Carlo models have been designed to allow for more complex morphologies (226–228), and microMRI/ contrast-assisted microCT/ histology (229–231) could inform a 3D tissue-segmented model of the mouse hind paw. This would not guarantee invertibility since combinations of the parameters could potentially result in non-unique changes to the spectra but may offer improvements upon the layer model.

## 7.5 Multispectral Imaging for Rheumatoid Arthritis in Humans?

As discussed in section2.3.5, several optical imaging approaches have been attempted for the imaging of healthy joints and rheumatoid joints in patients, often specifically aiming to detect physiological changes in early arthritis. Several systems attempt tomographic reconstruction of tissue optical parameters. They are able to show differences occurring with arthritis onset in the patterns of optical parameters in the tissue and reconstruct distribution maps of estimated chromophore concentrations (45,46,52,53,232–234). Other systems, one of which is commercially available, use varying methods of analysis of the data from NIR spectroscopic methods, often with the use of pressure cuffs to temporally alter tissue contrast (40,41,235,236). In general, these systems are able to detect differences between healthy and arthritic joints and in some cases they exhibit sensitivity and specificity equivalent to other clinical imaging methods such as MRI and ultrasound, according to optimized classification algorithms with selected image features (53). In order for these systems to be adopted clinically, their cost-effectiveness and ability to detect and accurately grade subclinical synovitis must be proved.

Modelling of multispectral imaging for rheumatoid joints showed potential for multispectral imaging to detect changes in the joint in reflectance and transillumination set-ups (17). Later, hyperspectral reflectance imaging of RA patients detected differences between a group of healthy individuals and a group of patients using reconstructed estimates of tissue properties (237). To date, to the author's knowledge, no work has been published on widefield hyperspectral/ multispectral transillumination of the arthritic joint. Tomographic reconstruction of tissue properties from such images would be inappropriate given the number of potential sources, but analysis of the spectroscopic data or topographic tissue property reconstruction may be able to detect differences in the arthritic joint (preliminary human spectral data shown in section8.A8).

## 7.6 Final Conclusion

Overall, the results of this project showed that physiological changes occurring in the arthritic mouse paw are detectable in the reflectance and transmittance response of the tissue in the range 480nm to 1000nm. This could form the basis for a method of arthritis assessment which could be a more accurate and less biased method of grading the progression of arthritis symptoms. The benefits of such a system could be improved animal welfare and improved experimental design and data analysis.

# 8 Appendices

## A1 Implementation of MCML modelling

The input values for the mouse hind paw MCML model were set up for individual wavelengths via a Matlab script. The values were written into a mci file, a text file containing the input values for MCML in a format that can be read by the program. The data produced by MCML can then be read back into Matlab for analysis.

## A2 MCML additional outputs

The MCML algorithm outputs several values for each wavelength model. For all wavelengths, the MCML program records angular distribution of photon remission in reflectance/transmittance, the absorption map showing where photons deposit energy in the tissue, and radial distribution of photon remission/transmission. Figure 66 displays the angular and radial distribution of reflectance and transmittance and 4 example wavelengths of the absorption maps.

The angular distribution of both the reflectance and transmittance spectra, shown in Figure 66a and Figure 66b, can be seen to follow a Lambertian distribution where intensity is proportional to the angle from the surface normal. The graphs for radial distribution show decreasing reflectance and transmittance with distance from the radial origin of photon injection and faster attenuation of the shorter wavelengths in line with higher scattering properties and increased absorption. The absorbance maps, shown in Figure 66e, reveal the structure of the layer model and show the distribution of the deposition of photon weights at different wavelengths. The model also indicates that approximately 2% of the reflectance spectra is due to specular reflection from the tissue surface. This result is relatively wavelength independent.

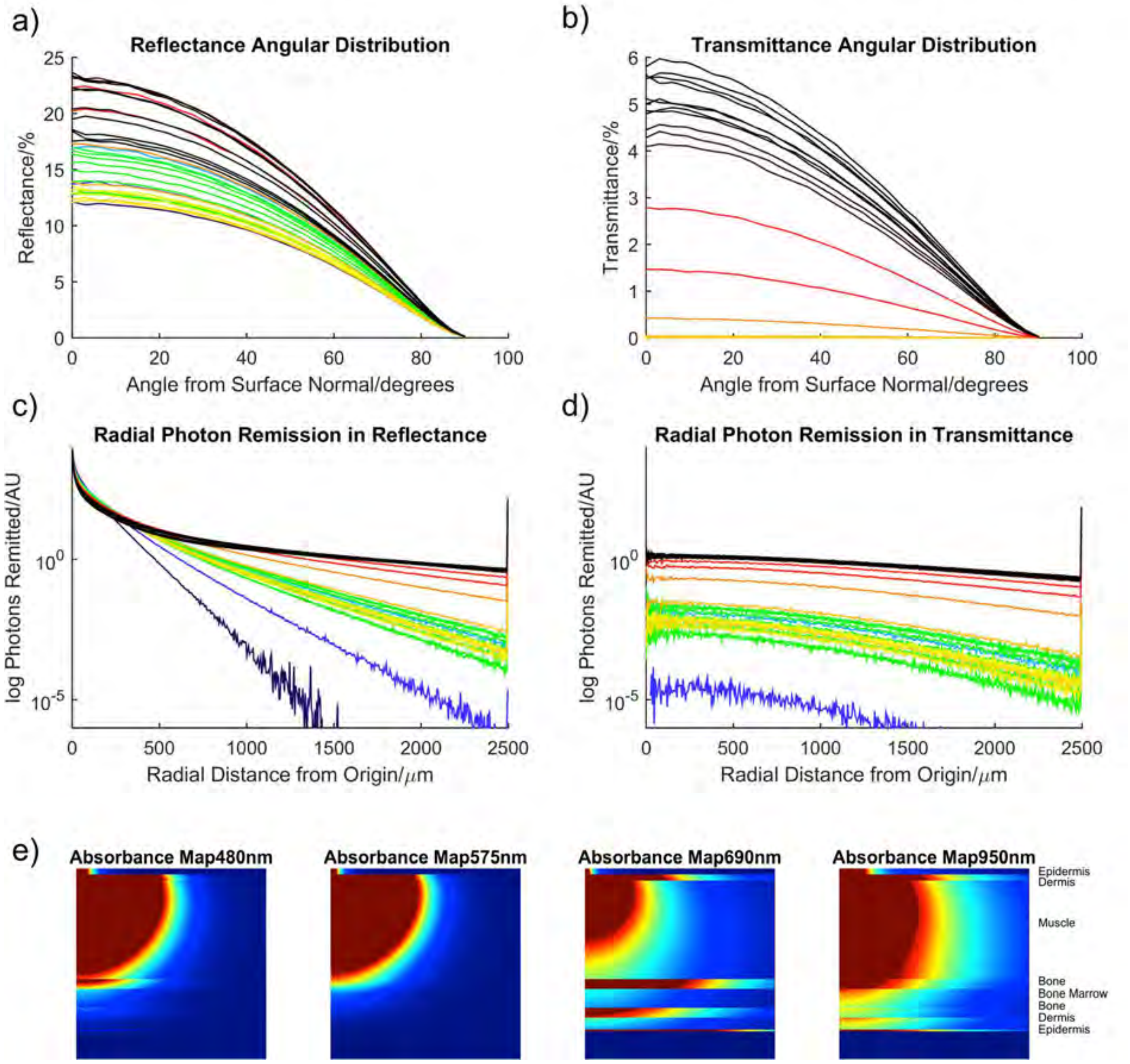

Figure 66: Results of Monte Carlo MCML simulations of light propagation in the model of normal mouse tissue described in section 3.4.1. a) The angular emission of photons in measured in the reflectance spectra, wavelength is indicated by colour. b) The angular distribution of the transmittance spectra, wavelength is indicated by colour. c) The radial distribution in distance from the origin of photon injection of photon remission in reflectance, wavelength is indicated by colour. d) The radial distribution in distance from the origin of photon injection in the radial axis of transmittance, wavelength is indicated by colour. e) Absorbance maps of the layer model showing absorption distribution within the modelled tissue for different wavelengths.

## A3 MCML Model for Alternative Regions of the Paw

Figure 19 includes a Monte Carlo simulation of the ‘midfoot’ region of the paw according to measurements made of H&E stained paw slides. Figure 67 displays the results for MCML spectra from hind paw models made using the measurements from the other three anatomical areas of the paw, the heel, the joints and the toes.

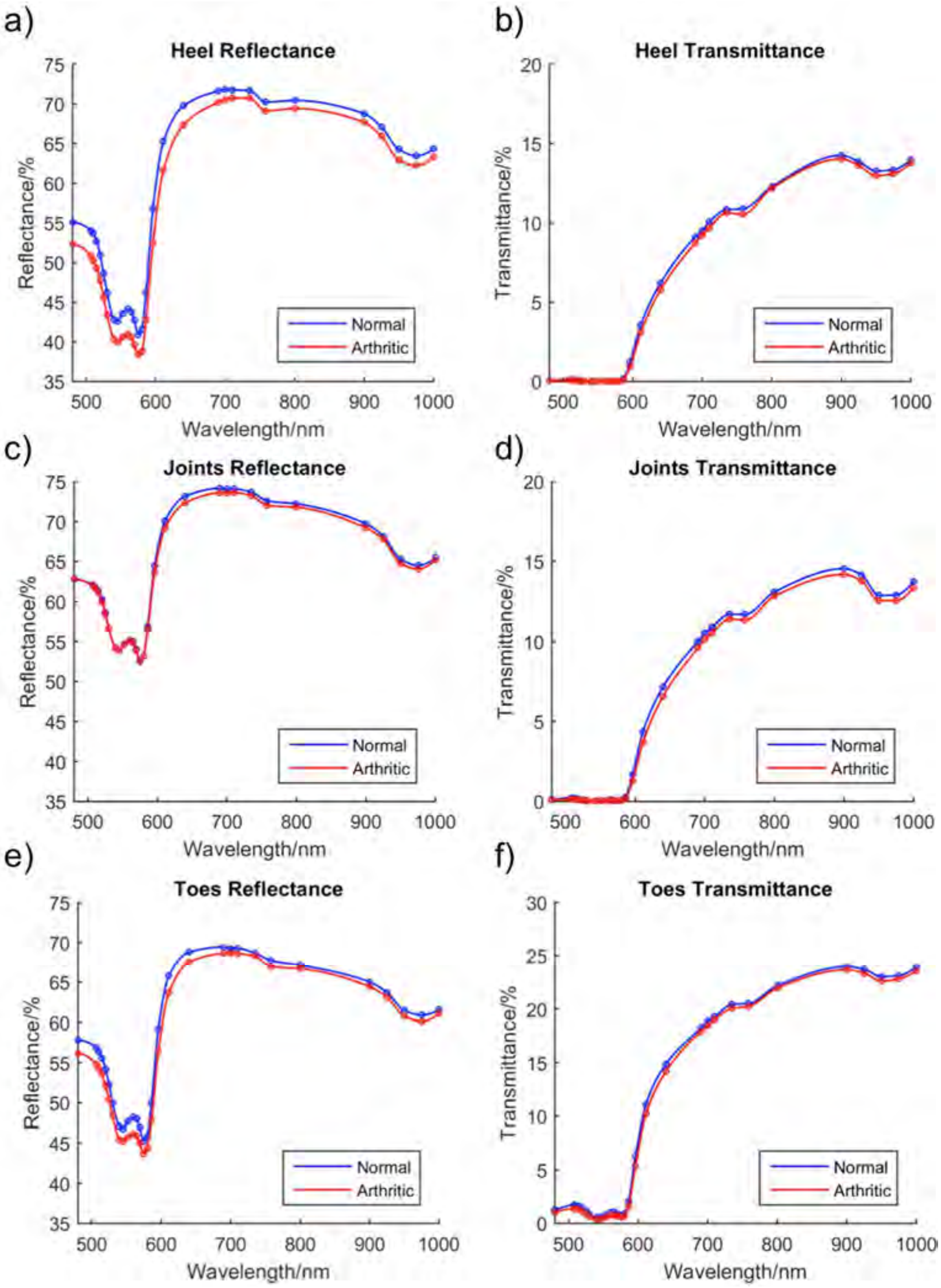

Figure 67: Reflectance and transmittance spectra from a Monte Carlo model of the heel, joints, and toes mouse hind paw in a 'normal' and 'arthritic' state. a and b) MCML reflectance and transmittance spectra for a hind paw Monte Carlo model simulating the heel region of the foot. Measurements of the tissue layers are described in section 3.3.1.2, and changes with arthritis are described in section 3.4.1 c and d) MCML reflectance and transmittance spectra for a hind paw model simulating the 'joints' region of the foot. e and f) MCML reflectance and transmittance spectra for a hind paw model simulating the toes regions of the foot.

## A4 Tophat Diffuser vs Lambertian Diffuser

The transillumination system set up described in section 5.3.1.2 calibrates transmittance data by division of the sample transmittance image by transmission of the diffuser in the stage floor. This method of calibration assumes the light to be an equivalent scatterer to the tissue. The diffuser however is a ‘tophat’ diffuser where 100% of the light exits within a set angle to the normal (25 degrees for the diffuser used in the system) and within this range the intensity is equal (Figure 68b). Assuming the light transmitted from the tissue is Lambertian, the calibration system is likely to underestimate tissue transmittance since a lower percentage of light is transmitted in the direction of the camera. Figure 68a shows a Lambertian profile of emission and Figure 68b shows the emission of the diffuser, normalized by area.

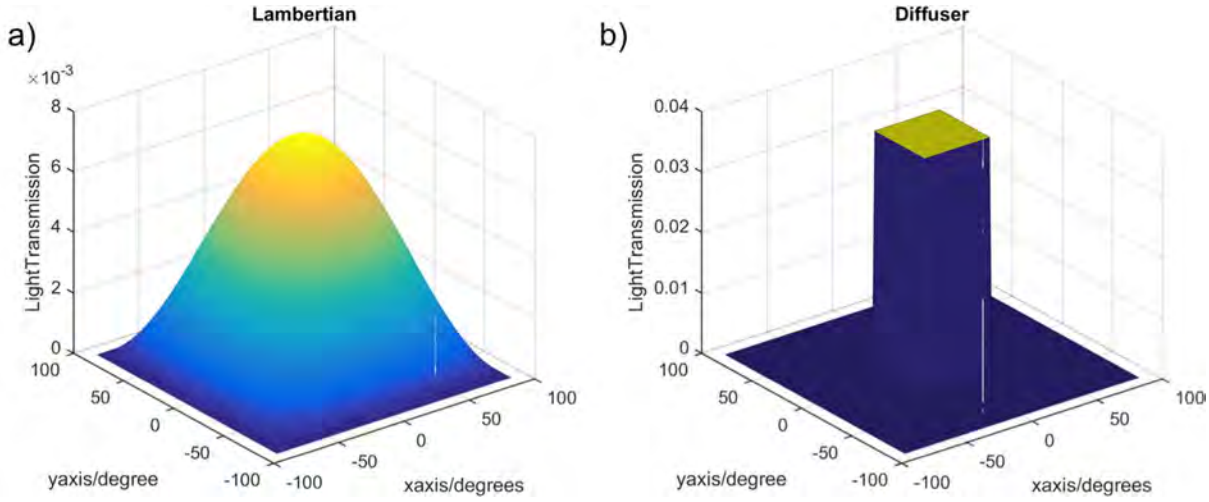

Figure 68: Difference in the detected transmittance of a Lambertian scatterer and a tophat diffuser. a) A profile of intensity for Lambertian light emission with angle from the normal to a surface. The profile is normalised so that the sum of all intensity’s is equal to 100. b) A profile of intensity for the tophat diffuser. The profile is normalised so that the sum of all intensity’s is equal to 100.

Given the distance of the camera from the stage and the size of the lens, the camera accepts light emitted within approximately 8 degrees of the surface normal. The ratio of light emitted within 8 degrees of the normal differs by approximately 5 times. The transmittance imaging system is therefore underestimating the absolute percentage of light transmission by a factor of around 5.

## A5 Change in the Spectral Output of the Light Source Over Time

The Thorlabs OSL1-EC used in the multispectral system requires time for the lamp to warm up and the spectral output to stabilize. Figure 69 shows the difference between 5 timepoints after the lamp is turned on from 0 minutes to 80 minutes and the spectral output measured at 100 minutes.

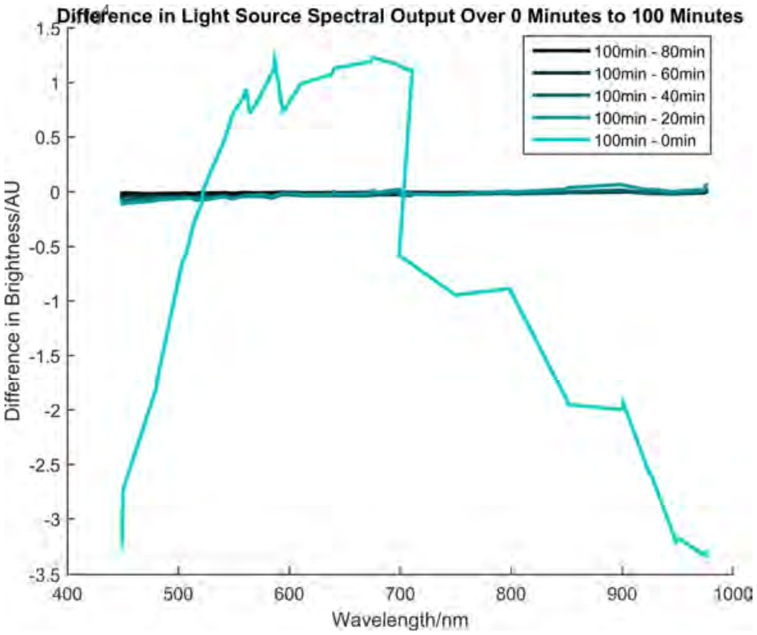

Figure 69: Difference over 0 minutes to 100 minutes of the Thorlabs OSL1-EC fibre light source. Difference between x and 100 minutes is plotted for 5 timepoints across the wavelengths 450nm to 975nm.

## A6 TNF dARE 12 week Imaging RMS Error

Figure 70 displays the root mean square error between the mean spectra of the normal group and the mean spectra of the arthritic group. Data are from the experiment detailed in section 6.4.1.1. In both reflectance and transmittance the raw spectra (non-normalized) were used to calculate RMS.

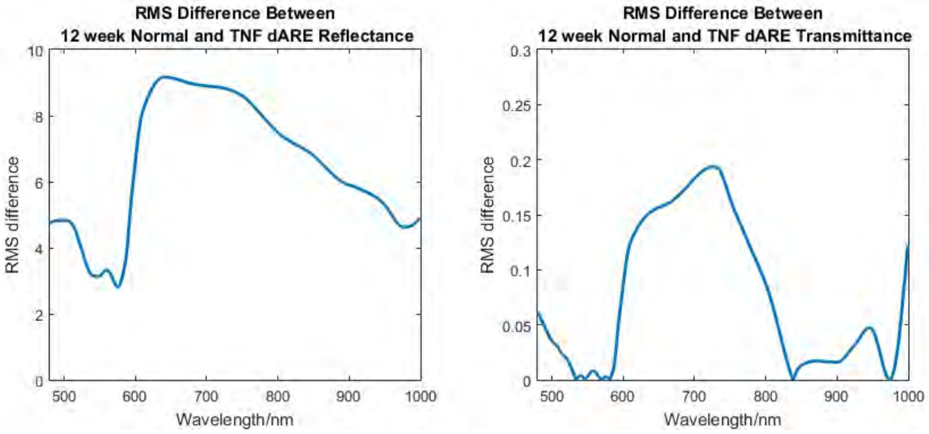

Figure 70: Root mean squared error for the difference between the mean of the raw spectra of the normal mice and the TNF dARE mice in reflectance and transmittance.

## A7 K/BxN ST RMS Error

Figure 70 displays the root mean square error between the mean spectra of the normal group and the mean spectra of the arthritic group. Data are from the experiment detailed in section 6.4.2.1. In both reflectance and transmittance the raw spectra (non-normalized) were used to calculate RMS.

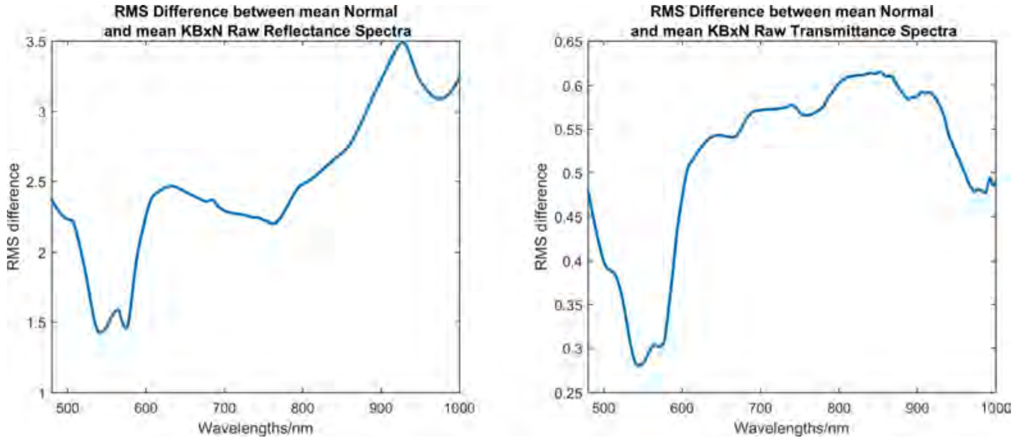

Figure 71: Root mean squared error for the difference between the mean of the raw spectra of the normal mice and the K/BxN ST mice in reflectance and transmittance.

## A8 Human Imaging

The system described in chapter 5 was used to image human finger joints. The layout of the system is adapted for mice rather than for human fingers, but two examples of finger reflectance spectra and of transmission spectra are displayed in Figure 72.

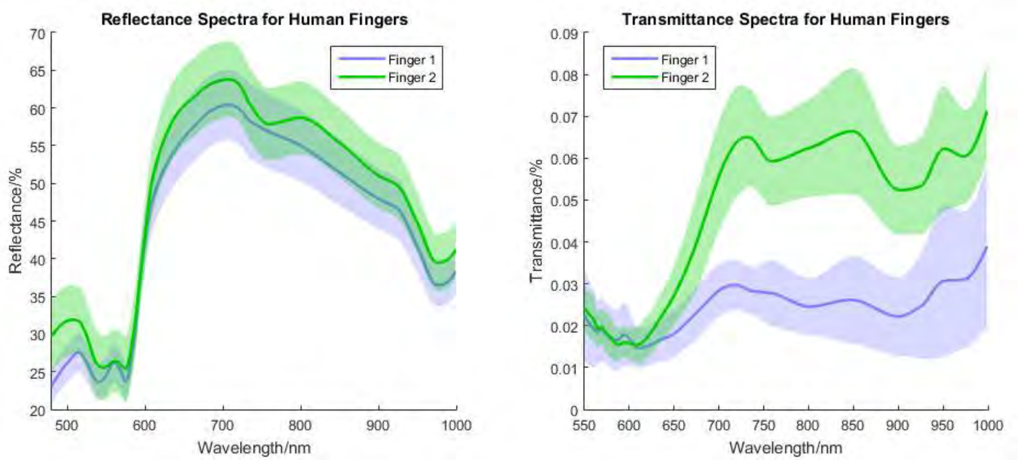

Figure 72: Reflectance spectra and transmittance spectra from human finger joints from 2 different subjects. Shaded area shows the standard deviation of the 20 spectra collected across the finger joint using the method described in section 6.3.2.

The two subjects of imaging show different characteristics in both reflectance and transmittance. The transmittance spectra particularly show a large difference due to the different size of the fingers imaged. In principle, the system described in chapter 5 could be adapted for humans and it is possible that features of rheumatoid arthritis would be detectable in the spectra.

# 9 References

1. Murphy K, Travers P, Walport M, Travers P, Walport M. Janeway's Immunobiology [Internet]. Garland Science; 2012 [cited 2019 Mar 3]. Available from: https://www.taylorfrancis.com/books/9781136977176

2. van Vollenhoven RF. Sex differences in rheumatoid arthritis: more than meets the eye... BMC Medicine. 2009 Mar 30;7:12.

3. Raza K, Filer A. Predicting the development of RA in patients with early undifferentiated arthritis. Best Practice & Research Clinical Rheumatology. 2009 Feb 1;23(1):25–36.

4. Schneider M, Krüger K. Rheumatoid Arthritis—Early Diagnosis and Disease Management. Dtsch Arztebl Int. 2013 Jul;110(27–28):477–84.

5. Hussain Manik Z, George J, Sockalingam S. Ultrasound Assessment of Synovial Thickness of Some of the Metacarpophalangeal Joints of Hand in Rheumatoid Arthritis Patients and the Normal Population [Internet]. Scientifica. 2016 [cited 2018 Sep 15]. Available from: https://www.hindawi.com/journals/scientifica/2016/5609132/

6. Doiron L. What are the Different Stages of Rheumatoid Arthritis? [Internet]. [cited 2017 Jul 10]. Available from: http://www.conversantbio.com/blog/bid/396167/what-are-the-different-stages-of-rheumatoid-arthritis

7. Raza K, Buckley CE, Salmon M, Buckley CD. Treating very early rheumatoid arthritis. Best Pract Res Clin Rheumatol. 2006 Oct;20(5):849–63.

8. Müller-Ladner U, Ospelt C, Gay S, Distler O, Pap T. Cells of the synovium in rheumatoid arthritis. Synovial fibroblasts. Arthritis Research & Therapy. 2007 Dec 20;9(6):223.

9. Schett G, Gravallese E. Bone erosion in rheumatoid arthritis: mechanisms, diagnosis and treatment. Nat Rev Rheumatol. 2012 Nov;8(11):656–64.

10. Haavardsholm EA, Bøyesen P, Østergaard M, Schildvold A, Kvien TK. Magnetic resonance imaging findings in 84 patients with early rheumatoid arthritis: bone marrow oedema predicts erosive progression. Annals of the Rheumatic Diseases. 2008 Jun 1;67(6):794–800.

11. McQueen FM, Benton N, Perry D, Crabbe J, Robinson E, Yeoman S, et al. Bone edema scored on magnetic resonance imaging scans of the dominant carpus at presentation predicts radiographic joint damage of the hands and feet six years later in patients with rheumatoid arthritis. Arthritis & Rheumatism. 2003 Jul 1;48(7):1814–27.

12. Cojocaru M, Cojocaru IM, Silosi I, Vrabie CD, Tanasescu R. Extra-articular Manifestations in Rheumatoid Arthritis. Maedica (Buchar). 2010 Dec;5(4):286–91.

13. Taylor PC, Sivakumar B. Hypoxia and angiogenesis in rheumatoid arthritis. Current Opinion in Rheumatology. 2005 May;17(3):293–298.

14. Lund-Olesen K. Oxygen tension in synovial fluids. Arthritis Rheum. 1970 Dec;13(6):769–76.

15. Ng CT, Biniecka M, Kennedy A, McCormick J, FitzGerald O, Bresnihan B, et al. Synovial tissue hypoxia and inflammation in vivo. Annals of the Rheumatic Diseases. 2010 Jul 1;69(7):1389–95.

16. Nasui OC, Chan MW, Nathanael G, Crawley A, Miller E, Belik J, et al. Physiologic characterization of inflammatory arthritis in a rabbit model with BOLD and DCE MRI at 1.5 Tesla. Eur Radiol. 2014 Nov 1;24(11):2766–78.

17. Milanic M, Paluchowski LA, Randeberg LL. Hyperspectral imaging for detection of arthritis: feasibility and prospects. J Biomed Opt. 2015;20(9):096011–096011.

18. van der Putten MA, Brewer JM, Harvey AR. Multispectral oximetry of murine tendon microvasculature with inflammation. Biomed Opt Express. 2017 May 8;8(6):2896–905.

19. Quiñonez-Flores CM, González-Chávez SA, Pacheco-Tena C. Hypoxia and its implications in rheumatoid arthritis. J Biomed Sci [Internet]. 2016 Aug 22 [cited 2018 Sep 15];23(1). Available from: https://www.ncbi.nlm.nih.gov/pmc/articles/PMC4994473/

20. Westra J, Molema G, Kallenberg CGM. Hypoxia-inducible factor-1 as regulator of angiogenesis in rheumatoid arthritis - therapeutic implications. Curr Med Chem. 2010;17(3):254–63.

21. Koch A. Angiogenesis as a target in rheumatoid arthritis. Ann Rheum Dis. 2003 Nov;62(Suppl 2):ii60–7.

22. Taylor PC, Steuer A, Gruber J, Cosgrove DO, Blomley MJK, Marsters PA, et al. Comparison of ultrasonographic assessment of synovitis and joint vascularity with radiographic evaluation in a randomized, placebo-controlled study of infliximab therapy in early rheumatoid arthritis. Arthritis & Rheumatism. 2004 Apr 1;50(4):1107–16.

23. Gayetskyy S, Museyko O, Käßer J, Hess A, Schett G, Engelke K. Characterization and quantification of angiogenesis in rheumatoid arthritis in a mouse model using µCT. BMC Musculoskeletal Disorders. 2014 Sep 6;15:298.

24. Scallan J, Huxley VH, Korthuis RJ. Capillary Fluid Exchange: Regulation, Functions, and Pathology [Internet]. San Rafael (CA): Morgan & Claypool Life Sciences; 2010 [cited 2017 Oct 2]. (Integrated Systems Physiology: from Molecule to Function to Disease). Available from: http://www.ncbi.nlm.nih.gov/books/NBK53447/

25. Perilli E, Cantley M, Marino V, Crotti TN, Smith MD, Haynes DR, et al. Quantifying Not Only Bone Loss, but Also Soft Tissue Swelling, in a Murine Inflammatory Arthritis Model Using Micro-Computed Tomography. Scand J Immunol. 2015 Feb;81(2):142–50.

26. Colebatch AN, Edwards CJ, Østergaard M, Heijde D van der, Balint PV, D'Agostino M-A, et al. EULAR recommendations for the use of imaging of the joints in the clinical management of rheumatoid arthritis. Annals of the Rheumatic Diseases. 2013 Mar 20;annrheumdis-2012-203158.

27. Østergaard M, Pedersen SJ, Døhn UM. Imaging in rheumatoid arthritis – status and recent advances for magnetic resonance imaging, ultrasonography, computed

tomography and conventional radiography. Best Practice & Research Clinical Rheumatology. 2008 Dec 1;22(6):1019–44.

28. Rowbotham EL, Grainger AJ. Rheumatoid Arthritis: Ultrasound Versus MRI. American Journal of Roentgenology. 2011 Sep 1;197(3):541–6.

29. Tan YK, Østergaard M, Conaghan PG. Imaging tools in rheumatoid arthritis: ultrasound vs magnetic resonance imaging. Rheumatology (Oxford). 2012 Dec 1;51(suppl_7):vii36–42.

30. Patil P, Dasgupta B. Role of diagnostic ultrasound in the assessment of musculoskeletal diseases. Ther Adv Musculoskelet Dis. 2012 Oct;4(5):341–55.

31. Sudoł-Szopińska I, Ćwikła JB. Current imaging techniques in rheumatology: MRI, scintigraphy and PET. Pol J Radiol. 2013;78(3):48–56.

32. Rosado-de-Castro PH, Lopes de Souza SA, Alexandre D, Barbosa da Fonseca LM, Gutfilen B. Rheumatoid arthritis: Nuclear Medicine state-of-the-art imaging. World J Orthop. 2014 Jul 18;5(3):312–8.

33. Werner SG, Langer H-E, Ohrndorf S, Bahner M, Schott P, Schwenke C, et al. Inflammation assessment in patients with arthritis using a novel in vivo fluorescence optical imaging technology. Annals of the Rheumatic Diseases. 2012 Apr 1;71(4):504–10.

34. Kisten Y, Györi N, Klint E af, Rezaei H, Levitsky A, Karlsson A, et al. Detection of clinically manifest and silent synovitis in the hands and wrists by fluorescence optical imaging. RMD Open. 2015 Jun 1;1(1):e000106.

35. Meier R, Thürmel K, Moog P, Noël PB, Ahari C, Sievert M, et al. Detection of synovitis in the hands of patients with rheumatologic disorders: Diagnostic performance of optical imaging in comparison with magnetic resonance imaging. Arthritis & Rheumatism. 2012 Aug 1;64(8):2489–98.

36. Zhao J, Chen J, Ma S, Liu Q, Huang L, Chen X, et al. Recent developments in multimodality fluorescence imaging probes. Acta Pharmaceutica Sinica B. 2018 May 1;8(3):320–38.

37. Borojević N, Kolarić D, Grazio S, Grubišić F, Antonini S, Nola IA, et al. Thermography of rheumatoid arthritis and osteoarthritis. In: Proceedings ELMAR-2011. 2011. p. 293–5.

38. Lerkvaleekul B, Jaovisidha S, Sungkarat W, Chitrapazt N, Praman Fuangfa, Ruangchaijatuporn T, et al. The comparisons between thermography and ultrasonography with physical examination for wrist joint assessment in juvenile idiopathic arthritis. Physiol Meas. 2017;38(5):691.

39. Sun Y, Sobel ES, Jiang H. First assessment of three-dimensional quantitative photoacoustic tomography for in vivo detection of osteoarthritis in the finger joints. Med Phys. 2011 Jul;38(7):4009–17.

40. Meier AJL, Rensen WHJ, Bokx PK de, Nijs RNJ de. Potential of optical spectral transmission measurements for joint inflammation measurements in rheumatoid arthritis patients. JBO, JBOPFO. 2012 Aug;17(8):081420.

41. Besselink NJ, van der Meijde P, Rensen WHJ, Meijer PBL, Marijnissen ACA, van Laar JM, et al. Optical spectral transmission to assess inflammation in hand and wrist joints of rheumatoid arthritis patients. Rheumatology (Oxford). 2018 01;57(5):865–72.

42. Onna M van, Cate DFT, Tsoi KL, Meier AJL, Jacobs JWG, Westgeest A a. A, et al. Assessment of disease activity in patients with rheumatoid arthritis using optical spectral transmission measurements, a non-invasive imaging technique. Annals of the Rheumatic Diseases. 2016 Mar 1;75(3):511–8.

43. Hielscher AH, Klose AD, Scheel AK, Moa-Anderson B, Backhaus M, Uwe Netz, et al. Sagittal laser optical tomography for imaging of rheumatoid finger joints. Phys Med Biol. 2004;49(7):1147.

44. Scheel AK, Backhaus M, Klose AD, Moa-Anderson B, Netz UJ, Hermann K-GA, et al. First clinical evaluation of sagittal laser optical tomography for detection of synovitis in arthritic finger joints. Annals of the Rheumatic Diseases. 2005 Feb 1;64(2):239–45.

45. Lasker JM, Fong CJ, Ginat DT, Dwyer E, Hielscher AH. Dynamic optical imaging of vascular and metabolic reactivity in rheumatoid joints. JBO, JBOPFO. 2007 Sep;12(5):052001.

46. Lighter D, Hughes J, Styles I, Filer A, Dehghani H. Multispectral, non-contact diffuse optical tomography of healthy human finger joints. Biomed Opt Express, BOE. 2018 Apr 1;9(4):1445–60.

47. Wu HY, Filer A, Styles I, Dehghani H. Development of a multi-wavelength diffuse optical tomography system for early diagnosis of rheumatoid arthritis: simulation, phantoms and healthy human studies. Biomed Opt Express. 2016 Oct 27;7(11):4769–86.

48. Stanislavsky A. Rheumatoid arthritis (musculoskeletal manifestations) | Radiology Reference Article | Radiopaedia.org [Internet]. Radiopaedia. [cited 2017 Nov 16]. Available from: https://radiopaedia.org/articles/rheumatoid-arthritis-musculoskeletal-manifestations-2

49. Navalho M, Resende C, Rodrigues AM, Ramos F, Gaspar A, Pereira da Silva JA, et al. Bilateral MR Imaging of the Hand and Wrist in Early and Very Early Inflammatory Arthritis: Tenosynovitis Is Associated with Progression to Rheumatoid Arthritis. Radiology. 2012 Sep 1;264(3):823–33.

50. The Pros and Cons of Ultrasonography for Rheumatologic Conditions | Rheumatology Network [Internet]. [cited 2017 Nov 16]. Available from: http://www.rheumatologynetwork.com/imaging-rheumatology/pros-and-cons-ultrasonography-rheumatologic-conditions

51. Glimm A-M, Werner SG, Burmester GR, Backhaus M, Ohrndorf S. Analysis of distribution and severity of inflammation in patients with osteoarthitis compared to rheumatoid arthritis by ICG-enhanced fluorescence optical imaging and musculoskeletal ultrasound: a pilot study. Annals of the Rheumatic Diseases. 2015 Aug 25;annrheumdis-2015-207345.

52. Montejo LD, Jia J, Kim HK, Netz UJ, Blaschke S, Müller GA, et al. Computer-aided diagnosis of rheumatoid arthritis with optical tomography, Part 1: feature extraction. J

Biomed Opt [Internet]. 2013 Jul;18(7). Available from: http://www.ncbi.nlm.nih.gov/pmc/articles/PMC3710917/

53. Montejo LD, Jia J, Kim HK, Netz UJ, Blaschke S, Müller GA, et al. Computer-aided diagnosis of rheumatoid arthritis with optical tomography, Part 2: image classification. J Biomed Opt [Internet]. 2013 Jul;18(7). Available from: http://www.ncbi.nlm.nih.gov/pmc/articles/PMC3710916/

54. Chamberland D, Jiang Y, Wang X. Optical imaging: new tools for arthritis. Integrative Biology. 2010;2(10):496–509.

55. Caplazi P, Baca M, Barck K, Carano RAD, DeVoss J, Lee WP, et al. Mouse Models of Rheumatoid Arthritis. Vet Pathol. 2015 Sep 1;52(5):819–26.

56. Li P, Schwarz EM. The TNF-α transgenic mouse model of inflammatory arthritis. Springer Semin Immunopathol. 2003 Aug 1;25(1):19–33.

57. Moelants EA, Mortier A, Van Damme J, Proost P. Regulation of TNF-α with a focus on rheumatoid arthritis. Immunol Cell Biol. 2013 Jul;91(6):393–401.

58. Kontoyiannis D, Pasparakis M, Pizarro TT, Cominelli F, Kollias G. Impaired on/off regulation of TNF biosynthesis in mice lacking TNF AU-rich elements: implications for joint and gut-associated immunopathologies. Immunity. 1999 Mar;10(3):387–98.

59. Yamanaka H. TNF as a Target of Inflammation in Rheumatoid Arthritis [Internet]. Endocrine, Metabolic & Immune Disorders - Drug Targets. 2015 [cited 2018 Sep 15]. Available from: http://www.eurekaselect.com/129531/article

60. Kouskoff V, Korganow AS, Duchatelle V, Degott C, Benoist C, Mathis D. Organ-specific disease provoked by systemic autoimmunity. Cell. 1996 Nov 29;87(5):811–22.

61. Kyburz D, Corr M. The KRN mouse model of inflammatory arthritis. Springer Semin Immunopathol. 2003 Aug 1;25(1):79–90.

62. Ditzel HJ. The K/BxN mouse: a model of human inflammatory arthritis. Trends in Molecular Medicine. 2004 Jan 1;10(1):40–5.

63. Studelska DR, Mandik-Nayak L, Zhou X, Pan J, Weiser P, McDowell LM, et al. High Affinity Glycosaminoglycan and Autoantigen Interaction Explains Joint Specificity in a Mouse Model of Rheumatoid Arthritis. The Journal of Biological Chemistry. 2009 Jan 23;284(4):2354.

64. Bevaart L, Vervoordeldonk MJ, Tak PP. Evaluation of therapeutic targets in animal models of arthritis: How does it relate to rheumatoid arthritis? Arthritis & Rheumatism. 2010 Aug 1;62(8):2192–205.

65. Plows D, Kontogeorgos G, Kollias G. Mice Lacking Mature T and B Lymphocytes Develop Arthritic Lesions after Immunization with Type II Collagen. The Journal of Immunology. 1999 Jan 15;162(2):1018–23.

66. Luross JA, Williams NA. The genetic and immunopathological processes underlying collagen-induced arthritis. Immunology. 2001 Aug;103(4):407–16.

67. Hawkins P, Armstrong R, Boden T, Garside P, Knight K, Lilley E, et al. Applying refinement to the use of mice and rats in rheumatoid arthritis research. Inflammopharmacology. 2015;23(4):131–50.

68. Langford DJ, Bailey AL, Chanda ML, Clarke SE, Drummond TE, Echols S, et al. Coding of facial expressions of pain in the laboratory mouse. Nature Methods. 2010 Jun 1;7(6):447–9.

69. Perl A. Autoimmunity: Methods and Protocols. Springer Science & Business Media; 2004. 432 p.

70. Khairnar A, Marchand F, Vidal A, Etienne M, Miladi I, Auzeloux P, et al. 99mTc-NTP 15-5 Imaging for Cartilage Involvement in Experimental Rheumatoid Arthritis: Comparison with Routinely Used Molecular Imaging Methods and Sensitivity to Chronic Nonsteroidal Antiinflammatory Drug Treatment. J Nucl Med. 2015 May 1;56(5):798–804.

71. Put S, Schoonooghe S, Devoogdt N, Schurgers E, Avau A, Mitera T, et al. SPECT Imaging of Joint Inflammation with Nanobodies Targeting the Macrophage Mannose Receptor in a Mouse Model for Rheumatoid Arthritis. J Nucl Med. 2013 May 1;54(5):807–14.

72. Post AM, Katsikis PD, Tait JF, Geaghan SM, Strauss HW, Blankenberg FG. Imaging Cell Death with Radiolabeled Annexin V in an Experimental Model of Rheumatoid Arthritis. J Nucl Med. 2002 Oct 1;43(10):1359–65.

73. Laverman P, Geest T van der, Terry SYA, Gerrits D, Walgreen B, Helsen MM, et al. Immuno-PET and Immuno-SPECT of Rheumatoid Arthritis with Radiolabeled Anti–Fibroblast Activation Protein Antibody Correlates with Severity of Arthritis. J Nucl Med. 2015 May 1;56(5):778–83.

74. Terry SYA, Koenders MI, Franssen GM, Nayak TK, Freimoser-Grundschober A, Klein C, et al. Monitoring Therapy Response of Experimental Arthritis with Radiolabeled Tracers Targeting Fibroblasts, Macrophages, or Integrin αvβ3. J Nucl Med. 2016 Mar 1;57(3):467–72.

75. Irmler IM, Gebhardt P, Hoffmann B, Opfermann T, Figge M-T, Saluz HP, et al. 18 F-Fluoride positron emission tomography/computed tomography for noninvasive in vivo quantification of pathophysiological bone metabolism in experimental murine arthritis. Arthritis Research & Therapy. 2014 Jul 22;16:R155.

76. Fuchs K, Kohlhofer U, Quintanilla-Martinez L, Lamparter D, Kötter I, Reischl G, et al. In Vivo Imaging of Cell Proliferation Enables the Detection of the Extent of Experimental Rheumatoid Arthritis by 3′-Deoxy-3′-18F-Fluorothymidine and Small-Animal PET. J Nucl Med. 2013 Jan 1;54(1):151–8.

77. Franc BL, Goth S, MacKenzie J, Li X, Blecha J, Lam T, et al. In Vivo PET Imaging of the Activated Immune Environment in a Small Animal Model of Inflammatory Arthritis. Mol Imaging. 2017 Jan 1;16:1536012117712638.

78. Herschman HR. Micro-PET imaging and small animal models of disease. Current Opinion in Immunology. 2003 Aug 1;15(4):378–84.

79. Jacobson PB, Morgan SJ, Wilcox DM, Nguyen P, Ratajczak CA, Carlson RP, et al. A new spin on an old model: In vivo evaluation of disease progression by magnetic resonance imaging with respect to standard inflammatory parameters and histopathology in the adjuvant arthritic rat. Arthritis & Rheumatism. 1999 Oct 1;42(10):2060–73.

80. Proulx ST, Kwok E, You Z, Papuga MO, Beck CA, Shealy DJ, et al. Longitudinal assessment of synovial, lymph node, and bone volumes in inflammatory arthritis in mice by in vivo magnetic resonance imaging and microfocal computed tomography. Arthritis & Rheumatism. 2007 Dec 1;56(12):4024–37.

81. Lee S-W, Greve JM, Leaffer D, Lollini L, Bailey P, Gold GE, et al. Early findings of small-animal MRI and small-animal computed tomography correlate with histological changes in a rat model of rheumatoid arthritis. NMR Biomed. 2008 Jun 1;21(5):527–36.

82. Lutz AM, Seemayer C, Corot C, Gay RE, Goepfert K, Michel BA, et al. Detection of Synovial Macrophages in an Experimental Rabbit Model of Antigen-induced Arthritis: Ultrasmall Superparamagnetic Iron Oxide–enhanced MR Imaging. Radiology. 2004 Oct 1;233(1):149–57.

83. Dardzinski BJ, Schmithorst VJ, Holland SK, Boivin GP, Imagawa T, Watanabe S, et al. MR imaging of murine arthritis using ultrasmall superparamagnetic iron oxide particles☆. Magnetic Resonance Imaging. 2001 Nov 1;19(9):1209–16.

84. Chen C-L, Siow TY, Chou C-H, Lin C-H, Lin M-H, Chen Y-C, et al. Targeted Superparamagnetic Iron Oxide Nanoparticles for In Vivo Magnetic Resonance Imaging of T-Cells in Rheumatoid Arthritis. Mol Imaging Biol. 2017 Apr 1;19(2):233–44.

85. Vollmer S, Gemeinhardt I, Vater A, Schnorr B, Schnorr J, Voigt J, et al. In vivo therapy monitoring of experimental rheumatoid arthritis in rats using near-infrared fluorescence imaging. J Biomed Opt. 2014;19(3):036011–036011.

86. Meier R, Krug C, Golovko D, Boddington S, Piontek G, Rudelius M, et al. Indocyanine green–enhanced imaging of antigen-induced arthritis with an integrated optical imaging/radiography system. Arthritis & Rheumatism. 2010 Aug 1;62(8):2322–7.

87. Ryu JH, Lee A, Chu J-U, Koo H, Ko C-Y, Kim HS, et al. Early diagnosis of arthritis in mice with collagen-induced arthritis, using a fluorogenic matrix metalloproteinase 3–specific polymeric probe. Arthritis & Rheumatism. 2011 Dec 1;63(12):3824–32.

88. Lee A, Park K, Choi S-J, Seo D-H, Kim K, Kim HS, et al. Prediction of Antiarthritic Drug Efficacies by Monitoring Active Matrix Metalloproteinase-3 (MMP-3) Levels in Collagen-Induced Arthritic Mice Using the MMP-3 Probe. Mol Pharmaceutics. 2014 May 5;11(5):1450–8.

89. Wunder A, Tung C-H, Müller-Ladner U, Weissleder R, Mahmood U. In vivo imaging of protease activity in arthritis: A novel approach for monitoring treatment response. Arthritis & Rheumatism. 2004 Aug 1;50(8):2459–65.

90. Chen W-T, Mahmood U, Weissleder R, Tung C-H. Arthritis imaging using a near-infrared fluorescence folate-targeted probe. Arthritis Res Ther. 2005 Jan 14;7:R310.

91. Hansch A, Frey O, Sauner D, Hilger I, Haas M, Malich A, et al. In vivo imaging of experimental arthritis with near-infrared fluorescence. Arthritis & Rheumatism. 2004 Mar 1;50(3):961–7.

92. Scales HE, Ierna M, Smith KM, Ross K, Meiklejohn GR, Patterson-Kane JC, et al. Assessment of murine collagen-induced arthritis by longitudinal non-invasive duplexed molecular optical imaging. Rheumatology (Oxford). 2016 Mar 1;55(3):564–72.

93. Dustin ML. In vivo imaging approaches in animal models of rheumatoid arthritis. Arthritis Res Ther. 2003 May 1;5:165.

94. Son T, Yoon H-J, Lee S, Jang WS, Jung B, Kim W-U. Continuous monitoring of arthritis in animal models using optical imaging modalities. J Biomed Opt. 2014;19(10):106010–106010.

95. Rajaram A, Ioussoufovitch S, Morrison LB, St Lawrence K, Lee T-Y, Bureau Y, et al. Joint blood flow is more sensitive to inflammatory arthritis than oxyhemoglobin, deoxyhemoglobin, and oxygen saturation. Biomed Opt Express. 2016 Sep 1;7(10):3843–54.

96. Jasemian Y, Svendsen P, Deleuran B, Dagnaes-Hansen F. Refinement of the Collagen Induced Arthritis Model in Rats by Infrared Thermography. http://sciencedomain.org/abstract/256 [Internet]. 2011 Oct [cited 2017 Aug 25]; Available from: http://imsear.hellis.org/handle/123456789/162760

97. Snekhalatha U, Anburajan M, Venkatraman B, Menaka M, Raj B. Evaluation of rheumatoid arthritis in small animal model using Thermal imaging. In: 2011 International Conference on Signal Processing, Communication, Computing and Networking Technologies. 2011. p. 785–91.

98. Bouta EM, Banik PD, Wood RW, Rahimi H, Ritchlin CT, Thiele RG, et al. Validation of Power Doppler Versus Contrast-Enhanced Magnetic Resonance Imaging Quantification of Joint Inflammation in Murine Inflammatory Arthritis. J Bone Miner Res. 2015 Apr 1;30(4):690–4.

99. Clavel G, Marchiol-Fournigault C, Renault G, Boissier M-C, Fradelizi D, Bessis N. Ultrasound and Doppler micro-imaging in a model of rheumatoid arthritis in mice. Annals of the Rheumatic Diseases. 2008 Dec 1;67(12):1765–72.

100. Rajian JR, Shao X, Chamberland DL, Wang X. Characterization and treatment monitoring of inflammatory arthritis by photoacoustic imaging: a study on adjuvant-induced arthritis rat model. Biomed Opt Express, BOE. 2013 Jun 1;4(6):900–8.

101. Chamberland DL, Wang X, Roessler BJ. Photoacoustic tomography of carrageenan-induced arthritis in a rat model. JBO, JBOPFO. 2008 Jan;13(1):011005.

102. Vonnemann J, Beziere N, Böttcher C, Riese SB, Kuehne C, Dernedde J, et al. Polyglycerolsulfate Functionalized Gold Nanorods as Optoacoustic Signal Nanoamplifiers for In Vivo Bioimaging of Rheumatoid Arthritis. Theranostics. 2014 Mar 20;4(6):629–41.

103. Optoacoustic Imaging and Staging of Inflammation in a Murine Model of Arthritis - Beziere - 2014 - Arthritis & Rheumatology - Wiley Online Library [Internet]. [cited 2017 Sep 12]. Available from: http://onlinelibrary.wiley.com/doi/10.1002/art.38642/full

104. Claridge E, Preece SJ. An inverse method for the recovery of tissue parameters from colour images. Inf Process Med Imaging. 2003 Jul;18:306–17.

105. Brown JM, Ross E, Desanti G, Saghir A, Clark A, Buckley C, et al. Detection and characterisation of bone destruction in murine rheumatoid arthritis using statistical shape models. Medical Image Analysis. 2017 Aug;40:30–43.

106. Lister T, Wright PA, Chappell PH. Optical properties of human skin. JBO, JBOPFO. 2012 Sep;17(9):090901.

107. Optical properties of the human skin / Optičke osobine ljudske kože (PDF Download Available) [Internet]. ResearchGate. [cited 2017 Jul 11]. Available from: https://www.researchgate.net/publication/269514946_Optical_properties_of_the_human_skin_Opticke_osobine_ljudske_koze

108. Mourant JR, Freyer JP, Hielscher AH, Eick AA, Shen D, Johnson TM. Mechanisms of light scattering from biological cells relevant to noninvasive optical-tissue diagnostics. Appl Opt, AO. 1998 Jun 1;37(16):3586–93.

109. Cheong WF, Prahl SA, Welch AJ. A review of the optical properties of biological tissues. IEEE Journal of Quantum Electronics. 1990 Dec;26(12):2166–85.

110. Binzoni T, Leung TS, Gandjbakhche AH, Rüfenacht D, Delpy DT. The use of the Henyey–Greenstein phase function in Monte Carlo simulations in biomedical optics. Phys Med Biol. 2006;51(17):N313.

111. Boas DA, Pitris C, Ramanujam N. Handbook of Biomedical Optics. CRC Press; 2016. 816 p.

112. Johnsen S, Widder EA. The Physical Basis of Transparency in Biological Tissue: Ultrastructure and the Minimization of Light Scattering. Journal of Theoretical Biology. 1999 Jul 21;199(2):181–98.

113. Xia J, Yao G. Angular distribution of diffuse reflectance in biological tissue. Appl Opt, AO. 2007 Sep 10;46(26):6552–60.

114. Hoffmann J, Lübbers DW, Heise HM. Applicability of the Kubelka-Munk theory for the evaluation of reflectance spectra demonstrated for haemoglobin-free perfused heart tissue. Phys Med Biol. 1998;43(12):3571.

115. Prahl SA, Gemert MJC van, Welch AJ. Determining the optical properties of turbid media by using the adding–doubling method. Appl Opt, AO. 1993 Feb 1;32(4):559–68.

116. Guo Z, Kim K. Ultrafast-laser-radiation transfer in heterogeneous tissues with the discrete-ordinates method. Appl Opt, AO. 2003 Jun 1;42(16):2897–905.

117. Slovick B, Flom Z, Zipp L, Krishnamurthy S. Transfer matrix method for four-flux radiative transfer. Appl Opt, AO. 2017 Jul 20;56(21):5890–6.

118. Zhou J, Chen JK, Zhang Y. Theoretical analysis of thermal damage in biological tissues caused by laser irradiation. Mol Cell Biomech. 2007 Mar;4(1):27–39.

119. Dehghani H, Srinivasan S, Pogue BW, Gibson A. Numerical modelling and image reconstruction in diffuse optical tomography. Philos Transact A Math Phys Eng Sci. 2009 Aug 13;367(1900):3073–93.

120. Watté R, Aernouts B, Van Beers R, Herremans E, Ho QT, Verboven P, et al. Modeling the propagation of light in realistic tissue structures with MMC-fpf: a meshed Monte Carlo method with free phase function. Opt Express. 2015 Jun 29;23(13):17467–86.

121. Fang Q. Mesh-based Monte Carlo method using fast ray-tracing in Plücker coordinates. Biomed Opt Express. 2010 Jul 15;1(1):165–75.

122. Arridge SR, Dehghani H, Schweiger M, Okada E. The finite element model for the propagation of light in scattering media: A direct method for domains with nonscattering regions. Medical Physics. 2000;27(1):252–64.

123. Xu Y, Zhang Q, Jiang H. Optical image reconstruction of non-scattering and low scattering heterogeneities in turbid media based on the diffusion approximation model. J Opt A: Pure Appl Opt. 2003 Sep;6(1):29–35.

124. Custo A, Iii WMW, Barnett AH, Hillman EMC, Boas DA. Effective scattering coefficient of the cerebral spinal fluid in adult head models for diffuse optical imaging. Appl Opt, AO. 2006 Jul 1;45(19):4747–55.

125. Zhu C, Liu Q. Review of Monte Carlo modeling of light transport in tissues. Journal of Biomedical Optics. 2013 May 10;18(5):050902.

126. Wang L, Jacques SL, Zheng L. MCML—Monte Carlo modeling of light transport in multi-layered tissues. Computer Methods and Programs in Biomedicine. 1995 Jul 1;47(2):131–46.

127. Suzuki S, Takasaki S, Ozaki T, Kobayashi Y. Tissue oxygenation monitor using NIR spatially resolved spectroscopy. In: Optical Tomography and Spectroscopy of Tissue III [Internet]. International Society for Optics and Photonics; 1999 [cited 2018 Sep 16]. p. 582–93. Available from: https://www.spiedigitallibrary.org/conference-proceedings-of-spie/3597/0000/Tissue-oxygenation-monitor-using-NIR-spatially-resolved-spectroscopy/10.1117/12.356862.short

128. Abdul WM, Tobita N, Nishidate I, Kawauchi S, Sato S. Multispectral imaging of hemoglobin concentration and tissue scattering in mice during cutaneous two-stage chemical carcinogenesis. In: 2017 OPJ-OSA Joint Symposia on Nanophotonics and Digital Photonics (2017), paper 30aOD2 [Internet]. Optical Society of America; 2017 [cited 2018 Sep 16]. p. 30aOD2. Available from: https://www.osapublishing.org/abstract.cfm?uri=OPJ-2017-30aOD2

129. Nishidate I, Maeda T, Niizeki K, Aizu Y. Estimation of melanin and hemoglobin using spectral reflectance images reconstructed from a digital RGB image by the Wiener estimation method. Sensors (Basel). 2013 Jun 19;13(6):7902–15.

130. Shi T, DiMarzio CA. Multispectral method for skin imaging: development and validation. Appl Opt, AO. 2007 Dec 20;46(36):8619–26.

131. Vogel A, Chernomordik VV, Riley JD, Hassan M, Amyot F, Dasgeb B, et al. Using noninvasive multispectral imaging to quantitatively assess tissue vasculature. J Biomed Opt. 2007;12(5):051604.

132. Styles IB, Calcagni A, Claridge E, Orihuela-Espina F, Gibson JM. Quantitative analysis of multi-spectral fundus images. Med Image Anal. 2006 Aug;10(4):578–97.

133. Levenson RM, Mansfield JR. Multispectral imaging in biology and medicine: Slices of life. Cytometry. 2006 Aug 1;69A(8):748–58.

134. Binzoni T, Vogel A, Gandjbakhche AH, Marchesini R. Detection limits of multi-spectral optical imaging under the skin surface. Phys Med Biol. 2008;53(3):617.

135. Tomatis S, Carrara M, Bono A, Bartoli C, Lualdi M, Tragni G, et al. Automated melanoma detection with a novel multispectral imaging system: results of a prospective study. Phys Med Biol. 2005;50(8):1675.

136. Farina B, Bartoli C, Bono A, Colombo A, Lualdi M, Tragni G, et al. Multispectral imaging approach in the diagnosis of cutaneous melanoma: potentiality and limits. Phys Med Biol. 2000;45(5):1243.

137. Jolivot R, Vabres P, Marzani F. Reconstruction of hyperspectral cutaneous data from an artificial neural network-based multispectral imaging system. Computerized Medical Imaging and Graphics. 2011 Mar 1;35(2):85–8.

138. Jolivot R, Benezeth Y, Marzani F. Skin Parameter Map Retrieval from a Dedicated Multispectral Imaging System Applied to Dermatology/Cosmetology. Journal of Biomedical Imaging. 2013 Jan;2013:26:26–26:26.

139. Everdell NL, Styles IB, Calcagni A, Gibson J, Hebden J, Claridge E. Multispectral imaging of the ocular fundus using light emitting diode illumination. Review of Scientific Instruments. 2010 Sep 1;81(9):093706.

140. Claridge E, Hidović-Rowe D. Model Based Inversion for Deriving Maps of Histological Parameters Characteristic of Cancer From Ex-Vivo Multispectral Images of the Colon. IEEE Transactions on Medical Imaging. 2014 Apr;33(4):822–35.

141. Descoteaux M, Maier-Hein L, Franz A, Jannin P, Collins DL, Duchesne S. Medical Image Computing and Computer-Assisted Intervention − MICCAI 2017: 20th International Conference, Quebec City, QC, Canada, September 11-13, 2017, Proceedings. Springer; 2017. 737 p.

142. Wirkert SJ, Kenngott H, Mayer B, Mietkowski P, Wagner M, Sauer P, et al. Robust near real-time estimation of physiological parameters from megapixel multispectral images with inverse Monte Carlo and random forest regression. International Journal of Computer Assisted Radiology and Surgery [Internet]. 2016 Jun 1 [cited 2017 Sep 26];(Volume 11, Issue 6). Available from: http://paperity.org/p/76170896/robust-near-real-time-estimation-of-physiological-parameters-from-megapixel-multispectral

143. Zhang S, Gnyawali S, Huang J, Ren W, Gordillo G, Sen CK, et al. Multimodal imaging of cutaneous wound tissue. J Biomed Opt [Internet]. 2015 Jan [cited 2017 Sep 26];20(1). Available from: http://www.ncbi.nlm.nih.gov/pmc/articles/PMC4300315/

144. Wilson RH, Nadeau KP, Jaworski FB, Rowland R, Nguyen JQM, Crouzet C, et al. Quantitative short-wave infrared multispectral imaging of <italic<in vivo</italic< tissue optical properties. JBO, JBOPFO. 2014 Aug;19(8):086011.

145. Free Microscope Software ZEN lite from ZEISS Microscopy [Internet]. [cited 2018 Jul 20]. Available from: https://www.zeiss.com/microscopy/int/products/microscope-software/zen-lite.html

146. Hale GM, Querry MR. Optical Constants of Water in the 200-nm to 200-μm Wavelength Region. Appl Opt, AO. 1973 Mar 1;12(3):555–63.

147. Prahl SA. Tabulated Molar Extinction Coefficient for Hemoglobin in Water [Internet]. [cited 2018 Jun 14]. Available from: https://omlc.org/spectra/hemoglobin/summary.html

148. Veen RLP van, Sterenborg H j c m, Pifferi A, Torricelli A, Cubeddu R. Determination of VIS- NIR absorption coefficients of mammalian fat, with time- and spatially resolved diffuse reflectance and transmission spectroscopy. In: Biomedical Topical Meeting (2004), paper SF4 [Internet]. Optical Society of America; 2004 [cited 2018 Jun 14]. p. SF4. Available from: https://www.osapublishing.org/abstract.cfm?uri=BIO-2004-SF4

149. Jacques SL, McAuliffe DJ. The Melanosome: Threshold Temperature for Explosive Vaporization and Internal Absorption Coefficient During Pulsed Laser Irradiation. Photochemistry and Photobiology. 53(6):769–75.

150. Jacques SL. Optical properties of biological tissues: a review. Phys Med Biol. 2013;58(11):R37.

151. Weisstein EW. Least Squares Fitting--Exponential [Internet]. [cited 2017 Jul 21]. Available from: http://mathworld.wolfram.com/LeastSquaresFittingExponential.html

152. Anderson RR, Parrish JA. The Optics of Human Skin. Journal of Investigative Dermatology. 1981 Jul 1;77(1):13–9.

153. Sheng C, Pogue BW, Dehghani H, O'Hara JA, Hoopes PJ. Numerical light dosimetry in murine tissue: analysis of tumor curvature and angle of incidence effects upon fluence in the tissue. In: Optical Methods for Tumor Treatment and Detection: Mechanisms and Techniques in Photodynamic Therapy XII [Internet]. International Society for Optics and Photonics; 2003 [cited 2018 Jun 14]. p. 39–48. Available from: https://www.spiedigitallibrary.org/conference-proceedings-of-spie/4952/0000/Numerical-light-dosimetry-in-murine-tissue--analysis-of-tumor/10.1117/12.474081.short

154. Hidović-Rowe D, Claridge E. Modelling and validation of spectral reflectance for the colon. Phys Med Biol. 2005 Mar 21;50(6):1071–93.

155. The Biochemistry and Physiology of Bone [Internet]. Elsevier; 1956 [cited 2018 Jun 14]. Available from: http://linkinghub.elsevier.com/retrieve/pii/C20130125330

156. Bashkatov AN, Genina ÉA, Kochubey VI, Tuchin VV. Optical properties of the subcutaneous adipose tissue in the spectral range 400–2500 nm. Opt Spectrosc. 2005 Nov 1;99(5):836–42.

157. Chapman G. The body fluids and their functions. Edward Arnold; 1967. 88 p.

158. Meglinski IV, Matcher SJ. Quantitative assessment of skin layers absorption and skin reflectance spectra simulation in the visible and near-infrared spectral regions. Physiological Measurement. 2002 Nov 1;23(4):741–53.

159. Yudovsky D, Pilon L. Retrieving skin properties from in vivo spectral reflectance measurements. J Biophotonics. 2011 May;4(5):305–14.

160. Kaniusas E. Biomedical Signals and Sensors II: Linking Acoustic and Optic Biosignals and Biomedical Sensors [Internet]. Berlin Heidelberg: Springer-Verlag; 2015 [cited 2018 Jun 18]. (Biological and Medical Physics, Biomedical Engineering). Available from: //www.springer.com/gb/book/9783662451052

161. Zonios G, Bykowski J, Kollias N. Skin Melanin, Hemoglobin, and Light Scattering Properties can be Quantitatively Assessed In Vivo Using Diffuse Reflectance Spectroscopy. Journal of Investigative Dermatology. 2001 Dec 1;117(6):1452–7.

162. Streif JUG, Hiller K-H, Waller C, Nahrendorf M, Wiesmann F, Bauer WR, et al. In vivo assessment of absolute perfusion in the murine skeletal muscle with spin labeling MRI. Magnetic resonance imaging. J Magn Reson Imaging. 2003 Jan;17(1):147–52.

163. Villard JW, Feldman MD, Kim J, Milner TE, Freeman GL. Use of a blood substitute to determine instantaneous murine right ventricular thickening with optical coherence tomography. Circulation. 2002 Apr 16;105(15):1843–9.

164. Tzoumas S, Nunes A, Olefir I, Stangl S, Symvoulidis P, Glasl S, et al. Eigenspectra optoacoustic tomography achieves quantitative blood oxygenation imaging deep in tissues. Nature Communications. 2016 Jun 30;7:12121.

165. Tsai AG, Cabrales P, Winslow RM, Intaglietta M. Microvascular oxygen distribution in awake hamster window chamber model during hyperoxia. Am J Physiol Heart Circ Physiol. 2003 Oct;285(4):H1537-1545.

166. Kimura M, Takemori S, Yamaguchi M, Umazume Y. Differential osmotic behavior of water components in living skeletal muscle resolved by 1H-NMR. Biophys J. 2005 Aug;89(2):1143–9.

167. Mitchell HH, Hamilton TS, Steggerda FR, Bean HW. The Chemical Composition of the Adult Human Body and Its Bearing on the Biochemistry of Growth. J Biol Chem. 1945 May 1;158(3):625–37.

168. Karampinos DC, Ruschke S, Dieckmeyer M, Diefenbach M, Franz D, Gersing AS, et al. Quantitative MRI and spectroscopy of bone marrow. J Magn Reson Imaging. 2018 Feb;47(2):332–53.

169. Lassailly F, Foster K, Lopez-Onieva L, Currie E, Bonnet D. Multimodal imaging reveals structural and functional heterogeneity in different bone marrow compartments: functional implications on hematopoietic stem cells. Blood. 2013 Sep 5;122(10):1730–40.

170. Maeda T, Arakawa N, Takahashi M, Aizu Y. Monte Carlo simulation of spectral reflectance using a multilayered skin tissue model. OPT REV. 2010 May 1;17(3):223–9.

171. Fredriksson I, Larsson M, Strömberg T. Inverse Monte Carlo method in a multilayered tissue model for diffuse reflectance spectroscopy. JBO. 2012 Apr;17(4):047004.

172. Fredriksson I, Burdakov O, Larsson M, Strömberg T. Inverse Monte Carlo in a multilayered tissue model: merging diffuse reflectance spectroscopy and laser Doppler flowmetry. Journal of Biomedical Optics. 2013 Dec 18;18(12):127004.

173. Wangpraseurt D, Jacques SL, Petrie T, Kühl M. Monte Carlo Modeling of Photon Propagation Reveals Highly Scattering Coral Tissue. Front Plant Sci [Internet]. 2016 [cited 2019 Feb 20];7. Available from: https://www.frontiersin.org/articles/10.3389/fpls.2016.01404/full

174. Spectralon® Diffuse Reflectance Standards - Labsphere | Internationally Recognized Photonics Company [Internet]. [cited 2018 Sep 16]. Available from: https://www.labsphere.com/labsphere-products-solutions/materials-coatings-2/targets-standards/diffuse-reflectance-standards/diffuse-reflectance-standards/

175. Yoshimi R, Hama M, Takase K, Ihata A, Kishimoto D, Terauchi K, et al. Ultrasonography is a potent tool for the prediction of progressive joint destruction during clinical remission of rheumatoid arthritis. Modern Rheumatology. 2013 May;23(3):456–65.

176. RetigaEXi.pdf [Internet]. [cited 2019 Feb 14]. Available from: https://www.meyerinst.com/html/qimaging/retigaexi/RetigaEXi.pdf

177. Thorlabs.com - Engineered Diffusers™ [Internet]. [cited 2019 Feb 14]. Available from: https://www.thorlabs.com/NewGroupPage9_PF.cfm?ObjectGroup_ID=1660

178. Wire Grid Polarizing Film | Edmund Optics [Internet]. [cited 2019 Feb 14]. Available from: /f/Wire-Grid-Polarizing-Film/14980/

179. Mounted N-BK7 Reflective Neutral Density Filters [Internet]. [cited 2019 Feb 20]. Available from: https://www.thorlabs.com/newgrouppage9.cfm?objectgroup_id=119

180. Ray S. Scientific Photography and Applied Imaging. CRC Press; 2015. 584 p.

181. Guggenheim JA, Bargigia I, Farina A, Pifferi A, Dehghani H. Time resolved diffuse optical spectroscopy with geometrically accurate models for bulk parameter recovery. Biomed Opt Express, BOE. 2016 Sep 1;7(9):3784–94.

182. Ariana DP, Lu R. Evaluation of internal defect and surface color of whole pickles using hyperspectral imaging. Journal of Food Engineering. 2010 Feb 1;96(4):583–90.

183. Ariana DP, Lu R. Quality evaluation of pickling cucumbers using hyperspectral reflectance and transmittance imaging—Part II. Performance of a prototype. Sens & Instrumen Food Qual. 2008 Sep 1;2(3):152–60.

184. Zarco-Tejada PJ, Berjón A, López-Lozano R, Miller JR, Martín P, Cachorro V, et al. Assessing vineyard condition with hyperspectral indices: Leaf and canopy reflectance simulation in a row-structured discontinuous canopy. Remote Sensing of Environment. 2005 Nov 30;99(3):271–87.

185. Leiva-Valenzuela GA, Lu R, Aguilera JM. Assessment of internal quality of blueberries using hyperspectral transmittance and reflectance images with whole spectra or

selected wavelengths. Innovative Food Science & Emerging Technologies. 2014 Aug 1;24:2–13.

186. Qin J, Chao K, Kim MS, Lu R, Burks TF. Hyperspectral and multispectral imaging for evaluating food safety and quality. Journal of Food Engineering. 2013 Sep 1;118(2):157–71.

187. Lu G, Fei B. Medical hyperspectral imaging: a review. J Biomed Opt [Internet]. 2014 Jan [cited 2019 Feb 19];19(1). Available from: https://www.ncbi.nlm.nih.gov/pmc/articles/PMC3895860/

188. Gat N. Imaging spectroscopy using tunable filters: a review. In: Wavelet Applications VII [Internet]. International Society for Optics and Photonics; 2000 [cited 2019 Feb 20]. p. 50–65. Available from: https://www.spiedigitallibrary.org/conference-proceedings-of-spie/4056/0000/Imaging-spectroscopy-using-tunable-filters-a-review/10.1117/12.381686.short

189. Kharitonov V. Software CTAnalyser, version 1.10. 9.0. Kontich, Bélgica, DVD licenciado. 2003;

190. Lorensen WE, Cline HE. Marching Cubes: A High Resolution 3D Surface Construction Algorithm. In: Proceedings of the 14th Annual Conference on Computer Graphics and Interactive Techniques [Internet]. New York, NY, USA: ACM; 1987 [cited 2019 Feb 28]. p. 163–169. (SIGGRAPH ’87). Available from: http://doi.acm.org/10.1145/37401.37422

191. Jolliffe IT. Principal Component Analysis [Internet]. New York: Springer-Verlag; 1986 [cited 2019 Feb 14]. (Springer Series in Statistics). Available from: https://www.springer.com/us/book/9781475719048

192. Liu Z-P. Linear Discriminant Analysis. In: Dubitzky W, Wolkenhauer O, Cho K-H, Yokota H, editors. Encyclopedia of Systems Biology [Internet]. New York, NY: Springer New York; 2013 [cited 2019 Feb 14]. p. 1132–3. Available from: https://doi.org/10.1007/978-1-4419-9863-7_395

193. mouse TNF driven spondyloarthritis (TNFΔARE) - Biomedcode [Internet]. [cited 2017 Jul 26]. Available from: http://www.biomedcode.com/gr/en/content/mouse-tnf-driven-spondyloarthritis-tnfdare

194. Nell VPK, Machold KP, Eberl G, Stamm TA, Uffmann M, Smolen JS. Benefit of very early referral and very early therapy with disease-modifying anti-rheumatic drugs in patients with early rheumatoid arthritis. Rheumatology (Oxford). 2004 Jul 1;43(7):906–14.

195. Linden MPM van der, Cessie S le, Raza K, Woude D van der, Knevel R, Huizinga TWJ, et al. Long-term impact of delay in assessment of patients with early arthritis. Arthritis & Rheumatism. 2010 Dec 1;62(12):3537–46.

196. Cootes TF, Taylor CJ, Cooper DH, Graham J. Active Shape Models-Their Training and Application. Computer Vision and Image Understanding. 1995 Jan 1;61(1):38–59.

197. Bathon JM, Martin RW, Fleischmann RM, Tesser JR, Schiff MH, Keystone EC, et al. A comparison of etanercept and methotrexate in patients with early rheumatoid arthritis. N Engl J Med. 2000 Nov 30;343(22):1586–93.

198. Jiang Y, Genant HK, Watt I, Cobby M, Bresnihan B, Aitchison R, et al. A multicenter, double-blind, dose-ranging, randomized, placebo-controlled study of recombinant human interleukin-1 receptor antagonist in patients with rheumatoid arthritis: radiologic progression and correlation of Genant and Larsen scores. Arthritis Rheum. 2000 May;43(5):1001–9.

199. Google Code Archive - Long-term storage for Google Code Project Hosting. [Internet]. [cited 2019 Feb 28]. Available from: https://code.google.com/archive/p/gpumcml/

200. The Laboratory Mouse [Internet]. Elsevier; 2004 [cited 2018 Jun 11]. Available from: http://linkinghub.elsevier.com/retrieve/pii/B9780123364258X50511

201. Flecknell P. ADVANCES IN THE ASSESSMENT AND ALLEVIATION OF PAIN IN LABORATORY AND DOMESTIC ANIMALS. Journal of Veterinary Anaesthesia. 1994 Dec 1;21(2):98–105.

202. Yang C, Lu L, Lin H, Guan R, Shi X, Liang Y. A Fuzzy-Statistics-Based Principal Component Analysis (FS-PCA) Method for Multispectral Image Enhancement and Display. IEEE Transactions on Geoscience and Remote Sensing. 2008 Nov;46(11):3937–47.

203. Pu H, He W, Zhang G, Zhang B, Liu F, Zhang Y, et al. Separating structures of different fluorophore concentrations by principal component analysis on multispectral excitation-resolved fluorescence tomography images. Biomed Opt Express, BOE. 2013 Oct 1;4(10):1829–45.

204. Rodarmel C, Shan J. Principal Component Analysis for Hyperspectral Image Classification. 62(2):9.

205. Kainerstorfer JM, Ehler M, Amyot F, Hassan M, Demos SG, Chernomordik VV, et al. Principal component model of multispectral data for near real-time skin chromophore mapping. JBO. 2010 Jul;15(4):046007.

206. Bandos TV, Bruzzone L, Camps-Valls G. Classification of Hyperspectral Images With Regularized Linear Discriminant Analysis. IEEE Transactions on Geoscience and Remote Sensing. 2009 Mar;47(3):862–73.

207. Paquit VC, Tobin KW, Price JR, Mériaudeau F. 3D and Multispectral Imaging for Subcutaneous Veins Detection. Opt Express, OE. 2009 Jul 6;17(14):11360–5.

208. Akhloufi MA, Bendada A, Batsale J-C. Multispectral face recognition using non linear dimensionality reduction. In: Rahman Z-U, Reichenbach SE, Neifeld MA, editors. Orlando, Florida, USA; 2009 [cited 2019 Feb 20]. p. 73410J. Available from: http://proceedings.spiedigitallibrary.org/proceeding.aspx?doi=10.1117/12.818275

209. Marenzana M, Velde GV. Refine, reduce, replace: Imaging of fibrosis and arthritis in animal models. Best Practice & Research Clinical Rheumatology. 2015 Dec 1;29(6):715–40.

210. Sim JH, Lee WK, Lee YS, Kang JS. Assessment of collagen antibody-induced arthritis in BALB/c mice using bioimaging analysis and histopathological examination. Lab Anim Res. 2016 Sep;32(3):135–43.

211. Mitra A, Kundu-Raychaudhuri S, Abria C, Rona A, Chaudhari AJ, Raychaudhuri SP. In-vivo quantitative assessment of the therapeutic response in a mouse model of collagen-induced arthritis using 18F-fluorodeoxyglucose positron emission tomography. Clin Exp Immunol. 2017 May;188(2):293–8.

212. Jacobs BY, Kloefkorn HE, Allen KD. Gait analysis methods for rodent models of osteoarthritis. Curr Pain Headache Rep. 2014 Oct;18(10):456.

213. Bains RS, Wells S, Sillito RR, Armstrong JD, Cater HL, Banks G, et al. Assessing mouse behaviour throughout the light/dark cycle using automated in-cage analysis tools. Journal of Neuroscience Methods. 2018 Apr 15;300:37–47.

214. Lin Y, Yan H, Nalcioglu O, Gulsen G. Quantitative fluorescence tomography with functional and structural a priori information. Appl Opt. 2009 Mar 1;48(7):1328–36.

215. Lin Y, Barber WC, Iwanczyk JS, Roeck W, Nalcioglu O, Gulsen G. Quantitative fluorescence tomography using a combined tri-modality FT/DOT/XCT system. Opt Express. 2010 Mar 31;18(8):7835–50.

216. Stuker F, Ripoll J, Rudin M. Fluorescence Molecular Tomography: Principles and Potential for Pharmaceutical Research. Pharmaceutics. 2011 Apr 26;3(2):229–74.

217. Levenson RM, Lynch DT, Kobayashi H, Backer JM, Backer MV. Multiplexing with multispectral imaging: from mice to microscopy. ILAR J. 2008;49(1):78–88.

218. Lv Y, Zhang J, Zhang D, Cai W, Chen N, Luo J. In vivo simultaneous multispectral fluorescence imaging with spectral multiplexed volume holographic imaging system. JBO, JBOPFO. 2016 Jun;21(6):060502.

219. Mansfield JR, Gossage KW, Hoyt CC, Levenson RM. Autofluorescence removal, multiplexing, and automated analysis methods for in-vivo fluorescence imaging. J Biomed Opt. 2005 Aug;10(4):41207.

220. Namvaran A, Mahmoudi J, Sadigh-Eteghad S, Shotorbani SS, Reyhani-Rad S. A Visualized Guideline for Cancer Chemotherapy Induced Neuropathic Pain in Mice Using Cisplatin. Journal of Experimental and Clinical Neurosciences. 2015 Jul 22;2(1):1–4.

221. Corlu A, Durduran T, Choe R, Schweiger M, Hillman EMC, Arridge SR, et al. Uniqueness and wavelength optimization in continuous-wave multispectral diffuse optical tomography. Opt Lett, OL. 2003 Dec 1;28(23):2339–41.

222. Eames ME, Wang J, Pogue BW, Dehghani H. Wavelength band optimization in spectral near-infrared optical tomography improves accuracy while reducing data acquisition and computational burden. J Biomed Opt. 2008;13(5):054037.

223. Chen L-Y, Pan M-C, Yan C-C, Pan M-C. Wavelength optimization using available laser diodes in spectral near-infrared optical tomography. Appl Opt, AO. 2016 Jul 20;55(21):5729–37.

224. OSA | Evaluation and unification of some methods for estimating reflectance spectra from RGB images [Internet]. [cited 2018 Jul 3]. Available from: https://www.osapublishing.org/josaa/abstract.cfm?uri=josaa-25-10-2444

225. Valero EM, Hu Y, Hernández-Andrés J, Eckhard T, Nieves JL, Romero J, et al. Comparative performance analysis of spectral estimation algorithms and computational optimization of a multispectral imaging system for print inspection. Color Research & Application. 39(1):16–27.

226. Li P, Liu C, Li X, He H, Ma H. GPU acceleration of Monte Carlo simulations for polarized photon scattering in anisotropic turbid media. Appl Opt. 2016 Sep 20;55(27):7468–76.

227. Yao R, Intes X, Fang Q. Generalized mesh-based Monte Carlo for wide-field illumination and detection via mesh retessellation. Biomed Opt Express. 2015 Dec 18;7(1):171–84.

228. Ren N, Liang J, Qu X, Li J, Lu B, Tian J. GPU-based Monte Carlo simulation for light propagation in complex heterogeneous tissues. Opt Express, OE. 2010 Mar 29;18(7):6811–23.

229. Pauwels E, Van Loo D, Cornillie P, Brabant L, Van Hoorebeke L. An exploratory study of contrast agents for soft tissue visualization by means of high resolution X-ray computed tomography imaging. J Microsc. 2013 Apr;250(1):21–31.

230. Rose S, Waters EA, Haney CR, Meade CTJ, Perlman H. High Resolution MRI of Arthritic Murine Ankle Joints Discriminates Inflammation and Bone Destruction in a Quantifiable Manner. Arthritis Rheum. 2013 Sep;65(9):2279–89.

231. Schaad L, Hlushchuk R, Barré S, Gianni-Barrera R, Haberthür D, Banfi A, et al. Correlative Imaging of the Murine Hind Limb Vasculature and Muscle Tissue by MicroCT and Light Microscopy. Scientific Reports. 2017 Feb 7;7:41842.

232. Hielscher AH, Kim HK, Montejo LD, Blaschke S, Netz UJ, Zwaka PA, et al. Frequency-Domain Optical Tomographic Imaging of Arthritic Finger Joints. IEEE Transactions on Medical Imaging. 2011 Oct;30(10):1725–36.

233. Yuan Z, Zhang Q, Sobel ES, Jiang H. Image-guided optical spectroscopy in diagnosis of osteoarthritis: a clinical study. Biomed Opt Express. 2010 Jul 14;1(1):74–86.

234. Scheel AK, Netz UJ, Hermann K-GA, Hielscher AH, Klose AD, Tresp V, et al. Laser Imaging Techniques for Follow-up Analysis of Joint Inflammation in Patients with Rheumatoid Arthritis. Medical Laser Application. 2003 Jan 1;18(3):198–205.

235. Canvin JMG, Bernatsky S, Hitchon CA, Jackson M, Sowa MG, Mansfield JR, et al. Infrared spectroscopy: shedding light on synovitis in patients with rheumatoid arthritis. Rheumatology (Oxford). 2003 Jan;42(1):76–82.

236. Onna M van, Cate DFT, Tsoi KL, Meier AJL, Jacobs JWG, Westgeest A a. A, et al. Assessment of disease activity in patients with rheumatoid arthritis using optical spectral transmission measurements, a non-invasive imaging technique. Annals of the Rheumatic Diseases. 2015 Oct 9;annrheumdis-2015-207315.

237. Paluchowski LA, Milanic M, Bjorgan A, Grandaunet B, Dhainaut A, Hoff M, et al. Identification of inflammation sites in arthritic joints using hyperspectral imaging. In: Imaging, Manipulation, and Analysis of Biomolecules, Cells, and Tissues XII [Internet]. International Society for Optics and Photonics; 2014 [cited 2018 Aug 21]. p. 89470H. Available from: https://www.spiedigitallibrary.org/conference-proceedings-of-

spie/8947/89470H/Identification-of-inflammation-sites-in-arthritic-joints-using-hyperspectral-imaging/10.1117/12.2040499.short